

**ASSESSMENTS OF MULTISCALE PRECIPITATION DATA FUSION AND SOIL
MOISTURE DATA ASSIMILATION AND THEIR ROLES IN HYDROLOGICAL
FORECASTS**

by

Shugong Wang

BS, Lanzhou University, 2000

PHD, Graduate University of Chinese Academy of Sciences, China, 2006

Submitted to the Graduate Faculty of
Swanson School of Engineering in partial fulfillment
of the requirements for the degree of
Doctor of Philosophy

University of Pittsburgh

2011

UNIVERSITY OF PITTSBURGH
SWANSON SCHOOL OF ENGINEERING

This dissertation was presented

by

Shugong Wang

It was defended on

August 05, 2011

and approved by

Daniel J. Bain, Ph.D., Assistant Professor, Department of Geology and Planetary Science

Jorge D. Abad, Ph.D., Assistant Professor, Department of Civil and Environmental Engineering

Zhi-Hong Mao, Ph.D. Assistant Professor, Department of Electrical and Computer Engineering

Dissertation Director: Xu Liang, Ph.D., Associate Professor, Department of Civil and Environmental
Engineering

Copyright © by Shugong Wang

2011

ASSESSMENTS OF MULTISCALE PRECIPITATION DATA FUSION AND SOIL MOISTURE DATA ASSIMILATION AND THEIR ROLES IN HYDROLOGICAL FORECASTS

Shugong Wang, PhD

University of Pittsburgh, 2011

Precipitation is the most important input for hydrological simulations and soil moisture contents (SMCs) are the most important state variables of hydrological system. We can improve hydrological simulations by improving the quality of precipitation data and assimilating satellite-measured SMC data into land surface simulation. Multiscale data fusion is an effective approach to derive precipitation data due to the multiscale characteristics of precipitation measurements. Multiscale data assimilation is the exact approach to **assimilate** satellite-measured SMC data into land surface simulations when measurements and model simulations are not at the same spatial resolution. To date, no systematic assessments of these approaches have been conducted in hydrological simulations. For the purpose of improving hydrological forecast, this study assesses influences of precipitation data fusion and soil moisture data assimilation on the simulations of streamflow, SMCs and evapotranspiration over 14 watersheds selected from the Ohio River Basin.

As the technical basis of this study, a large-scale flow routing scheme and a parameter calibration scheme with multiple precipitation inputs are developed for Noah LSM. A multiscale data fusion algorithm, namely Multiscale Kalman Smoother (MKS) based framework, which plays an important role in multiscale precipitation data fusion and multiscale soil moisture data

assimilation, is assessed in a large experimental site with 2246 precipitation events in 2003. Three precipitation data products are derived by fusing NLDAS-2 precipitation data product and NEXRAD MPE precipitation data product with the MKS-based framework. For the assessment over the 14 watersheds in three individual years, essential improvements of hydrological simulation have been found for a half number of cases. Findings of this assessment show that precipitation data fusion is a statistically effective approach to improve hydrological simulations. To assess the influences of soil moisture data assimilation on hydrological simulation, AMSR-E SMC data are assimilated into land surface simulation by Noah LSM. Results show that soil moisture data assimilation has not improved hydrological simulations for most of cases because AMSR-E data underestimate SMC compared with model simulations. However, for those cases in which precipitation data overestimate real precipitation, the soil moisture data assimilation has been proved as an effective approach to improve hydrological simulations.

TABLE OF CONTENTS

ACKNOWLEDGMENTS	XXXI
1.0 INTRODUCTION.....	1
1.1 RESEARCH MOTIVATIONS.....	1
1.2 RESEARCH QUESTIONS.....	13
1.3 RESEARCH DESIGN.....	14
2.0 A LARGE-SCALE FLOW ROUTING SCHEME FOR LAND SURFACE MODEL. 16	
2.1 INTRODUCTION	16
2.2 LARGE-SCALE FLOW NETWORK DERIVATION ALGORITHM.....	20
2.3 GRID-ORDERING ALGORITHM.....	22
2.4 FLOW ROUTING METHODS.....	26
2.4.1 In-Grid routing.....	26
2.4.2 Between-Grid routing.....	28
2.5 APPLICATIONS AND DISCUSSIONS.....	29
2.5.1 Analysis of derived flow network	32
2.5.2 Comparison of assumptions for baseflow routing	34
2.5.3 Comparison of approximations for unit hydrograph.....	36
2.5.4 Comparison of approximations for channel length	39
2.5.5 Investigation on the redundancy of the routing scheme	40

2.6	SUMMARY	43
3.0	A PARAMETER CALIBRATION SCHEME FOR NOAH LAND SURFACE MODEL WITH MULTIPLE PRECIPITATION INPUTS	45
3.1	INTRODUCTION	45
3.2	BRIEF DESCRIPTION OF NOAH LSM	49
3.3	FOUR-COEFFICIENT APPROXIMATION.....	54
3.4	FORMULATION OF OPTIMIZATION PROBLEM.....	59
3.5	MPI-BASED MOPSO ALGORITHM	61
3.6	EVALUATIONS	66
3.7	SUMMARY	75
4.0	ASSESSMENT OF MULTISCALE DATA FUSION ALGORITHM IN PRECIPITATION DATA FUSION	77
4.1	INTRODUCTION	77
4.2	MULTISCALE KALMAN SMOOTHER-BASED (MKS-BASED) FRAMEWORK	80
4.3	STUDY AREA AND DATA	84
4.4	EXPERIMENTS AND RESULTS	85
4.4.1	Experiment Design.....	85
4.4.2	Results and Discussion.....	93
4.4.2.1	Experiment 1	93
4.4.2.2	Discussion.....	104
4.4.2.3	Experiment 2	107
4.5	CONCLUSIONS.....	118
5.0	ASSESSMENT OF PRECIPITATION DATA FUSION ON HYDROLOGICAL SIMULATIONS	122

5.1	INTRODUCTION	122
5.2	METHOD FOR PRECIPITATION DATA FUSION	129
5.3	EXPERIMENTAL WATERSHEDS AND DATA ANALYSIS	135
5.3.1	Experimental watersheds	135
5.3.2	Data analysis.....	137
5.4	SETTINGS OF PRECIPITATION DATA FUSION	144
5.5	ASSESSMENT OF FUSED PRECIPITATION DATA.....	146
5.5.1	Assessment with streamflow simulations.....	146
5.5.2	Assessment with soil moisture simulations	191
5.5.3	Assessment with evapotranspiration simulations	209
5.6	SUMMARY AND CONCLUSIONS	218
6.0	ASSESSMENT OF SOIL MOISTURE DATA ASSIMILATION ON HYDROLOGICAL SIMULATIONS.....	223
6.1	INTRODUCTION	223
6.2	EXPERIMENT DESIGN	229
6.2.1	Experimental watersheds	229
6.2.2	Data assimilation experiments	229
6.3	ANALYSIS OF AMSR-E DATA	232
6.3.1	Data missing and processing	232
6.3.2	Magnitudes of the AMSR-E data	234
6.4	ASSESSMENTS OF SOIL MOISTURE DATA ASSIMILATION	245
6.4.1	Assessment in the simulation of soil moisture contents.....	245
6.4.2	Assessments in streamflow simulation	255

6.4.3	Assessment in the simulation of evapotranspiration	269
6.5	SUMMARY AND CONCLUSIONS	277
7.0	SUMMARY AND CONCLUSIONS.....	279
	BIBLIOGRAPHY.....	283

LIST OF TABLES

Table 2.1 Ranges of parameters in calibration.....	30
Table 2.2 Calibrated parameters and corresponding Nash-Sutcliffe efficiencies (NSEs) of Experiment 1, 2, 3, 4 and 5.	31
Table 3.1 Default parameter values for 15 soil types used in Noah LSM.....	55
Table 3.2 Optimal parameters used in streamflow simulation	57
Table 3.3 Yearly Nash-Sutcliffe Efficiencies (NSEs) in the calibration period (2003-2005) and the validation period (2006-2007) in KINT1 watershed corresponding the five precipitation inputs.....	70
Table 3.4 Yearly Nash-Sutcliffe Efficiencies (NSEs) in the calibration period (2003-2005) and the validation period (2006-2007) in SERI3 watershed corresponding the five precipitation inputs.....	71
Table 4.1 A list of twenty-one noise levels used in generating Type-I errors	90
Table 4.2 A list of fifteen bias levels used in generating Type-II errors	90
Table 4.3 A list of various <i>Corr</i> and <i>RMSE</i> values for Experiment 1 and Experiment 2 for an individual storm occurring at 9:00 AM of September 22, 2003.....	116
Table 5.1 Areas, elevation ranges and descriptions of the 14 experimental watersheds	162
Table 5.2 Nash-Sutcliffe Efficiencies (NSEs) corresponding to the five precipitation inputs in ALDS2 watershed.....	164
Table 5.3 Nash-Sutcliffe Efficiencies (NSEs) corresponding to the five precipitation inputs in ALPI2 watershed	167
Table 5.4 Nash-Sutcliffe Efficiencies (NSEs) corresponding to the five precipitation inputs in BAKI3 watershed.....	168

Table 5.5 Nash-Sutcliffe Efficiencies (NSEs) corresponding to the five precipitation inputs in BSNK2 watershed.....	169
Table 5.6 Nash-Sutcliffe Efficiencies (NSEs) corresponding to the five precipitation inputs in CLAI2 watershed.....	173
Table 5.7 Nash-Sutcliffe Efficiencies (NSEs) corresponding to the five precipitation inputs in CRWI3 watershed.....	176
Table 5.8 Nash-Sutcliffe Efficiencies (NSEs) corresponding to the five precipitation inputs in CYCK2 watershed.....	178
Table 5.9 Nash-Sutcliffe Efficiencies (NSEs) corresponding to the five precipitation inputs in DBVO1 watershed.....	180
Table 5.10 Nash-Sutcliffe Efficiencies (NSEs) corresponding to the five precipitation inputs in ELRP1 watershed.....	181
Table 5.11 Nash-Sutcliffe Efficiencies (NSEs) corresponding to the five precipitation inputs in FDYO1 watershed.....	183
Table 5.12 Nash-Sutcliffe Efficiencies (NSEs) corresponding to the five precipitation inputs in KINT1 watershed.....	184
Table 5.13 Nash-Sutcliffe Efficiencies (NSEs) corresponding to the five precipitation inputs in NHSO1 watershed.....	185
Table 5.14 Nash-Sutcliffe Efficiencies (NSEs) corresponding to the five precipitation inputs in PSNW2 watershed.....	187
Table 5.15 Nash-Sutcliffe Efficiencies (NSEs) corresponding to the five precipitation inputs in SERI3 watershed.....	190
Table 5.16 Flags of essential improvement (Y), negligible change (=) and deterioration (N) for the 14 experimental watersheds over 2003, 2004 and 2005.....	190
Table 6.1 Correlations between the average AMSR-E and the mean of daily-averaged liquid soil moisture content of the near surface layer simulated by Noah LSM with NLDAS-2, RADAR, FUSED-1, FUSED-2 and FUSED-3 precipitation inputs in ALDW2 watershed.....	238
Table 6.2 Correlations between the average AMSR-E and the mean of daily-averaged liquid soil moisture content of the near surface layer simulated by Noah LSM with NLDAS-2, RADAR, FUSED-1, FUSED-2 and FUSED-3 precipitation inputs in ALPI3 watershed.....	238

Table 6.3 Correlations between the average AMSR-E and the mean of daily-averaged liquid soil moisture content of the near surface layer simulated by Noah LSM with NLDAS-2, RADAR, FUSED-1, FUSED-2 and FUSED-3 precipitation inputs in BAKI3 watershed.	239
Table 6.4 Correlations between the average AMSR-E and the mean of daily-averaged liquid soil moisture content of the near surface layer simulated by Noah LSM with NLDAS-2, RADAR, FUSED-1, FUSED-2 and FUSED-3 precipitation inputs in BSNK2 watershed.	239
Table 6.5 Correlations between the average AMSR-E and the mean of daily-averaged liquid soil moisture content of the near surface layer simulated by Noah LSM with NLDAS-2, RADAR, FUSED-1, FUSED-2 and FUSED-3 precipitation inputs in CLAI2 watershed.	240
Table 6.6 Correlations between the average AMSR-E and the mean of daily-averaged liquid soil moisture content of the near surface layer simulated by Noah LSM with NLDAS-2, RADAR, FUSED-1, FUSED-2 and FUSED-3 precipitation inputs in CRWI3 watershed.	240
Table 6.7 Correlations between the average AMSR-E and the mean of daily-averaged liquid soil moisture content of the near surface layer simulated by Noah LSM with NLDAS-2, RADAR, FUSED-1, FUSED-2 and FUSED-3 precipitation inputs in CYCK2 watershed.	241
Table 6.8 Correlations between the average AMSR-E and the mean of daily-averaged liquid soil moisture content of the near surface layer simulated by Noah LSM with NLDAS-2, RADAR, FUSED-1, FUSED-2 and FUSED-3 precipitation inputs in DBVO1 watershed.	241
Table 6.9 Correlations between the average AMSR-E and the mean of daily-averaged liquid soil moisture content of the near surface layer simulated by Noah LSM with NLDAS-2, RADAR, FUSED-1, FUSED-2 and FUSED-3 precipitation inputs in ELRP1 watershed.	242
Table 6.10 Correlations between the average AMSR-E and the mean of daily-averaged liquid soil moisture content of the near surface layer simulated by Noah LSM with NLDAS-2, RADAR, FUSED-1, FUSED-2 and FUSED-3 precipitation inputs in FDYO1 watershed.	242
Table 6.11 Correlations between the average AMSR-E and the mean of daily-averaged liquid soil moisture content of the near surface layer simulated by Noah LSM with NLDAS-2, RADAR, FUSED-1, FUSED-2 and FUSED-3 precipitation inputs in KINT1 watershed.	243

Table 6.12 Correlations between the average AMSR-E and the mean of daily-averaged liquid soil moisture content of the near surface layer simulated by Noah LSM with NLDAS-2, RADAR, FUSED-1, FUSED-2 and FUSED-3 precipitation inputs in NHSO1 watershed.	243
Table 6.13 Correlations between the average AMSR-E and the mean of daily-averaged liquid soil moisture content of the near surface layer simulated by Noah LSM with NLDAS-2, RADAR, FUSED-1, FUSED-2 and FUSED-3 precipitation inputs in PSNW2 watershed.	244
Table 6.14 Correlations between the average AMSR-E and the mean of daily-averaged liquid soil moisture content of the near surface layer simulated by Noah LSM with NLDAS-2, RADAR, FUSED-1, FUSED-2 and FUSED-3 precipitation inputs in SERI3 watershed.	244

LIST OF FIGURES

Figure 1.1 Control volume of hydrological modeling	5
Figure 2.1 Three types of grid outlets. Type #1 and #2 outlets are the cells with the 1 st and the 2 nd largest flow accumulations. Type #O outlet is the cell with the largest flow accumulation from cells within grid	23
Figure 2.2 Three types of downstream grids. The type T1, T2 and T3 grids are the 1 st grid, the 2 nd grid and the 3 rd grid that the main downstream channel of current grid C goes to.....	23
Figure 2.3 Flow chart of large-scale flow network derivation algorithm	24
Figure 2.4 Flowchart of grid-ordering algorithm. For each grid, tracking of upstream grid starts from southeast (lower right) and then go to next directions as shown in the sequence of tracking directions.	25
Figure 2.5 Map of SERI3 watershed. In the figure, square boxes are grids at 1/8 degree resolution; numbers are routing orders of grids.....	33
Figure 2.6 Observed and simulated streamflows in SERI3 watershed. The upper panel includes the routed streamflow with linear reservoir for baseflow. The lower panel includes the routed streamflow with the assumption of equilibrium groundwater.....	35
Figure 2.7 Observed and simulated streamflows in BAKI3 watershed. Other descriptions are the same as Figure 2.6.....	36
Figure 2.8 Observed and simulated streamflows at the outlets of SERI3 and BAKI3 watersheds. PDF of two-parameter Gamma distribution is used to approximate unit hydrograph and groundwater are assumed in an equilibrium status.	38
Figure 2.9 Observed and simulated streamflows at the outlets of SERI3 and BAKI3 watersheds. Flow length is approximated by tracking main river channel derived from DEM at 1/2048 degree resolution.....	40

Figure 2.10 Observed and simulated streamflows of Experiment 5 at the outlet of SERI3 and BAKI3 watershed. No in-grid routing is used and the flow length for between-grid routing is approximated with the orthogonal and the diagonal dimension of grid. 42

Figure 3.1 A schematic representation of Noah land surface model. 50

Figure 3.2 Plot of porosity (in red color), field capacity (in green color) and wilting point (in blue color) of 13 soil types when $\rho_1 = 1.0$ (default values), $\rho_1 = 0.5$, $\rho_1 = 0.75$ and $\rho_1 = 1.25$. Names of soil types corresponding to SOIL TYPE ID are listed in Table 3.1..... 58

Figure 3.3 Flowchart of MPI-based multiobjective particle swarm optimization algorithm (MOPSO)..... 63

Figure 3.4 Map of KINT1 watershed. Soil type map is at 1/32 degree resolution; grid in black color is at 1/8 degree resolution; river networks in white color are derived from DEM data at 1/2048 degree resolution; the red circle represents the outlet of SERI3 watershed. 67

Figure 3.5 Map of SERI3 watershed. Soil type map is at 1/32 degree resolution; grid in black color is at 1/8 degree resolution; river networks in white color are derived from DEM data at 1/2048 degree resolution; the red circle represents the outlet of SERI3 watershed. 68

Figure 3.6 Pie charts of soil types in KINT1 (left panel) and SERI3 (right panel) watersheds. .. 68

Figure 3.7 Nash-Sutcliffe Efficiencies (NSEs) of Pareto set of parameters of KINT1 (left panel) and SERI3 (right panel) watersheds corresponding to five precipitation inputs, namely NLDAS, RADAR, FUSED-1, FUSED-2, and FUSED-3..... 70

Figure 3.8 Observed and simulated streamflows in KINT1 watershed. Calibration period includes 2002, 2003, and 2004; validation period includes 2006 and 2007. In each plot, horizontal axis represents time and vertical axis represents streamflow rate (cft/s)..... 72

Figure 3.9 Observed and simulated streamflows in SERI3 watershed. Calibration period includes 2002, 2003, and 2004; validation period includes 2006 and 2007. In each plot, horizontal axis represents time and vertical axis represents streamflow rate (cft/s)... 74

Figure 4.1 A schematic of a 2-D multiscale tree with three different spatial scales, 0, 1, and 2. For node t at scale 1, $t\bar{\gamma}$ represents its parent node and $t\alpha_n$ ($n = 1, 2, 3, 4$) represents its child nodes. Without a parent, the node at scale 0 (i.e., the coarsest resolution) is called a root node; without any children, the nodes at scale 2 (i.e., the finest resolution) are called leaf nodes. 82

Figure 4.2 Location of our study area bounded by longitudes (-88, -84) and latitudes (37.75, 41.75) which contains 32×32 gray grids at 1/8 degree resolution..... 85

Figure 4.3 (A) Time series of the means of the true precipitation data at 1/32 degree resolution (i.e., scale 7); (B) time series of the standard deviations of the true precipitation data at 1/32 degree resolution; (C) time series of the relative differences between the means of the true precipitation data at 1/32 degree resolution and those at 1/8 degree resolution; and (D) time series of the relative differences between the standard deviations of the true precipitation data at 1/32 degree resolution and those at 1/8 degree resolution. All of these statistics are calculated over the precipitation-covered areas based on the 2246 hourly precipitation data in 2003..... 87

Figure 4.4 Average percentage of grid cells whose synthetic precipitation values are regenerated for Experiment 1 (panel A) and Experiment 2 (panel B) over the 2246 precipitation hours in 2003..... 90

Figure 4.5 Color-filled contour plots of $\overline{Corr_j^-}$, $\overline{Corr_j^+}$ and $\overline{\Delta Corr_j}$ for scale 5 (i.e., $j = 5$, upper panel) and scale 7 (i.e., $j = 7$, lower panel), respectively, for Experiment 1. In each plot, the horizontal axis and the vertical axis represent, respectively, the noise levels at scales 7 and 5. In addition, the two horizontal and the two vertical gray lines indicate the boundaries, respectively, between the fair and moderate, and between the moderate and large categories of the noise levels specified in Figure 4.1..... 96

Figure 4.6 Color-filled contour plots of $\overline{\Delta Corr_5^{E1}} - \overline{\Delta Corr_5^{B1}}$ and $\overline{\Delta Corr_7^{E1}} - \overline{\Delta Corr_7^{B1}}$, where the superscript *E1* denotes Experiment 1 and the superscript *B1* denotes the benchmark experiment. Both experiments use the same erroneous precipitation data with the Type-I errors. The meanings of the horizontal and vertical axes are the same as in Figure 4.5..... 100

Figure 4.7 Color-filled contour plots of $\overline{RMSE_j^-}$, $\overline{RMSE_j^+}$ and $\overline{\Delta RMSE_j}$ for scale 5 (i.e., $j = 5$, upper panel) and for scale 7 (i.e., $j = 7$, lower panel), respectively, for Experiment 1. The meanings of the horizontal and vertical axes and the meanings of the two horizontal and vertical gray lines and are the same as in Figure 4.5..... 101

Figure 4.8 Color-filled contour plots of $\overline{\Delta RMSE_5^{E1}} - \overline{\Delta RMSE_5^{B1}}$ and $\overline{\Delta RMSE_7^{E1}} - \overline{\Delta RMSE_7^{B1}}$, where the superscript *E1* denotes Experiment 1 and superscript *B1* denotes the benchmark experiment. Both experiments use the same erroneous precipitation data with the Type-I errors. The meanings of the horizontal and vertical axes are the same as in Figure 4.5..... 102

Figure 4.9 Color-filled contour plots of $\overline{Corr_j^-}$, $\overline{Corr_j^+}$ and $\overline{\Delta Corr_j}$ for scale 5 (i.e., $j = 5$, upper panel) and scale 7 (i.e., $j = 7$, lower panel) for Experiment 2. In each plot, the horizontal axis and the vertical axis represent, respectively, the bias levels at scales 7 and 5. 108

Figure 4.10 Color-filled contour plots of $\overline{\Delta Corr_5^{E2}} - \overline{\Delta Corr_5^{B2}}$ and $\overline{\Delta Corr_7^{E2}} - \overline{\Delta Corr_7^{B2}}$, where the superscript *E2* denotes Experiment 2 and the superscript *B2* denotes the benchmark experiment. Both experiments use the same erroneous precipitation data with the Type-II errors. The meanings of the horizontal and vertical axes are the same as in Figure 4.9. 110

Figure 4.11 Color-filled contour plots of $\overline{RMSE_j^-}$, $\overline{RMSE_j^+}$ and $\overline{\Delta RMSE_j}$ for scale 5 (i.e., $j = 5$, upper panel) and scale 7 (i.e., $j = 7$, lower panel) for Experiment 2. The meanings of the horizontal and vertical axes are the same as in Figure 4.9. 112

Figure 4.12 Color-filled contour plots of $\overline{\Delta RMSE_5^{E2}} - \overline{\Delta RMSE_5^{B2}}$ and $\overline{\Delta RMSE_7^{E2}} - \overline{\Delta RMSE_7^{B2}}$, where the superscript *E2* denotes Experiment 2 and the superscript *B2* denotes the benchmark experiment. Both experiments use the same erroneous precipitation data with the Type-II errors. The meanings of the horizontal and vertical axes are the same as in Figure 4.9. 115

Figure 4.13 Comparison of the images among the true, erroneous, and fused precipitation for an individual storm occurred at 9:00 am of September 22, 2003. X_j^{true} , Y_j^{error} and X_j^{fused} ($j = 5$ and 7) denoted the true, synthetic, and fused precipitation images at scales 5 (upper panel) and 7 (lower panel), respectively. The synthetic precipitation data are generated with the Type-I errors in which the noise levels are $x_9 = 2.0$ for both scales 5 and 7. The horizontal and vertical axes in each plot represent, respectively, the longitudes and latitudes of our study area. 116

Figure 4.14 Comparison of the images among the true, erroneous, and fused precipitation for an individual storm occurred at 9:00 am of September 22, 2003. X_j^{true} , Y_j^{error} and X_j^{fused} ($j = 5$ and 7) denoted the true, synthetic, and fused precipitation images at scales 5 (upper panel) and 7 (lower panel), respectively. The synthetic precipitation data are generated with the Type-II errors in which the noise levels are $x_9 = 2.0$ and the bias levels are $y_{10} = 1.0$, respectively, for both scales 5 and 7. The horizontal and vertical axes of each plot have the same meanings as in Figure 4.13. 117

Figure 5.1 Schematic representation of Multiscale Kalman Smoother (MKS) algorithm. The three images, denoted as $scale = 0$, $scale = 1$ and $scale = 3$ respectively, represent measurements of the same region from the coarsest resolution to the finest resolution. The varying colors in these images represent different values of measurements. Each pixel of image is called a node. All nodes are organized into a tree shape, called multiscale tree while the node and the nodes at the coarsest resolution and the finest resolution are called root node and leaf nodes, respectively.	130
Figure 5.2 Maps of the 14 Experimental watersheds in the Ohio River Basin. For each watershed, the circle represents the location of outlet. SERI3 also includes the area of BAKI3 since the latter is a sub-watershed of the former.....	136
Figure 5.3 Relative missing numbers in the 14 experimental watersheds in the calibration period (2003, 2004 and 2005).....	139
Figure 5.4 Boxplots of correlation between hourly NLDAS-2 and RADAR precipitation data over the 14 experimental watersheds in the three years of the calibration period (2003, 2004, and 2005). Marker “x” represents the mean of correlations.	141
Figure 5.5 Histograms of $mean(NLDAS-2) - mean(RADAR)$ in the 14 experimental watersheds in 2003. From left to right, the five red “x” markers in each plot represent the 10 th , 25 th , 50 th , 75 th and 90 th percentiles. The green line represents the mean of data.....	143
Figure 5.6 Histograms of $mean(NLDAS-2) - mean(RADAR)$ in the 14 experimental watersheds in 2004. From left to right, the five red “x” markers in each plot represent the 10 th , 25 th , 50 th , 75 th and 90 th percentiles. The green line represents the mean of data.....	143
Figure 5.7 Histograms of $mean(NLDAS-2) - mean(RADAR)$ in the 14 experimental watersheds in 2005. From left to right, the five red “x” markers in each plot represent the 10 th , 25 th , 50 th , 75 th and 90 th percentiles. The green line represents the mean of data.....	144
Figure 5.8 DEM, flow network, soil types, and land use types in ALDW2 site. Except DEM is at 1/2048 degree resolution, all other data are at 1/8 degree resolution. Gridded region is the ALDW2 watershed, whose outlet is marked with the red circle.	148
Figure 5.9 DEM, flow network, soil types, and land use types in ALPI3 site. Except DEM is at 1/2048 degree resolution, all other data are at 1/8 degree resolution. Gridded region is the ALPI3 watershed, whose outlet is marked with the red circle.....	149
Figure 5.10 DEM, flow network, soil types, and land use types in BAKI3 site. Except DEM is at 1/2048 degree resolution, all other data are at 1/8 degree resolution. Gridded region is the BAKI3 watershed, whose outlet is marked with the red circle.....	150

Figure 5.11 DEM, flow network, soil types, and land use types in BSNK2 site. Except DEM is at 1/2048 degree resolution, all other data are at 1/8 degree resolution. Gridded region is the BSNK2 watershed, whose outlet is marked with the red circle.....	151
Figure 5.12 DEM, flow network, soil types, and land use types in CLAI2 site. Except DEM is at 1/2048 degree resolution, all other data are at 1/8 degree resolution. Gridded region is the CLAI2 watershed, whose outlet is marked with the red circle.	152
Figure 5.13 DEM, flow network, soil types, and land use types in CRWI3 site. Except DEM is at 1/2048 degree resolution, all other data are at 1/8 degree resolution. Gridded region is the CRWI3 watershed, whose outlet is marked with the red circle.	153
Figure 5.14 DEM, flow network, soil types, and land use types in CYCK2 site. Except DEM is at 1/2048 degree resolution, all other data are at 1/8 degree resolution. Gridded region is the CYCK2 watershed, whose outlet is marked with the red circle.	154
Figure 5.15 DEM, flow network, soil types, and land use types in DBVO1 site. Except DEM is at 1/2048 degree resolution, all other data are at 1/8 degree resolution. Gridded region is the DBVO1 watershed, whose outlet is marked with the red circle.	155
Figure 5.16 DEM, flow network, soil types, and land use types in ELRP1 site. Except DEM is at 1/2048 degree resolution, all other data are at 1/8 degree resolution. Gridded region is the ELRP1 watershed, whose outlet is marked with the red circle.....	156
Figure 5.17 DEM, flow network, soil types, and land use types in FDYO1 site. Except DEM is at 1/2048 degree resolution, all other data are at 1/8 degree resolution. Gridded region is the FDYO1 watershed, whose outlet is marked with the red circle.....	157
Figure 5.18 DEM, flow network, soil types, and land use types in KINT1 site. Except DEM is at 1/2048 degree resolution, all other data are at 1/8 degree resolution. Gridded region is the KINT1 watershed, whose outlet is marked with the red circle.	158
Figure 5.19 DEM, flow network, soil types, and land use types in NHSO1 site. Except DEM is at 1/2048 degree resolution, all other data are at 1/8 degree resolution. Gridded region is the NHSO1 watershed, whose outlet is marked with the red circle.....	159
Figure 5.20 DEM, flow network, soil types, and land use types in PSNW2 site. Except DEM is at 1/2048 degree resolution, all other data are at 1/8 degree resolution. Gridded region is the PSNW2 watershed, whose outlet is marked with the red circle.	160
Figure 5.21 DEM, flow network, soil types, and land use types in SERI3 site. Except DEM is at 1/2048 degree resolution, all other data are at 1/8 degree resolution. Gridded region is the SERI3 watershed, whose outlet is marked with the red circle.....	161

- Figure 5.22 Observed streamflow and simulated streamflow with NLDAS-2, RADAR, FUSED-1, FUSED-2 and FUSED-3 precipitation data in calibration period (2003, 2004 and 2005) in ALDW2 watershed. The unit of streamflow is cubic feet per second (cft/s). Corresponding Nash-Sutcliffe Efficiencies (NSE) are given in the titles of plots. .. 164
- Figure 5.23 Observed streamflow and simulated streamflow with NLDAS-2, RADAR, FUSED-1, FUSED-2 and FUSED-3 precipitation data in calibration period (2003, 2004 and 2005) in ALPI3 watershed. The unit of streamflow is cubic feet per second (cft/s). Corresponding Nash-Sutcliffe Efficiencies (NSE) are given in the titles of plots. .. 166
- Figure 5.24 Observed streamflow and simulated streamflow with NLDAS-2, RADAR, FUSED-1, FUSED-2 and FUSED-3 precipitation data in calibration period (2003, 2004 and 2005) in BAKI3 watershed. The unit of streamflow is cubic feet per second (cft/s). Corresponding Nash-Sutcliffe Efficiencies (NSE) are given in the titles of plots. .. 168
- Figure 5.25 Observed streamflow and simulated streamflow with NLDAS-2, RADAR, FUSED-1, FUSED-2 and FUSED-3 precipitation data in calibration period (2003, 2004 and 2005) in BSNK2 watershed. The unit of streamflow is cubic feet per second (cft/s). Corresponding Nash-Sutcliffe Efficiencies (NSE) are given in the titles of plots. .. 170
- Figure 5.26 Observed streamflow and simulated streamflow with NLDAS-2, RADAR, FUSED-1, FUSED-2 and FUSED-3 precipitation data in calibration period (2003, 2004 and 2005) in CLAI2 watershed. The unit of streamflow is cubic feet per second (cft/s). Corresponding Nash-Sutcliffe Efficiencies (NSE) are given in the titles of plots. .. 173
- Figure 5.27 Observed streamflow and simulated streamflow with NLDAS-2, RADAR, FUSED-1, FUSED-2 and FUSED-3 precipitation data in calibration period (2003, 2004 and 2005) in CRWI3 watershed. The unit of streamflow is cubic feet per second (cft/s). Corresponding Nash-Sutcliffe Efficiencies (NSE) are given in the titles of plots ... 175
- Figure 5.28 Observed streamflow and simulated streamflow with NLDAS-2, RADAR, FUSED-1, FUSED-2 and FUSED-3 precipitation data in calibration period (2003, 2004 and 2005) in CYCK2 watershed. The unit of streamflow is cubic feet per second (cft/s). Corresponding Nash-Sutcliffe Efficiencies (NSE) are given in the titles of plots. .. 177
- Figure 5.29 Observed streamflow and simulated streamflow with NLDAS-2, RADAR, FUSED-1, FUSED-2 and FUSED-3 precipitation data in calibration period (2003, 2004 and 2005) in DBVO1 watershed. The unit of streamflow is cubic feet per second (cft/s). Corresponding Nash-Sutcliffe Efficiencies (NSE) are given in the titles of plots. .. 179
- Figure 5.30 Observed streamflow and simulated streamflow with NLDAS-2, RADAR, FUSED-1, FUSED-2 and FUSED-3 precipitation data in calibration period (2003, 2004 and 2005) in ELRP1 watershed. The unit of streamflow is cubic feet per second (cft/s). Corresponding Nash-Sutcliffe Efficiencies (NSE) are given in the titles of plots. .. 181

- Figure 5.31 Observed streamflow and simulated streamflow with NLDAS-2, RADAR, FUSED-1, FUSED-2 and FUSED-3 precipitation data in calibration period (2003, 2004 and 2005) in FDYO1 watershed. The unit of streamflow is cubic feet per second (cft/s). Corresponding Nash-Sutcliffe Efficiencies (NSE) are given in the titles of plots. .. 182
- Figure 5.32 Observed streamflow and simulated streamflow with NLDAS-2, RADAR, FUSED-1, FUSED-2 and FUSED-3 precipitation data in calibration period (2003, 2004 and 2005) in KINT1 watershed. The unit of streamflow is cubic feet per second (cft/s). Corresponding Nash-Sutcliffe Efficiencies (NSE) are given in the titles of plots. .. 184
- Figure 5.33 Observed streamflow and simulated streamflow with NLDAS-2, RADAR, FUSED-1, FUSED-2 and FUSED-3 precipitation data in calibration period (2003, 2004 and 2005) in NHSO1 watershed. The unit of streamflow is cubic feet per second (cft/s). Corresponding Nash-Sutcliffe Efficiencies (NSE) are given in the titles of plots. .. 186
- Figure 5.34 Observed streamflow and simulated streamflow with NLDAS-2, RADAR, FUSED-1, FUSED-2 and FUSED-3 precipitation data in calibration period (2003, 2004 and 2005) in PSNW2 watershed. The unit of streamflow is cubic feet per second (cft/s). Corresponding Nash-Sutcliffe Efficiencies (NSE) are given in the titles of plots. .. 188
- Figure 5.35 Observed streamflow and simulated streamflow with NLDAS-2, RADAR, FUSED-1, FUSED-2 and FUSED-3 precipitation data in calibration period (2003, 2004 and 2005) in SERI3 watershed. The unit of streamflow is cubic feet per second (cft/s). Corresponding Nash-Sutcliffe Efficiencies (NSE) are given in the titles of plots. .. 189
- Figure 5.36 Spatial average of simulated soil moisture contents of the 1st, 2nd, 3rd and 4th layer (SMC₁, SMC₂, SMC₃ and SMC₄) over ALDW2 watershed in 2004 with NLDAS-2, RADAR, FUSED-1, FUSED-2 and FUSED-3 precipitation inputs. The unit of soil moisture is volumetric ratio (m³/m³)..... 193
- Figure 5.37 Spatial average of simulated soil moisture contents of the 1st, 2nd, 3rd and 4th layer (SMC₁, SMC₂, SMC₃ and SMC₄) over ALPI3 watershed in 2004 with NLDAS-2, RADAR, FUSED-1, FUSED-2 and FUSED-3 precipitation inputs. The unit of soil moisture is volumetric ratio (m³/m³)..... 194
- Figure 5.38 Spatial average of simulated soil moisture contents of the 1st, 2nd, 3rd and 4th layer (SMC₁, SMC₂, SMC₃ and SMC₄) over BAKI3 watershed in 2004 with NLDAS-2, RADAR, FUSED-1, FUSED-2 and FUSED-3 precipitation inputs. The unit of soil moisture is volumetric ratio (m³/m³)..... 195
- Figure 5.39 Spatial average of simulated soil moisture contents of the 1st, 2nd, 3rd and 4th layer (SMC₁, SMC₂, SMC₃ and SMC₄) over BSNK2 watershed in 2004 with NLDAS-2, RADAR, FUSED-1, FUSED-2 and FUSED-3 precipitation inputs. The unit of soil moisture is volumetric ratio (m³/m³)..... 196

Figure 5.40 Spatial average of simulated soil moisture contents of the 1st, 2nd, 3rd and 4th layer (SMC₁, SMC₂, SMC₃ and SMC₄) over CLAI2 watershed in 2004 with NLDAS-2, RADAR, FUSED-1, FUSED-2 and FUSED-3 precipitation inputs. The unit of soil moisture is volumetric ratio (m³/m³)..... 197

Figure 5.41 Spatial average of simulated soil moisture contents of the 1st, 2nd, 3rd and 4th layer (SMC₁, SMC₂, SMC₃ and SMC₄) over CRWI3 watershed in 2004 with NLDAS-2, RADAR, FUSED-1, FUSED-2 and FUSED-3 precipitation inputs. The unit of soil moisture is volumetric ratio (m³/m³)..... 198

Figure 5.42 Spatial average of simulated soil moisture contents of the 1st, 2nd, 3rd and 4th layer (SMC₁, SMC₂, SMC₃ and SMC₄) over CYCK2 watershed in 2004 with NLDAS-2, RADAR, FUSED-1, FUSED-2 and FUSED-3 precipitation inputs. The unit of soil moisture is volumetric ratio (m³/m³)..... 199

Figure 5.43 Spatial average of simulated soil moisture contents of the 1st, 2nd, 3rd and 4th layer (SMC₁, SMC₂, SMC₃ and SMC₄) over DBVO1 watershed in 2004 with NLDAS-2, RADAR, FUSED-1, FUSED-2 and FUSED-3 precipitation inputs. The unit of soil moisture is volumetric ratio (m³/m³)..... 200

Figure 5.44 Spatial average of simulated soil moisture contents of the 1st, 2nd, 3rd and 4th layer (SMC₁, SMC₂, SMC₃ and SMC₄) over ELRP1 watershed in 2004 with NLDAS-2, RADAR, FUSED-1, FUSED-2 and FUSED-3 precipitation inputs. The unit of soil moisture is volumetric ratio (m³/m³)..... 201

Figure 5.45 Spatial average of simulated soil moisture contents of the 1st, 2nd, 3rd and 4th layer (SMC₁, SMC₂, SMC₃ and SMC₄) over FDYO1 watershed in 2004 with NLDAS-2, RADAR, FUSED-1, FUSED-2 and FUSED-3 precipitation inputs. The unit of soil moisture is volumetric ratio (m³/m³)..... 202

Figure 5.46 Spatial average of simulated soil moisture contents of the 1st, 2nd, 3rd and 4th layer (SMC₁, SMC₂, SMC₃ and SMC₄) over KINT1 watershed in 2004 with NLDAS-2, RADAR, FUSED-1, FUSED-2 and FUSED-3 precipitation inputs. The unit of soil moisture is volumetric ratio (m³/m³)..... 203

Figure 5.47 Spatial average of simulated soil moisture contents of the 1st, 2nd, 3rd and 4th layer (SMC₁, SMC₂, SMC₃ and SMC₄) over NHSO1 watershed in 2004 with NLDAS-2, RADAR, FUSED-1, FUSED-2 and FUSED-3 precipitation inputs. The unit of soil moisture is volumetric ratio (m³/m³)..... 204

Figure 5.48 Spatial average of simulated soil moisture contents of the 1st, 2nd, 3rd and 4th layer (SMC₁, SMC₂, SMC₃ and SMC₄) over PSNW2 watershed in 2004 with NLDAS-2, RADAR, FUSED-1, FUSED-2 and FUSED-3 precipitation inputs. The unit of soil moisture is volumetric ratio (m³/m³)..... 205

Figure 5.49 Spatial average of simulated soil moisture contents of the 1st, 2nd, 3rd and 4th layer (SMC₁, SMC₂, SMC₃ and SMC₄) over SERI3 watershed in 2004 with NLDAS-2, RADAR, FUSED-1, FUSED-2 and FUSED-3 precipitation inputs. The unit of soil moisture is volumetric ratio (m³/m³)..... 206

Figure 5.50 Simulated soil moisture contents of the 1st, 2nd, 3rd and 4th layer of Noah LSM in ALDW2 watershed at 08/01/2004 17:00:00 (UTC time) with NLDAS-2, RADAR, FUSED-1, FUSED-2 and FUSED-3 precipitation inputs. From top to bottom, the four rows are corresponding to the four layers; from left to right, the five columns are corresponding to the five precipitation inputs. 208

Figure 5.51 Simulated soil moisture contents of the 1st, 2nd, 3rd and 4th layer of Noah LSM in SERI3 watershed at 08/01/2004 17:00:00 (UTC time) with NLDAS-2, RADAR, FUSED-1, FUSED-2 and FUSED-3 precipitation inputs. From top to bottom, the four rows are corresponding to the four layers; from left to right, the five columns are corresponding to the five precipitation inputs. 209

Figure 5.52 Spatial average of daily total evapotranspiration simulated by Noah LSM with NLDAS-2, RADAR, FUSED-1, FUSED-2 and FUSED-3 precipitation inputs over ALDW2 watershed during February, May, August and November of 2004. The Unit is W/m³..... 211

Figure 5.53 Spatial average of daily total evapotranspiration simulated by Noah LSM with NLDAS-2, RADAR, FUSED-1, FUSED-2 and FUSED-3 precipitation inputs over ALPI3 watershed during February, May, August and November of 2004. The Unit is W/m³..... 212

Figure 5.54 Spatial average of daily total evapotranspiration simulated by Noah LSM with NLDAS-2, RADAR, FUSED-1, FUSED-2 and FUSED-3 precipitation inputs over BAKI3 watershed during February, May, August and November of 2004. The Unit is W/m³..... 212

Figure 5.55 Spatial average of daily total evapotranspiration simulated by Noah LSM with NLDAS-2, RADAR, FUSED-1, FUSED-2 and FUSED-3 precipitation inputs over BSNK2 watershed during February, May, August and November of 2004. The Unit is W/m³..... 213

Figure 5.56 Spatial average of daily total evapotranspiration simulated by Noah LSM with NLDAS-2, RADAR, FUSED-1, FUSED-2 and FUSED-3 precipitation inputs over CLAI2 watershed during February, May, August and November of 2004. The Unit is W/m³..... 213

Figure 5.57 Spatial average of daily total evapotranspiration simulated by Noah LSM with NLDAS-2, RADAR, FUSED-1, FUSED-2 and FUSED-3 precipitation inputs over CRWI3 watershed during February, May, August and November of 2004. The Unit is W/m³..... 214

Figure 5.58 Spatial average of daily total evapotranspiration simulated by Noah LSM with NLDAS-2, RADAR, FUSED-1, FUSED-2 and FUSED-3 precipitation inputs over CYCK2 watershed during February, May, August and November of 2004. The Unit is W/m^3	214
Figure 5.59 Spatial average of daily total evapotranspiration simulated by Noah LSM with NLDAS-2, RADAR, FUSED-1, FUSED-2 and FUSED-3 precipitation inputs over DBVO1 watershed during February, May, August and November of 2004. The Unit is W/m^3	215
Figure 5.60 Spatial average of daily total evapotranspiration simulated by Noah LSM with NLDAS-2, RADAR, FUSED-1, FUSED-2 and FUSED-3 precipitation inputs over ELRP1 watershed during February, May, August and November of 2004. The Unit is W/m^3	215
Figure 5.61 Spatial average of daily total evapotranspiration simulated by Noah LSM with NLDAS-2, RADAR, FUSED-1, FUSED-2 and FUSED-3 precipitation inputs over FDYO1 watershed during February, May, August and November of 2004. The Unit is W/m^3	216
Figure 5.62 Spatial average of daily total evapotranspiration simulated by Noah LSM with NLDAS-2, RADAR, FUSED-1, FUSED-2 and FUSED-3 precipitation inputs over KINT1 watershed during February, May, August and November of 2004. The Unit is W/m^3	216
Figure 5.63 Spatial average of daily total evapotranspiration simulated by Noah LSM with NLDAS-2, RADAR, FUSED-1, FUSED-2 and FUSED-3 precipitation inputs over NHSO1 watershed during February, May, August and November of 2004. The Unit is W/m^3	217
Figure 5.64 Spatial average of daily total evapotranspiration simulated by Noah LSM with NLDAS-2, RADAR, FUSED-1, FUSED-2 and FUSED-3 precipitation inputs over PSNW2 watershed during February, May, August and November of 2004. The Unit is W/m^3	217
Figure 5.65 Spatial average of daily total evapotranspiration simulated by Noah LSM with NLDAS-2, RADAR, FUSED-1, FUSED-2 and FUSED-3 precipitation inputs over SERI3 watershed during February, May, August and November of 2004. The Unit is W/m^3	218
Figure 5.66 Simulated hourly total evapotranspiration by Noah LSM with NLDAS-2, RADAR, FUSED-1, FUSED-2 and FUSED-3 precipitation inputs in ALDW2 site at 14:00, 17:00, 20:00 and 23:00 of 08/17/2004 (UTC time)	219

Figure 5.67 Simulated hourly total evapotranspiration by Noah LSM with NLDAS-2, RADAR, FUSED-1, FUSED-2 and FUSED-3 precipitation inputs in SERI3 site at 14:00, 17:00, 20:00 and 23:00 of 08/16/2004 (UTC time)	221
Figure 6.1 Cumulative missing percentage of AMSR-E data over the 14 experimental watersheds.	233
Figure 6.2 Scatter plots of the mean of AMSR-E data and the mean of daily liquid soil moisture data in near surface layer simulated by Noah LSM with NLDAS-2 precipitation data for the 14 experimental watersheds over the period of 2003 to 2005. In each plot, the dashed line is 1:1 line.....	234
Figure 6.3 Scatter plots of the mean of AMSR-E data and the mean of daily liquid soil moisture data in near surface layer simulated by Noah LSM with RADAR precipitation data for the 14 experimental watersheds over the period of 2003 to 2005. In each plot, the dashed line is 1:1 line.....	235
Figure 6.4 Scatter plots of the mean of AMSR-E data and the mean of daily liquid soil moisture data in near surface layer simulated by Noah LSM with FUSED-1 precipitation data for the 14 experimental watersheds over the period of 2003 to 2005. In each plot, the dashed line is 1:1 line.....	236
Figure 6.5 Scatter plots of the mean of AMSR-E data and the mean of daily liquid soil moisture data in near surface layer simulated by Noah LSM with FUSED-2 precipitation data for the 14 experimental watersheds over the period from 2003 to 2005. In each plot, the dashed line is 1:1 line.....	236
Figure 6.6 Scatter plots of the mean of AMSR-E data and the mean of daily liquid soil moisture data in near surface layer simulated by Noah LSM with FUSED-3 precipitation data for the 14 experimental watersheds over the period of 2003 to 2005. In each plot, the dashed line is 1:1 line.....	237
Figure 6.7 Spatial averages of simulated soil moisture contents (m^3/m^3) with and without data assimilation by Noah LSM and NLDAS-2 forcing data in ALDW2 watershed for 2004. SMC ₁ , SMC ₂ , SMC ₃ and SMC ₄ represent average soil moisture contents in layers 1, 2, 3, and 4.	247
Figure 6.8 Spatial averages of simulated soil moisture contents (m^3/m^3) with and without data assimilation by Noah LSM and NLDAS-2 forcing data in ALPI3 watershed for 2004. SMC ₁ , SMC ₂ , SMC ₃ and SMC ₄ represent average soil moisture contents in layers 1, 2, 3, and 4.....	248
Figure 6.9 Spatial averages of simulated soil moisture contents (m^3/m^3) with and without data assimilation by Noah LSM and NLDAS-2 forcing data in BAKI3 watershed for 2004. SMC ₁ , SMC ₂ , SMC ₃ and SMC ₄ represent average soil moisture contents in layers 1, 2, 3, and 4.....	248

Figure 6.10 Spatial averages of simulated soil moisture contents (m^3/m^3) with and without data assimilation by Noah LSM and NLDAS-2 forcing data in BSNK2 watershed for 2004. SMC₁, SMC₂, SMC₃ and SMC₄ represent average soil moisture contents in layers 1, 2, 3, and 4..... 249

Figure 6.11 Spatial averages of simulated soil moisture contents (m^3/m^3) with and without data assimilation by Noah LSM and NLDAS-2 forcing data in CLAI2 watershed for 2004. SMC₁, SMC₂, SMC₃ and SMC₄ represent average soil moisture contents in layers 1, 2, 3, and 4..... 249

Figure 6.12 Spatial averages of simulated soil moisture contents (m^3/m^3) with and without data assimilation by Noah LSM and NLDAS-2 forcing data in CRWI3 watershed for 2004. SMC₁, SMC₂, SMC₃ and SMC₄ represent average soil moisture contents in layers 1, 2, 3, and 4..... 250

Figure 6.13 Spatial averages of simulated soil moisture contents (m^3/m^3) with and without data assimilation by Noah LSM and NLDAS-2 forcing data in CYCK2 watershed for 2004. SMC₁, SMC₂, SMC₃ and SMC₄ represent average soil moisture contents in layers 1, 2, 3, and 4..... 250

Figure 6.14 Spatial averages of simulated soil moisture contents (m^3/m^3) with and without data assimilation by Noah LSM and NLDAS-2 forcing data in DBVO1 watershed for 2004. SMC₁, SMC₂, SMC₃ and SMC₄ represent average soil moisture contents in layers 1, 2, 3, and 4. 251

Figure 6.15 Spatial averages of simulated soil moisture contents (m^3/m^3) with and without data assimilation by Noah LSM and NLDAS-2 forcing data in ELRP1 watershed for 2004. SMC₁, SMC₂, SMC₃ and SMC₄ represent average soil moisture contents in layers 1, 2, 3, and 4..... 251

Figure 6.16 Spatial averages of simulated soil moisture contents (m^3/m^3) with and without data assimilation by Noah LSM and NLDAS-2 forcing data in FDYO1 watershed for 2004. SMC₁, SMC₂, SMC₃ and SMC₄ represent average soil moisture contents in layers 1, 2, 3, and 4..... 252

Figure 6.17 Spatial averages of simulated soil moisture contents (m^3/m^3) with and without data assimilation by Noah LSM and NLDAS-2 forcing data in KINT1 watershed for 2004. SMC₁, SMC₂, SMC₃ and SMC₄ represent average soil moisture contents in layers 1, 2, 3, and 4..... 252

Figure 6.18 Spatial averages of simulated soil moisture contents (m^3/m^3) with and without data assimilation by Noah LSM and NLDAS-2 forcing data in NHSO1 watershed for 2004. SMC₁, SMC₂, SMC₃ and SMC₄ represent average soil moisture contents in layers 1, 2, 3, and 4..... 253

Figure 6.19 Spatial averages of simulated soil moisture contents (m^3/m^3) with and without data assimilation by Noah LSM and NLDAS-2 forcing data in PSNW2 watershed for 2004. SMC₁, SMC₂, SMC₃ and SMC₄ represent average soil moisture contents in layers 1, 2, 3, and 4..... 253

Figure 6.20 Spatial averages of simulated soil moisture contents (m^3/m^3) with and without data assimilation by Noah LSM and NLDAS-2 forcing data in SERI3 watershed for 2004. SMC₁, SMC₂, SMC₃ and SMC₄ represent average soil moisture contents in layers 1, 2, 3, and 4..... 254

Figure 6.21 Nash-Sutcliffe Efficiencies with and without data assimilation in 2004 and 2005 over the 14 experimental watersheds. NLDAS-2 precipitation data are used in Noah LSM simulation..... 257

Figure 6.22 Nash-Sutcliffe Efficiencies with and without data assimilation in 2004 and 2005 over the 14 experimental watersheds. RADAR precipitation data are used in Noah LSM simulation..... 257

Figure 6.23 Nash-Sutcliffe Efficiencies with and without data assimilation in 2004 and 2005 over the 14 experimental watersheds. FUSED-1 precipitation data are used in Noah LSM simulation..... 258

Figure 6.24 Nash-Sutcliffe Efficiencies with and without data assimilation in 2004 and 2005 over the 14 experimental watersheds. FUSED-2 precipitation data are used in Noah LSM simulation..... 258

Figure 6.25 Nash-Sutcliffe Efficiencies with and without data assimilation in 2004 and 2005 over the 14 experimental watersheds. FUSED-3 precipitation data are used in Noah LSM simulation..... 259

Figure 6.26 Observed streamflow series and simulated streamflow series with and without data assimilation by Noah LSM and NLDAS-2 forcing data in ALDW2 watershed for 2004 and 2005..... 262

Figure 6.27 Observed streamflow series and simulated streamflow series with and without data assimilation by Noah LSM and NLDAS-2 forcing data in ALPI3 watershed for 2004 and 2005..... 262

Figure 6.28 Observed streamflow series and simulated streamflow series with and without data assimilation by Noah LSM and NLDAS-2 forcing data in BAKI3 watershed for 2004 and 2005..... 263

Figure 6.29 Observed streamflow series and simulated streamflow series with and without data assimilation by Noah LSM and NLDAS-2 forcing data in BSKN2 watershed for 2004 and 2005..... 263

Figure 6.30 Observed streamflow series and simulated streamflow series with and without data assimilation by Noah LSM and NLDAS-2 forcing data in CLAI2 watershed for 2004 and 2005.....	264
Figure 6.31 Observed streamflow series and simulated streamflow series with and without data assimilation by Noah LSM and NLDAS-2 forcing data in CRWI3 watershed for 2004 and 2005.....	264
Figure 6.32 Observed streamflow series and simulated streamflow series with and without data assimilation by Noah LSM and NLDAS-2 forcing data in CYCK2 watershed for 2004 and 2005.....	265
Figure 6.33 Observed streamflow series and simulated streamflow series with and without data assimilation by Noah LSM and NLDAS-2 forcing data in DBVO1 watershed for 2004 and 2005.....	265
Figure 6.34 Observed streamflow series and simulated streamflow series with and without data assimilation by Noah LSM and NLDAS-2 forcing data in ELRP1 watershed for 2004 and 2005.....	266
Figure 6.35 Observed streamflow series and simulated streamflow series with and without data assimilation by Noah LSM and NLDAS-2 forcing data in FDYO1 watershed for 2004 and 2005.....	266
Figure 6.36 Observed streamflow series and simulated streamflow series with and without data assimilation by Noah LSM and NLDAS-2 forcing data in KINT1 watershed for 2004 and 2005.....	267
Figure 6.37 Observed streamflow series and simulated streamflow series with and without data assimilation by Noah LSM and NLDAS-2 forcing data in NHSO1 watershed for 2004 and 2005.....	267
Figure 6.38 Observed streamflow series and simulated streamflow series with and without data assimilation by Noah LSM and NLDAS-2 forcing data in PSNW2 watershed for 2004 and 2005.....	268
Figure 6.39 Observed streamflow series and simulated streamflow series with and without data assimilation by Noah LSM and NLDAS-2 forcing data in SERI3 watershed for 2004 and 2005.....	268
Figure 6.40 Spatial averages of simulated total evapotranspiration (W/m^2) with and without data assimilation by Noah LSM and NLDAS-2 forcing data in ALDW2 watershed in February, May, August and November of 2004.	270

Figure 6.41 Spatial averages of simulated total evapotranspiration (W/m^2) with and without data assimilation by Noah LSM and NLDAS-2 forcing data in ALPI3 watershed in February, May, August and November of 2004.	270
Figure 6.42 Spatial averages of simulated total evapotranspiration (W/m^2) with and without data assimilation by Noah LSM and NLDAS-2 forcing data in BAKI3 watershed in February, May, August and November of 2004.	271
Figure 6.43 Spatial averages of simulated total evapotranspiration (W/m^2) with and without data assimilation by Noah LSM and NLDAS-2 forcing data in BSNK2 watershed in February, May, August and November of 2004.	271
Figure 6.44 Spatial averages of simulated total evapotranspiration (W/m^2) with and without data assimilation by Noah LSM and NLDAS-2 forcing data in CLAI2 watershed in February, May, August and November of 2004.	272
Figure 6.45 Spatial averages of simulated total evapotranspiration (W/m^2) with and without data assimilation by Noah LSM and NLDAS-2 forcing data in CRWI3 watershed in February, May, August and November of 2004.	272
Figure 6.46 Spatial averages of simulated total evapotranspiration (W/m^2) with and without data assimilation by Noah LSM and NLDAS-2 forcing data in CYCK2 watershed in February, May, August and November of 2004.	273
Figure 6.47 Spatial averages of simulated total evapotranspiration (W/m^2) with and without data assimilation by Noah LSM and NLDAS-2 forcing data in DBVO1 watershed in February, May, August and November of 2004.	273
Figure 6.48 Spatial averages of simulated total evapotranspiration (W/m^2) with and without data assimilation by Noah LSM and NLDAS-2 forcing data in ELRP1 watershed in February, May, August and November of 2004.	274
Figure 6.49 Spatial averages of simulated total evapotranspiration (W/m^2) with and without data assimilation by Noah LSM and NLDAS-2 forcing data in FDYO1 watershed in February, May, August and November of 2004.	274
Figure 6.50 Spatial averages of simulated total evapotranspiration (W/m^2) with and without data assimilation by Noah LSM and NLDAS-2 forcing data in KINT1 watershed in February, May, August and November of 2004.	275
Figure 6.51 Spatial averages of simulated total evapotranspiration (W/m^2) with and without data assimilation by Noah LSM and NLDAS-2 forcing data in NHSO1 watershed in February, May, August and November of 2004.	275

Figure 6.52 Spatial averages of simulated total evapotranspiration (W/m^2) with and without data assimilation by Noah LSM and NLDAS-2 forcing data in PSNW2 watershed in February, May, August and November of 2004. 276

Figure 6.53 Spatial averages of simulated total evapotranspiration (W/m^2) with and without data assimilation by Noah LSM and NLDAS-2 forcing data in SERI3 watershed in February, May, August and November of 2004. 276

ACKNOWLEDGMENTS

I would like to thank my advisor, Dr. Xu Liang, for her thorough academic training, and rest members of my dissertation committee: Dr. Daniel Bain, Dr. Jorge Abad and Dr. Zhi-Hong Mao, for their time spent on my dissertation. Also, I would like to express my thanks to my friends: Dr. Zhuotong Nan and Dr. Jeen-Shang Lin, for their helps on my study and living in Pittsburgh.

I must thank my family: my parents, my sister and my brother, for their love, encourage and support. Most especially, I thank my wife, Yan, for everything she has done for me and for our family, and my daughter, Emma, for her waiting for play and a house of our own.

1.0 INTRODUCTION

1.1 RESEARCH MOTIVATIONS

The principle goal of hydrological forecast is to predict streamflow, for some more complicated cases, soil moisture and evapotranspiration as well. Hydrological models, which simulate water and energy budgets in watersheds, are the foundation of hydrological forecast. Meteorological inputs, such as temperature, pressure and humidity of air, surface wind speed, radiation and precipitation, drive the evolution of hydrological systems. If we build up our understandings to a watershed on the basis of physical laws, then the hydrological model is a set of governing equations, which describe dynamics within and between components of hydrological process, and the meteorological inputs are the boundary conditions of those equations. Reliable hydrological forecasts require not only realistic hydrological model but also accurate meteorological inputs. Therefore, hydrological forecast can be improved through two ways: one is to choose or develop more realistic models and the other is to use or derive more accurate meteorological inputs.

Hydrological process can be either simulated with rainfall-runoff models or land surface models (LSMs). LSMs simultaneously simulate water and energy balances in land surface process, which have more physical basis than simple rainfall-runoff models. After almost 40

years' development, LSMs have been mature in the past decade. In terms of hydrological simulation, LSMs, such as VIC (Liang et al. 1994; Liang and Xie 2001; Liang and Xie 2003), CLM (Dai et al. 2003; Lawrence et al. 2010; Bonan et al. 2011) and Noah (Chen et al. 1996; Chen et al. 1997; Koren et al. 1999; Chen and Dudhia 2001; Ek et al. 2003), share similar functions and structures. Firstly, all of them can simulate basic components of hydrological cycle, including runoff generation, evapotranspiration, and dynamics of moisture and temperature in soil layers, at the watershed scale or the grid scale of climate model, e.g. 1/8 degree to 1 degree. Secondly, the same governing equations have been applied to describe mechanisms of hydrological process. For example, Richards' equation is used to simulate the movement of soil moisture in unsaturated zone and the thermal diffusion equation is used for simulating the fluxes of heat in soil layers. For some comprehensive models which consider groundwater explicitly, Darcy's law may be used to simulate the flow of ground water (Du et al. 2007). In large watersheds where flow routing has to be considered, Saint Venant equations and their simplified forms are usually used for routing water flows over land surface and in river channel (Jain et al. 2004; Jain and Singh 2005; Liu et al. 2009). Because of close formulations for hydrological process, none of LSMs have been proved absolutely superior to others in hydrological forecast so far. In addition, it seems that it is hard to significantly improve hydrological forecast by developing more advanced LSMs since the existing ones have incorporated most hydrological knowledge.

On the contrary, it is more promising to improve hydrological forecast by improving the quality of meteorological inputs for LSMs. Nowadays, hydrological forecast is not limited by the availability of meteorological inputs; but indeed, it is limited by their accuracies After the launch

of the first satellite in 1957, more and more platforms, as well as instruments, are emerging for measuring meteorological inputs. Especially, satellite-borne sensors and ground-borne radars, which measure meteorological inputs continuously in space rather than the point measurements of tradition meteorological stations, have facilitated hydrological forecast significantly. However, even with cutting-edge hydrological models and meteorological inputs produced by modern technologies, the accuracy of hydrological forecast still cannot fully fulfill the requirements of operational applications. Even though available meteorological measurements are not reliable enough, they have distinctive advantages respectively. More reliable meteorological data may be derived by combining the advantages of existing measurements. Therefore, the problem of improving hydrological forecast can be partially solved by deriving more accurate meteorological inputs through data fusion.

Precipitation is the most important meteorological input for LSMs. Its accuracy directly affects the reliability of hydrological forecast. Intuitively, precipitation is the source of all forms of water in watershed. Specifically, the importance of precipitation can be explained through mechanisms inside the control volume of hydrological modeling, as depicted in Figure 1.1. For hydrological simulation with LSMs, the study domain, i.e. the watershed, is usually discretized into a number of rectangular grids. Each grid is corresponding to a control volume of hydrological model, which describes all components of hydrological process except flow routing. The control volume starts from the bottom of soil layer and ends at the top of canopy, which is usually composed of a layered soil column and a layer of vegetation growing in it. Vegetation interacts with soil layers through their roots, which penetrate one or more soil layers and extract water to fulfill the water demanding by transpiration. From the top to the bottom,

canopy, snowpack and soil column can be abstracted as a series of buckets with holes at side or bottom to describe reallocation of precipitation within the control volume. Among them, the bucket for soil column is directly related to runoff generation. As shown in Figure 1.1, the side hole of the bucket is used to describe surface flow generation. After certain amount of precipitation, if soil water content reaches to some threshold, e.g. the height of side hole, then extra precipitation will be turned into surface runoff. Reversely, if the soil water content is under the height of side hole, then all precipitation will be absorbed by soil layers. Base flow, which recharges groundwater aquifer from soil layers, is through the bottom hole in the form of free drainage forced by gravity in most of land surface models (Zeng and Decker 2009). Same as the bucket for soil column, other buckets describing intercepted precipitation and snowpack also have thresholds of storage for the purpose of separating precipitation. The existence of storage thresholds in those buckets for hydrological components represents the nonlinear nature of precipitation redistribution. It means that the amounts of precipitation allocated to canopy interception, snow pack and soil moisture contents are not always linearly proportional to certain factors, for example, storage capacities of buckets. Even the minor change of precipitation quantity may vary the proportions of precipitation redistributions significantly. Therefore, surface flow, base flow, and storages in each component simulated by hydrological model are very sensitive to the quantity of precipitation. In other words, if we can improve the accuracy of precipitation by any means, it is likely that hydrological forecast will be improved and the improvement may be significant as well.

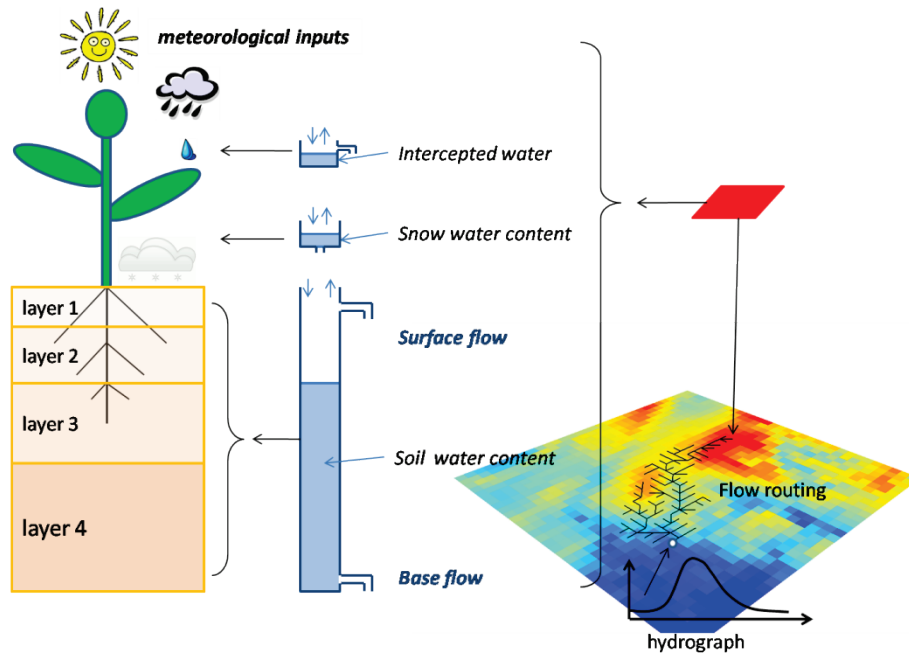


Figure 1.1 Control volume of hydrological modeling

Data fusion is an effective approach to derive new precipitation datasets by taking advantages of existing measurements, such as rain gauge measurement, radar measurement and satellite measurement. These measurements all have their advantages and limitations. For example, rain gauges provide the most accurate measurement of precipitation but they are only available discretely at points. Interpolation algorithms can help to interpolate rain gauge measurements over space but they cannot compensate for the insufficiency of rain gauges. Geostationary satellites with infrared sensors boarded and polar orbit satellite with microwave sensors boarded, which measure precipitation through the temperature of clouds and microwave echoes respectively, are good at continuous measurement of precipitation over large areas, but limited in the accuracies and spatial resolutions. Ground mounted precipitation radars fall between rain gauges and satellites in terms of accuracy, coverage as well as spatial resolutions. Specifically, for the cases of hydrological forecast, measurements of precipitation by rain gauge,

radar and satellite may exist simultaneously. Then, derivation of better precipitation data needs to deal with precipitation measurements at different spatial resolution and with different accuracies. Multiscale data fusion is an exact solution for our goal, since it takes advantage of measurements for the same phenomenon but at different spatial resolutions.

Given meteorological inputs and hydrological model, i.e. governing equations and their parameters, hydrological forecasts can also be improved by rectifying state variables of LSMs. LSMs can simulate two types of variables, which describe dynamic properties of watersheds in hydrological cycle. One type of variables describes water or energy, which will leave the control volume after one step of simulation and no longer interact with hydrological components in the control volume. For example, evapotranspiration and generated runoffs, they leave the control volume either by the movement of atmosphere or overland and groundwater flows. We call this type of variables as model outputs. The other type of variables describes water or energy related factors, which will stay in the control volume after current step of simulation and further interact with hydrological components in the control volume at the next step of simulation. For example, intercepted water by canopy, moisture and temperature in soil layers will be the initial conditions in the next step simulation. We call this type of variables as model states. Together with meteorological inputs at the current time step, model states of the previous time step will feed the current step model simulation. Since either hydrological models or meteorological inputs may come with errors, it is unavoidable that computed model states are erroneous. If we accept the reality that both hydrological models and meteorological inputs are imperfect, so as a matter of course, we can reduce errors in hydrological forecasts by rectifying model states before the next step simulation. The technique, which aims to improve model simulation by means of rectifying

model states through incorporating measurements directly or indirectly related to them, is called data assimilation.

Soil moisture measurements are much like precipitation measurements in terms of accuracy and spatial coverage. They are available at varying spatial resolutions with different accuracies. *In situ* measurements are the most accurate ones but they are discrete both in time and space. Besides, compared with the need of soil moisture data assimilation for hydrological forecasts, the number of *in situ* measurements is very limited. Moreover, soil moisture is highly heterogeneous in space because it is affected by too many factors, for example, soil property, precipitation and vegetation. Therefore, interpolation is not an effective approach to distribute *in situ* point measurements to the whole watershed. Same as precipitation, soil moisture contents can also be measured by satellite-borne sensors of microwave radiometry. As an advantage, satellite measured soil moisture data continuously cover large area, which is good for soil moisture data assimilation in the hydrological forecast. However, there are also two main limitations coming with satellite-measured soil moisture contents. One is that the soil moisture derived from the microwave brightness temperature of land surface is usually erroneous because microwave is absorbed and scattered by cloud and vegetation. The other is that satellite-measured soil moisture contents data are usually at very coarse spatial resolutions. For example, for the wavebands used to derive soil moisture, the Special Sensor Microwave/Imager (SSM/I) sensor has a resolution of $69 \times 43 \text{ km}^2$ at 19 GHz (Ku-band) (Drusch et al. 1999); the Tropical Rainfall Measurement Mission Microwave Imager (TRMM/TMI) has a resolution of $63 \times 37 \text{ km}^2$ at 10.65 GHz (X-band) (Cashion et al. 2005); and the Advanced Microwave Scanning Radiometer (AMSR-E) has a resolution of $75 \times 43 \text{ km}^2$ at 6.925 GHz (C-band) (Crow et al. 2001). The

mapping resolutions of soil moisture products may be a little bit finer than the resolutions of sensors. However, they are still very coarse. For example, the resolution of SSM/I soil moisture is 25 km. The spatial resolution of hydrological forecast, i.e. the horizontal size of control volume, varies according to application purposes and it is not necessarily the same as spatial resolution of any satellite soil moisture data product. So, the resolution related problem, how to estimate soil moisture more accurately based on erroneous soil moisture measurements by satellite and simulations by LSMs at multiple spatial resolutions, comes again. Similar to the case of precipitation, this problem can be solved by the strength of multiscale approach, more specifically, multiscale data assimilation technique.

The purpose of using multiscale approaches is to fully utilize the information of data and to avoid introducing extra errors by means of aggregation or disaggregation. The principle philosophies of multiscale precipitation fusion and multiscale soil moisture data assimilation are exactly the same. It is to estimate more accurate precipitation or soil moisture based on multiple erroneous measurements or simulations at different spatial resolutions. The reasons of doing data fusion in a multiscale way can be explained from two aspects. One is the scale-dependent nature of measurements and their corresponding errors. Both measurements and errors are related to their resolutions. From the perspective of hydrological forecast, such scale-dependence can be explained on the heterogeneities of precipitation and soil moisture. Because both of precipitation and soil moisture varies significantly over space, the measured quantities will be mostly different if changing resolution of measurement, i.e. the extent of a single measure. From the perspective of data fusion theory, if we adopt the Multiresolution Model (MR model) for signal and image processing (Chou et al. 1991; Basseville et al. 1992; Chou et al. 1993; Willsky 2002), then

multiscale measurements and their associated errors can be described by linear Gaussian models and Lyapunov equation respectively. In other words, both of them are functions of resolution. The other is the limitation of aggregation and disaggregation. Suppose that we don't use multiscale approaches, then we have to aggregate or disaggregate measurements if their resolutions are finer or coarser than the resolution of hydrological forecast. Information will be lost in the aggregation process and no information will be gained in the disaggregation process. Besides, more errors may be introduced by aggregation or disaggregation. Moreover, it is hard to estimate statistical features of those added errors. By doing data fusion or data assimilation in a multiscale way, we can fully utilize information from measurements, especially those finer than hydrological forecasts.

Multiscale recursive estimation was proposed as a methodology for merging multisensory and multiscale measurements in order to obtain estimations and their error statistics at desired scales in 1990s (Chou and Willisky 1991; Basseville et al. 1992; Chou et al. 1993; Chou et al. 1994). With the name of scale recursive estimation (SRE), the multiscale data fusion technique was firstly used in fusing precipitation measurements by different instruments at different spatial resolutions, e.g. SSM/I derived precipitation at $15 \text{ km} \times 15 \text{ km}$ and radar derived precipitation at $2.5 \text{ km} \times 2.5 \text{ km}$ resolution (Gorenburg et al. 2001). A multiplicative random cascade model (Gupta and Waymire 1993; Over and Gupta 1994) was used to describe the multiscale variability of precipitation (Gorenburg et al. 2001). In order to fit the linear Gaussian Model between scales in the multiscale data fusion framework (Willisky 2002), measurements of precipitation or their normalization forms were mapped into a log space (Gorenburg et al. 2001). Logarithm transform facilitates the normality approximation of measurements; however it also introduces difficulty

in handling zero values coming from the spatial intermittency of precipitation phenomenon. In order to solve this problem, a lognormal model (LN) and a bounded lognormal model (BLN) were developed by *Tustison et al.* in their verification of quantitative precipitation forecast (Tustison et al. 2002). *Gupta et al.* investigated limitations of LN and BLN together with multiplicative random cascade model and proposed a power transform to precipitation measurement for a better approximation of normality. In doing so, precipitation measurements were taken a power of 0.17 for their specific data and then, the multiscale data fusion was conducted in a real space instead of a log space. Besides, an Expectation Maximization (EM) algorithm, which was built up on the work of (Kannan et al. 2000), was introduced to estimate error variances in the multiscale data fusion framework. Employing the multiplicative random cascade model to precipitation, *Bocchiola* fused precipitations derived from TRMM (PR and TMI) and NEXRAD by using LN and BLN by *Tustison et al.* as well as EM algorithm to assure normality and to estimate parameter respectively. A tree-pruning technique was applied by *Bocchiola* to exclude zero rainfalls in those intermittent areas. Inspired by the works of *Gupta et al.* and *Bocchiola*, *de Vyver and Roulin* developed a new normalization method by taking a power transform to assure that the process noises and measurement noises are normally distributed. *de Vyver and Roulin's* approach also came with an EM algorithm for parameter identification. After the power transform, precipitation measurements were in a real space. Therefore, just like what *Gupta et al.* did, *de Vyver and Roulin's* approach was not bothered by the zero-rainfalls. An evolution trace can be found from above-mentioned studies, which is started from the simple application of multiscale data fusion technique to further development of methodology with respect to the features of precipitation. Those studies showed the capability of multiscale data fusion technique in precipitation fusion. However, it is worth mentioning that all of those studies

just demonstrated multiscale data fusion technique on the precipitation snapshots at a certain time. Besides, the techniques for normality approximations, e.g. the logarithm transform and the power transform, are highly nonlinear, which may introduce extra errors and uncertainties when achieve normality. So far, two research gaps have been in hydrological forecast. One is that a robust model is needed to describe multiscale variability of precipitation and the corresponding approach is to assure the normality. The other is that systematical evaluation of multiscale data fusion technique for precipitation over a long time period for all possible precipitation types, e.g. convective precipitation and stratiform precipitation, is greatly needed. Only with these two gaps to be filled, multiscale data fusion techniques can be applied in operational hydrological forecast.

Multiscale data fusion approach was firstly discussed by *Kumar* (Kumar 1999) on consistent estimate of soil moisture across scales given multiscale measurements, for example, derived from remote sensing and *in situ* technique. By adopting a fractal model to describe multiscale variability of soil moisture, the usefulness of multiscale Kalman filtering (MKF) has been demonstrated in *Kumar's* study. However, *Kumar* also pointed out that the variability of estimated soil moisture by MKF might be less than reality due to the smoothing nature of this algorithm. The application of MKF in soil moisture data assimilation was formally began in the work of *Parada* and *Liang* (Parada and Liang 2004), in which, extended with an EM algorithm, MKF was used to assimilate near surface soil moisture (at 800 m resolution) derived from electronically scanned thin array radiometer (ESTAR) into VIC-3L land surface model (at 3200 m resolution). A further study about impacts of spatial resolutions and data quality on multiscale soil moisture data assimilation was also conducted by *Parada* and *Liang* (Parada and Liang 2008). One interesting finding in this study is that land surface model running at coarser

resolution can be rectified considerably by assimilating soil moisture at finer scales; even the finer measurements are much noisier. For other related studies about multiscale soil moisture data assimilation, it is necessary to clarify a confusing approach, namely “ensemble multiscale filter” (Zhou et al. 2008) or “multiscale Ensemble filtering” (Pan and Wood 2009; Pan et al. 2009). Essentially this type of algorithms is just a kind of Ensemble Kalman Filtering (EnKF) which works with measurements at the same scale of land surface model. The “multiscale” in the studies of *Zhou* and *Pan* means that the updated step of each ensemble of EnKF was conducted in a multiscale manner in order to reduce the dimension of error covariance matrix, Kalman gain, etc. To summarize, the study of multiscale soil moisture data assimilation is still in an exploration stage. For the purpose of the practical application in hydrological forecast, a lot of work is need to be done, for example, assessing the role of multiscale soil moisture data assimilation for the improvement of simulations of streamflow, soil moisture and evapotranspiration as well.

Essentially, the scale recursive estimation (SRE) algorithm used in precipitation data fusion and the multiscale Kalman filtering (MKF) algorithm used in soil moisture data assimilation are the same. Both of them include a Kalman filtering step and a Kalman smoothing step. Since the fused data by these algorithms are estimates conditioned on all measurements, it is more like a smoothing algorithm. Therefore, we call this kind of data fusion algorithm as Multiscale Kalman Smoother (MKS) algorithm.

1.2 RESEARCH QUESTIONS

Three research questions are proposed in this study. Two of them are more scientific and one question is more technical. The two scientific questions are listed as follows:

1. What are the influences of precipitation data fusion on hydrological simulations? In other words, what are the improvements in the simulations of streamflow, soil moisture contents and evapotranspiration made by using fused precipitation data?
2. What are the influences of soil moisture data assimilation on hydrological simulations? In other words, what are the improvements in the simulations of streamflow, soil moisture contents and evapotranspiration made by assimilating satellite-measured soil moisture data into land surface simulation?

In this study, both precipitation data fusion and soil moisture data assimilation are multiscale data. The MKS algorithm will be used in precipitation data fusion and soil moisture data assimilation. In order to find out whether this data fusion algorithm is effective to investigate research questions (1) and (2), it is necessary to test the performance of the MKS algorithm. Therefore, the technical research questions is:

3. What is the performance of the MKS algorithm in multiscale precipitation data fusion and multiscale soil moisture data assimilation?

1.3 RESEARCH DESIGN

In order to address these three research questions, a complete hydrological simulation system with land surface simulation, flow routing, parameter calibration, precipitation data fusion and soil moisture data assimilation should be established at first. In addition, due to the purpose of providing guidelines for operational hydrological forecast, this study should be conducted in multiple watersheds with operational land surface model, widely used precipitation datasets and satellite-measured soil moisture data. In this study, we select the operational LSM of National Weather Service (NWS), namely Noah LSM to simulate land surface process. Meanwhile, we select the phase-2 precipitation product of North-American Land Data Assimilation System (NLDAS-2) and NEXRAD MPE precipitation data of NWS as the inputs to derive precipitation datasets through multiscale data fusion. At last, 14 experimental watersheds are selected in the Ohio River Basin and research questions (2) and (3) will be investigated in all of these experimental watersheds.

To answer these questions, this study has conducted the following work:

- Developing a large-scale flow routing scheme for Noah LSM since it doesn't have flow routing functions. In Chapter 2.0, a large-scale flow routing scheme is proposed. It will be used in parameter calibration for Noah LSM and assessments of the influences of precipitation data fusion and soil moisture data assimilation on streamflow simulation.
- Developing a parameter calibration scheme for Noah LSM with multiple precipitation inputs. In Chapter 3.0, a parameter calibration scheme is proposed for Noah LSM, which is featured

with a four-coefficient approximation for parameters in Noah LSM and multiobjective optimization of multiple precipitation inputs.

- Assessing the performance of the MKS algorithm. In Chapter 4.0, the performance of the MKS algorithm is assessed with multiscale precipitation data fusion. Findings of this assessment also work for multiscale soil moisture data assimilation.
- Assessing the influences of precipitation data fusion on hydrological simulations. In Chapter 5.0, influences of precipitation data fusion on the simulations of streamflow, soil moisture contents and evapotranspiration are investigated over the 14 experimental watersheds.
- Assessing the influences of soil moisture data assimilation on hydrological simulations. In Chapter 6.0, influences of soil moisture data assimilation on the simulation of streamflow, soil moisture contents and evapotranspiration are investigated over 14 experimental watersheds.
- Summarizing the major findings of this study. Major findings of this study are summarized and concluded in Chapter 7.0.

2.0 A LARGE-SCALE FLOW ROUTING SCHEME FOR LAND SURFACE MODEL

2.1 INTRODUCTION

Land surface models (LSMs) have been increasingly used in hydrological studies in recent years. Leading LSMs, such as VIC (Liang et al. 1994; Liang and Xie 2001; Liang and Xie 2003) , Noah (Chen et al. 1996; Chen et al. 1997; Koren et al. 1999; Chen and Dudhia 2001; Ek et al. 2003), and CLM (Lawrence et al. 2010; Bonan et al. 2011), have integrated comprehensive descriptions of energy and water balances in soil-vegetation-atmosphere continuum. Compared with conceptual hydrological models, LSMs simulate evapotranspiration and runoff generations on clear physical laws. In addition, LSMs can be easily coupled with weather or climate models for scenario simulations. With increasing interests in global climate change, LSMs will gain much more extensive applications in hydrology in the near future. However, a gap still exists between LSMs and hydrology, since LSMs cannot directly simulate streamflow but runoffs. Streamflow is not only a conventional measurement of hydrology but also the most important forecast in hydrological services. To fill the gap, flow routing schemes are demanded. The values of flow routing scheme lie in two aspects. One is to simulate streamflow and the other is to validate land surface simulations. Even though LSMs can simulate most variables of hydrological processes, streamflow is the only one that can be widely validated. Therefore, it is critical to develop flow routing scheme for the further application of LSMs in hydrology.

The flow routing schemes for LSMs are generally called large-scale flow routing schemes because the computational unit of LSMs is usually at relatively coarse spatial resolutions, such as 1/8 degree, 1/4 degree and 1/2 degree. Because of large size of grid, large-scale flow routing scheme has three features compared with routing scheme developed for finer resolutions. First of all, the lag of water movement should be considered both within a grid and between neighboring grids. Simulated runoffs may take hours or even days to reach the outlet of a grid or move from an upstream grid to a downstream grid. Secondly, flow network cannot be derived directly from DEM data at large scales. At the resolutions of LSMs, DEM data are too coarse to capture geomorphic features controlling routing. Therefore, large-scale flow network can only be derived from finer resolution DEM data or upscaled from flow network at finer resolutions. Lastly, requirement of computational resource is also one concern of large-scale flow routing scheme. Land surface simulation is typically conducted at coarse spatial resolutions but very fine temporal resolutions, e.g. from minutes to one hours. Routing of long series of simulated runoffs over large watersheds requires massive computation resources. In terms of computational requirement, routing algorithms can be categorized into two types. One is recursive algorithm and the other is sequential algorithm. The former is easy to implement but requires more computational resources. The later needs an auxiliary grid-ordering algorithm but is more computationally efficient. Sequential algorithms are preferred in large-scale flow routing. Considering these features, a complete large-scale flow routing scheme should include three components. The first is a large-scale flow network derivation algorithm, which is the basis of large-scale flow routing. The second is a grid-ordering algorithm. This algorithm can order all grids in a watershed into such a sequence, in which any downstream grid has larger order than its

upstream grids. The third is the formulation of in-grid routing and between-grid routing. The purpose of this study is to develop a complete scheme for large-scale routing.

Studies on large scale flow routing started in 1990s along with water balance simulations at continental scales using General Circulation Models (GCMs) (Liston et al. 1994; Marengo et al. 1994; Miller et al. 1994; Hagemann and Dumenil 1998; Arora and Boer 1999; Arora et al. 1999; Coe 2000; Olivera et al. 2000; Arora 2001) and using land surface models and hydrological model at large scales (Lohmann et al. 1996; Coe 1998; Lohmann et al. 1998; Oki et al. 1999; Guo et al. 2004; Gong et al. 2009). In most of these studies, routing processes in grid box and between grid boxes were formulated separately. In-grid routing is usually formulated with linear reservoir(Liston et al. 1994; Hagemann and Dumenil 1998), given flow speed (Marengo et al. 1994; Miller et al. 1994; Coe 1998; Oki et al. 1999; Coe 2000), given residence time(Costa and Foley 1997), Manning's equation (Arora and Boer 1999) and unit hydrograph methods (Lohmann et al. 1996; Lohmann et al. 1998; Mengelkamp et al. 2001). Between-grid routing, also called channel routing in literature, is usually formulated with linear reservoir (Hagemann and Dumenil 1998), Manning's equation (Arora and Boer 1999; Arora et al. 1999; Arora et al. 2001) and linearized Saint Venant equation (Lohmann et al. 1996; Naden et al. 1999; Olivera and Maidment 1999; Olivera et al. 2000; Gong et al. 2009). The results in literatures showed that combinations of each in-grid routing and between-grid routing methods could generate realistic streamflows if parameters of these methods are well calibrated. However, none of these methods are complete flow routing schemes. All of reviewed studies relied on existing flow networks. Once flow network data are not available or mismatch the scale of land surface simulation, flow routing cannot be conducted.

Particularly for LSMs, both surface runoff and baseflow need to be routed within a grid. Compared with other methods, unit hydrograph (UH) method has been widely applied in overland flow routing at watershed scales. The instant unit hydrograph (IUH) of UH method can be either derived on DEM data or approximated with some functions, such as the probability density function (PDF) of Gamma distribution (Croley 1980; Aron and White 1982; Singh and Chowdhury 1985; Mengelkamp et al. 2001). If assume grid of land surface simulation is a close sub-watershed, UH method is a good choice for the routing of surface runoff within a grid. On the other hand, linear reservoir is a parsimonious method for the routing of simulated baseflow within a grid (Liston et al. 1994; Hagemann and Dumenil 1998). In the proposed routing scheme of this study, UH method and linear reservoir method are chosen as alternative methods for the in-grid flow routing.

Flow network is the basis of grid-to-grid flow routing. The accuracy of flow network has strong influence on routed streamflow. A reliable algorithm of deriving large-scale flow network can remove the dependence of land surface simulation on existing flow network data, such as the Total Runoff Integrating Pathways (TRIP) data (Oki and Sud 1998). In recent decades, a number of automatic algorithms have been developed to derive large-scale flow networks (Renssen and Knoop 2000; Vorosmarty et al. 2000; Fekete et al. 2001; Olivera and Raina 2003; Reed 2003; Paz et al. 2006; Arora and Harrison 2007). With these algorithms, flow network at coarser resolution can be derived from DEM data at finer resolutions. For the convenience of expression, the grid at finer resolution is called cell henceforth, which is relative to grid at coarser resolution. According to the assessment of derivation algorithms conducted by (Davies and Bell 2009), cell outlet tracking based method (Reed 2003; Paz et al. 2006) is better than network scaling method

(Fekete et al. 2001) and network tracing method (Olivera and Raina 2003), which is similar to network burning method (Renssen and Knoop 2000). As a part of the proposed routing scheme, a sophisticated large-scale flow network derivation algorithm is developed based on cell outlet tracking method.

In the rest parts of this paper, the details of the proposed large-scale flow routing scheme are described in section 2.2, 2.3 and 2.4. Application and discussion of the routing scheme is given in section 2.5. At last, this study is summarized in section 2.6.

2.2 LARGE-SCALE FLOW NETWORK DERIVATION ALGORITHM

Nowadays, high-resolution DEM data are widely available for hydrological applications. For example, United State Geology Survey (USGS) provides National Elevation Dataset (NED)¹, which is available at 1, 1/3 and 1/9 arc second resolution over the entire U.S. These DEM data are ready for deriving large-scale flow networks, which will be used in land surface simulations. In this study, an algorithm is developed to derive large-scale flow networks based on much finer resolution DEM data, e.g. 1/8 degree flow network based on 1/2048 degree DEM data. The algorithm is designed to be totally automatic and simple to use. Basically, it is a kind of cell outlet tracking algorithm. In order to be free from manual correction of flow networks, possible situations of river network over large-scale grids are considered with combinations of three abstractions of grid outlets and three abstractions of downstream grids. For the simplicity of use,

¹ <http://ned.usgs.gov/>

the only input of the algorithm is the flow accumulation at finer resolution, which can be easily made with general GIS tools.

In the algorithm, flow directions of all grids are determined with two sequential steps. Step 1 is to determine the outlet of grid. As shown in Figure 2.1, grid outlets are abstracted into three types. Type #1 and #2 outlets are the cells with the 1st and 2nd largest flow accumulations within grid. Type #O is the cell with the largest flow accumulation from cells within grid. It may overlap with type #1 or type #2 outlet. Once the type #1 and #2 outlets are identified, their upstream channels can be determined by cell tracking based on flow accumulation data. If the upstream channel of the #1 outlet meanders more than one quadrant of grid, the #1 outlet is set to be the outlet of grid (see panel (1) of Figure 2.1). On the contrary, if the upstream channel of the #1 outlet just crosses a corner of grid and the upstream channel of #2 outlet meanders more than one quadrant of grid, then #2 outlet is set to be the outlet of grid (see panel (2) of Figure 2.1). If both the upstream channel of the #1 and the #2 outlet just cross corners of grid, then the #O outlet is set to be the outlet of grid (see panel (3) of Figure 2.1). After the determination of the outlet of grid, then the algorithm goes to step 2. As shown in Figure 2.2, three types of downstream grids are abstracted to determine the flow direction of the current grid. Type T1, T2 and T3 downstream grids are the 1st grid, 2nd grid and 3rd that the main downstream channel of the current grid goes to. In step 2, if the main downstream channel meanders more than one quadrant of grid T1, then set the flow direction of current grid to T1 (see panel (1) of Figure 2.2). If the downstream channel of current grid just crosses a corner of T1 but meanders more than one quadrants of T2, then set the flow direction to T2 (see panel (2) of Figure 2.2). But if the

main downstream channel just crosses corners of T1 and T2, then set the flow direction to T3 (see panel (3) of Figure 2.2). The flowchart of the derivation algorithm is given in Figure 2.3.

With the three abstractions of grid outlet and three abstractions of downstream grid, the proposed algorithm can deal with the most probable situations of real river channel over the grid of land surface simulation. Applications in 14 watersheds in the Ohio River basin show that the algorithm can derive realistic large-scale flow networks in all watersheds (see Chapter 5.0 and Chapter 6.0). An example in SERI3 watershed in Indiana will be demonstrated in the application and discussion section.

2.3 GRID-ORDERING ALGORITHM

A grid-ordering algorithm is required by high-performance sequential flow routing. In the proposed routing scheme, we use the grid-ordering algorithm developed by Croley et. al. (Croley 1980; Croley and He 2005) to calculate the order of grids in watershed. If flow routing starts from the grid with the smallest order, e.g. 0, all grids in the contributing area of a grid should have smaller routing orders than that of the grid. This assures that once flow routing proceeds to a grid, all of its upstream grids have been routed. The procedures of the grid-ordering algorithm are shown in Figure 2.4. Flow direction derived with the algorithm described in the previous section is the only input for the grid-ordering algorithm.

Grid ordering starts from the outlet grid of watershed. The algorithm recursively tracks all upstream grids of each grid and assign smaller orders to upstream grids and larger orders to downstream grids. For the same watershed, the grid ordering results can be different if the sequence of tracking directions (see Figure 2.4) is different. To generate valid ordering of grid, the sequence of tracking directions can be arbitrary if all upstream directions can be traversed.

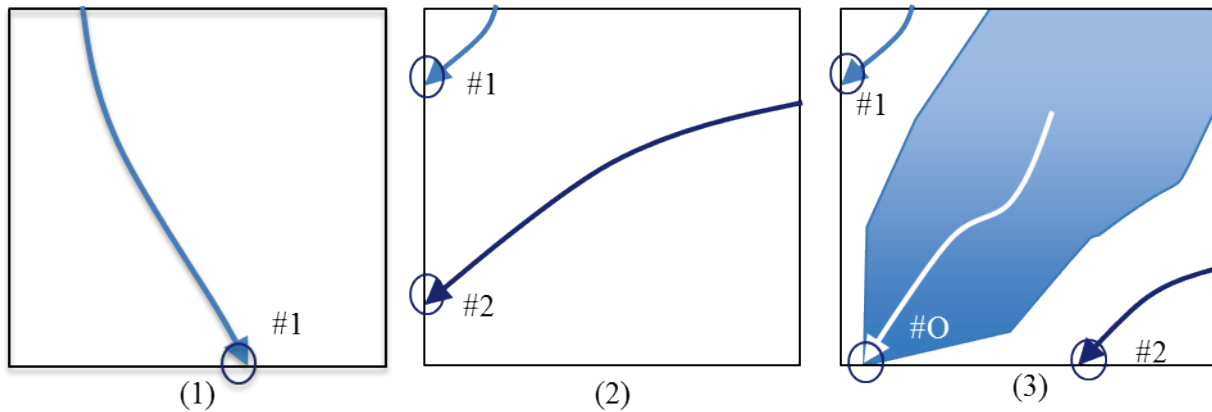


Figure 2.1 Three types of grid outlets. Type #1 and #2 outlets are the cells with the 1st and the 2nd largest flow accumulations. Type #0 outlet is the cell with the largest flow accumulation from cells within grid

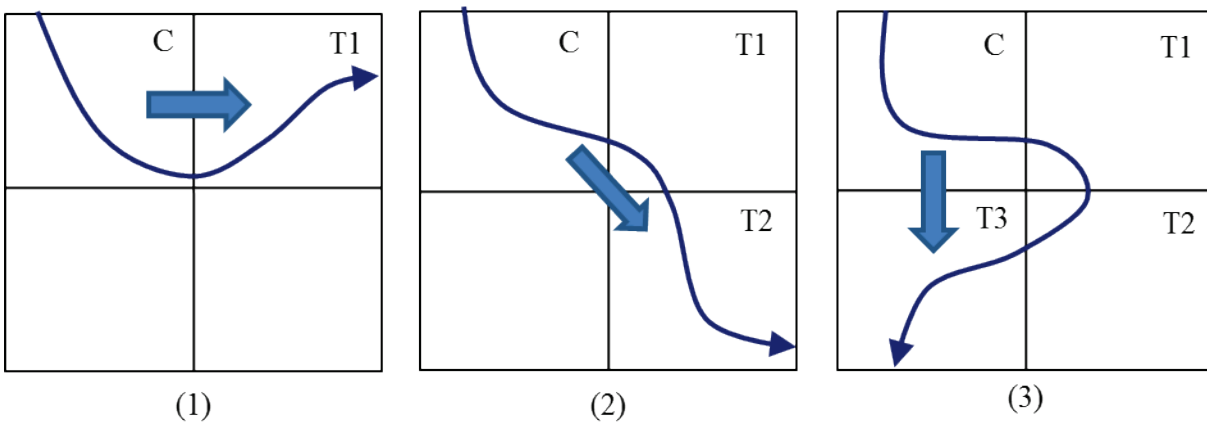


Figure 2.2 Three types of downstream grids. The type T1, T2 and T3 grids are the 1st grid, the 2nd grid and the 3rd grid that the main downstream channel of current grid C goes to.

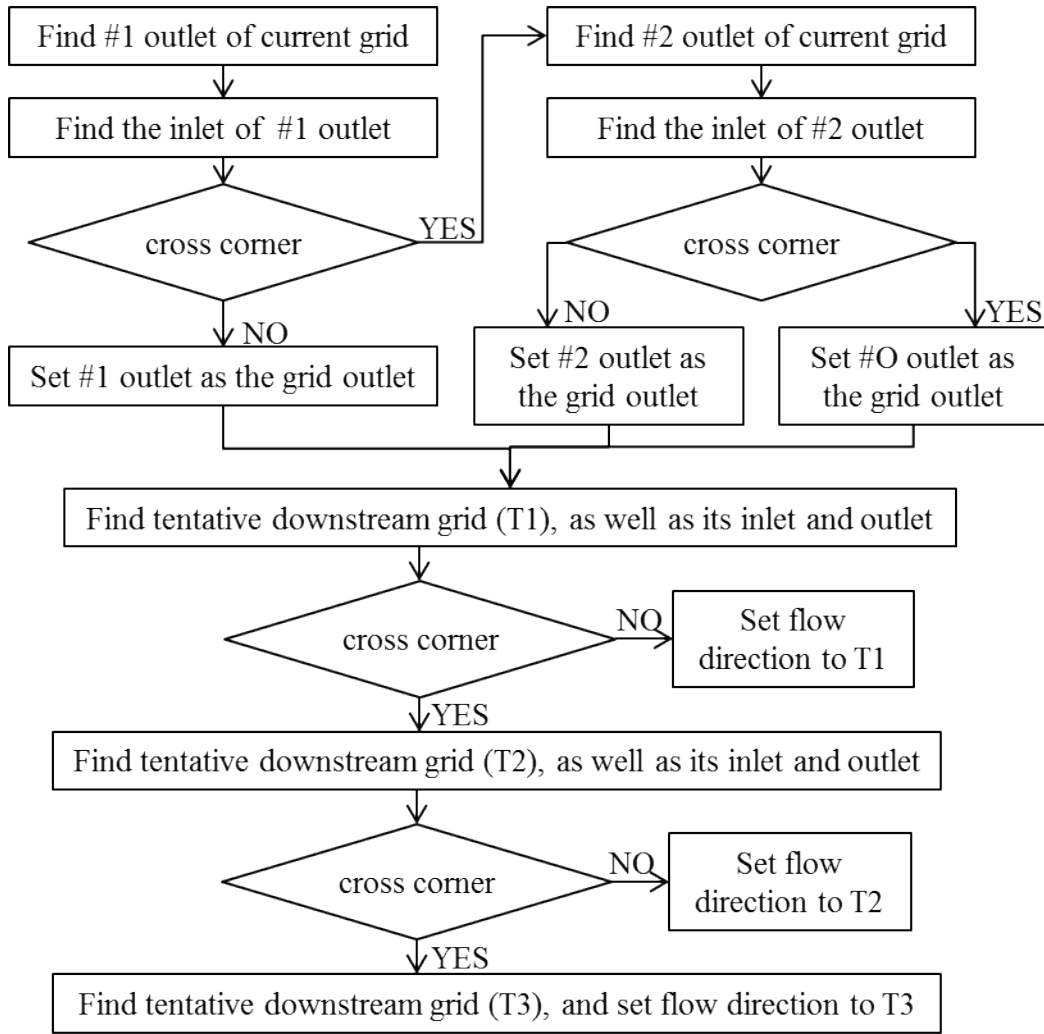


Figure 2.3 Flow chart of large-scale flow network derivation algorithm

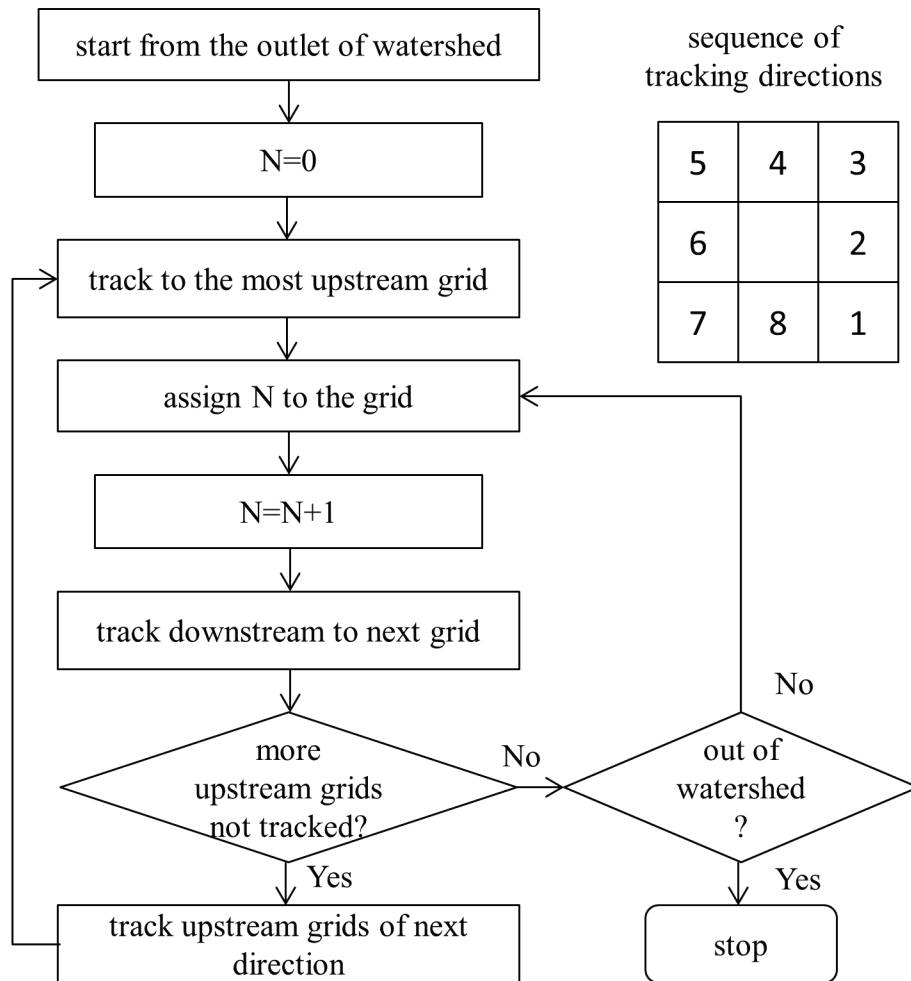


Figure 2.4 Flowchart of grid-ordering algorithm. For each grid, tracking of upstream grid starts from southeast (lower right) and then go to next directions as shown in the sequence of tracking directions.

2.4 FLOW ROUTING METHODS

2.4.1 In-Grid routing

Flow routing methods include formulations for in-grid routing and between-grid routing. In the formulation of in-grid routing in the proposed scheme, surface runoff and base flow are routed separately. Once routed streamflows of surface runoff and baseflow reach to the outlet of grid, they will be added together as the input of between-grid routing.

As mentioned in the introduction section, unit hydrograph (UH) method is adopted in the proposed routing scheme for surface runoff routing. For the UH method, the key is to determine unit hydrograph in a reasonable way. If assuming the grid box of land surface simulation is a closed watershed, the simulated streamflow of surface runoff at the outlet of grid can be calculated as

$$Q_s(t) = \int_0^{\infty} UH(\tau) R_s(t - \tau) d\tau \quad (2-1)$$

where t is time, UH is the unit hydrograph, R_s is the simulated surface runoff. In this study, two approaches are investigated to approximate UH. The first approach is based on finer resolution DEM data. A grid can be discretized into cells at a finer resolution. Therefore, the flow distances of cells to the outlet of grid can be calculated at the finer resolution. Assuming that the flow rate is constant over all cells within grid, then UH can be approximated by scaling the histogram of flow distances of cells to the outlet of grid. To scale UH according to the flow rate, a scaling coefficient, denoted with α , is needed to stretch or compress the histogram. The second

approach is based on synthetic unit hydrograph with the probability density function (PDF) of a two-parameter Gamma distribution

$$UH(t, k, \theta) = t^{k-1} \frac{\exp\left(-\left(\frac{t}{\theta}\right)\right)}{\Gamma(k)\theta^k} \quad (2-2)$$

where k and θ are the shape and the scaling parameters of the synthetic unit hydrograph. Literature (Croley 1980; Aron and White 1982; Singh and Chowdhury 1985) proves that the PDF of the two-parameter Gamma distribution is flexible enough to approximate unit hydrographs derived from real data. In terms of application, these two approaches are complementary to each other. The first approach just has one parameter but needs to derive the histogram based on finer resolution DEM data. The second approach has one more parameter but it doesn't rely on any other inputs.

The routing of baseflow relates to assumptions on groundwater. For the scale of land surface simulation, groundwater within a grid can be either assumed to be in a time-varying mode or an equilibrium status. Linear reservoir is used to route baseflow if assuming the storage of groundwater is changing over time. The simulated streamflow of baseflow can be calculated as

$$Q_b(t) = K \cdot S(t) \quad (2-3)$$

where $S(t)$ is the storage of groundwater at time t , K is the recession coefficient of linear reservoir, which is calibrated. If assuming groundwater is in an equilibrium status within the grid of land surface simulation, then the discharge of groundwater to river channel is equal to the recharge, the baseflow simulated by LSMs. Therefore, baseflow should be directly added to the simulated streamflow at the outlet of grid.

2.4.2 Between-Grid routing

Once surface runoff and baseflow are routed to the outlet of grid, the next step is between-grid routing. Linearized Saint-Venant equation

$$\frac{\partial Q}{\partial t} = D \frac{\partial^2 Q}{\partial x^2} - C \frac{\partial Q}{\partial x} \quad (2-4)$$

is used to describe the inflow and outflow of river channel between neighboring grids, where Q represents flow rate in river channel, x represents the flow distance along river channel, C and D are the velocity and diffusivity of flood wave. In the proposed scheme, the streamflow at the outlet of river channel is calculated with the convolution integral solution of equation (2-4) as

$$Q(x, t) = \int_0^t I(t-s) h(x, s) ds \quad (2-5)$$

where $h(x, t) = \frac{x}{2t\sqrt{\pi t D}} \exp\left(-\frac{(ct-x)^2}{4Dt}\right)$ is the impulse response function (IRF), $I(t)$ is the sum of incoming streamflows from upstream channels or grids at time t . Even parameter C and D can be associated with channel shapes, slopes and other attributes of river channel, but more parameters will be introduced. In the proposed scheme, C and D are treated as effective parameters and determined through calibration.

Theoretically, parameters of the routing scheme can be calibrated for each grid of watershed. However, there will be a large number of parameters if doing so, which means too much freedom in parameter calibration. In order to effectively identify parameters and avoid parameter equifinality, all routing parameters are treated as global parameters. In other words, each parameter has the same value over all grids.

2.5 APPLICATIONS AND DISCUSSIONS

The proposed routing scheme has been examined extensively in the Ohio River Basin. Specifically, the capability and performance of the routing scheme is demonstrated through an example of application in SERI3 watershed. SERI3 watershed is the east fork of the White River, a branch of the Ohio River. The outlet of SERI3 is near Seymour, Indiana, USGS 03365500. With elevation ranging from 128 m to 381 m, SERI3 watershed has a mild topography over a drainage area of 6063 km² (see Figure 2.5). The proposed routing scheme is calibrated at the outlet of SERI3 watershed and validated at the outlet of BAKI3 watershed, namely the east fork of the White River at Columbus, which is a sub-watershed of SERI3. At the outlet of BAKI3, USGS locates 03364000 streamflow gage. Both the outlets of SERI3 and BAKI3 watersheds are marked in the map of Figure 2.5.

In the applications, surface runoff and baseflow are simulated at 1/8 degree resolution with Noah LSM. All atmospheric inputs, including air temperature, air pressure, specific humidity, wind speed, incoming shortwave and long wave radiations, and precipitation, are the phase 2 forcing data of the North American Land Data Assimilation System (NLDAS-2). Flow network at 1/8 degree resolution is derived from DEM data at 1/2048 degree resolution, which are resampled from the National Elevation Dataset (NED) 1 Arc Second (1/3600 degree) DEM data. For each 1/8 degree grid, there are 256×256 cells at 1/2048 degree resolution. For each 1/8 degree grid, the histogram of flow distances from cells to the outlet of grid is derived from flow direction data at 1/2048 degree resolution. And the histogram is used to approximate unit hydrography for the surface flow routing within the grid. To facilitate the evaluation of the derived flow network at 1/8 degree resolution, main river channels of the experimental watershed

is derived from the DEM data at 1/2048 degree. In addition, the lengths of the segments of main river channel within all grids are also derived through cell tracking.

Table 2.1 Ranges of parameters in calibration

Parameter name	Range
Scaling parameter for histogram based unit hydrograph (α)	0.002-0.5
Shape parameter of Gamma PDF (k)	0.5-10
Scaling parameter of Gamma PDF (θ)	0.5-20
Recession coefficient of linear reservoir (K)	0.01-1.0
Wave velocity (C)	0.05-4.0 (m/s)
Wave diffusivity (D)	500-3000 (m ² /s)

Parameters, including the scaling parameter for flow distance histogram, the shape and the scaling parameters of the two-parameter Gamma PDF, the recession coefficient of linear reservoir, and the wave velocity and the wave diffusivity of linearized Saint Venent equation for between-grid routing are calibrated with a Particle Swarm Optimization (PSO) algorithm (Wang 2010). The ranges of routing parameters are listed in Table 2.1. Nash-Sutcliffe Efficiency (NSE) is used as the goodness of fit in parameter calibration, which is defined as the following

$$NSE = 1 - \frac{\sum_{t=1}^T (Q_o^t - Q_s^t)^2}{\sum_{t=1}^T (Q_o^t - \overline{Q_o})^2} \quad (2-6)$$

where t represents time step and T represents the total time step, Q_o^t and Q_s^t represent observed and simulated streamflow at time step t , $\overline{Q_o}$ is the mean of observed streamflow over calibration period. In this study, flow routing is conducted at hourly time step and then simulated hourly

streamflow is aggregated into daily time step for NSE computation because the observed streamflows are measured at daily time step at both the outlet of SERI3 and BAKI3 watersheds.

Table 2.2 Calibrated parameters and corresponding Nash-Sutcliffe efficiencies (NSEs) of Experiment 1, 2, 3, 4 and 5.

	α or k	K or θ	C	D	NSE (SERI3)	NSE (BAKI3)
Experiment 1	0.1452	0.9504	0.4686	2940.619	0.8428	0.7411
Experiment 2	0.1643	X	0.4610	2995.767	0.8456	0.7055
Experiment 3	2.6579	13.0373	0.4652	2971.601	0.8368	0.7752
Experiment 4	9.7300	3.3881	0.4300	2851.384	0.8493	0.7873
Experiment 5	X	X	0.4109	2038.949	0.8056	0.7434

Note:

- (1) Column 2: α for Experiment 1 and 2, k for Experiment 3 and 4
- (2) Column 3: K for Experiment 1, θ for Experiment 3 and 4

In the following example of application, the derived flow network is firstly analyzed. And then, five experiments are conducted to discuss the assumptions for baseflow routing, the approximations of unit hydrograph, the approximations of flow length between grids and redundancy of routing scheme will be conducted. To simulate surface runoff and baseflow, land surface simulation of Noah LSM starts from 01/01/2000 to 12/31/2005. Among this period, the first three years (01/01/2000 to 12/31/2002) play as the warm-up period for Noah LSM and the last three years (01/01/2003 to 12/31/2005) are the period of calibration. The goodness of routed streamflow depends on both the simulated runoffs of Noah LSM and the routing scheme. In order to avoid the influences of Noah simulation on the analysis of the routing scheme, the

investigations on the routing scheme are conducted just in the calibration period instead of a validation period. However, the routed streamflow at the outlet of sub-watershed (BAKI3) can be regarded as kind of validation since calibration is conducted at the outlet of SERI3 watershed.

2.5.1 Analysis of derived flow network

The derived flow network of SERI3 watershed is given in Figure 2.5. First of all, derived flow network is consistent with the main river channel, which is derived from the DEM data at 1/2048 degree resolution. The grid-wise topology of the main river channel segments is mostly reserved by the derived network. This is because the algorithm of flow network derivation has comprehensively considered possible shapes of river channel. For example, the main river channel in the grid with routing order 12 (called #12 grid and similarly for other grids) is from #27 grid and goes to #56 grid. But the main channel just meanders in a small portion of #12 grid, i.e. less than a quadrant. In addition, most part of #12 grid is the contributing area of #58 grid. Therefore, the flow direction of #12 grid is pointed to #58 grid, instead of the downstream grid of the main channel, namely #56 grid. Nevertheless, the algorithm of flow network derivation also has some limitations. The topology of main river channel segments may be violated at small probabilities. For example, the flow direction of #14 grid points to its left neighboring grid (#24 grid). But the main river channel from #14 grid doesn't go to the main river channel of #24 grid. Moreover, the downstream river channel of #14 meanders more than one quadrant of #24 grid. Therefore, #24 grid is the T1 type (see Figure 2.2) downstream grid. It is correct to point the flow direction of #14 grid to #24 grid according to rules set in the derivation algorithm. The same situation also happens to #38 grid. This kind of problem doesn't mean any defects of the algorithm of deriving large-scale flow network. Instead, it is unavoidable because of the large

size of LSM grid and the assumption of the single flow direction, which is implicitly used in this study. However, such a problem will not significantly influence flow routing since the contributing areas of problematic grids are usually relative small.

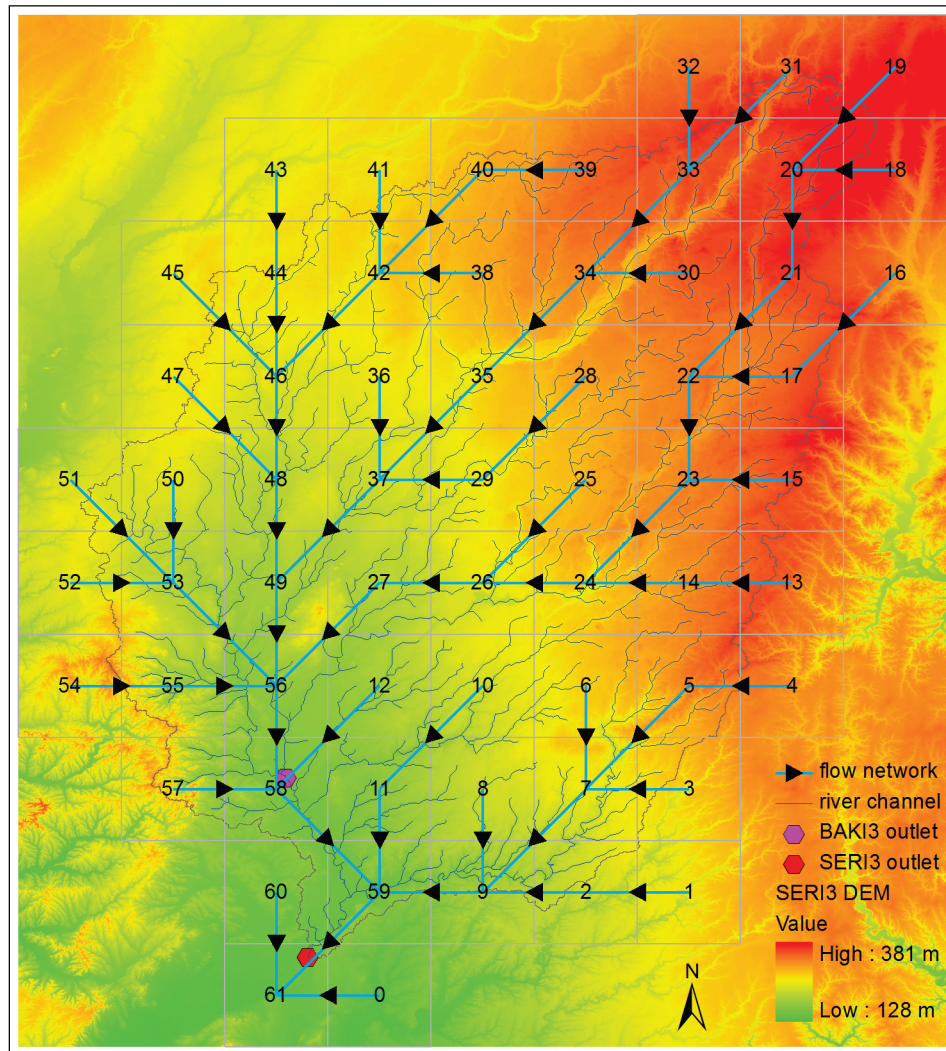


Figure 2.5 Map of SERI3 watershed. In the figure, square boxes are grids at 1/8 degree resolution; numbers are routing orders of grids.

As a summary of Figure 2.5, the derived flow network at 1/8 degree resolution is good for flow routing since it realistically reproduces the topology of the main river channels derived from DEM data at a very fine resolution (1/2048 degree). In addition, the routing orders

annotated in the center of grids in Figure 2.5 comply with the requirement of the sequential flow routing. That is, all upstream grids should have smaller routing orders than that of the downstream grid if routing starts from grid with smaller routing order. It indicates that the grid-ordering algorithm matches the objective of sequential routing in the proposed scheme.

2.5.2 Comparison of assumptions for baseflow routing

At the scale of land surface simulation, based flow generated by LSM cannot be routed using groundwater dynamics for mainly two reasons. First, the computation unit of LSM, namely grid, is usually not a closed groundwater unit. Second, information about groundwater aquifers, initial conditions and boundary conditions are very hard to obtain at the scale of LSM. Therefore, most of LSMs don't describe the interaction between generated baseflow and groundwater at the level of physical dynamics. Indeed, the routing of baseflow heavily relies on simple and effective conceptual methods with specific assumptions. As mentioned in Section 2.4.1, the proposed routing scheme respectively considers two assumptions for baseflow routing. One assumes time-varying groundwater and the other assumes balanced groundwater, which is in equilibrium status. In this section, two experiments, namely Experiment 1 and Experiment 2, are conducted in SERI3 watershed to compare these two assumptions. Taking the assumption of time-varying groundwater, Experiment 1 uses linear reservoir to describe the time lag of generated runoff within grid. While in Experiment 2, generated runoff is added to between-grid routing directly because the recharge and the discharge of groundwater are assumed balanced.

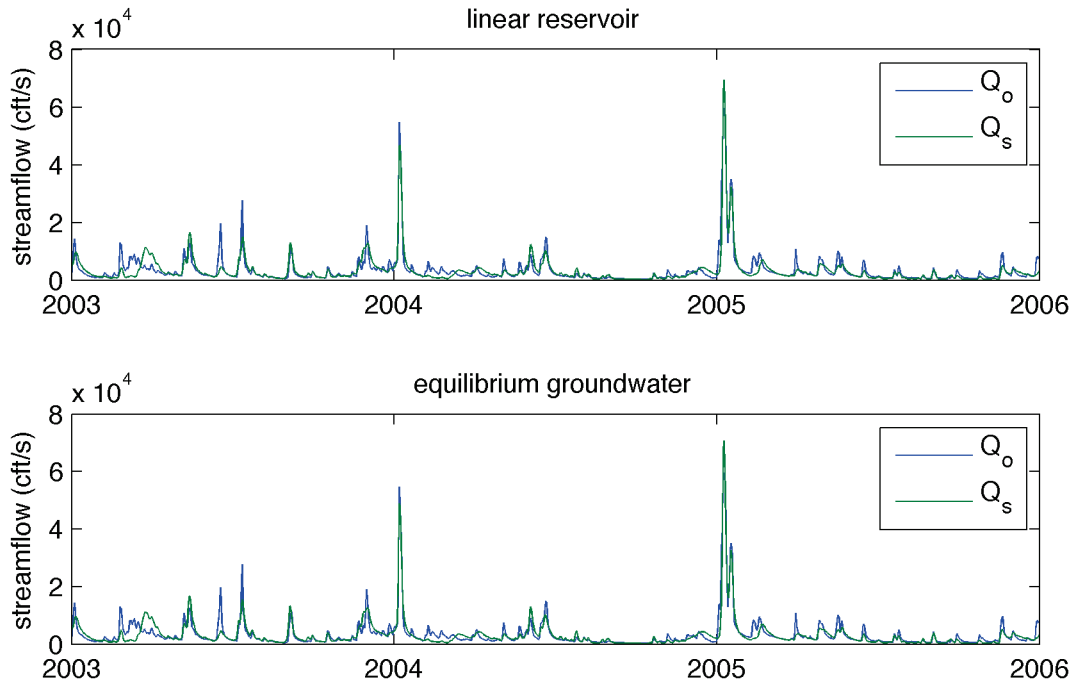


Figure 2.6 Observed and simulated streamflows in SERI3 watershed. The upper panel includes the routed streamflow with linear reservoir for baseflow. The lower panel includes the routed streamflow with the assumption of equilibrium groundwater.

Parameter calibrations are conducted respectively for the two experiments. Calibrated parameters and corresponding NSEs at the outlets of SERI3 and BAKI3 watersheds are listed in Table 2.2. The NSEs of the two experiments reach almost the same value at the outlet of SERI3 watershed (i.e. 0.8428 and 0.8456). Observed and simulated streamflows in the calibration period are shown in Figure 2.6. It can be seen that the simulated streamflows of both experiments are well agreed with the observed streamflows at the outlet of calibration. This result indicates that both assumptions, namely time-varying groundwater and balanced groundwater, work well in baseflow routing. As a kind of validation, streamflow at the outlet of BAKI3 watershed, as shown in Figure 2.7, is also routed with observed streamflow in the calibration period. Similar to

Figure 2.6, simulated streamflows of both experiments have good fits to observations. This means that the whole framework of the proposed routing scheme is well designed for the objective of grid-by-grid routing for land surface simulations. While the NSEs at the outlet of BAKI3 watershed, as shown in Table 2.2, indicate that the assumption of time-varying groundwater is a little bit more robust than the assumption of balanced groundwater.

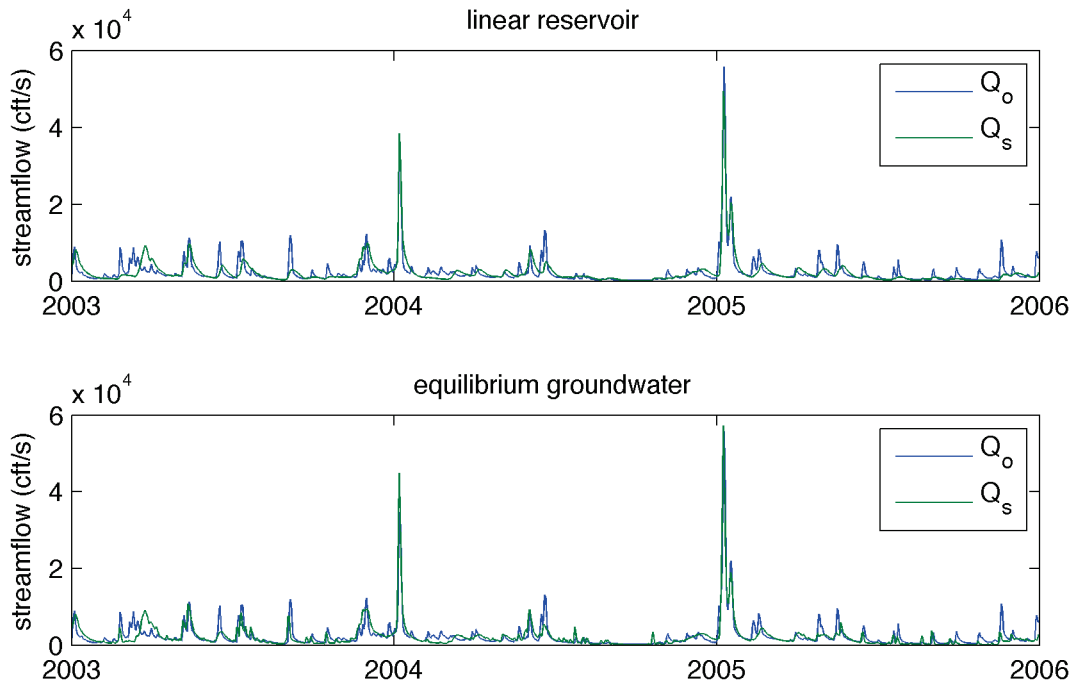


Figure 2.7 Observed and simulated streamflows in BAKI3 watershed. Other descriptions are the same as Figure 2.6.

2.5.3 Comparison of approximations for unit hydrograph

Unit hydrograph (UH) method is an intuitive approach for overland flow routing. The success of UH method for the routing of surface runoff simulated by LSM relies on unit hydrograph, which should be realistic and easy to derive. In this section, two approximations of

unit hydrograph are compared. Each has pros and cons. For example, if approximated with the histogram of flow distances within grid, unit hydrograph has clear physical meanings. However, it also has drawbacks. Firstly, single flow direction doesn't hold at the scale of land surface simulation. Even an outlet of grid can be defined but it hardly happens that all generated runoffs over an entire grid reach the outlet. Therefore, within a grid, the contributing area of the outlet is mostly just a part of the grid and the histogram of flow distances can only be derived from the contributing area. In addition, derivation of such histogram also requires high-resolution DEM data and cannot be done with general GIS tools, such as ArcGIS and GRASS. On the contrary, it is much easier to approximate unit hydrograph with the PDF of the two-parameter Gamma distribution or other mathematic functions. Unit hydrograph doesn't have much physical meaning. To evaluate the goodness of these two approximations, an experiment, namely Experiment 3, is designed to compare these two approximations with the results of Experiment 2. In Experiment 3, the PDF of the two-parameter Gamma distribution is used to approximate unit hydrograph while Experiment 2 uses scaled histogram of flow distances to approximate unit hydrograph. In both Experiment 2 and 3, groundwater is assumed in an equilibrium status. So, the only difference between these two experiments is the approximation of unit hydrograph.

Figure 2.8 shows the observed and simulated streamflows at the outlets of SERI3 and BAKI3 watersheds. It can be seen that simulated streamflows at the outlet of SERI3 has a good fit to observed streamflow. This result indicates that the approximation of unit hydrograph with the PDF of two-parameter Gamma distribution is good for the overland flow routing. Moreover, the simulated streamflow at the outlet of BAKI3 watershed also well fits the observed streamflow. Additionally, it can be seen that the NSE (BAKI3) of Experiment 3 is obviously

larger than the NSE (BAKI3) of Experiment 2. The routed streamflow of Experiment 3 is good not only at the outlet of calibration but also at internal grids. This means that the approximation of Experiment 3 is more reliable than the approximation of Experiment 2 in terms of grid-wise flow routing.

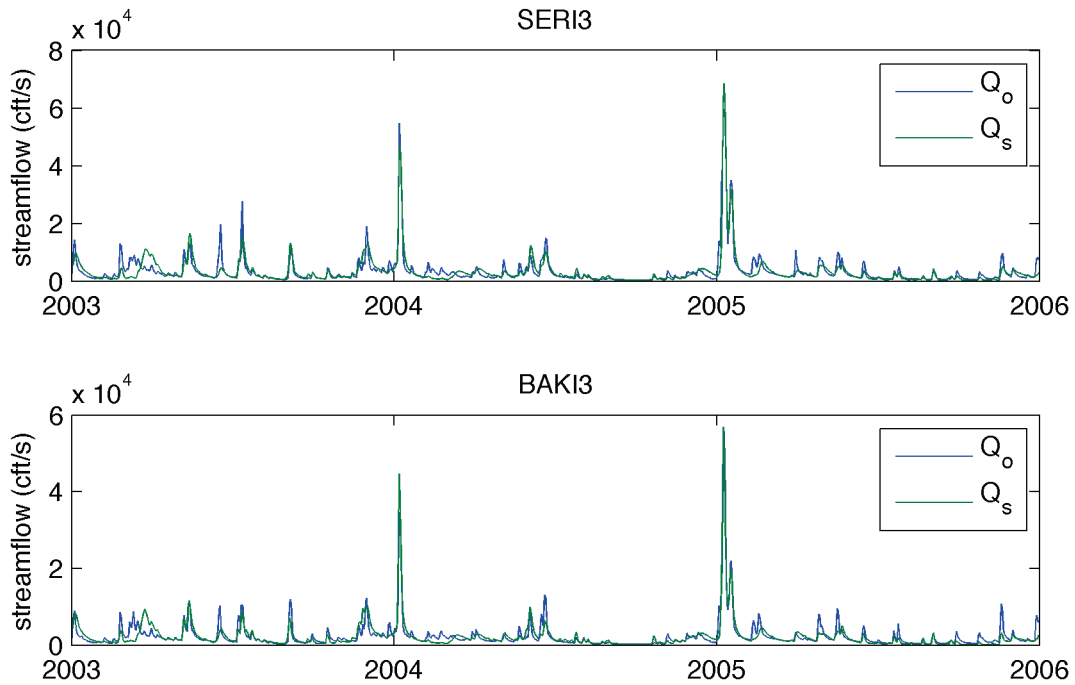


Figure 2.8 Observed and simulated streamflows at the outlets of SERI3 and BAKI3 watersheds. PDF of two-parameter Gamma distribution is used to approximate unit hydrograph and groundwater are assumed in an equilibrium status.

2.5.4 Comparison of approximations for channel length

Flow length, namely the variable x in equation (2-4) and (2-5), is one of inputs for between-grid routing. It directly affects the traveling time of streamflow between grids. Flow length can be approximated either at grid scale or at finer scale. The former takes the orthogonal or the diagonal dimension of grid as the flow length within a grid. The latter approximates flow length by tracking the main river channel, which is derived from DEM at finer resolution. Technically, the former is easy to use but not as accurate as the latter. The latter is good at accuracy but has higher complexity due to the tracking of main river channel. In this section, Experiment 4 is designed to investigate how much improvement that the latter approach can make compared with the former approach. In Experiment 4, (1) surface runoff is routed with unit hydrograph approximated with the PDF of two-parameter Gamma distribution; (2) baseflow is directly added to grid outlet since balanced groundwater is assumed; (3) for between-grid routing, flow length within grid is approximated by tracking main river channel derived from the DEM data at 1/2048 degree resolution. The settings of Experiment 4 are the same as those of Experiment 3, except that flow length within grid is approximated with the orthogonal or the diagonal dimension of grid in Experiment 3.

Figure 2.9 shows the observed and the simulated streamflows of Experiment 4 at the outlets of SERI3 and BAKI3 watersheds. It can be seen that simulated streamflows have good fits to observed streamflows at both outlets. NSEs at these two outlets are also listed in Table 2.2. Both NSEs of Experiment 4 are slightly larger than the corresponding ones in Experiment 3. This indicates that the performance of the proposed routing scheme can be improved if flow length is approximated at finer resolution by tracking main river channel. However, the improvements are

very limited at both the outlet of calibration and the inner grid of watershed. Even though the approximation of flow length with the orthogonal or the diagonal dimension of grid is not as accurate as the other approximation, it is also a good option for large-scale flow routing due to its simplicity and its very limited drop of performance.

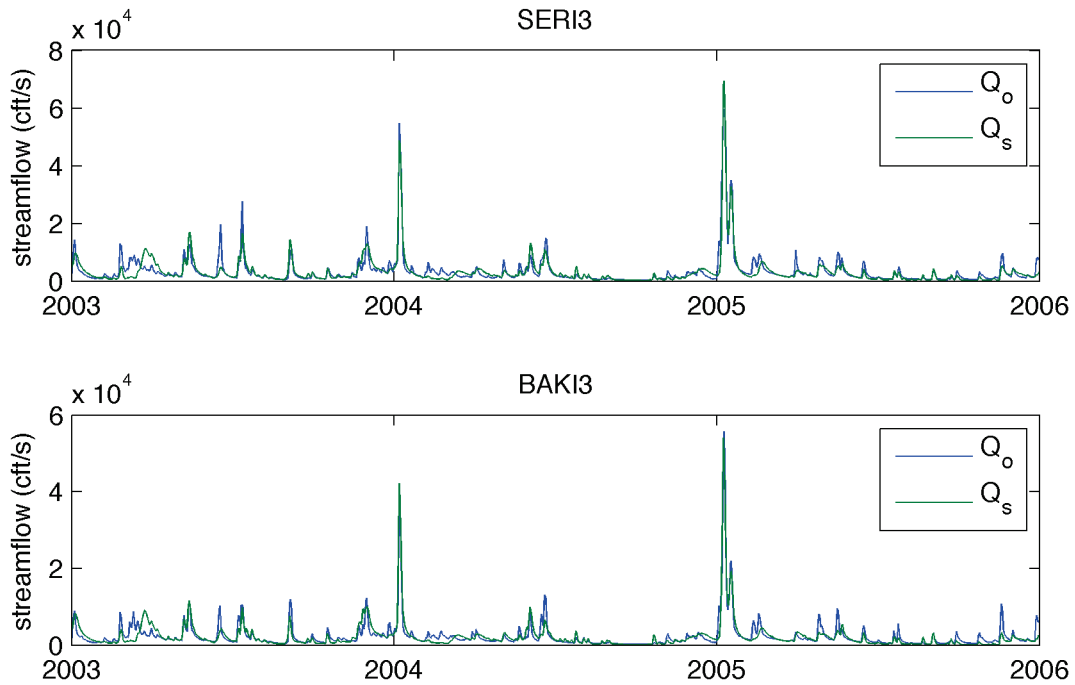


Figure 2.9 Observed and simulated streamflows at the outlets of SERI3 and BAKI3 watersheds. Flow length is approximated by tracking main river channel derived from DEM at 1/2048 degree resolution.

2.5.5 Investigation on the redundancy of the routing scheme

In the proposed routing scheme, the in-grid routing deals with the travelling time of runoffs within grid while the between-grid routing deals with the travelling time of streamflow between grids. By keeping both of them, a routing scheme has clear physical sense. However,

there is also a problem coming with the in-grid routing and the between-grid routing in the parameter calibration of the routing scheme. Generally, optimal parameters are identified by the best fit of simulated streamflow to observed streamflow at the outlet of calibration. It is very hard to separate the influences of the in-grid routing and the between-grid routing on simulated streamflow in calibration. Therefore, there is a large possibility that the parameters of the in-grid routing interact with the parameters of the between-grid routing. It means even the travelling times of water within grids and between grids are not realistic but the overall performance of routing scheme may be optimal at the outlet of watershed. In other words, the routing scheme is redundant in terms of performance. If not considering the physical sense of flow routing, a routing scheme may also have acceptable performance just with between-grid description. The travelling time within grid can be effectively included in the travelling time between grids. In this section, Experiment 5 is designed to investigate the redundancy of the proposed routing scheme. In this experiment, the in-grid routing is no considered. Both surface runoff and baseflow are added directly to the outlet of grid and then go to between-grid routing. For the between-grid routing, flow length is approximated with the orthogonal and the diagonal dimension of grid. Thus, the results of Experiment 5 are comparable with the results of Experiment 1, 2 and 3, which use the same setting of between-grid routing.

Figure 2.10 shows the observed and the simulated streamflows of Experiment 5 at the outlets of SERI3 and BAKI3 watersheds. It can be seen that simulated streamflows also have good fits to observed streamflow at both outlets. It is hard to find differences between the simulated hydrographs of Experiment 5 and those of Experiment 1, 2, and 3 by visual checking. However, NSE (SERI3) of Experiment 5, as listed in Table 2.2, is smaller than those of

Experiment 1, 2, and 3. It means that the proposed routing scheme drops a little bit performance if not considering the in-grid routing process. NSE (BAKI3) is at the same magnitude of NSE (BAKI3) of Experiment 1 and 3 and it is also a larger than NSE (BAKI3) of Experiment 2. These results indicate that redundancy does exist in the proposed routing scheme. By adjusting parameters, the between-grid routing can partially describe the effect of the within-grid routing. But it is still worthwhile keeping the within-grid routing in the proposed scheme. Firstly, there is no performance lose due to the redundancy. On the contrary, slight improvements of performance can be found at the outlet of calibration if the in-grid routing is counted. Secondly, the routing scheme is more physically complete if having both the in-grid routing and the between-grid routing. Nevertheless, further study is necessary for reducing the interaction between parameters of the in-grid routing and the between-grid routing.

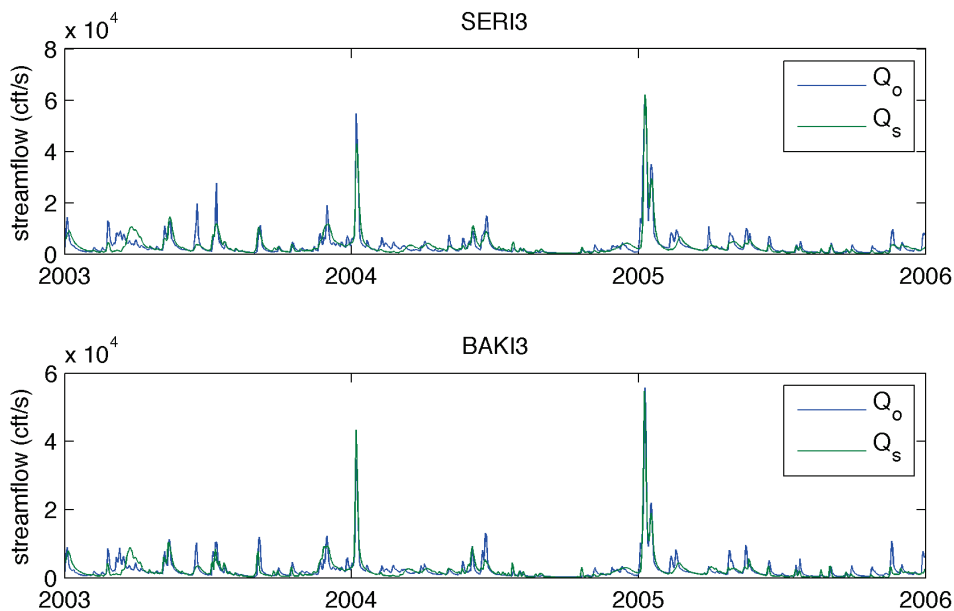


Figure 2.10 Observed and simulated streamflows of Experiment 5 at the outlet of SERI3 and BAKI3 watershed. No in-grid routing is used and the flow length for between-grid routing is approximated with the orthogonal and the diagonal dimension of grid.

2.6 SUMMARY

This paper proposed a complete scheme of large-scale flow routing for land surface simulation. It includes three parts: (1) an algorithm of large-scale flow network derivation, (2) a grid-ordering algorithm and (3) descriptions of the in-grid routing and the between-grid routing. Based on cell tracking, the algorithm of large-scale flow network derivation is used to derive flow network at the scale of land surface simulation from DEM data at a much finer resolution. With the grid-ordering algorithm, all downstream grids are ranked after their upstream grids and then sequential flow routing can be conducted. The travelling of generated runoffs and streamflows within watershed is described with the in-grid routing and the between-grid routing processes. Unit hydrograph method is used for the surface runoff routing within grid. Two alternative assumptions about groundwater within grid and the corresponding baseflow routing methods are given and compared. Linearized Saint-Venant equation is used to describe the movement of streamflow between neighboring grids. In addition to the routing scheme, assumptions for baseflow, approximations of unit hydrograph, approximation of flow length, and redundancy are also investigated in the study.

In the experiment watershed, namely SERI3, flow network at 1/8 degree resolution is derived from the DEM data at 1/2048 degree resolution, as shown in Figure 2.5. The derived flow network is consistent with the main river channel derived from the DEM data at 1/2048 degree. Topology of the main river channel is reserved by the derived flow network. Therefore, the derived flow network is good for large-scale flow routing.

With different settings of baseflow routing, surface runoff routing, and approximations of flow length, five experiments have been conducted in SERI3 watershed in the Ohio River Basin. Investigations show that (1) both the assumptions of time-varying groundwater and balanced groundwater can be used for baseflow routing while the former is a little bit more robust than the latter; (2) the PDF of the two-parameter Gamma distribution is a good approximation of unit hydrograph for surface runoff routing within a grid; (3) both the approximation of flow length at grid scale or at finer scale work well for between-channel routing but the latter has a little bit higher performance than the former; and (4) redundancy exists in the proposed flow routing scheme but it is better to keep both the in-grid routing and the between-grid routing for better performance and physical completeness.

In conclusion, the proposed routing scheme has good performance for routing surface runoff and baseflow simulated by land surface models. However, there are still some rooms for improvement. Further studies will be conducted to impose more physical constraints to parameters of the routing scheme. For example, to associate the shape and the scaling parameters of the PDF of the two-parameter Gamma distribution with topographies within grid and to associate the wave velocity and the wave diffusivity of linearized Saint-Venant equation with river channels derived from high-resolution DEM data.

3.0 A PARAMETER CALIBRATION SCHEME FOR NOAH LAND SURFACE MODEL WITH MULTIPLE PRECIPITATION INPUTS

3.1 INTRODUCTION

Land surface models (LSMs) have great potential in hydrological applications. Compared with traditional rainfall-runoff hydrological models, LSMs can not only simulate surface and subsurface runoffs, but also fluxes of water and heat within soil-vegetation-atmosphere continuum. LSMs have more comprehensive and clearer descriptions of physics than rainfall-runoff models, which makes LSMs ready to simulate the response of water resources to climate changes by coupling with climate model (Klingaman et al. 2008). In addition, LSMs can play the role of distributed hydrological models with flow routing schemes. The potential of LSMs has been widely demonstrated by increasing applications, such as investigation of hydrological variability (Li et al. 2005), assessment or correction of precipitation data (Sheffield et al. 2004; Pan et al. 2010), land surface process simulation (Nijssen et al. 2001; Slater et al. 2007; Ozdogan et al. 2010), and streamflow simulation (Lohmann et al. 2004; Gusev et al. 2008). However, successful application of LSMs depends on effective parameter calibration (Nasonova and Gusev 2008). From the viewpoint of structure, LSMs are composed of equations and parameters. Equations, such as Richards' equation governing soil water flux and heat diffusion equation governing temperatures within soil column, represent the generality of LSMs. These equations

have the same forms in many simulation domains. Parameters are associated with characteristics of land surface; for example, porosity, field capacity, wilting point and saturated hydraulic conductivity are specifically related to the soil type within LSM grid. In order to describe the spatial heterogeneity of study domain, parameters of LSMs are usually spatially distributed. It is often hard to accurately specify these parameters without resorting to model calibration, which is to obtain optimal model parameters by best fitting model simulations against independent observations. Finally, parameter calibration is turned to be optimization problems and solved by automatic optimization algorithms.

Particularly, parameter calibration of LSMs has two features. One is the high dimension and complex structure of the feasible space of parameter and the other is the intensive computational requirement. Land surface simulation is typically a kind of distributed simulation, which means that simulation domain is discretized into sub-units, called grids. Each grid comes with a set of parameters associated with soil, vegetation and others. In order to best fit simulations to observations, parameters of all grids should be optimal to observations. This means the dimension of optimization problem is very high if there are a large number of grids in the simulation domain. Moreover, most parameters of LSMs interact with each other. For example, the wilting point should be smaller than the field capacity and the field capacity should be smaller than the porosity for same soil type. Another example, the porosity of clay should be smaller than the porosity of loam, and the porosity of loam should be smaller than the porosity of sandy loam. These constraints impose complex structure of the feasible space of parameters. Even though the spatial size of LSM grid is usually large, for example 0.125° , the temporal resolution of land surface simulation is usually small, mostly not longer than 1 hour. It means

that there are a big number of iterations for the duration of hydrological application, which is usually at the order of year. Due to the complicated structure of LSMs, the optimization problems of parameter calibration are typically solved by random search algorithms, which rely on massive model simulations and need huge computational resources. Therefore, intensive computation is required to calibrate parameters of LSM. The computational intensity may be extremely high when land surface simulation is conducted over a large area for a long time period, which is often the case of practical application of LSMs.

To date, parameter calibration for LSMs is basically based on the theories and methods of parameter calibration for hydrological models. Optimal parameters are identified by solving optimization problems with random search optimization algorithms. From the viewpoint of optimization problem, the parameter calibration of LSMs can be categorized into two types. One is calibration with single measurements and the other is calibration with multiple measurements. For the former type, measurement is usually streamflow (Xie et al. 2007; Troy et al. 2008; Nasonova et al. 2011). Streamflow is an essential objective of hydrological simulation. In addition, streamflow is also the most reliable measurements related to outputs of LSMs. The latter type addresses the multiple-output nature of LSMs. For this type, parameters are identified jointly against some or all of sensible and latent heat fluxes and other related measurements (Crow et al. 2003; Harris et al. 2004; Demarty et al. 2005; Johnsen et al. 2005; McCabe et al. 2005; Matsui et al. 2007). These studies used optimization algorithms, including SCE-UA (Crow et al. 2003; Troy et al. 2008; Nasonova et al. 2011), MOSCEM-UA (Johnsen et al. 2005), simulated annealing (Xia et al. 2004) and MOGSA (Bastidas et al. 2006). SCE-UA (Duan et al. 1992; Duan et al. 1994) and MOSCEM-UA (Vrugt et al. 2003) are random search algorithms,

which are widely used in hydrological parameter calibration. Existing studies of parameter calibration for LSMs filled the gap between LSMs and their application. However, further studies are still needed to develop parameter calibration schemes for LSMs. For example, parameters are usually confined by upper and lower boundaries in these existing studies. Little regard is given to the physical constraints of parameters. To address this problem, it is necessary to develop new parameter calibration scheme. Moreover, few studies have dealt with the computational intensity of parameter calibration for LSMs. Furthermore there are no existing studies, which calibrate parameters of LSM for multiple forcing data. To facilitate the parameter calibration of LSMs, effective and efficient optimization algorithms has to be developed for high-performance computational platforms.

In this study, a parameter scheme is developed for Noah LSM (Chen et al. 1996; Chen et al. 1997; Koren et al. 1999; Chen and Dudhia 2001; Ek et al. 2003) with multiple precipitation inputs. Consistencies between parameters are considered and a parallel optimization algorithm is designed to identify a single set of parameters for Noah LSM. The optimal set of parameters is required to be good for large simulation domain and multiple precipitation inputs over a long simulation period. The primary goal of this study is to assess the applicability of multiple precipitation datasets in streamflow simulation with Noah LSM, an operational LSM used in National Weather Services (NWS). However, the proposed scheme also can be used to calibrate LSM in the ensemble simulation of streamflow with multiple forcing datasets. In the proposed scheme, the parameters of Noah LSM are constrained with a default parameter tables. In addition, only four global coefficients are to be calibrated without losing the description of spatial heterogeneity in the simulation domain. An MPI (Message Passing Interface) based

multiobjective particle swarm optimization algorithm (MPI-based MOPSO) is designed and implemented for identifying the four coefficients on parallel computers.

In the rest parts of this paper, Noah LSM will be briefly introduced in section 3.2. The four-coefficient approximation and the formulation of optimization problem will be described in section 3.3 and 3.4. And then the MPI-based MOPSO algorithm is given in section 3.5. The evaluation of proposed scheme is going to be conducted in section 3.6 in two watersheds. In the end, this study will be summarized in section 3.7.

3.2 BRIEF DESCRIPTION OF NOAH LSM

A schematic representation of Noah LSM is given in Figure 3.1. Noah LSM describes the processes of soil thermodynamics, soil hydrology, interception of water by canopy, heat fluxes to/from snowpack, soil and canopy. It simulates soil moisture (both water and ice), soil temperature, skin temperature of land surface, snowpack depth, snow water equivalent, canopy-intercepted water, the energy flux and the water flux of soil column, surface runoff, and subsurface runoff. The purpose of this study is to develop a parameter calibration scheme of Noah LSM to assess precipitation datasets in terms of streamflow simulation. So only the soil hydrology part of Noah LSM is described in the followings due to its direct relation to the runoff generation.

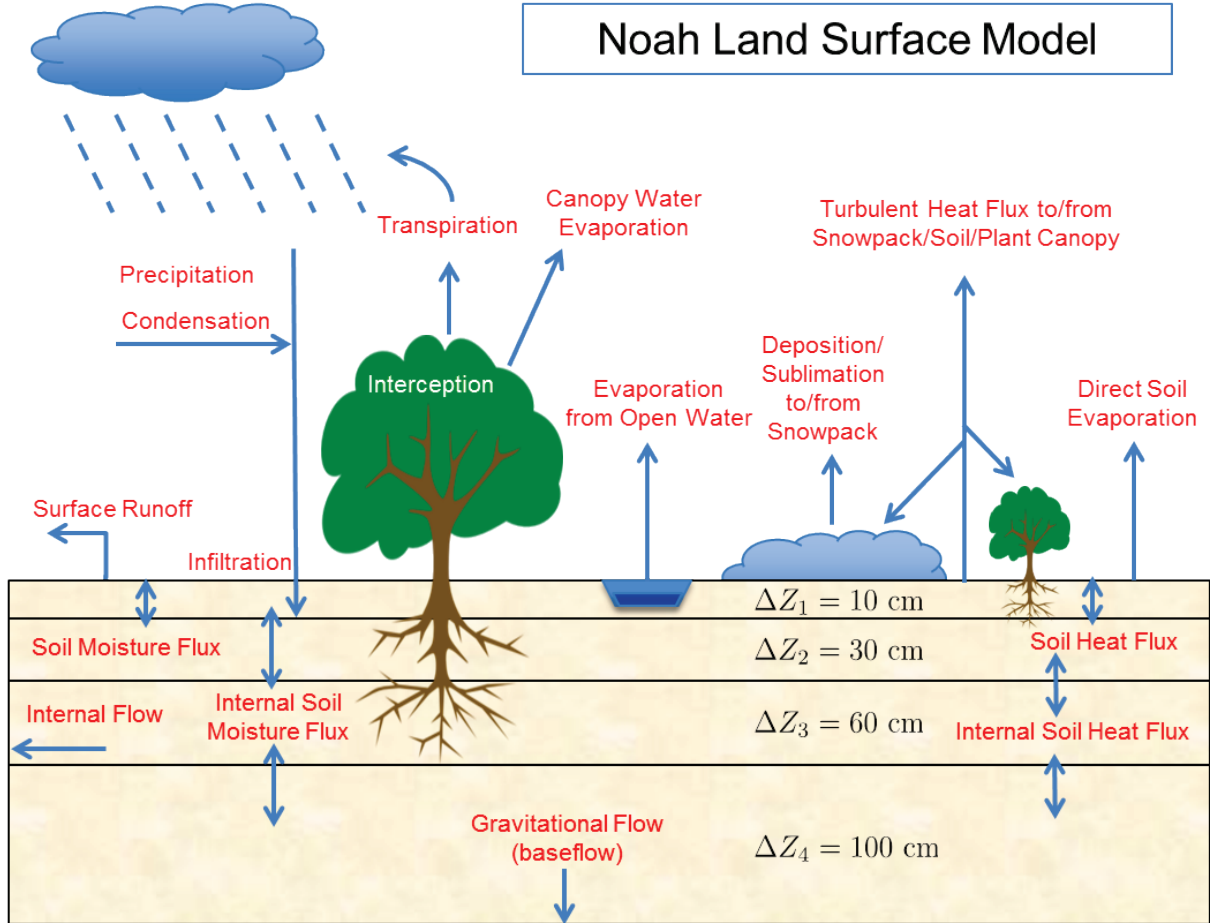


Figure 3.1 A schematic representation of Noah land surface model.

In Noah LSM, volumetric soil moisture content (θ) is governed by Richards' equation

$$\frac{\partial \theta}{\partial t} = \frac{\partial}{\partial z} \left(D \frac{\partial \theta}{\partial z} \right) + \frac{\partial K}{\partial z} + F_{\theta} \quad (3-1)$$

where K is soil water conductivity, D is soil water diffusivity, F_{θ} is the term of sources and sinks (i.e. infiltration, evapotranspiration, and runoff), and z is soil depth. Both K and D are functions of soil moisture content θ . In Noah LSM, K is computed as

$$K(\theta) = K_s \left(\frac{\theta}{\theta_s} \right)^{2b+3} \quad (3-2)$$

where K_s is the saturated soil water conductivity and b is a curve-fitting parameter. D is computed as

$$D(\theta) = K(\theta) \left(\frac{\partial \Psi}{\partial \theta} \right) = D_s \left(\frac{\theta}{\theta_s} \right)^{b+2} \quad (3-3)$$

where Ψ is the soil water potential, which is also a function of soil moisture content θ as

$$\Psi(\theta) = \Psi_s \left(\frac{\theta}{\theta_s} \right)^{-b} \quad (3-4)$$

where Ψ_s is saturated soil water potential, D_s is saturated hydraulic diffusivity ($D_s = -\frac{b\Psi_s K_s}{\theta_s}$).

Parameters K_s , Ψ_s and b depend on soil types.

As shown in Figure 3.1, there are four soil layers in Noah LSM. By integrating equation (3-1) for each layer and expending F_θ , water balance by layer is described as follows:

$$d_{z_1} \frac{\partial \theta_1}{\partial t} = -D \left(\frac{\partial \theta}{\partial z} \right)_{z_1} - K_{z_1} + I - E_{dir} - E_{t_1}, \quad (3-5)$$

$$d_{z_2} \frac{\partial \theta_2}{\partial t} = D \left(\frac{\partial \theta}{\partial z} \right)_{z_1} - D \left(\frac{\partial \theta}{\partial z} \right)_{z_2} + K_{z_1} - K_{z_2} - E_{t_2}, \quad (3-6)$$

$$d_{z_3} \frac{\partial \theta_3}{\partial t} = D \left(\frac{\partial \theta}{\partial z} \right)_{z_2} - D \left(\frac{\partial \theta}{\partial z} \right)_{z_3} + K_{z_2} - K_{z_3} - E_{t_3}, \quad (3-7)$$

and

$$d_{z_4} \frac{\partial \theta_4}{\partial t} = D \left(\frac{\partial \theta}{\partial z} \right)_{z_3} + K_{z_3} - K_{z_4}. \quad (3-8)$$

where d_{z_i} is the thickness of the i^{th} soil layer, I is the infiltration, E_{t_i} is the canopy transpiration extracted from i^{th} soil layer, and E_{dir} is the direct evaporation from bare soil. At

the bottom of the 4th soil layer, soil water diffusivity is assumed to be zero, so that the soil flux is only the gravitational drainage, also named baseflow. As the main discharge of soil column, infiltration I is determined according to the throughfall precipitation P_d and maximum infiltration I_{max} , which is formulated with the saturation deficit of soil column D_x and a time step coefficient kdt as

$$I_{max} = P_d \frac{D_x [1 - \exp(-kdt \cdot \delta_i)]}{P_d + D_x [1 - \exp(-kdt \cdot \delta_i)]} \quad (3-9)$$

$$D_x = \sum_{i=1}^4 d_{z_i} (\theta_s - \theta_i) \quad (3-10)$$

and

$$kdt = kdt_{ref} \frac{K_s}{K_{ref}} \quad (3-11)$$

where θ_s and θ_i are the porosity and the soil moisture of i^{th} soil layer; δ_i is the conversion of the current model step dt (in terms of seconds) into daily values (i.e. $\delta_i = dt / 86400$); $kdt_{ref} = 3.0$ and $K_{ref} = 2 \times 10^{-6} \text{ ms}^{-1}$. Infiltration $I = \min(P_d, I_{max})$. Surface runoff $R = P_d - I_{max}$ when $P_d > I_{max}$. Direct evaporation of bare soil from the 1st soil layer is formulated as

$$E_{dir} = E_p (1 - \sigma_f) \frac{\theta_1 - \theta_w}{\theta_{ref} - \theta_w} \quad (3-12)$$

where E_p is the potential evaporation, θ_w and θ_{ref} are the wilting point and the field capacity of soil, σ_f is the green vegetation fraction. Evapotranspiration E_t is formulated as

$$E_t = \sigma_f E_p P_c \left[1 - \left(\frac{W_c}{W_{cmax}} \right)^{n_c} \right] \quad (3-13)$$

where W_c is the intercepted water by canopy, W_{cmax} is the maximum value of W_c , n_c is a curve-fitting parameter, P_c is the plant coefficient, which is a function of canopy resistance as

$$P_c = \frac{1 + \frac{\Delta}{R_r}}{1 + R_c C_h + \frac{\Delta}{R_r}} \quad (3-14)$$

where C_h is the surface exchange coefficient for heat and moisture; Δ is the slope of the saturation specific humidity curve; R_r is a function of surface air temperature, surface pressure and C_h ; and R_c is the canopy resistance and formulated as

$$\left\{ \begin{array}{l} R_c = \frac{R_{cmin}}{LAI \cdot F_1 \cdot F_2 \cdot F_3 \cdot F_4} \\ F_1 = \frac{R_{cmin}/R_{cmax} + f}{1 + f} \\ F_2 = \frac{1}{1 + h_s [q_s(T_a) - q_a]} \\ F_3 = 1 - 0.0016(298 - T_a)^2 \\ F_4 = \sum_{i=1}^3 \frac{(\theta_i - \theta_w) d_{z_i}}{(\theta_{ref} - \theta_w)(d_{z_1} + d_{z_2})} \end{array} \right. \quad 3-15$$

where F_1 , F_2 , F_3 , and F_4 represent the effects of solar radiation, vapor pressure deficit, air temperature, and soil moisture. In equation set (3-15), $q_s(T_a)$ is the saturated water vapor mixing ratio at the temperature T_a ; R_{cmin} and R_{cmax} is the minimum and the maximum stomatal resistances; LAI is the leaf area index; R_g is incoming solar radiation; h_s is a canopy stress parameter; and $f = 0.55 \frac{R_g}{R_{gl}} \frac{2}{LAI}$.

3.3 FOUR-COEFFICIENT APPROXIMATION

The hydrological part of Noah model has been described in section 3.2. To simulate surface runoff (R) and baseflow (K_{z_4}), parameters in equations (3-1) – (3-15) should be specified with reasonable values. However, due to data availability and scaling issues, most of these parameters need to be determined through calibration. In order to represent the heterogeneity of the simulation domain with model parameters, each grid should have a set of parameters. Therefore, a big number of parameters need to be calibrated, which brings computational difficulty and uncertainty to the searching of optimal parameters. To solve this problem, two steps can be used. The first step is to reduce the number of free parameters. Only those that are essentially related to runoff simulation should be chosen for calibration since this study aims to develop a parameter calibration scheme for assessing precipitation datasets with streamflow simulation. In this study, we choose the porosity (θ_s), the field capacity (θ_{ref}), the wilting point (θ_w), the saturated hydraulic conductivity (K_s), the b parameter, and the leaf index (LAI). These parameters in Noah model are directly related to water fluxes within the soil column of every LSM grid in the simulation domain, but we have to note that the leaf index is not from measurement but a turning parameter in Noah model. The second is to associate parameters with soil type or vegetation type. Actually this step has been done in Noah model, which uses look-up tables for parameters corresponding to soil or vegetation types. With the association, parameter calibration is going to be conducted for a limited number of soil or vegetation types instead of all LSM grids in the simulation domain.

Table 3.1 Default parameter values for 15 soil types used in Noah LSM

SOIL TYPE	TYPE ID	B	DRYSMC	MAXSMC	REFSMC	SATPSI	SATDK	WLTSMC
SAND	1	2.79	0.01	0.339	0.236	0.069	1.07E-06	0.01
LOAMY SAND	2	4.26	0.028	0.421	0.383	0.036	1.41E-05	0.028
SANDY LOAM	3	4.74	0.047	0.434	0.383	0.141	5.23E-06	0.047
SILT LOAM	4	5.33	0.084	0.476	0.36	0.759	2.81E-06	0.084
SILT	5	5.33	0.084	0.476	0.383	0.759	2.81E-06	0.084
LOAM	6	5.25	0.066	0.439	0.329	0.355	3.38E-06	0.066
SANDY CLAY LOAM	7	6.66	0.067	0.404	0.314	0.135	4.45E-06	0.067
SILTY CLAY LOAM	8	8.72	0.12	0.464	0.387	0.617	2.04E-06	0.12
CLAY LOAM	9	8.17	0.103	0.465	0.382	0.263	2.45E-06	0.103
SANDY CLAY	10	10.73	0.1	0.406	0.338	0.098	7.22E-06	0.1
SILTY CLAY	11	10.39	0.126	0.468	0.404	0.324	1.34E-06	0.126
CLAY	12	11.55	0.138	0.468	0.412	0.468	9.74E-07	0.138
ORGANIC MATERIAL	13	5.25	0.066	0.439	0.329	0.355	3.38E-06	0.066

Even with reduced number of parameters and association with soil or vegetation types, consistency is not guaranteed between parameters of a soil or vegetation type and between the same parameter of different soil or vegetation types. To hold the consistency in parameter calibration, a four-coefficient approximation is developed in this study. In the scheme, a default parameter table of Noah LSM is used to constrain free parameters. For widely-used land surface models, such as Noah and VIC, default parameter tables have been developed by model developers. Those default parameter tables are derived under certain conditions, which may not suit for describing soil and vegetation everywhere. Nevertheless, they provide reasonable estimates of relative magnitudes between parameters of the same type of soil or vegetation and between the same parameters of different soil or vegetation types. For example, the magnitude of

the wilting point, the field capacity and the porosity of sand in the default parameter table may not be directly applied to a LSM grid with sand soil type. However, these parameters in the LSM grid can be approximated through scaling corresponding values in the default parameter table. By doing so, the consistency is reserved between porosity, field capacity and wilting point. Without such a constraint, the optimal estimate of field capacity may be larger than that of porosity for a soil type. If a scaling coefficient is global for all types of soil or vegetation, then the relative magnitudes of the same parameter among different soil or vegetation types are also reserved. Therefore, the optimal estimate to the porosity of a sand type is always larger than that of a sandy loam type. Based on the default soil parameter table of Noah LSM as shown in **Table 3.1** Default parameter values for 15 soil types used in Noah LSM, the wilting point (θ_w), field capacity (θ_{ref}), porosity (θ_s), saturated hydraulic conductivity (K_s), saturated hydraulic diffusivity (D_s) and b parameters of each soil type are formulated with three global scaling coefficients (ρ_1 , ρ_2 and ρ_3) as

$$\theta_w = \rho_1 (WL TSMC - DRYSMC) + DRYSMC \quad (3-16)$$

$$\theta_{ref} = \rho_1 (REFSMC - DRYSMC) + DRYSMC \quad (3-17)$$

$$\theta_s = \rho_1 (MAXSMC - DRYSMC) + DRYSMC \quad (3-18)$$

$$b = \rho_2 \cdot B \quad (3-19)$$

$$K_s = \rho_3 \cdot SATDK \quad (3-20)$$

and

$$D_s = \frac{b \cdot SATPSI \cdot K_s}{\theta_s} \quad (3-21)$$

where *DRYSMC* is the default dry soil moisture of the soil type; *WLTSMC* is the default wilting point of the soil type; *REFSMC* is the default reference soil moisture of the soil type; *MAXSMC* is the default porosity of the soil type, *B* is the default *b* parameter of the soil type, *SATDK* is the default parameter of saturated hydraulic conductivity, and *SATPSI* is the default saturated soil water potential. Figure 3.2 gives an example of wilting point, filed capacity, and porosity scaled with $\rho_1 = 0.5$, $\rho_1 = 0.75$, $\rho_1 = 1.0$ and $\rho_1 = 1.25$ for the 13 soil types listed in Table 3.2. It can be seen that both the consistency between parameters and the consistency between soil types are reserved among scaled parameter values. The leaf index (LAI) of Noah LSM is a parameter related to vegetation type. Since the seasonality of vegetation type is described in monthly green vegetation fraction, so LAI is already a global parameter for all vegetation types. In the calibration scheme, the optimal estimate LAI (*lai*) is calculated as

$$lai = \rho_4 \cdot LAI \quad (3-22)$$

where *LAI* is the default LAI parameter of Noah LSM.

Table 3.2 Optimal parameters used in streamflow simulation

Watershed	ρ_1	ρ_2	ρ_3	ρ_4
KINT1	0.501	1.613	1.624	1.343
SERI3	0.512	1.993	1.991	1.993

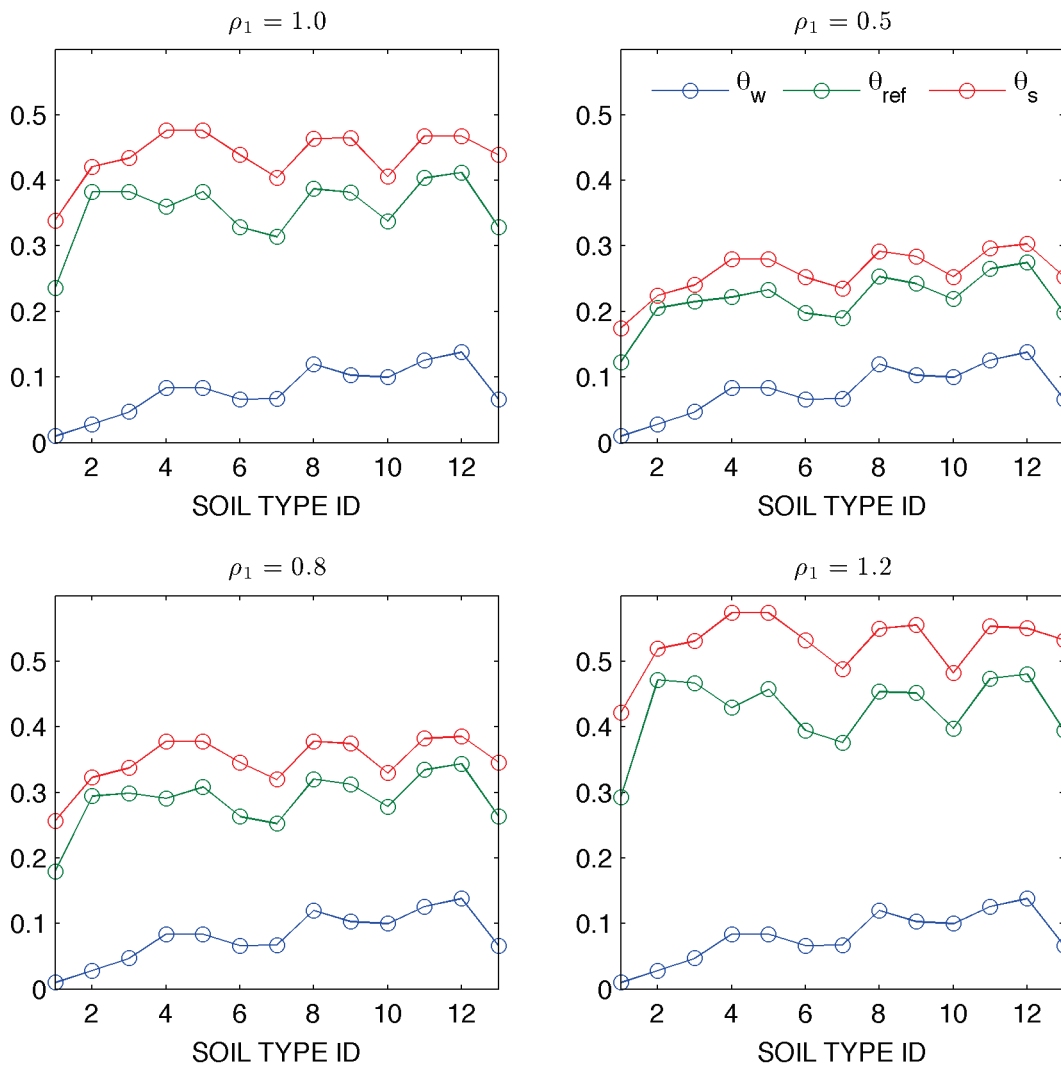


Figure 3.2 Plot of porosity (in red color), field capacity (in green color) and wilting point (in blue color) of 13 soil types when $\rho_1 = 1.0$ (default values), $\rho_1 = 0.5$, $\rho_1 = 0.75$ and $\rho_1 = 1.25$. Names of soil types corresponding to SOIL TYPE ID are listed in Table 3.1.

So far, the hydrological parameters of Noah LSM have been related to the four scaling coefficients. By tuning these four coefficients, surface runoff generation, baseflow generation and evapotranspiration call can be adjusted. Moreover, with the constraints and relative magnitudes provided by the default parameter table, the heterogeneity of the simulation domain

can be effectively described by the four scaling coefficients. Meanwhile, the consistencies are also reserved between parameters and between soil types. The dimension of corresponding optimization problem is also reduced significantly.

3.4 FORMULATION OF OPTIMIZATION PROBLEM

Formulation of optimization problem is an essential step of automatic parameter calibration while objective functions are the basis of an optimization problem. Choosing objective functions depends on the expectation of model simulation. In this study, the goal is to facilitate the assessment of multiple precipitation datasets through the streamflow simulation with Noah LSM. The precipitation dataset is regarded as the best if it generates streamflow, the best-fit observation. Therefore, Nash-Sutcliffe Efficiency (NSE) is chosen as the form of objective function in this study. Given a land surface model and a routing scheme, the simulated streamflow is a function of atmospheric input which is also named forcing data (F) and model parameters, in this case, the four scaling coefficients ($\Theta = \{\rho_1, \rho_2, \rho_3, \rho_4\}$). The forcing data of Noah LSM includes air temperature, air pressure, wind speed, specific humidity, incoming shortwave radiation and long wave radiation, and precipitation. NSE is defines as the following

$$NSE(F, \Theta) = 1.0 - \frac{\sum_{n=1}^N (Q_n^{obs} - Q_n^{sim})^2}{\sum_{n=1}^N (Q_n^{obs} - \overline{Q^{obs}})^2} \quad (3-23)$$

where Q_n^{obs} and Q_n^{sim} are the observed and the simulated streamflow at the n^{th} time step; N is the total number of time steps; and $\overline{Q^{obs}}$ is the mean of the observed streamflow over the simulation period. Nash-Sutcliffe efficiency has a range from $-\infty$ to 1. An NSE of 1 corresponds

a perfect match of simulated streamflow to the observed data. An NSE of 0 indicates that simulation is as accurate as the mean of observed data, whereas an NSE less than zero occurs when the mean of observed streamflow is a better predictor than model simulation.

To confine the influences of other atmospheric inputs and scaling coefficients on streamflow, a single set of parameters is going to be optimized, which is good for streamflow simulations with all precipitation datasets. In addition, except precipitation, rest atmospheric inputs are the same for all simulations, in other words, NLDAS-2 data. Let's use F_i to represent the forcing data for the streamflow simulation with the i^{th} precipitation dataset, and then the optimization problem of this study is formulated as the following

maximize :

$$\left\{ \begin{array}{l} NSE(F_1, \Theta) \\ NSE(F_2, \Theta) \\ \vdots \\ NSE(F_M, \Theta) \end{array} \right. \quad (3-24)$$

subject: Θ in feasible space, where M is the total number of precipitation datasets.

Based on the four-coefficient approximation, the optimization problem is featured with simple structure and low dimension. Complexity is not an obstacle to solve the optimization problem. Theoretically, any random-search based multiobjective optimization algorithm can be used to solve the problem. However, computational intensity is an issue that has to be considered in searching for optimal parameters. In order to evaluate an objective function, Noah LSM must be run over the entire simulation domain for the whole simulation period. For example, the running time of each evaluation is at the order of minutes or even hours if Noah LSM runs at

hourly time step for years in large watersheds, such as 32×32 or 64×64 LSM grids in the case studies of section 3.6. Such a running time is not manageable for a random search algorithm if it just runs on a single computer, especially when the algorithm has large population or a big number of iterations. To solve the optimization problem, the only practical way is to use parallel optimization algorithm, which distributes the evaluation of objective functions to multiple computational nodes.

3.5 MPI-BASED MOPSO ALGORITHM

An effective and efficient parallel optimization algorithm is designed and implemented based on particle swarm optimization (PSO) algorithm (Kennedy and Eberhart 1995). PSO algorithm is a kind of random search algorithm and is characterized by simplicity and efficiency. Multiobjective PSO algorithms can be easily developed and customized for specific applications, for example, parameter calibration of hydrological models (Gill et al. 2006). PSO algorithm is developed based on a social-psychological metaphor, which involves individuals interacting with each other. Each individual is called a particle including a position vector (X) and a velocity vector (V), while the position vector corresponds to the variables of the optimization problem formulated in section 3.4. The set of all individuals is called a swarm. The evolution mechanism of PSO algorithm is that all particles keep tracking the particle with the best position in the solution space of optimization problem. For a maximization problem, such as the one of this study, best position means that the parameter set corresponds to the highest NSE values among all particles. For the convenience of notation, the particle with the best position is represented by

g_{best} . Once g_{best} is determined, all particles in the swarm evolve to the next iteration according to the following formula:

$$\begin{cases} V = w \times V + r(X^{g_{best}} - X) \\ X = X + V \end{cases} \quad (3-25)$$

where w is the inertial coefficient, r is a uniformly distributed random number from 0 to 1.0, $X^{g_{best}}$ is the position of g_{best} . Through such evolution, all particles of the swarm are going to converge to a small domain of the solution space, which is centered with the optimal parameter set of Noah LSM.

The challenge of applying PSO algorithm in the multiobjective optimization problem comes from the selection of g_{best} . PSO algorithm is originally designed for single objective optimization problem. g_{best} can be easily identified by comparing the fitness of all particles. For the case of this study, there is just one NSE for each set of parameters if only having one precipitation dataset. Therefore, it is straightforward to determine g_{best} . For multiobjective optimization problem, things are much more complicated. In this study, we use the concept of Pareto optimal to determine g_{best} . In addition to the swarm, another population of particle, called solution pool, is maintained in the proposed optimization algorithm. Solution pool is used to store Pareto solutions. A particular method of choosing g_{best} is designed here based on the solution pool. For a specific particle, N nearest particles in the solution pool can be identified and then g_{best} is randomly selected from them. This method cannot only choose a g_{best} but also help to keep the diversity of the swarm, with which the optimization algorithm will not converge prematurely.

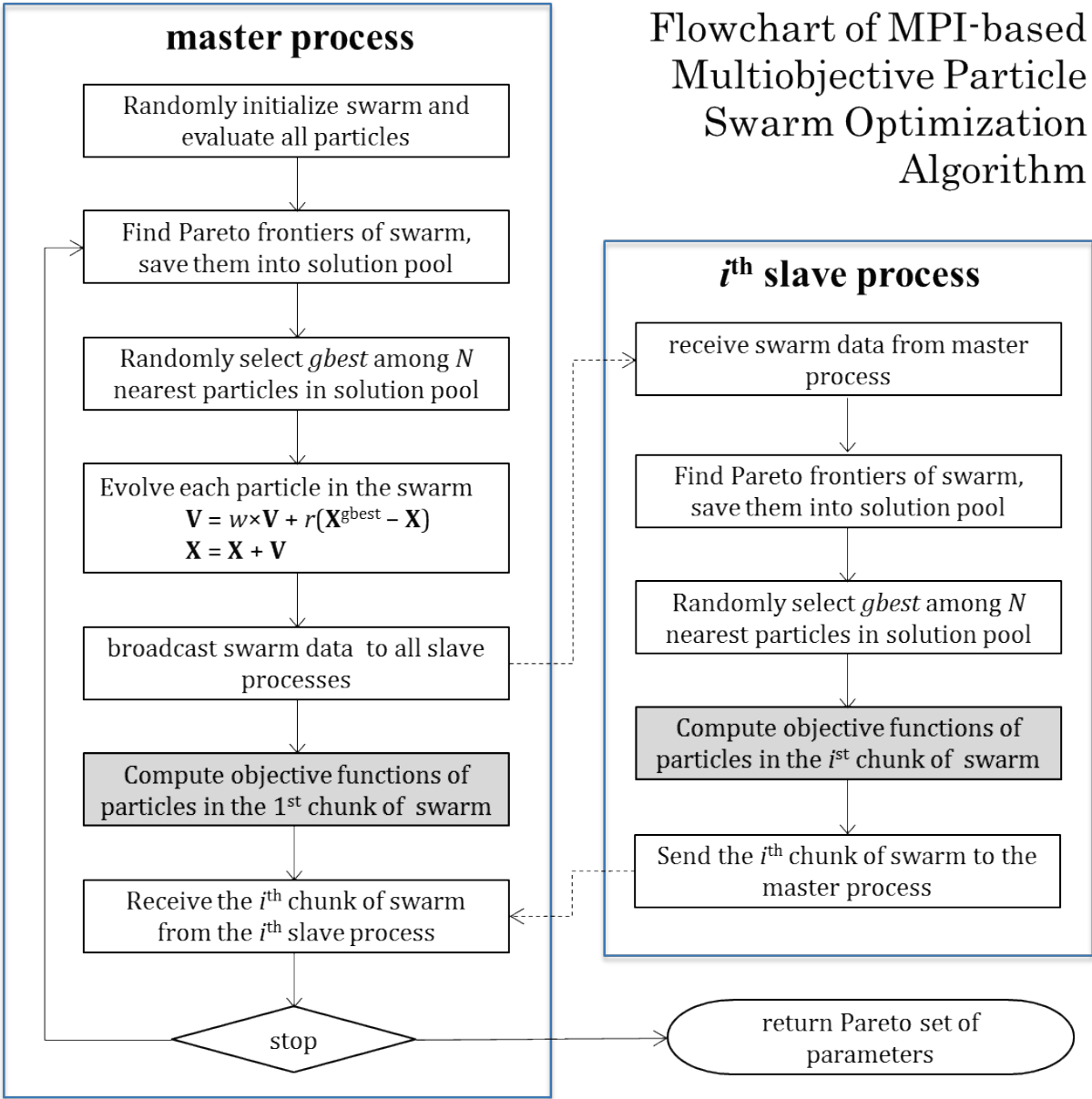


Figure 3.3 Flowchart of MPI-based multiobjective particle swarm optimization algorithm (MOPSO)

With the method of choosing *gbest*, PSO algorithm now can be applied to multiobjective optimization problems. To solve the optimization problem in section 3.5, a multiobjective PSO algorithm is developed based on the Message Passing Interface (MPI) technique, which is abbreviated as MPI-based MOPSO algorithm. When running a PSO algorithm, computational

time is mostly spent on evaluating all particles in the swarm. Each evaluation includes multiple runs of Noah LSM over the entire simulation domain for the whole simulation period. In the case of this study, the computational time of such evaluation is at the order of minutes or even hours for a large watershed and simulation of multiple years. To reduce computational time, the proposed MOPSO algorithm distributes the evaluation of all particles into multiple processes including a master process and many slave processes. Each process just evaluates particles in a chunk of the swarm, except that the master process also communicates data between all processes. The reduction of computational time depends on the number of processes. The more processes, the less computational time will be.

As shown in the flowchart of the MOPSO algorithm in Figure 3.3, there are seven steps in the master process and five steps in the slave processes.

- Steps in the master process
 1. Randomly initialize all particles in the swarm and evaluate them.
 2. Find Pareto frontiers of the swarm and save them into the solution pool, then find and kick out inferior particle in the solution pool. Some existing Pareto solutions may be inferior solutions compared with the newly found Pareto frontiers. Those inferior solutions need to be kicked out from the solution pool.
 3. For each particle in the swarm, randomly select *gbest* from N nearest particles in the solution pool.
 4. Evolve all particles in the swarm according to equation (3-25).
 5. Broadcast swarm data, including all the information of particles, to all slave processes.

6. Evaluate the particles in the 1st chunk of the swarm by computing all objective functions.
 7. Receive the i^{th} chunk from the i^{th} slave process, for $i = 2, 3, \dots, N_p$, where N_p is the total number of processes.
- Steps in the slave processes
 1. Receive swarm data from the master process. This step is following the step 5 of the master process.
 2. Find Pareto frontiers of the swarm and save them into the solution pool, then find and kick out inferior particles in the solution pool. This step is the same as the step 2 of the master process. Each slave process maintains a solution pool. Therefore, the master process doesn't need to broadcast the data of the solution pool, which can reduce the time of communication between processes.
 3. For each particle in the swarm, randomly select g_{best} from N nearest particles in the solution pool. This step is the same as the step 3 of the master process.
 4. Evaluate the particles in the i^{th} chunk of the swarm by computing all objective functions.
 5. Send the data of i^{th} chunk of the swarm to the master process.

The MPI-based MOPSO algorithm stops after a given number of iterations or all the particles of the swarm converging to a point in the solution space. The positions of the particles in the solution pool are then the Pareto solutions of the optimization problem.

There are three configuration parameters of the MPI-based MOPSO algorithm, including the size of swarm (N_{swarm}), the number of processes (N_{proc}) and the size of nearest neighborhood for choosing $gbest$ (N_{gbest}). N_{swarm} represents the number of particles in the swarm. Generally speaking, a larger N_{swarm} should be specified if the optimization problem is more complicated. N_{proc} should be equal to the number of computation units, for example, the number of CPU cores in parallel computing platforms. A larger N_{proc} will speed up the searching of optimal parameters. In order to effectively use computational resources, N_{swarm} should be divided exactly by N_{proc} . N_{gbest} is related to the capability of global search. When setting N_{gbest} , there is a tradeoff between the capability of global search and converge time. The algorithm has higher capability of global search when N_{gbest} is larger; however, it will take more computational time to converge.

3.6 EVALUATIONS

The proposed scheme is evaluated in two watersheds of the Ohio River Basin with five precipitation inputs. KINT1 watershed is a contributing area of the Harpeth River near Kingston Spring, Tennessee and SERI3 watershed is a contributing area of the East Fork White River at Seymour, Indiana. The drainage areas of these two watersheds are 2,341 square miles and 681 square miles respectively. In the evaluation experiments, Noah LSM runs at 1/32 degree resolution and hourly time step. To run Noah LSM, land surface data, such as soil types and land use types in simulation domain, should be specified in advance. Except LAI, all other free

parameters of the four-coefficient approximation are related to soil types. To illustrate the spatial variability of these parameters, the soil type maps of the KINT1 and the SERI3 watersheds are given in Figure 3.4 and Figure 3.5, while Figure 3.6 gives the areal percentage of each soil type in both watersheds. In KINT1 watershed, silt loam takes about a half area and rest types, including clay, clay loam, and silty clay loam, have relatively even shares of areal percentage. In SERI3 watershed, silty clay loam and clay loam are the first dominant and the second dominant soil types, which cover 60% and 26% areas of the watershed respectively. KINT1 watershed represents a case of watersheds in which multiple soil types account for the heterogeneity of parameters while SERI3 watershed represents a case of watersheds in which one or two dominant soil types account for the heterogeneity of parameters.

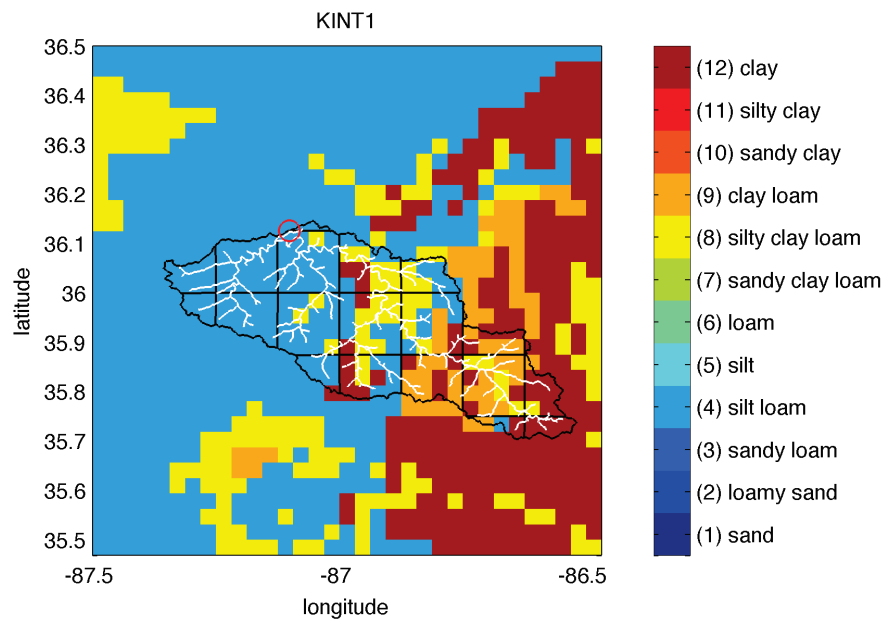


Figure 3.4 Map of KINT1 watershed. Soil type map is at 1/32 degree resolution; grid in black color is at 1/8 degree resolution; river networks in white color are derived from DEM data at 1/2048 degree resolution; the red circle represents the outlet of SERI3 watershed.

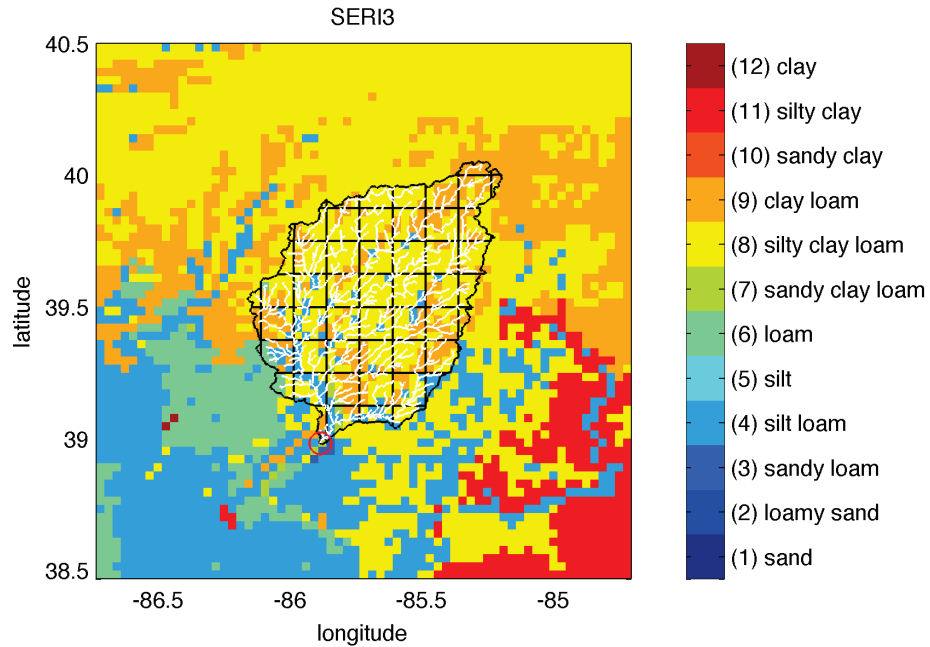


Figure 3.5 Map of SERI3 watershed. Soil type map is at 1/32 degree resolution; grid in black color is at 1/8 degree resolution; river networks in white color are derived from DEM data at 1/2048 degree resolution; the red circle represents the outlet of SERI3 watershed.

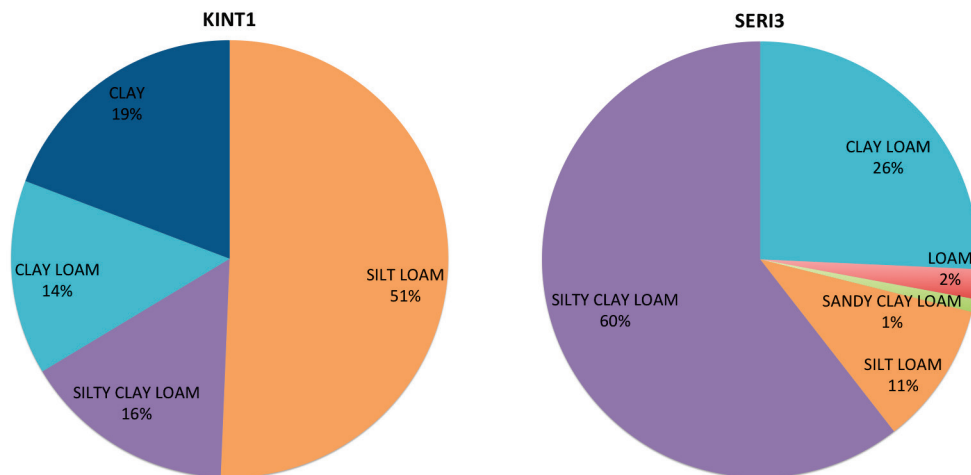


Figure 3.6 Pie charts of soil types in KINT1 (left panel) and SERI3 (right panel) watersheds.

The five precipitation inputs include NLDAS-2 (North American Land Data Assimilation System, version 2) precipitation data, RADAR (Next Generation Weather Radar (NEXRAD) Multisensor Precipitation Estimation (MPE) precipitation data and three precipitation data

derived by fusing NLDAS-2 and RADAR precipitation data. All precipitation data are at hourly time step while NLDAS-2 and RADAR precipitation data are at spatial resolutions of 1/8 degree and 1/32 degree, respectively. A multiscale data fusion algorithm, namely Multiscale Kalman Smoother (MKS)-based framework (Wang et al. 2011), is used to derive new precipitation data by fusing NLDAS-2 and RADAR precipitation data. Given a prior estimate of the areal mean of precipitation, the MKS-based framework can effectively merge the spatial patterns of precipitation measurements at multiple spatial resolutions. Three precipitation datasets has been derived at 1/32 degree resolutions, namely FUSED-1, FUSED-2 and FUSED-3, which take $[\text{mean}(\text{NLDAS-2}) + \text{mean}(\text{RADAR})]/2.0$, $\max[\text{mean}(\text{NLDAS-2}), \text{mean}(\text{RADAR})]$ and $\text{mean}(\text{NLDAS})$ as the prior estimates of the areal mean of precipitation. In addition to precipitation, rest atmospheric inputs including air temperature, air pressure, wind speed, specific humidity, and incoming shortwave and long wave radiation are NLDAS-2 data, which have been resampled into 1/32 degree resolution from 1/8 degree resolution. In the evaluation experiments, the surface runoff and the baseflow generated by Noah LSM are routed into streamflow time series at the outlets of watersheds with the flow routing scheme given in Chapter 2.0. The flow routing scheme separately deals with in-grid routing and between-grid (channel) routing, which uses unit hydrograph method and the linearized Saint Venant equation respectively. Evaluation experiments in the two watersheds include a three-year calibration period (01/01/2003 to 12/31/2005) and a two-year validation period (01/01/2006 to 12/31/2007), in which the four coefficients are calibrated and validated against daily streamflow.

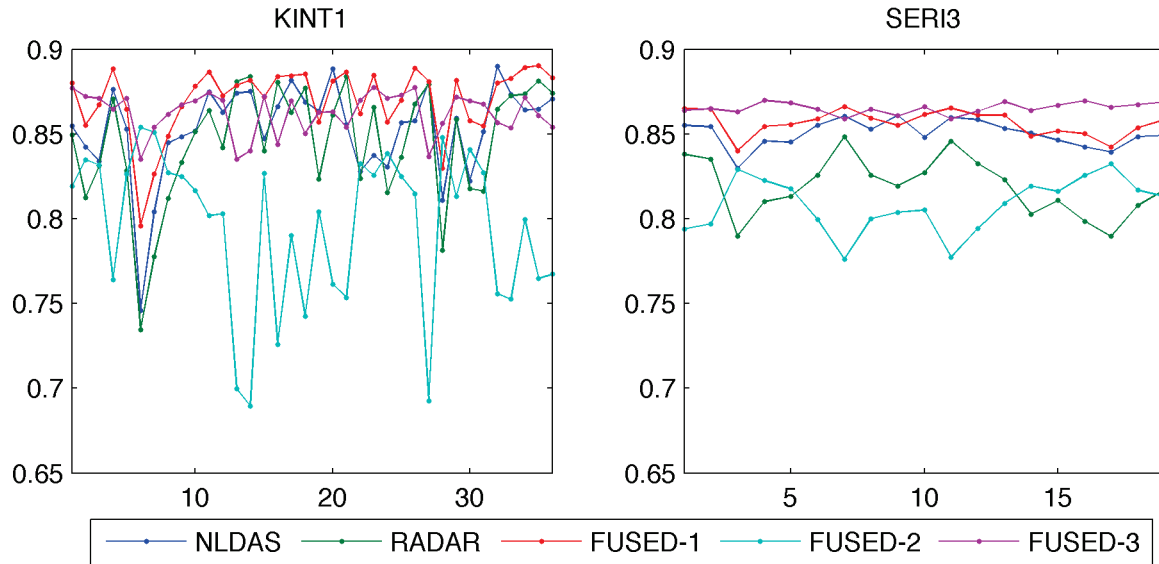


Figure 3.7 Nash-Sutcliffe Efficiencies (NSEs) of Pareto set of parameters of KINT1 (left panel) and SERI3 (right panel) watersheds corresponding to five precipitation inputs, namely NLDAS, RADAR, FUSED-1, FUSED-2, and FUSED-3.

Table 3.3 Yearly Nash-Sutcliffe Efficiencies (NSEs) in the calibration period (2003-2005) and the validation period (2006-2007) in KINT1 watershed corresponding the five precipitation inputs.

	Year	NLDAS	RADAR	FUSED-1	FUSED-2	FUSED-3
Calibration period	2003	0.911	0.933	0.926	0.798	0.856
	2004	0.824	0.827	0.854	0.693	0.856
	2005	0.807	0.847	0.867	0.846	0.882
Validation period	2006	0.772	0.751	0.781	0.856	0.803
	2007	0.234	0.545	0.606	-1.100	0.302

Table 3.4 Yearly Nash-Sutcliffe Efficiencies (NSEs) in the calibration period (2003-2005) and the validation period (2006-2007) in SERI3 watershed corresponding the five precipitation inputs.

	Year	NLDAS	RADAR	FUSED-1	FUSED-2	FUSED-3
Calibration period	2003	0.477	0.396	0.502	0.520	0.597
	2004	0.913	0.888	0.899	0.810	0.898
	2005	0.895	0.864	0.911	0.894	0.916
Validation period	2006	0.823	0.822	0.841	0.817	0.847
	2007	0.704	0.732	0.736	0.337	0.711

With the setting of $N_{swarm} = 128$, $N_{procs} = 32$ and $N_{gbest} = 5$, optimization has been conducted in the two experimental watersheds. Two sets of Pareto solutions, one has the size of 36 and the other has the size of 19, have been identified for KINT1 and SERI3 watersheds over the whole calibration period. The corresponding NSEs of these solutions are plotted in **Figure 3.7**. It can be seen that all NSEs are larger than 0.65 and most of them are around 0.85. This indicates that the four-coefficient approximation is able to describe the absolute and the relative magnitudes of parameters. In addition, the MPI-based MOPSO algorithm can search the globally optimal solutions to the optimization problem. For each watershed, differences between NSEs of the Pareto solutions come from the differences of precipitation inputs. Therefore, the reliability of precipitation dataset can be assessed with the parameter calibration scheme.

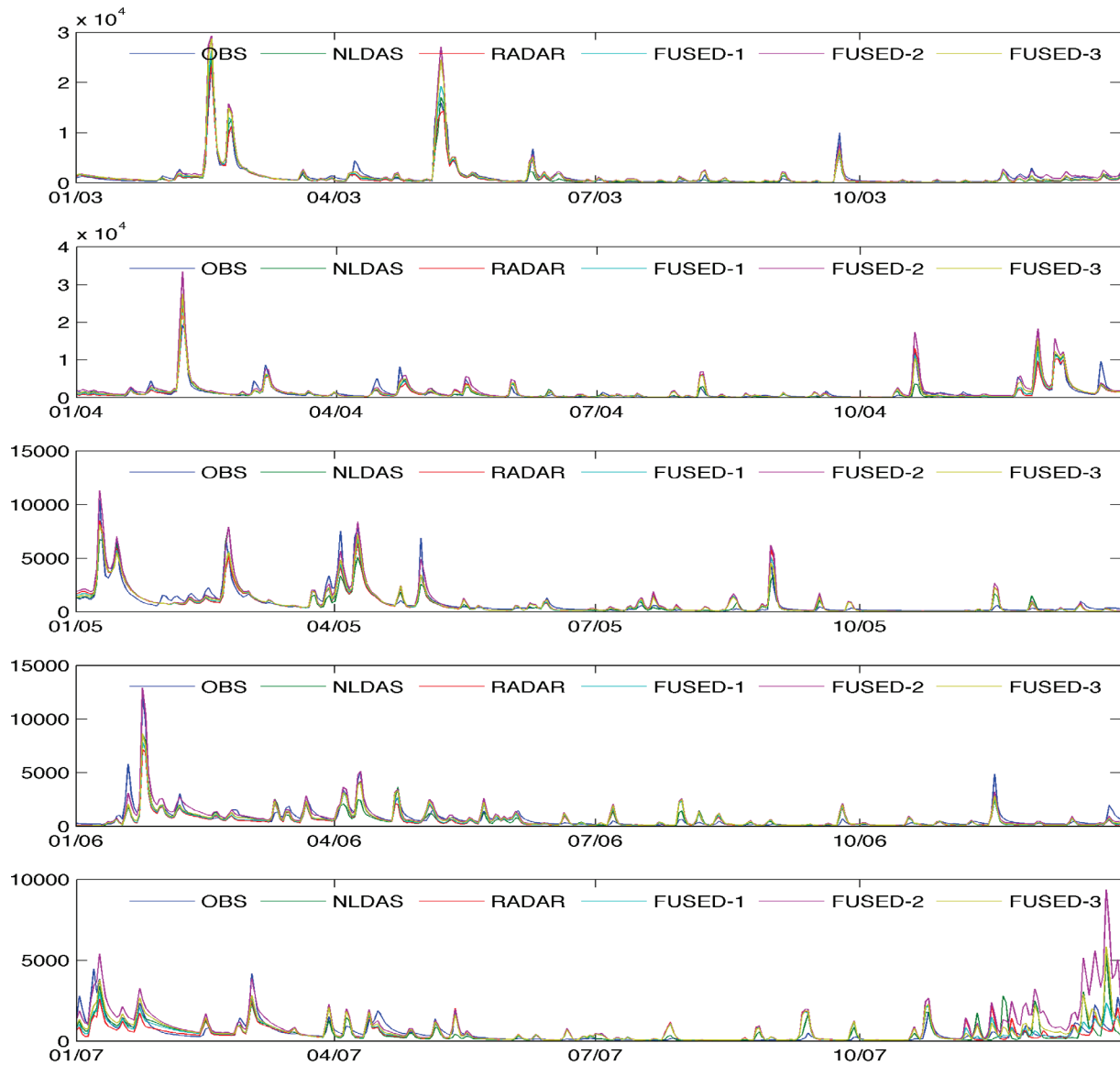


Figure 3.8 Observed and simulated streamflows in KINT1 watershed. Calibration period includes 2002, 2003, and 2004; validation period includes 2006 and 2007. In each plot, horizontal axis represents time and vertical axis represents streamflow rate (cft/s).

In order to further evaluate the proposed parameter calibration scheme against streamflow, two single sets of coefficients with the maximum sum of the five NSEs among all Pareto solutions have been chosen for KINT1 and SERI3 watersheds, as listed in **Table 3.2** Optimal parameters used in streamflow simulation. Yearly Nash-Sutcliffe Efficiencies (NSEs) in the calibration

period and the validation period have been calculated and listed in Table 3.3 for KINT1 watershed and Table 3.4 for SERI3 watershed. Corresponding yearly streamflows are plotted in Figure 3.8 and Figure 3.9. For KINT1 watershed, the streamflow series simulated by the five precipitation datasets well reproduce the magnitude and the timing of the observed streamflow series except FUSED-2 in 2002 and 2003. In the validation period, all of the five precipitation datasets fairly simulate the streamflow in year 2006 since all NSEs are larger than 0.75. For SERI3 watershed, all of the five precipitation datasets also well reproduce the observed streamflow series in 2004 and 2005. For the validation period, all of the five precipitation datasets also well simulate streamflows since all NSEs are larger than 0.8. These results once again indicate that the four-coefficient approximation is a reasonable simplification and approximation of the parameters of Noah LSM, which are related to runoff generation. In addition, the performance the MPI-based MOPSO algorithm is also demonstrated in terms of searching global optimal. From the NSEs listed in Table 3.3 and Table 3.4 and the streamflow series plotted in Figure 3.8 and Figure 3.9, it also can be noticed that the five precipitation datasets have poor performance in streamflow simulation in year 2007 for both watersheds. Simulated streamflows fairly reproduce the timing of the observed streamflow but the magnitudes are pretty off. Similar situation also happen to SERI3 watershed in 2003. Such problems are because of the poor qualities of the NLDAS-2 data and the RADAR data in these years, which are very possible due to the changes of algorithms used in RADAR precipitation data derivation. To summarize, the proposed parameter calibration scheme for Noah LSM have good performances in both the calibration period (e.g. in 2004 and 2005) and validation period (e.g. in 2006) for the two experimental watersheds.

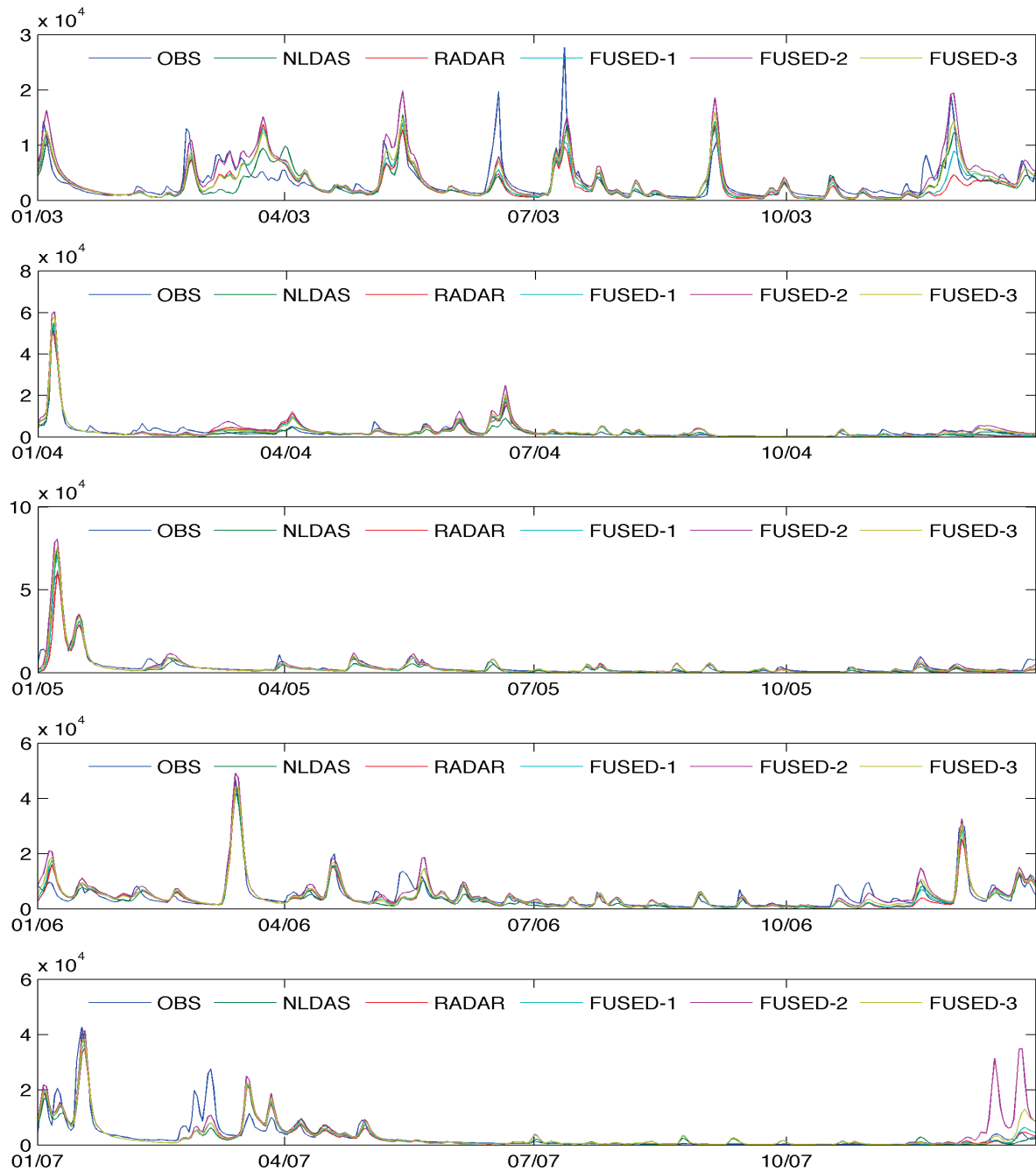


Figure 3.9 Observed and simulated streamflows in SERI3 watershed. Calibration period includes 2002, 2003, and 2004; validation period includes 2006 and 2007. In each plot, horizontal axis represents time and vertical axis represents streamflow rate (cft/s).

3.7 SUMMARY

In this study, a complete parameter calibration scheme is developed for Noah LSM, which includes a four-coefficient approximation of parameters and a parallel optimization algorithm. Through introducing the default soil parameter table as constraints, the consistencies among parameters of the same soil type and among the same parameters of different soil types are hold by the four-coefficient approximation. By associating with soil types, the four-coefficient approximation can also describe the spatial heterogeneity of parameters. In addition, the four-coefficient approximation is an effective simplification of the parameter calibration problem in Noah LSM. The dimension of the corresponding optimization problem has been dramatically reduced. Furthermore, the proposed scheme is designed for calibrate Noah LSM with more than one precipitation data inputs. It can be not only used in precipitation data evaluation but also good for ensemble simulations of hydrological process with multiple forcing data.

Particularly aiming at the high computational intensity of land surface simulation and the problem of assessing multiple precipitation datasets with Noah LSM, an multiobjective particle swarm optimization is developed based on the Message Passing Interface technique, called MPI-based MOPSO algorithm. In the process of parameter calibration, it can easily distribute the computation of land surface simulations into multiple nodes of high-performance computational platform with parallel architecture. Compared with the serial optimization algorithm, the computational time can be significantly reduced by the MPI-based MOPSO algorithm, which makes it possible to calibrate Noah LSM over large simulation domain.

The proposed parameter calibration scheme has been evaluated in KINT1 and SERI3 watersheds. The results indicate that the four-coefficient approximation can effectively describe the absolute magnitudes of parameters of the same soil type and the relative magnitudes of the same parameters among different soil types. With the proposed parameter calibration scheme, influences of parameters on simulated streamflow can be minimized and then, multiple precipitation datasets can be assessed in terms of the streamflow simulation by Noah LSM. In addition, the results also prove that the MPI-based MOPSO algorithm is capable of optimal searching.

At last, the proposed parameter calibration scheme is not limited to Noah LSM. It can be applied to other LSMs and even distributed hydrological models with one or multiple forcing datasets. In the future, more studies are needed to reduce the uncertainty of calibrated parameters by introducing more physical and empirical constraints of parameters.

4.0 ASSESSMENT OF MULTISCALE DATA FUSION ALGORITHM IN PRECIPITATION DATA FUSION

4.1 INTRODUCTION

Precipitation plays an important role in land surface models (LSMs). It affects hydrological processes and the water and energy fluxes. Improvements in the quality of precipitation data can significantly improve the simulations of land surface models on soil moistures, evapotranspiration, runoff, and other water and energy fluxes as well.

There are three typical ways to measure precipitation, namely rain gauge, radar and satellite. Each of them has its strengths and weaknesses in terms of accuracy, resolution, and coverage. Rain gauges are most accurate at a point or local scale but poor in capturing spatial patterns over a large area. The ground-based Next Generation Radar (NEXRAD) network in the U.S. provides measurements of precipitation with good spatial coverage at a much higher spatial resolution. However, magnitudes of the radar precipitation are criticized for systematic bias and random errors (Smith et al. 1996; Seo et al. 1999; Krajewski et al. 2010). In recent decades, the satellite-borne infrared imager and microwave imager make it possible to measure precipitation at a global scale with coarser spatial resolutions than that of the NEXRAD network. Satellite derived precipitation data products, with a larger spatial coverage but lower spatial resolutions

than NEXRAD network, also suffer from biases and noises (Grimes et al. 1999; Anagnostou et al. 2001).

Data fusion is an effective approach to derive higher-quality precipitation data products by combining multiple sources of precipitation measurements. For example, the Multisensor Precipitation Estimator (MPE) of NEXRAD precipitation data are based on the NEXRAD Stage II and rain gauge precipitation data. The NLDAS precipitation data are combinations of daily reanalysis precipitation data with the NEXRAD Stage II precipitation data or the Eta model predicted precipitation data (Cosgrove et al. 2003). The PERSIANN system combines multiple precipitation measurements, such as the TRMM (Tropical Rainfall Measuring Mission) Microwave Imager (TMI) and GOES-IR (Geosynchronous Satellite Longwave Infrared Imagery) precipitation, using artificial neural networks (Sorooshian et al. 2000). Among the data fusion algorithms employed, the Kalman filter and its derived algorithms are widely used, such as the direct application of the Kalman filter (Seo 1998; Seo 1998) and the scale recursive regression. The latter is essentially a Multiscale Kalman Smoother (MKS) (Willsky 2002).

The MKS algorithm was originally proposed to process digital signals and images at multiple spatial resolutions (Chou et al. 1994). It has been extensively used in a variety of applications together with the Expectation-Maximization (EM) algorithm for optimal parameter estimation (Kannan et al. 2000), such as signal and image processing (Simone et al. 2000; Farina et al. 2001; Nounou 2006), precipitation data fusion (Gorenburg et al. 2001; Tustison et al. 2002; Bocchiola and Rosso 2006; Bocchiola 2007; de Vyver and Roulin 2009), data assimilation for soil moisture (Kumar 1999; Parada and Liang 2004; Parada and Liang 2008), atmospheric

variables (Zhou et al. 2008), and altimetry data fusion (Slatton et al. 2001; Slatton et al. 2002). The MKS algorithm can be flexibly used in a time or a space domain. For example, the scale denotes the temporal resolution when precipitation measurements associated with different temporal resolutions are fused (Bocchiola and Rosso 2006). Additionally, the scale denotes the spatial resolution when precipitation measurements associated with different spatial resolutions are fused (Gorenburg et al. 2001; Tustison et al. 2002; Gupta et al. 2006; Bocchiola 2007; de Vyver and Roulin 2009). Through the MKS algorithm, precipitation measured at different temporal and spatial resolutions with different accuracies can be combined to produce higher-quality precipitation data products. Till now, the effectiveness of the MKS algorithm has only been evaluated with individual precipitation images (Gorenburg et al. 2001; Tustison et al. 2002; Gupta et al. 2006; Bocchiola 2007; de Vyver and Roulin 2009), systematic evaluations on this type of data fusion approach with massive precipitation data have not been conducted yet.

In this study, we use an extended MKS-based approach to first fuse two precipitation data sources at a coarser and a finer spatial resolution and then statistically investigate the improvements achieved through precipitation fusion. Correlation and root mean square error (RMSE) are applied as metrics of improvements. Particularly, we investigate two types of errors, white noise and bias. Evaluations are conducted based on hypothetical experiments using real precipitation data.

In the remaining sections, we briefly describe the MKS-based framework in Section 4.2. Then, we present the data and experiment area in Section 4.3. Experiment designs and results are described and discussed in Section 4.4. Finally, we summarize the findings of this study in Section 4.5.

4.2 MULTISCALE KALMAN SMOOTHER-BASED (MKS-BASED) FRAMEWORK

The MKS-based framework combines an extended MKS algorithm and a parameter estimation scheme (Parada and Liang 2004). Figure 4.1 depicts a multiscale tree with three spatial scales representing multiscale hidden states (i.e., fused precipitation). The MKS algorithm includes an upward sweep and a downward sweep. The former is a fine-to-coarse Kalman filtering step from the leaf nodes to the root node and the latter is a coarse-to-fine Kalman smoothing step from the root node to the leaf nodes. Both sweeps are along the multiscale tree. The dynamic equations for fusing multiscale precipitation are expressed as:

$$X(t) = A(t)X(t\bar{\gamma}) + w(t) \quad (4-1)$$

$$P(t) = A^2(t)P(t\bar{\gamma}) + Q(t) \quad (4-2)$$

where t represents a node in the multiscale tree, $t\bar{\gamma}$ represents the coarse scale node containing node t , $X(t)$ and $X(t\bar{\gamma})$ represent the hidden states (e.g., fused precipitation in this case) at a child node t and its parent node $t\bar{\gamma}$, respectively, $w(t)$ is the added detail at the child node following $N(0, Q(t))$, $Q(t)$ is the error variance of $w(t)$, $P(t)$ and $P(t\bar{\gamma})$ are the error variances of $X(t)$ and $X(t\bar{\gamma})$, and $A(t)$ is a transition operator mapping precipitation from a parent node to a child node. Given the prior estimate of precipitation at the root node $\bar{X}(0)$ and its error variance $\Sigma(0)$, the prior estimates of precipitation and associated error variances at the rest nodes of the multiscale tree can be inferred based on Eqs. 4-1 and 4-2. We refer to this step as initialization step. After this step, the upward sweep can be carried out using the inversed forms of Eqs. 4-1 and 4-2 together with a measurement equation expressed as follows:

$$Y(t) = C(t)X(t) + D(t) + v(t). \quad (4-3)$$

where $Y(t)$ represents the measurement (e.g., precipitation) of node t , $C(t)$ is a transition operator mapping precipitation to the measurement, $v(t)$ is the measurement noise following $N(0, R(t))$, $R(t)$ is the error variance of $v(t)$, and $D(t)$ is a bias compensator which is calculated as:

$$D(t) = \bar{Y}_s - C(t)\bar{X}(0) \quad (4-4)$$

where S is the scale of node t , \bar{Y}_s is the mean of the measurements at scale S , and $\bar{X}(0)$ is the mean of the root node. $D(t)$ is introduced in the observation equation by (Parada and Liang 2004) to minimize impacts of the inconsistency (e.g., bias) between measurements at different scales on the fused precipitation. Adding this term enables the MKS-based framework to achieve the same estimated mean of the fused precipitation at all scales. For example, if the precipitation measurements at different scales have different means, then the average of these means (i.e., the mean of the means) can be chosen – a case employed in this study – as the estimate of $\bar{X}(0)$.

The upward sweep includes three operations: (1) fine-to-coarse prediction, (2) prediction merging, and (3) observation update. In operation (1), the fine-to-coarse predictions of $X(t)$ are derived based on the updated states of its child nodes. In operation (2), multiple fine-to-coarse predictions of $X(t)$ are fused into a merged prediction of $X(t)$. In operation (3), the merged prediction of $X(t)$ is updated by $Y(t)$. From the leaf to the root, these operations are conducted at all nodes of the multiscale tree. If no measurement at node t , the updated prediction of $X(t)$ just takes the value of the merged prediction. Via the upward sweep, the finer resolution data add their influences to the estimates of the hidden states at coarser resolutions.

The downward sweep follows the upward sweep starting at the root node and moving toward the leaves of the multiscale tree. It refines the estimates of the hidden states further through a scale-recursive Kalman smoothing step. As a result, coarser resolution data add their influences to the estimates of the hidden states at finer resolutions. By means of the upward and the downward sweeps, information in multiscale measurements will propagate to all the nodes of the multiscale tree collectively. For more details about our extended MKS-based framework, please refer to (Parada and Liang 2004).

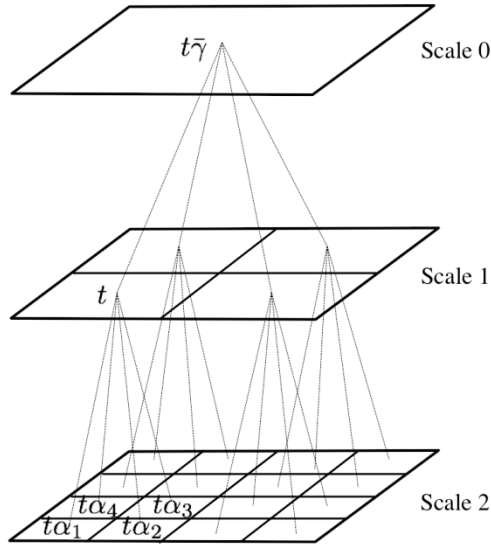


Figure 4.1 A schematic of a 2-D multiscale tree with three different spatial scales, 0, 1, and 2. For node t at scale 1, $t\bar{\gamma}$ represents its parent node and $t\alpha_n$ ($n = 1, 2, 3, 4$) represents its child nodes. Without a parent, the node at scale 0 (i.e., the coarsest resolution) is called a root node; without any children, the nodes at scale 2 (i.e., the finest resolution) are called leaf nodes.

The MKS-based framework has a set of parameters: $\bar{X}(0)$, $\Sigma(0)$, $A(t)$, $C(t)$, $Q(t)$ and $R(t)$, which need to be estimated. In this study, we set $A(t) = 1$ to keep mass conservation (i.e., to have the same total precipitation amount) at all scales. We also set $C(t) = 1$ because both the

measurements and the hidden states are precipitation. In the MKS-based framework, the areal mean precipitation over the study area, $\bar{X}(0)$, determines the total amount of the fused precipitation at all scales. Without preference given to any measurement source, we determine $\bar{X}(0)$ as:

$$\bar{X}(0) = \frac{1}{N} (\bar{Y}_{s_1} + \bar{Y}_{s_2} + \dots + \bar{Y}_{s_n}) \quad (4-5)$$

where S_1, S_2, \dots, S_n are scales with measurements available and N is the total number of scales with measurements. $\Sigma(0)$, $Q(t)$ and $R(t)$ are estimated using the EM algorithm, in which the log-likelihood function is formulated as:

$$\begin{aligned} \log L(Q(t), R(t)|Y) = & -\frac{1}{2} \sum_{t \in \mathcal{T}_c} \left\{ \log(Q(t)) + [X(t) - A(t)X(t\bar{y})]^2 Q(t)^{-1} \right\} \\ & -\frac{1}{2} \sum_{t \in \mathcal{T}_m} \left\{ \log(R(t)) + [Y(t) - C(t)X(t) - D(t)]^2 R(t)^{-1} \right\} + F, \end{aligned} \quad (4-6)$$

where \mathcal{T} is the set of all nodes at the multiscale tree, \mathcal{T}_m is a subset of \mathcal{T} with measurements, \mathcal{T}_c is a subset of \mathcal{T} except the root node, and F is a constant. To maximize the log-likelihood, two recursive steps, expectation step (E-step) and maximization step (M-step), are iterated. The E-step is to compute the expectations of precipitation estimates ($X(t), t \in \mathcal{T}$) conditioned on all available measurements. The two sweeps of the extended MKS algorithm together play the role of the E-step. The M-step is to maximize Eq. 6 given the estimated precipitation obtained at the E-step. In order to reduce the number of parameters, we further assume that $Q(t)$ and $R(t)$ are homogeneous at each scale. Finally, Eq. 6 is maximized using the Newton gradient method. More details about the EM algorithm can be found in (Kannan et al. 2000). In Eq. 6, the first half (i.e., the Q related terms) is a measure of the consistency among the fused precipitation data

along the multiscale tree and the second half (i.e., the R related terms) is a measure of the consistency between the fused precipitation and measurements. To enhance the contribution of measurements, we constrain $Q(t) > R(t)$ in the M-step.

4.3 STUDY AREA AND DATA

Our study area (Figure 4.2) is bounded by longitudes (-88, -84) and latitudes (37.75, 41.75), which contains 32×32 grids at 1/8 degree resolution and 128×128 grids at 1/32 degree resolution. It includes almost the entire state of Indiana and parts of Illinois, Kentucky, Ohio, and Michigan. Covering an area of $152,175 \text{ km}^2$, it is large enough for evaluating the MKS-based framework for precipitation data fusion. The average annual precipitation of this region is about 1000 mm. Precipitation is relatively evenly distributed throughout the year. Typically, precipitation is steady and of long duration during winter and early spring and short, but of high intensity during late spring and summer.

Hourly NEXRAD MPE precipitation data (DelGreco et al. 2005) from the Ohio River Forecast Center (OHRFC), National Weather Service (NWS) for the year 2003 are used in this study. The original data are at a spatial resolution of approximately 4 km in XMRG format, which is a binary file format used within the NWS to store gridded data. We re-sampled and projected the XMRG formatted precipitation data into the geographic coordinate system at two resolutions, 1/32 degree and 1/8 degree, respectively.

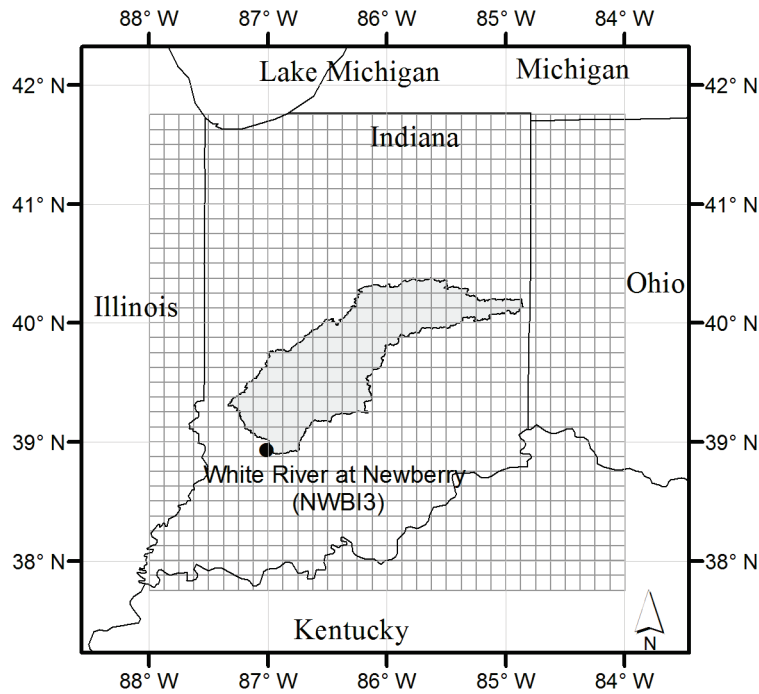


Figure 4.2 Location of our study area bounded by longitudes (-88, -84) and latitudes (37.75, 41.75) which contains 32×32 gray grids at 1/8 degree resolution.

4.4 EXPERIMENTS AND RESULTS

4.4.1 Experiment Design

Two hypothetic experiments are designed to investigate the effectiveness of the MKS-based framework in removing errors of the precipitation data from different sources. Two most common types of errors, Type-I errors and Type-II errors, are investigated. The Type-I errors are mainly resulted from random noise while the Type-II errors mainly contain errors due to systematic bias, such as instrument bias and algorithm bias. Experiment 1 investigates the effectiveness in filtering out the Type-I errors while Experiment 2 examines the effectiveness in

filtering out the Type-II errors. We use a synthetic experiment approach here due to its advantage of being able to control the magnitudes of errors to be included in the generated precipitation data. Thus, this approach is more effective in evaluating improvements of fused precipitation. In fact, the approach of using synthetic data has been widely used in data assimilation study for the convenience of performance evaluation (Walker and Houser 2004).

In both experiments, synthetic precipitation data are generated at 1/8 degree and 1/32 degree resolutions based on the hourly NEXRAD MPE precipitation data. In the study area, precipitation was recorded over a total of 3636 hours in 2003. Among all of these hourly-recorded precipitation data (called precipitation images), 2246 of them are revealed to be realistic in terms of spatial patterns and amounts through the OHRFC's manual inspection. Therefore, we use these 2246 hourly precipitation images as the truth at 1/32 degree resolution. In addition, we aggregate these data from 1/32 degree resolution to 1/8 degree resolution and also treat them as the truth at 1/8 degree resolution. Since the resolutions of 1/8 degree and 1/32 degree correspond to the scales 5 and 7 of the multiscale tree built for the study area, we also call the precipitation data at these two resolutions as the data at scales 5 and 7, respectively. The mean and the standard deviation of the true precipitation images at scale 7 are shown in Figure 4.3A and Figure 4.3B. Due to aggregation, the mean and the standard deviation of the true precipitation images at scale 5 are smaller than corresponding ones at scale 7. This is because the total amount of each hourly precipitation image is the same but the precipitation-covered area is larger at scale 5 than that at scale 7. The relative differences between scales 5 and 7 are shown in Figure 4.3C and Figure 4.3D, respectively. All of these statistics are calculated over precipitation-covered

areas, which are defined as a set of grids whose precipitation amounts are larger than zero. In the remaining parts of this paper, we use Ω to denote the precipitation-covered area.

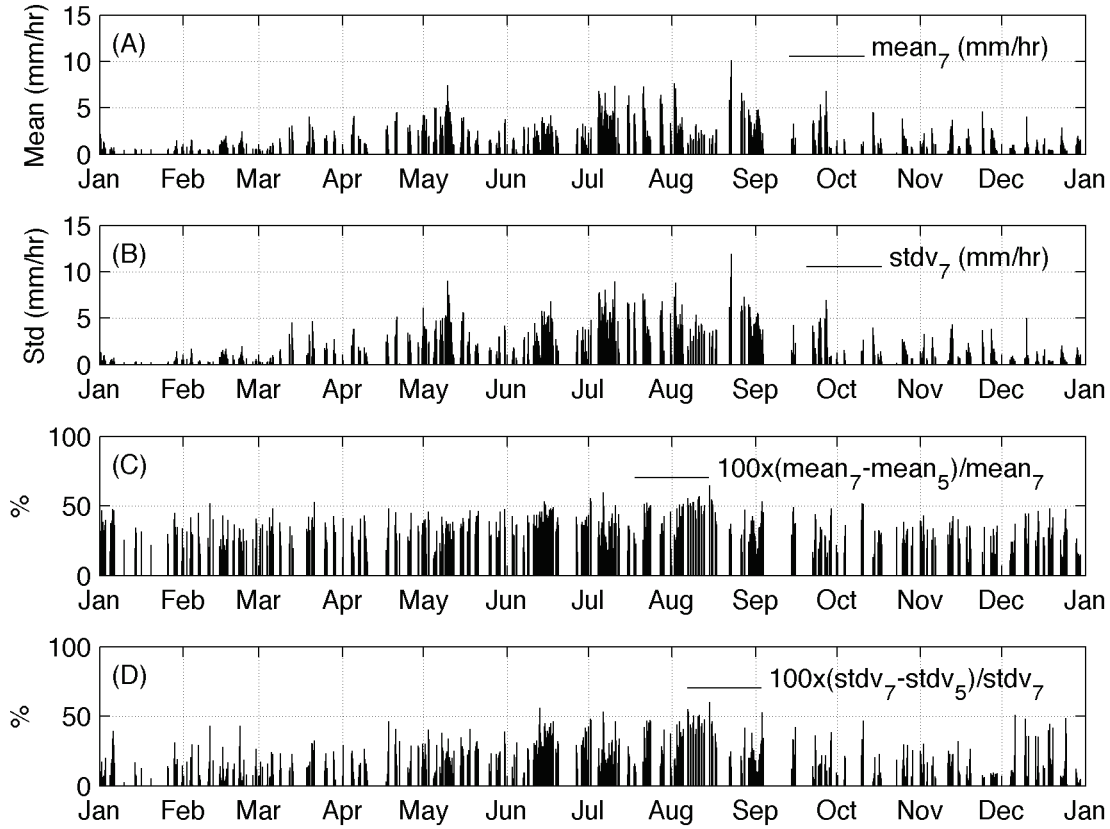


Figure 4.3 (A) Time series of the means of the true precipitation data at 1/32 degree resolution (i.e., scale 7); (B) time series of the standard deviations of the true precipitation data at 1/32 degree resolution; (C) time series of the relative differences between the means of the true precipitation data at 1/32 degree resolution and those at 1/8 degree resolution; and (D) time series of the relative differences between the standard deviations of the true precipitation data at 1/32 degree resolution and those at 1/8 degree resolution. All of these statistics are calculated over the precipitation-covered areas based on the 2246 hourly precipitation data in 2003.

In Experiment 1, the Type-I errors are generated based on Gaussian distributions with zero mean and different standard deviations prescribed according to the real data. That is, at each hour k , the prescribed standard deviation is proportional to the standard deviation of the true

precipitation image at hour k . For example, assuming the standard deviation of the true precipitation image at hour k is s_k , the Type-I error at hour k is then generated for each grid within Ω based on a Gaussian distribution of $N(0, x_i s_k)$ where x_i ($i = 1, 2, \dots, 21$) denoting a prescribed noise level. At the same hour, the generated errors for each grid are generally different from each other, but they follow the same distribution. As shown in Table 4.1, a total of 21 noise levels ranging from 0.1 to 5.0 are used to generate Type-I errors to mimic the white noise in real precipitation data. In addition, we categorize these 21 noise levels into three groups to represent scenarios of fair, moderate and large amounts of noise. Synthetic precipitation data are finally generated by adding the Type-I errors to true precipitation values. Since we have generated 21 levels of synthetic precipitation data at both scales 5 and 7, a total of 21×21 combinations are used in Experiment 1. For all combinations, data fusion is carried out on each of the 2246 hourly precipitation images.

In Experiment 2, the Type-II errors are generated based on Gaussian distributions with nonzero means and standard deviations prescribed according to the true data. At each hour, the mean and the standard deviation are again proportional to those of the true hourly precipitation images. For example, assuming the mean and the standard deviation of the precipitation image at hour k is m_k and s_k , the Type-II error at hour k is then generated for each grid within Ω based on a Gaussian distribution of $N(y_j m_k, x_i s_k)$, where y_j ($j = 1, 2, \dots, 15$) denoting a prescribed bias level and x_i ($i = 1, 2, \dots, 21$) denoting a noise level. As shown in Table 4.2, the range of the bias levels is wide enough to mimic the bias in real precipitation data. Since the focus of Experiment 2 is to evaluate the MKS-based framework on removing biased errors in the precipitation data, we set the noise level to $x_9 = 2.0$ when generating the Type-II errors at all of

the bias levels in scales 5 and 7. Synthetic precipitation data are then generated by adding the Type-II errors to the corresponding true precipitation values. Like Experiment 1, there are 15×15 combinations of the synthetic precipitation data series used in Experiment 2. Data fusion is once again carried out over each of the 2246 hourly precipitation images for all combinations. Because the synthetic precipitation data are erroneous, we use Y_5^{error} and Y_7^{error} to denote these synthetic precipitation images at scale 5 and scale 7, respectively.

Since precipitation data cannot have negative values, a strict non-negative value rule has to be applied when generating the synthetic precipitation data for both experiments. Once the value of the synthetic precipitation in a grid is negative, we regenerate the error until it is non-negative. Figure 4.4 shows the average percentage of grids whose synthetic precipitation values are regenerated for Experiments 1 and 2, respectively, over the 2246 precipitation hours in 2003. Due to the regeneration process, the means of the errors in the precipitation-covered area (Ω) are increased. The larger average percentage value in Figure 4.4 indicates that a higher bias is added to the synthetic precipitation data and that the distributions of the added errors are less normally distributed. For Experiments 1 and 2, we find the average percentage varies from almost zero to about 40% over the ranges of the noise levels or the bias levels. This implies that non-normality exists in the errors of the synthetic precipitation data in both experiments. However, the majority of the Type-I errors and the Type-II errors are still normally distributed. The range of the prescribed bias levels in Experiment 2 is asymmetric to reflect the reality that the absolute magnitude of the negative bias is generally not too large.

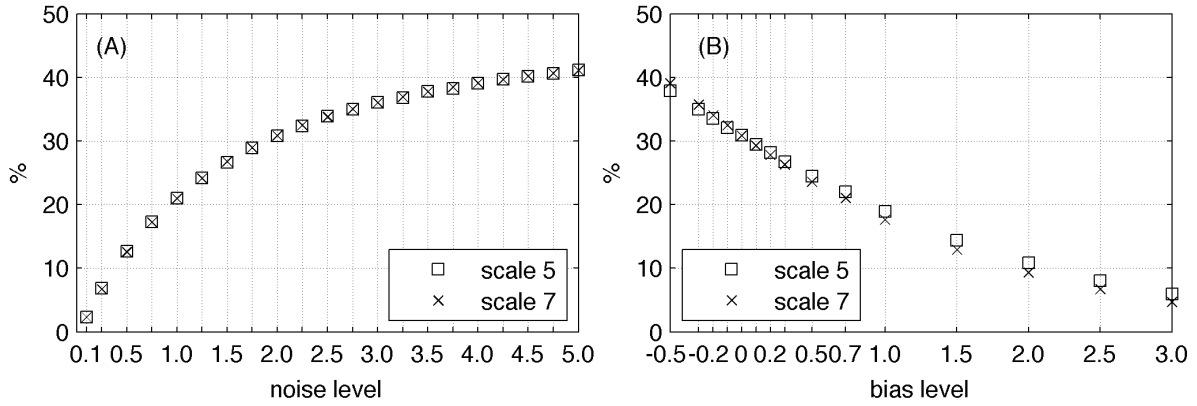


Figure 4.4 Average percentage of grid cells whose synthetic precipitation values are regenerated for Experiment 1 (panel A) and Experiment 2 (panel B) over the 2246 precipitation hours in 2003.

Table 4.1 A list of twenty-one noise levels used in generating Type-I errors

Category	Noise level ($x_i, i = 1, 2, \dots, 21$)
Fair	0.10, 0.25, 0.50, 0.75, 1.0, 1.25, 1.50
Moderate	1.75, 2.0, 2.25, 2.50, 2.75, 3.0
Large	3.25, 3.50, 3.75, 4.0, 4.25, 4.50, 4.75, 5.0

Table 4.2 A list of fifteen bias levels used in generating Type-II errors

Bias level ($y_i, i = 1, 2, \dots, 15$)
-0.50, -0.30, -0.20, -0.10, 0.00,
0.10, 0.20, 0.30, 0.50, 0.7,
1.0, 1.5, 2.0, 2.5, 3.0

In addition, benchmark experiments have been designed as companions to Experiments 1 and 2, respectively. In the benchmark experiments, a conventional data fusion method including two steps is applied to the data of Experiments 1 and 2, respectively. In Step 1, we either

aggregate the synthetic precipitation data at hour k of scale 7 (denoted as $Y_{7,k}^{error}$) to scale 5 (denoted as $Y_{7 \rightarrow 5,k}^{error}$) or disaggregate the synthetic precipitation data from scale 5 (denoted as $Y_{5,k}^{error}$) to scale 7 (denoted as $Y_{5 \rightarrow 7,k}^{error}$). In the aggregation process, we use the average precipitation values of the 4×4 $1/32$ degree resolution (scale 7) grids inside a $1/8$ degree resolution (scale 5) grid as the precipitation value of the grid at scale 5. In the disaggregation process, all of the 4×4 $1/32$ degree grids inside a $1/8$ degree resolution grid take the same precipitation value of the grid at scale 5. In step 2, we fuse the precipitation of scales 5 and 7 at each hour k as $X_{5,k}^{fused,B} = 0.5 \times (Y_{5,k}^{error} + Y_{7 \rightarrow 5,k}^{error})$ and $X_{7,k}^{fused,B} = 0.5 \times (Y_{7,k}^{error} + Y_{5 \rightarrow 7,k}^{error})$. We use $X_{5,k}^{fused,B}$ and $X_{7,k}^{fused,B}$ as the benchmarks for scales 5 and 7 and compare them with the corresponding fused precipitation data $X_{j,k}^{fused,E}$ ($j = 5, 7$) based on the MKS-based framework.

Two metrics are used in evaluation, namely correlation ($Corr$) and root mean square error ($RMSE$). Correlation is a measure of the consistency of the two images' spatial patterns. At hour k and scale j , the correlation between the true ($X_{j,k}^{true}$) and synthetic precipitation images ($Y_{j,k}^{error}$) is represented as:

$$Corr_{j,k}(X_{j,k}^{true}, Y_{j,k}^{error}) = \frac{\frac{1}{N_{\Omega}} \sum_{\omega \in \Omega} (X_{j,k}^{true}(\omega) - E(X_{j,k}^{true})) \cdot (Y_{j,k}^{error}(\omega) - E(Y_{j,k}^{error}))}{\text{var}(X_{j,k}^{true})^{1/2} \cdot \text{var}(Y_{j,k}^{error})^{1/2}}, \quad (4-7)$$

where $var(\cdot)$ represents variance of the precipitation values within the precipitation-covered area Ω , N_{Ω} is the number of measurements (i.e., grids), and $j = 5$ or 7 representing the scale. RMSE is a measure of the overall difference (magnitudes) between the two precipitation images. Similarly, RMSE is formulated as:

$$RMSE_{j,k} (X_{j,k}^{true}, Y_{j,k}^{error}) = \sqrt{\frac{1}{N_{\Omega}} \sum_{\omega \in \Omega} (X_{j,k}^{true}(\omega) - Y_{j,k}^{error}(\omega))^2} \quad (4-8)$$

Correlation and RMSE between the true and fused precipitation images are calculated by applying Eqs. 4-7 and 4-8 where $Y_{j,k}^{error}$ is replaced by either $X_{j,k}^{fused,E}$ or $X_{j,k}^{fused,B}$.

To investigate the effectiveness of the MKS-based framework in a statistic sense, we evaluate the overall performance of the data fusion over all of the 2246 precipitation hours in 2003 rather than over some selected individual hours. Thus, we use the means of correlations and RMSEs in our analyses and they are expressed as follows:

$$\overline{Corr_j (X_{j,k}^{true}, Z_{j,k})} = \frac{1}{N_T} \sum_{k=1}^{N_T} Corr_{j,k} (X_{j,k}^{true}, Z_{j,k}), \quad j = 5 \text{ or } 7, \quad (4-9)$$

$$\overline{RMSE_j (X_{j,k}^{true}, Z_{j,k})} = \frac{1}{N_T} \sum_{k=1}^{N_T} RMSE_{j,k} (X_{j,k}^{true}, Z_{j,k}), \quad j = 5 \text{ or } 7, \quad (4-10)$$

where N_T is the total number of precipitation hours (i.e., 2246), j denotes the spatial scale, and

$Z_{j,k}$ represents either $X_{j,k}^{fused,E}$, $X_{j,k}^{fused,B}$, or $Y_{j,k}^{error}$.

In the following analyses, we compare $\overline{Corr_j (X_{j,k}^{true}, Z_{j,k})}$ and $\overline{RMSE_j (X_{j,k}^{true}, Z_{j,k})}$ computed before and after the data fusion using both the MKS-based framework and the conventional method. For notational convenience, we use superscripts “-” and “+” to represent “before” and “after” data fusion. Therefore, $\overline{Corr_j^-}$ denotes the mean of the correlations between the true precipitation data and the synthetic precipitation data at scale j . $\overline{Corr_j^+}$ denotes the mean of the correlations between the true precipitation data and the fused precipitation data at

scale j . Similar meanings are applied for \overline{RMSE}_j^- and \overline{RMSE}_j^+ . Moreover, to facilitate the evaluation analyses, we define $\Delta\overline{Corr}_j = \overline{Corr}_j^+ - \overline{Corr}_j^-$ and $\Delta\overline{RMSE}_j = \overline{RMSE}_j^- - \overline{RMSE}_j^+$ for $j = 5$ or 7 . Positive values of $\Delta\overline{Corr}_j$ and $\Delta\overline{RMSE}_j$ indicate valuable effects of data fusion.

4.4.2 Results and Discussion

4.4.2.1 Experiment 1

By showing the color-filled contour plots of \overline{Corr}_j^- , \overline{Corr}_j^+ and $\Delta\overline{Corr}_j$ ($j = 5$ or 7), Figure 4.5 provides an overall picture about the effectiveness of the MKS-based framework in terms of restoring the spatial patterns of precipitation. Since no data fusion has been conducted yet, information associated with Y_j^{error} has no influence on \overline{Corr}_j^- . Therefore, contours of \overline{Corr}_j^- only change along the noise levels of scale 5. Similarly, contours of \overline{Corr}_j^+ only change along the noise levels of scale 7. It can be seen that \overline{Corr}_j^- ($j = 5$ and 7) decrease rapidly with an increase of the noise levels at scale j . In particular, the correlations are reduced from almost 1.0 to about 0.26 when the corresponding noise levels increase from $x_1 = 0.1$ to $x_{13} = 3.0$ (i.e., noise levels between fair and moderate). In the plots of \overline{Corr}_j^- and \overline{Corr}_j^+ , it can be found that $\overline{Corr}_j^- > 0.53$ for $j = 5$ and 7 as long as the Type-I errors are confined within the “fair category”. This indicates that Y_j^{error} ($j=5$ and 7) generated with errors in the “fair category” (see Table 4.1) still contain most of the patterns of the true precipitation data. On the other hand, Y_j^{error} ($j=5$ and 7) generated with errors confined in the “large category” lose most of the spatial

patterns of the true precipitation data, since $\overline{Corr_j^-} \leq 0.26$ for $j = 5$ and 7 . The loss of the spatial patterns for Y_j^{error} ($j=5$ and 7) generated with errors in the “moderate category” falls between that of the fair and large categories.

For each fused result at scale j , if $\overline{Corr_j^+} > \overline{Corr_j^-}$, it implies that the MKS-based framework can improve precipitation spatial pattern through removing some of the Type-I errors at scale j . Significant improvements can be seen at scale 5 in Figure 4.5. That is, the Type-I errors in Y_5^{error} are substantially removed by fusing Y_5^{error} with Y_7^{error} . $\overline{Corr_5^+}$ is greater than 0.6 for all of the combinations, even for those that Y_7^{error} are associated with the Type-I errors in the large category. For scale 5, the data fusion only degrades the spatial patterns of the precipitation when Y_5^{error} are associated with very small noise levels (e.g, the noise level of $x_i \leq 0.25$) while Y_7^{error} are associated with much higher noise levels. Compared to the plot of $\overline{Corr_5^+}$, improvements shown in the plot of $\overline{Corr_7^+}$ are much smaller, but still considerable. Two paired t-tests (one for scale 5 and the other for scale 7) between $\overline{Corr_j^-}$ and $\overline{Corr_j^+}$ over all of the 21×21 combinations reveal that the differences between $\overline{Corr_j^-}$ and $\overline{Corr_j^+}$ are statistically significant at the 95% confidence level. In other words, the synthetic precipitation data at a coarser resolution (i.e., scale 5) are also helpful in removing the Type-I errors and in improving the spatial patterns of the synthetic precipitation at a finer resolution (i.e., scale 7) through the MKS-based framework, even though the effect is not as much as it is for the opposite situation.

Moreover, plots of $\overline{\Delta Corr_5}$ and $\overline{\Delta Corr_7}$ provide direct measures of the improvements of the precipitation patterns at scales 5 and 7, respectively. Distinct differences in the pattern and magnitude are shown between the plots of $\overline{\Delta Corr_5}$ and $\overline{\Delta Corr_7}$. The contours of $\overline{\Delta Corr_5}$ are jointly controlled by the noise levels at scales 5 and 7. Denoting the synthetic data at scale 5 that are associated with the Type-I errors in the fair category as $Y_5^{error,f}$, we can see that when $Y_5^{error,f}$ are combined with the synthetic data at scale 7 (i.e., Y_7^{error}), $\overline{\Delta Corr_5}$ is more sensitive to the noise level at scale 5 rather than to the noise level at scale 7, since the color-filled contours are horizontal-like strips in the region. A negative zone of $\overline{\Delta Corr_5}$ can be seen in the region in the plot of $\overline{\Delta Corr_5}$, when the noise level at scale 7 is much greater than that at scale 5. However, the slight decrease of the correlation over the small region would not cause any concern since the absolute magnitudes of those negative $\overline{\Delta Corr_5}$ are very small. Over the negative region of $\overline{\Delta Corr_5}$, magnitudes of the corresponding $\overline{Corr_5^+}$ are mostly greater than 0.85, indicating that the fused precipitation data still represent most of the spatial features of the true precipitation images at scale 5. When the noise level of the Type-I errors associated with Y_5^{error} is getting larger, e.g., from the fair group to the moderate or large group, the effectiveness of the precipitation data fusion becomes increasingly significant. Meanwhile, the effectiveness depends on the quality of Y_5^{error} and Y_7^{error} . As expected, the improvement is more significant if the noise level at scale 7 is smaller.

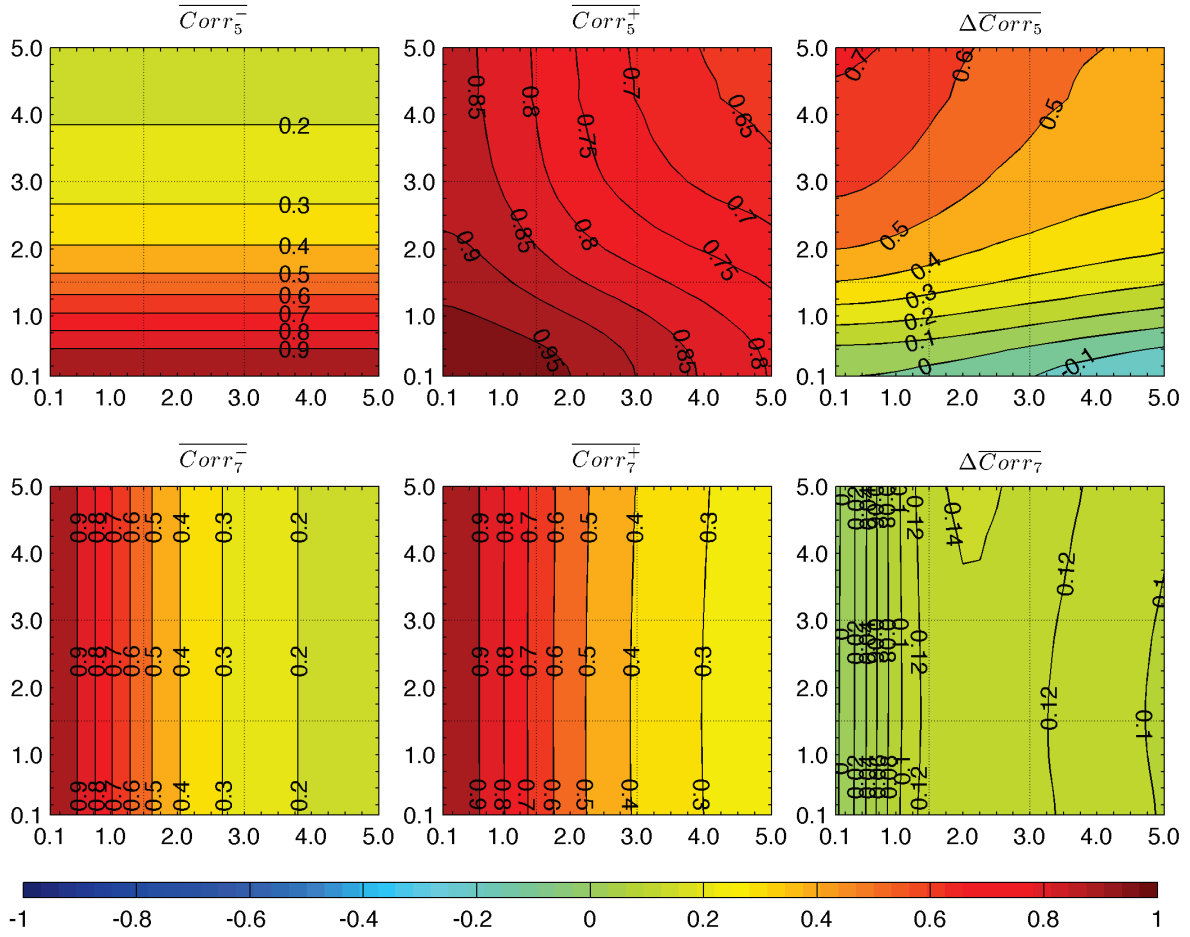


Figure 4.5 Color-filled contour plots of \overline{Corr}_j^- , \overline{Corr}_j^+ and $\Delta\overline{Corr}_j$ for scale 5 (i.e., $j = 5$, upper panel) and scale 7 (i.e., $j = 7$, lower panel), respectively, for Experiment 1. In each plot, the horizontal axis and the vertical axis represent, respectively, the noise levels at scales 7 and 5. In addition, the two horizontal and the two vertical gray lines indicate the boundaries, respectively, between the fair and moderate, and between the moderate and large categories of the noise levels specified in Figure 4.1.

Improvements indicated by $\Delta\overline{Corr}_7$ are much less than those by $\Delta\overline{Corr}_5$. The contours of $\Delta\overline{Corr}_7$ are mostly controlled by the noise levels at scale 7. Also, the magnitudes are much smaller than those of $\Delta\overline{Corr}_5$. This indicates that Y_5^{error} have relatively less influence than Y_7^{error} on the fused precipitation data at scale 7, no matter what the noise level is at scale 5. In other

words, we cannot significantly improve the spatial pattern of Y_7^{error} (at finer resolution) by fusing Y_5^{error} (at coarser resolution) with Y_7^{error} using the MKS-based framework. Both the magnitude and the pattern of $\overline{\Delta Corr_7}$ demonstrate that Y_7^{error} play a more significant role than Y_5^{error} in improving the spatial patterns at scale 7 in data fusion. This is because when Y_5^{error} are fused into the data at scale 7, much less new information on the spatial patterns can be added since the coarser resolution includes less spatial variability information. Nevertheless, Y_5^{error} do provide some new information, which is detected by the EM algorithm, to improve the spatial patterns of Y_7^{error} .

One reason for such a significant difference between $\overline{\Delta Corr_5}$ and $\overline{\Delta Corr_7}$ is that the EM algorithm in the MKS-based framework places more weight on the data for which there are a larger number of measurement points (see Eq. 6). In this study, the number of measurement points at scale 7 is 16 times of that at scale 5. Generally, if the noise levels at different resolutions are comparable to each other, more information is provided by the finer resolution data than that by the coarser resolution data. Thus, it makes sense that the finer data have more influence on the fused data than the coarser data. Such a general rule of the multiscale data fusion may not work if the finer resolution data are too noisy. This is why we see a region with negative values in $\overline{\Delta Corr_5}$ since the noise levels at the finer resolution are much higher than those at the coarser resolution. If, however, the two (or more) data sources used for fusion have the same spatial resolution or comparable noise levels, the EM algorithm in our MKS-based framework would be able to adjust its parameters to effectively place more weights on the data source with less errors and thus to improve the spatial patterns and magnitudes as shown here

and in *Parada and Liang* [2008] as well. Results here demonstrate an important value of the high-resolution data when combined with coarse resolution data to improve the spatial patterns of the coarse resolution data, even if the high-resolution data have larger (but not significantly larger) Type-I errors than those at the coarser resolution.

For the case of $\overline{\Delta Corr_7}$, improvements are even seen for the region over which the large noisy data at scale 5 are fused into the smaller or equally noisy data at scale 7. The largest occurs to the combinations of Y_5^{error} in the large category and Y_7^{error} in the moderate category where $\overline{\Delta Corr_7}$ ranges from 0.12 to 0.14. This indicates that the noisy data at scale 5 have the largest effects on improving the spatial patterns of Y_7^{error} in the moderate category. For the combinations with Y_7^{error} in the fair region (i.e., left of the first vertical line), small values in $\overline{\Delta Corr_7}$ are due to the high values of $\overline{Corr_7^-}$ prior to conducting the data fusion. For the combinations with Y_7^{error} in the large noise category (i.e., right of the second vertical line), smaller values in $\overline{\Delta Corr_7}$ indicate less influence of the noisy data at scale 5. But overall, there are still improvements to this large noisy data region at scale 7. The relative improvements in this region are actually not small compared to the original spatial patterns of the noisy data at scale 7 shown in the plot of $\overline{Corr_7^-}$. The almost equal values of $\overline{\Delta Corr_7}$ (i.e., the vertical-like color-filled contours) reveal an interesting feature. That is, there appears to be an almost equal contribution of the noisy data at scale 5 to the improvements of the spatial patterns at scale 7 due to the combined effects of the upward and downward sweeps and the EM algorithm involved in the MKS-based framework. When the correlation measure is employed, impacts on the fused data at scale 7 by the different

noise levels at scale 5 are minimized while such impacts are not if the RMSE measure is used. Results here confirm that one can fuse coarse resolution data with fine resolution data (as long as the coarse spatial resolution is not too coarse compared to the fine resolution) to improve the spatial patterns of the fine resolution data even if the data at the coarser resolution include a large amount of noise. The impacts of the coarser resolution data on the fused data at a finer resolution are much less than those the other way around. This is expected from the upward and downward sweeps and the EM algorithm as to-be-elaborated later.

In terms of restoring the spatial pattern of precipitation data, the results of Experiment 1 and its benchmark experiment are compared in Figure 4.6. We use $\overline{\Delta Corr_j}^{B1}$ to represent improvements in the spatial patterns obtained with the conventional data fusion while $\overline{\Delta Corr_j}^{E1}$ (i.e., the same as $\overline{\Delta Corr_j}$ shown in Figure 4.5 for Experiment 1) to represent improvements obtained with the MKS-based framework. Figure 4.6 shows the difference between $\overline{\Delta Corr_j}^{E1}$ and $\overline{\Delta Corr_j}^{B1}$ at scales 5 and 7 (i.e., $j=5$ and $j=7$). It can be seen that $\overline{\Delta Corr_5}^{E1}$ is significantly greater than $\overline{\Delta Corr_5}^{B1}$ except for a few combinations when the noise level at scale 5 is in the fair group while the noise level at scale 7 is much greater than the fair group. In addition, $\overline{\Delta Corr_7}^{E1}$ is larger than $\overline{\Delta Corr_7}^{B1}$ for more than half of the combinations, including all of the combinations when the noise levels at scale 5 are greater than those at scale 7. In general, given the noise levels at scale 5, the superiority of the MKS-based framework over the conventional approach decreases when the noise levels at scale 7 increase. On the contrary, given the noise levels at scale 7, the superiority of the MKS-based framework increases when the noise

levels at scale 5 increase. This is because the EM algorithm used in the MKS-based framework places more weights on the finer resolution data than the coarser resolution data while the conventional data fusion approach places equal weights to the data at both resolutions.

In Experiment 1, we also evaluate the effectiveness of the MKS-based framework in improving the magnitudes of the synthetic precipitation data using RMSE. Figure 4.7 shows the color-filled contour plots of \overline{RMSE}_j^- , \overline{RMSE}_j^+ and $\overline{\Delta RMSE}_j$ ($j = 5$ or 7). Since no data fusion is conducted yet, the contours of \overline{RMSE}_j^- only change along the noise levels at scale j . \overline{RMSE}_j^- increases rapidly when the noise levels at scale j increase for $j = 5$ and $j = 7$. Particularly, \overline{RMSE}_5^- ranges from almost 0 to about 8 and \overline{RMSE}_7^- ranges from almost 0 to more than 9 when the noise levels increase from $x_1 = 0.1$ to $x_{21} = 5.0$. For the same noise level, \overline{RMSE}_7^- is greater than \overline{RMSE}_5^- , indicating more variability in Y_7^{error} than Y_5^{error} .

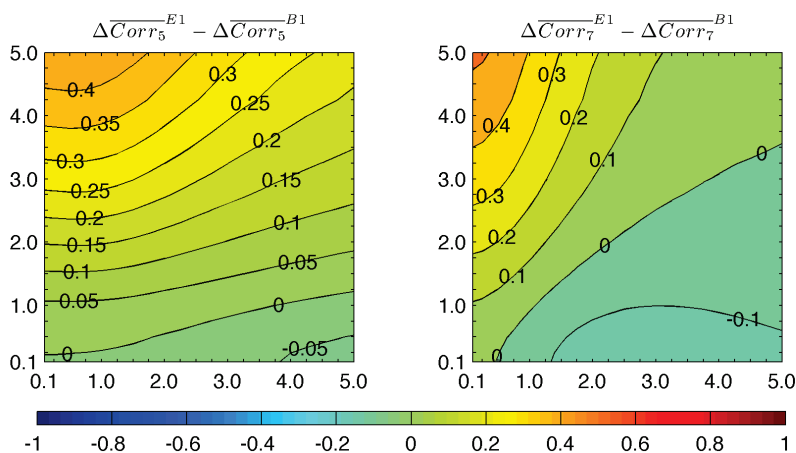


Figure 4.6 Color-filled contour plots of $\overline{\Delta Corr}_5^{E1} - \overline{\Delta Corr}_5^{B1}$ and $\overline{\Delta Corr}_7^{E1} - \overline{\Delta Corr}_7^{B1}$, where the superscript $E1$ denotes Experiment 1 and the superscript $B1$ denotes the benchmark experiment. Both experiments use the same erroneous precipitation data with the Type-I errors. The meanings of the horizontal and vertical axes are the same as in Figure 4.5.

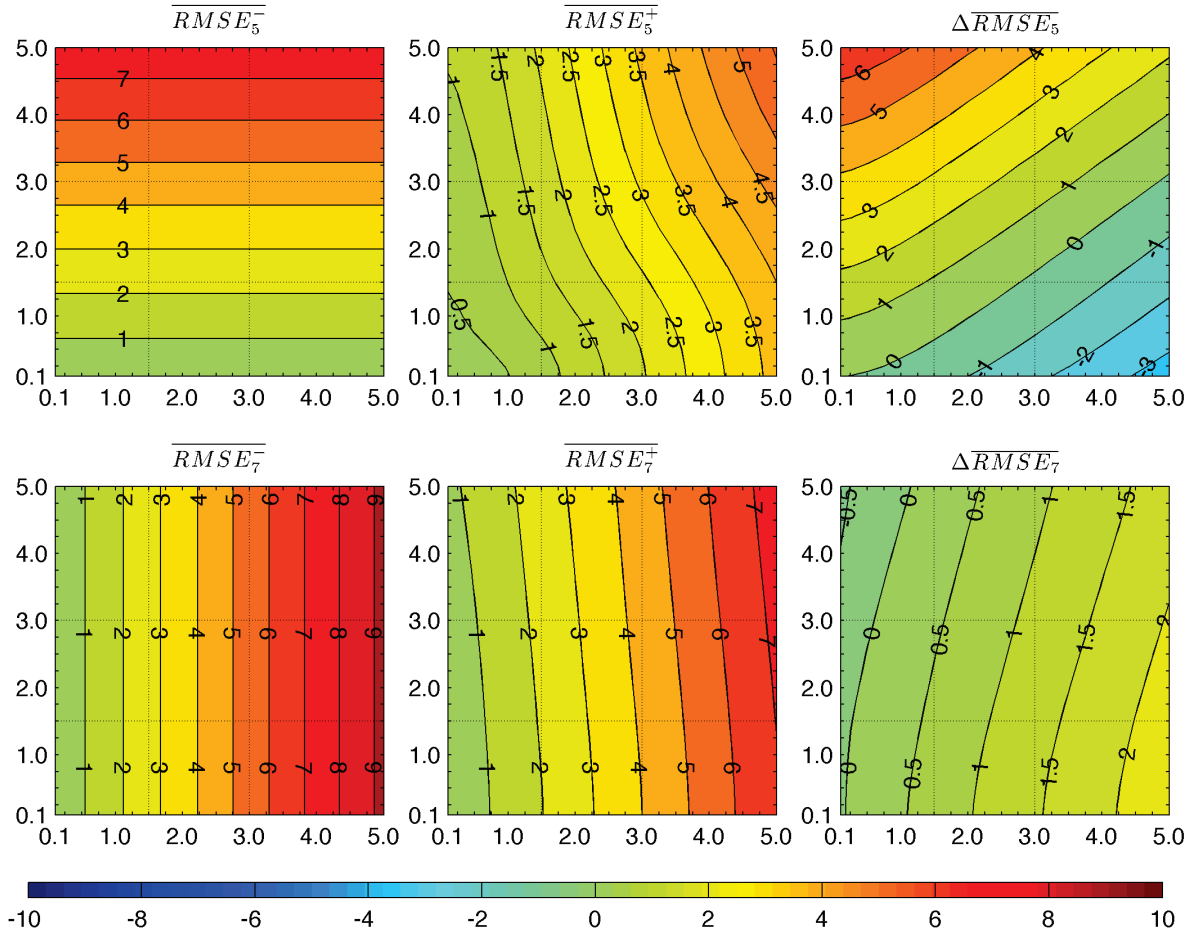


Figure 4.7 Color-filled contour plots of \overline{RMSE}_j^- , \overline{RMSE}_j^+ and $\Delta\overline{RMSE}_j$ for scale 5 (i.e., $j = 5$, upper panel) and for scale 7 (i.e., $j = 7$, lower panel), respectively, for Experiment 1. The meanings of the horizontal and vertical axes and the meanings of the two horizontal and vertical gray lines are the same as in Figure 4.5.

In Figure 4.7, \overline{RMSE}_j^+ ($j = 5$ and 7) reflects the joint influence of the information associated with Y_5^{error} and Y_7^{error} on the magnitudes and spatial patterns of the fused precipitation data. The contours of \overline{RMSE}_5^+ have a different pattern from the contours of \overline{RMSE}_7^+ . The former is affected by the noise levels at both scales while the latter is mostly controlled by the noise levels at scale 7. This indicates that the influence of the finer resolution data on the coarser

resolution data is much stronger than the other way around. Comparing with the plot of $\overline{Corr_5^+}$ in Figure 4.5, it can be seen that the contours of $\overline{RMSE_5^+}$ and $\overline{Corr_5^+}$ have similar patterns. In general, the spatial pattern and the absolute magnitude of the precipitation data at the coarser resolution (i.e., scale 5) can be improved simultaneously through the MKS-based framework. On the contrary, the pattern of the contours of $\overline{RMSE_7^+}$ is mostly affected by the noise levels at scale 7, similar to that of $\overline{Corr_7^+}$ in Figure 4.5. In addition, the average of $\overline{RMSE_5^+}$ is smaller than that of $\overline{RMSE_7^+}$. This is mainly because the variability associated with Y_5^{error} is smaller than that associated with Y_7^{error} (see plots of $\overline{RMSE_5^-}$ and $\overline{RMSE_7^-}$ in Figure 4.7).

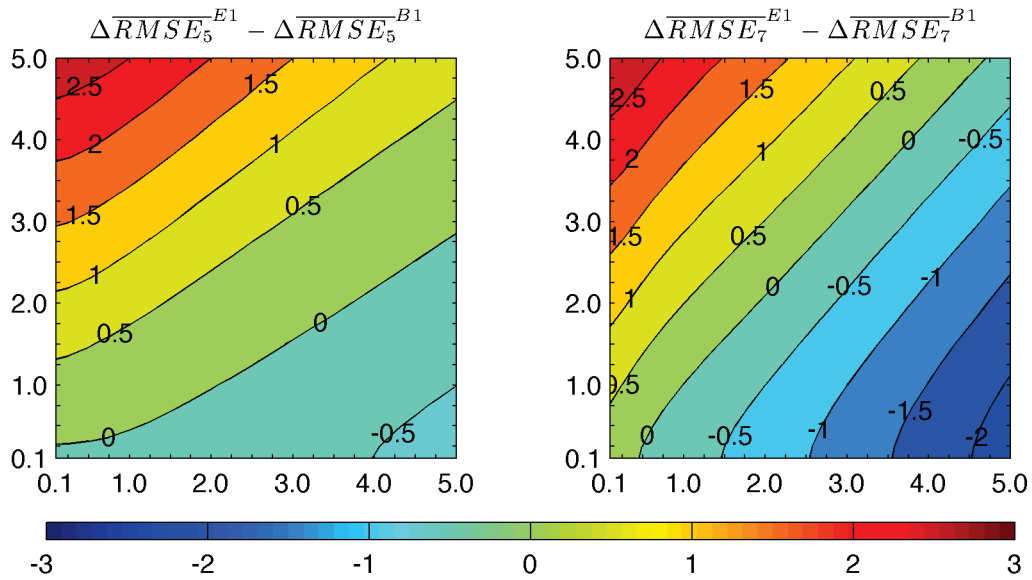


Figure 4.8 Color-filled contour plots of $\Delta \overline{RMSE}_5^{E1} - \Delta \overline{RMSE}_5^{B1}$ and $\Delta \overline{RMSE}_7^{E1} - \Delta \overline{RMSE}_7^{B1}$, where the superscript *E1* denotes Experiment 1 and superscript *B1* denotes the benchmark experiment. Both experiments use the same erroneous precipitation data with the Type-I errors. The meanings of the horizontal and vertical axes are the same as in Figure 4.5.

Moreover, Figure 4.7 depicts the color-filled contours of $\overline{\Delta RMSE}_5$ and $\overline{\Delta RMSE}_7$. Both plots can be divided by a zero-value contour. From the plot of $\overline{\Delta RMSE}_5$, we see that the magnitudes of Y_5^{error} are significantly improved if the noise levels at scale 7 are not substantially higher than that at scale 5. From the plot of $\overline{\Delta RMSE}_7$, it can be seen that the magnitudes of Y_7^{error} are also improved for most of the combinations, except when Y_7^{error} in the fair group are combined with Y_5^{error} in the large group. The overall improvements (i.e., positive $\overline{\Delta RMSE}_5$) at scale 5 are greater than those at scale 7 (i.e., positive $\overline{\Delta RMSE}_7$). However, the absolute magnitudes of the negative $\overline{\Delta RMSE}_5$ are also greater than those of the negative $\overline{\Delta RMSE}_7$. This indicates that precipitation data at the finer resolution (i.e., scale 7) have stronger influences on the magnitudes of the fused precipitation data at the coarser resolution (i.e., scale 5). Once again, this is partially due to the EM algorithm, which places more weights on the finer resolution data. If the finer precipitation data are not substantially noisier than the coarser precipitation data, the magnitudes of precipitation data at the coarser resolution will be significantly improved after the data fusion with the MKS-based framework. Otherwise, the magnitudes of the precipitation data at the coarser resolution may be degraded if the finer data are too noisy. The contours of $\overline{\Delta RMSE}_7$ are mainly controlled by the noise levels at scale 7. That is, Y_5^{error} contribute limited information to the improvement of the magnitudes of Y_7^{error} .

A comparison between the MKS-based framework and the conventional data fusion method using $\overline{\Delta RMSE}_j$ ($j = 5$ and 7) is also conducted. We use $\overline{\Delta RMSE}_j^{B1}$ and $\overline{\Delta RMSE}_j^{E1}$ to respectively represent the overall improvements (magnitudes and spatial patterns) obtained with

the conventional data fusion method and the MKS-based framework. Figure 4.8 shows the color-filled contour plots of $\overline{\Delta RMSE}_5^{E1} - \overline{\Delta RMSE}_5^{B1}$ and $\overline{RMSE}_7^{E1} - \overline{\Delta RMSE}_7^{B1}$. From Figure 4.8, we see that at scale 5, the MKS-based framework is significantly better than the conventional data fusion method for most of the combinations. This includes many of those whose noise levels at scale 7 are greater than the noise levels at scale 5. The magnitudes of $\overline{\Delta RMSE}_5^{E1} - \overline{\Delta RMSE}_5^{B1}$ are quite minor for the combinations when the MKS-based framework is not as good as the conventional data fusion method. This occurs when the noise levels at scale 7 are much greater than those at scale 5. In addition, we see that the MKS-based framework is superior to the conventional data fusion method at scale 7 for the combinations when the noise levels at scale 5 are greater than those at scale 7. Results of Figure 4.6 and Figure 4.8 consistently demonstrate that the MKS-based framework is superior to the conventional data fusion method in removing the Type-I errors for most parts.

4.4.2.2 Discussion

In Section 4.4.2.1, we have presented and discussed the effectiveness of the MKS-based framework in removing the Type-I errors and also compared the results with those of the conventional data fusion method. In this section, we further discuss why the MKS-based framework is sometimes more effective but less effective at other times.

In the MKS-based framework, data at a finer resolution affect the fusion through the upward sweep, which is a combination of three steps, fine-to-coarse prediction, the prediction merging, and the observation update. The fine-to-coarse prediction is from child nodes to their parent node. In our multiscale tree structure (Figure 4.1), each parent has four children.

Therefore, there are four predicted states (one from each child) for each parent node. The four predicted states (i.e., precipitation) are then merged based on a weighted summation with their corresponding error variances, which is more effective in reducing the noise than a simple averaging method. Thus, the prediction-merging step can decrease the amount of noise propagated to the parent node from the child nodes. For Experiment 1, the finer data are at scale 7 and the coarser data are at scale 5. Thus, the prediction merging step is conducted twice: one at scale 6 and the other at scale 5. After this step, the noise at scale 5 becomes much less than that at scale 7. Therefore, the “true” information included in the finer resolution data at scale 7 can contribute significantly to the fused data at scale 5. This is one reason that the finer data help more in improving the data quality at the coarser resolution (i.e., at scale 5). On the other hand, the coarser data affect the fused data at a finer resolution via the downward sweep. If at the parent nodes, the differences between the predicted and smoothed states (i.e., precipitation) are small, the updates to the child nodes through the downward sweep would be small. Since data at a coarser resolution are generally more homogeneous than those at a finer resolution, the differences between the predicted and smoothed states are small. Thus, the coarser resolution data have less influence on the fused data at a finer resolution. In Experiment 1, the coarser data affect the fused precipitation at the finer resolution (scale 7) by two Kalman smoothing steps via the downward sweep, from scale 5 to scale 6, and then from scale 6 to scale 7. In doing so, the influence becomes even weaker. This is partially why the coarser data only provide limited help to the fused precipitation at the finer resolution.

The other reason is related to the EM algorithm. The EM algorithm is used to estimate the parameters $Q(t)$ ($t \in \mathcal{T}_c$), and $R(t)$ ($t \in \mathcal{T}_m$), through maximizing the log-likelihood function of Eq. 6. Since the number of measurements at a child scale is four times of the number of measurements at its parent scale, the number of the measurement points at scale 7 would be 16 times more than that at scale 5. However, the contribution of each measurement point is equally weighted in Eq. 6. This is a reasonable assumption when the error level by each measurement point is comparable at different spatial scales. To maximize the log-likelihood, optimal parameters and fused data as well should better fit the measurements at finer resolutions than those at coarser resolutions. Accordingly, finer measurements would have more influence on the fused precipitation at the coarser resolutions than the other way around. In Experiment 1, the finer resolution has 16 times measurement points of that at the coarser resolution. Therefore, it is unavoidable that the MKS-based framework puts much more weights on the synthetic precipitation data at scale 7. Thus, the data quality at scale 7 becomes more influential than that at scale 5. Consequently, the importance of the finer resolution data sometimes is over emphasized as indicated in our results. This is a limitation of the EM algorithm when the noise levels at finer resolutions are much larger than those at coarser scales.

Due to these reasons, measurements at finer resolutions are thus more influential than those at coarser resolutions when the MKS-based framework is used to remove the Type-I errors. This is why we see the different color-filled contour patterns between scales 5 and 7 for the fused precipitation and why we see small negative regions shown in Figure 4.5 and Figure 4.7. In addition, these features of the MKS-based framework also explain the negative regions shown in Figure 4.6 and Figure 4.8. This is because in the conventional data fusion method, “weights” of

the measurements at scale 7 are the same as those at scale 5, not like that in the EM algorithm. Thus, the MKS-based framework is not superior to the conventional data fusion method for the combinations where the noise levels at scale 7 are much greater than those at scale 5.

4.4.2.3 Experiment 2

Experiment 2 is designed to evaluate the effectiveness of the MKS-based framework in removing the Type-II errors associated with the precipitation data. As described in Section 4.4.1 about generating the Type-II errors, the noise portion in the Type-II errors is set to a constant level of $x_9 = 2.0$. To investigate the influence of the bias portion of the Type-II errors on the effectiveness of the MKS-based framework, we compare the metrics of Experiment 2 with those of Experiment 1 whose noise levels correspond to $x_9 = 2.0$ at both scale 5 and scale 7. The same notations, i.e., $\overline{Corr_j^-}$, $\overline{Corr_j^+}$, $\Delta\overline{Corr_j}$, $\overline{RMSE_j^-}$, $\overline{RMSE_j^+}$, and $\Delta\overline{RMSE_j}$ ($j = 5$ and 7) are also used for analyzing the results of Experiment 2.

Figure 4.9 presents the color-filled contour plots of $\overline{Corr_j^-}$, $\overline{Corr_j^+}$ and $\Delta\overline{Corr_j}$ ($j = 5$ or 7) for Experiment 2. These plots provide an overall picture of the correlations before and after the data fusion, as well as the corresponding improvements at scale 5 and scale 7. Plots of $\overline{Corr_j^-}$ ($j = 5$ and 7) show a small variation range, from 0.38 to 0.46, in $\overline{Corr_j^-}$ ($j = 5$ and 7) across the 15 bias levels. These are close to the correlation values of their counterparts of $x_9 = 2.0$ shown in Figure 4.5 for Experiment 1. This indicates that the magnitudes of $\overline{Corr_j^-}$ ($j = 5$ and 7) are mainly controlled by the white noise portion of the Type-II errors included in the

precipitation data. The small variations of $\overline{Corr_j^-}$ ($j=5$ and 7) are due to the process of generating the synthetic precipitation data, which are affected by interactions between the bias and the noise.

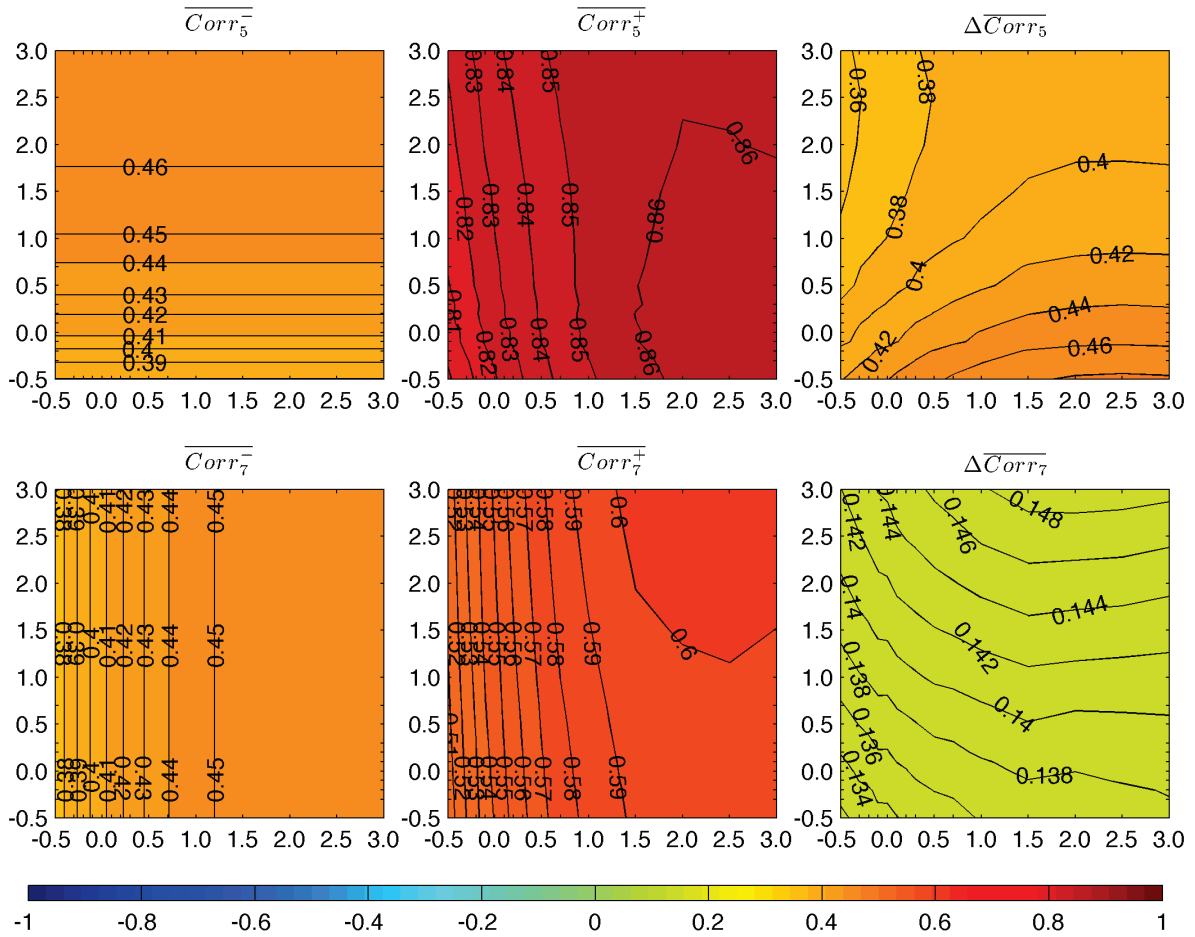


Figure 4.9 Color-filled contour plots of $\overline{Corr_j^-}$, $\overline{Corr_j^+}$ and $\Delta\overline{Corr_j}$ for scale 5 (i.e., $j=5$, upper panel) and scale 7 (i.e., $j=7$, lower panel) for Experiment 2. In each plot, the horizontal axis and the vertical axis represent, respectively, the bias levels at scales 7 and 5.

In Figure 4.9, plots of $\overline{Corr_5^+}$ and $\overline{Corr_7^+}$ reflect the joint influences of the information associated with Y_5^{error} and Y_7^{error} on the fused precipitation. Compared to the plot of $\overline{Corr_5^-}$ in Figure 4.9, the range of correlations at scale 5 increases from a range of (0.38, 0.46) to a range of (0.80, 0.86) after data fusion. Similarly, at scale 7, the spatial correlations increase from (0.38, 0.46) to (0.51, 0.60). Compared to the corresponding plots of $\overline{Corr_5^+}$ and $\overline{Corr_7^+}$ in Figure 4.5, the magnitudes of $\overline{Corr_j^+}$ ($j=5$ and 7) in Figure 4.9 are again close to the correlations of the counterparts of $x_9 = 2.0$ in Experiment 1. This indicates that improvements on the correlations are also mainly attributed to the improvements in removing the noise portion of the Type-II errors. In addition, the bias portion of the Type-II errors in the synthetic data does not essentially affect the ability of the MKS-based framework in removing the noise portion of the Type-II errors. $\overline{Corr_j^+}$ ($j=5$ and 7) just varies slightly with the different bias levels.

Plots of $\Delta\overline{Corr_5}$ and $\Delta\overline{Corr_7}$ show that improvements at both scales 5 and 7 in Experiment 2 are again close to those of their counterparts with $x_9 = 2.0$ in Experiment 1 (see Figure 4.5). In Experiment 1, without introducing any bias into the synthetic data, the magnitude of $\Delta\overline{Corr_5}$ is 0.413 and the magnitude of $\Delta\overline{Corr_7}$ is 0.135 when the noise levels at both scales are $x_9 = 2.0$. In Experiment 2, with 15 bias levels involved, the magnitudes of $\Delta\overline{Corr_5}$ are close to 0.413 and the magnitudes of $\Delta\overline{Corr_7}$ are also close to 0.135, albeit with small variations. Results in Figure 4.9 clearly indicate that the MKS-based framework can effectively recover the spatial patterns of precipitation due to the noise at both scales even when the noise is mixed with bias. Moreover, such a recovery in Experiment 2 is as effective as it is in Experiment 1, even

though in Experiment 2 the noise is blended into the bias as opposed to Experiment 1 where the errors only include noise.

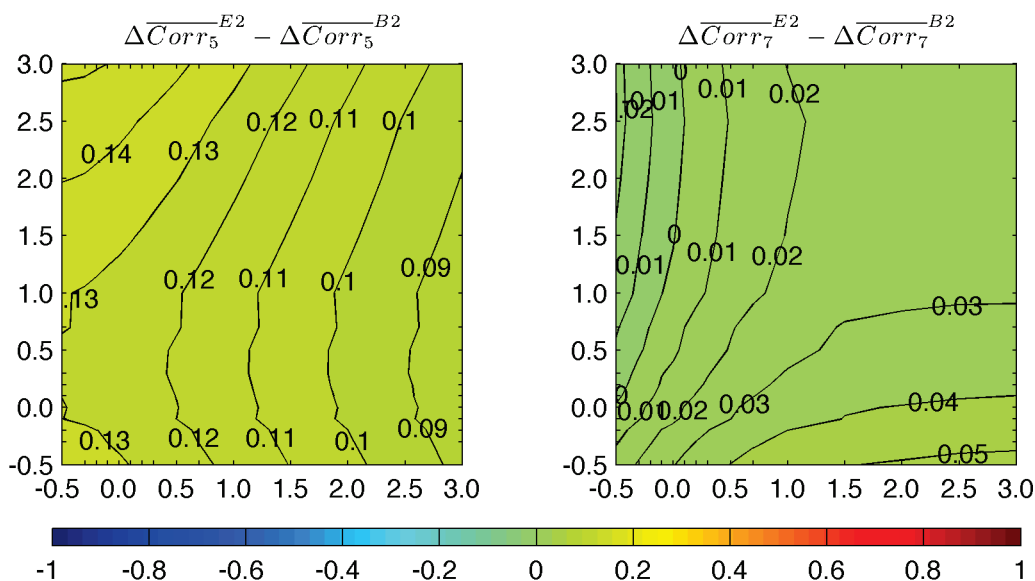


Figure 4.10 Color-filled contour plots of $\overline{\Delta Corr_5}^{E2} - \overline{\Delta Corr_5}^{B2}$ and $\overline{\Delta Corr_7}^{E2} - \overline{\Delta Corr_7}^{B2}$, where the superscript $E2$ denotes Experiment 2 and the superscript $B2$ denotes the benchmark experiment. Both experiments use the same erroneous precipitation data with the Type-II errors. The meanings of the horizontal and vertical axes are the same as in Figure 4.9.

Results of using the MKS-based framework are also compared to those using the conventional data fusion method. Figure 4.10 shows the color-filled contour plots of $\overline{\Delta Corr_5}^{E2} - \overline{\Delta Corr_5}^{B2}$ and $\overline{\Delta Corr_7}^{E2} - \overline{\Delta Corr_7}^{B2}$, where superscripts $E2$ and $B2$ denote the results of Experiment 2 and those of the benchmark experiment respectively. At scale 5, the MKS-based framework shows significant superiority to the conventional data fusion method (Figure 4.10). At scale 7, differences between the two data fusion schemes are reduced, but the MKS-based framework is still slightly more effective than the conventional one. Moreover, magnitudes of $\overline{\Delta Corr_5}^{E2} - \overline{\Delta Corr_5}^{B2}$ are close to 0.127, which is the magnitude of

$\overline{\Delta Corr_5}^{E1} - \overline{\Delta Corr_5}^{B1}$ when the noise levels at both scales 5 and 7 are $x_9 = 2.0$ in Figure 4.6. Similarly, magnitudes of $\overline{\Delta Corr_7}^{E2} - \overline{\Delta Corr_7}^{B2}$ are also close to $\overline{\Delta Corr_7}^{E1} - \overline{\Delta Corr_7}^{B1} = 0.018$ for $x_9 = 2.0$. These results confirm again that the bias in the Type-II errors associated with the precipitation data have little influence on the effectiveness of the MKS-based framework in terms of recovering the spatial patterns of the precipitation data.

Results so far have clearly suggested that given the synthetic precipitation data mixed with both noise and bias (i.e., Type-II errors), the MKS-based framework can restore the spatial patterns of the precipitation data as much as it does in the counterparts of Experiment 1 where the synthetic precipitation data only include the noise. This implies that the bias portion of the errors included in the Type-II errors negligibly affect the performance of the MKS-based framework. This is mainly due to a unique feature of our MKS-based framework (*Parada and Liang, 2004*). As shown in Eq. 3, a D term has been introduced to the observation equation. This D term minimizes impacts of the inconsistency (i.e., bias) among different measurement sources on the fused precipitation at different scales. With the D term, the MKS-based framework just fuses fluctuations (above and below their means) of the measurements. That is why the MKS-based framework is almost influence-free of the different bias when restoring the spatial patterns of the precipitation data. It is worth noting that this D term cannot remove the absolute bias involved in the final values of the fused precipitation data if the mean of the means selected (see Eq. 5) has a bias from the true mean. This is often the case because no one knows the true mean in practice.

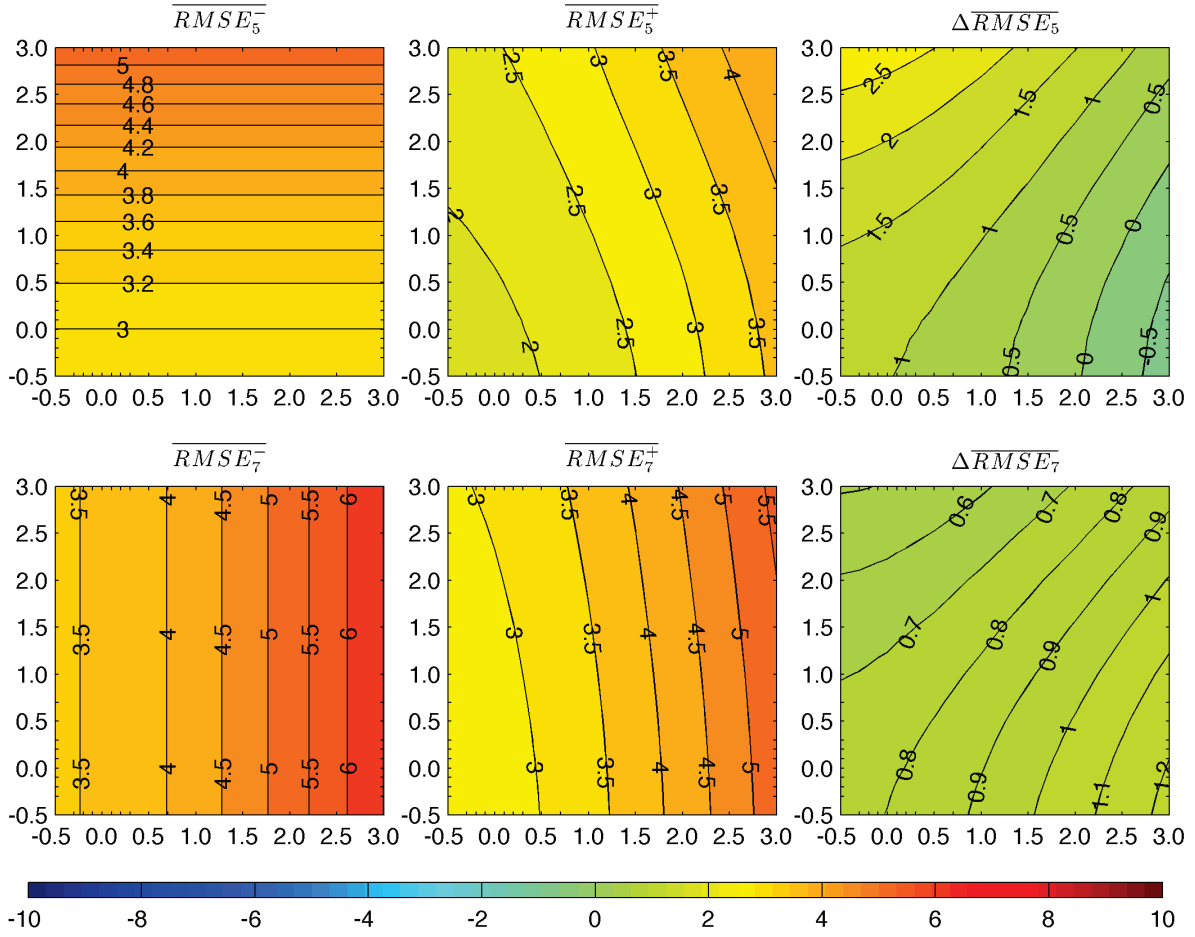


Figure 4.11 Color-filled contour plots of \overline{RMSE}_j^- , \overline{RMSE}_j^+ and $\overline{\Delta RMSE}_j$ for scale 5 (i.e., $j = 5$, upper panel) and scale 7 (i.e., $j = 7$, lower panel) for Experiment 2. The meanings of the horizontal and vertical axes are the same as in Figure 4.9.

Similar to the analysis for Experiment 1, we also conduct an analysis on the RMSE for Experiment 2. Figure 4.11 shows the color-filled contour plots of \overline{RMSE}_j^- , \overline{RMSE}_j^+ and $\overline{\Delta RMSE}_j$ for $j=5$ and $j=7$. From the plots of \overline{RMSE}_5^- and \overline{RMSE}_7^- , we see that the magnitudes of \overline{RMSE}_j^- ($j = 5$ and 7) increase with the increase of the bias levels at scale j . This is consistent with our experiment design. The ranges of \overline{RMSE}_5^- and \overline{RMSE}_7^- are from

about 3.0 to 5.0 and from 3.5 to 6.0 for scales 5 and 7, respectively. The former is a little bit smaller than the latter since the means of the true precipitation data at scale 5 are slightly smaller than the corresponding ones at scale 7. With both noise levels being $x_0 = 2.0$ at scales 5 and 7, the magnitude of $\overline{RMSE_5^-}$ is 3.0 and $\overline{RMSE_7^-}$ is 3.59 in Experiment 1. In Experiment 2, the magnitudes of most of $\overline{RMSE_5^-}$ and $\overline{RMSE_7^-}$ are greater than them due to the added bias in the synthetic data of Experiment 2.

Plots of $\overline{RMSE_5^+}$ and $\overline{RMSE_7^+}$ in Figure 4.11 illustrate the averages of the RMSE between the true and fused precipitation data at scales 5 and 7, respectively. Comparing to the plots of $\overline{RMSE_5^-}$ and $\overline{RMSE_7^-}$, the RMSE has been reduced at both scales 5 and 7 for most of the 15×15 combinations. This indicates that the MKS-based framework is also effective in restoring the magnitudes of the synthetic precipitation data associated with the Type-II errors. In Experiment 2, the magnitudes of $\overline{RMSE_5^+}$ range from about 2.0 to 4.0 while the counterpart in Experiment 1, with the noise level of $x_0 = 2.0$, is 1.91. In addition, the magnitudes of $\overline{RMSE_7^+}$ in Experiment 2 range from about 3.0 to 5.5 while the counterpart in Experiment 1 is 2.80. Generally, the magnitudes of $\overline{RMSE_j^+}$ ($j = 5$ or 7) in Experiment 2 are greater than the magnitudes of their counterparts in Experiment 1. This indicates that the MKS-based framework can remove some but not all of the added bias in the synthetic data at both scales.

Plots of $\overline{\Delta RMSE_5}$ and $\overline{\Delta RMSE_7}$ of Figure 4.11 illustrate the improvements at scales 5 and 7, respectively, for all of the 15×15 combinations. For both $j=5$ and 7, $\overline{\Delta RMSE_j}$ increases with an increase of the bias level at its own scale but decreases with an increase of the bias level at the other scale. The magnitudes of $\overline{\Delta RMSE_5}$ range from -0.73 to 2.86 while their counterpart, with $x_9 = 2.0$ in Experiment 1, is 1.1. The magnitudes of $\overline{\Delta RMSE_7}$ range from 0.49 to 1.23 while their counterpart in Experiment 1 is 0.78. If the bias level at scale j is higher than the bias level at the other scale, then $\overline{\Delta RMSE_j}$ is greater than its counterpart with $x_9 = 2.0$ in Experiment 1. For the opposite situation, $\overline{\Delta RMSE_j}$ in Experiment 2 is then smaller than its counterpart in Experiment 1. When the bias levels at both scales are close to each other, $\overline{\Delta RMSE_j}$ in Experiment 2 are close to their counterpart with $x_9 = 2.0$ in Experiment 1 for $j=5$ and $j=7$ as well. These results clearly indicate that the effectiveness of the MKS-based framework in restoring the magnitudes of the synthetic precipitation data associated with the Type-II errors depends on the bias levels at both scales. Basically, the MKS-based framework can effectively remove the bias included in the Type-II errors. However, it cannot completely remove all of it. In fact, reduction of the RMSE using the MKS-based framework is mainly determined by the way in which the areal mean of the precipitation, namely $\bar{X}(0)$, is calculated. As shown in Eq. 5, $\bar{X}(0)$ is calculated by averaging the means of the measurements at all scales. Once $\bar{X}(0)$ is determined, the mean of the fused precipitation data at each scale of the multiscale tree is determined and is equal to $\bar{X}(0)$. If, for example, $\bar{X}(0)$ is closer to the areal mean of the true precipitation data than the original mean of the precipitation data at scale 5, then $\overline{RMSE_5^+}$ could be smaller than $\overline{RMSE_5^-}$ in Figure 4.11. Otherwise, $\overline{RMSE_5^+}$ could be even larger than $\overline{RMSE_5^-}$ in Figure 4.11. This is why $\overline{\Delta RMSE_5^+}$ and $\overline{\Delta RMSE_7^+}$ have the patterns shown in Figure 4.11.

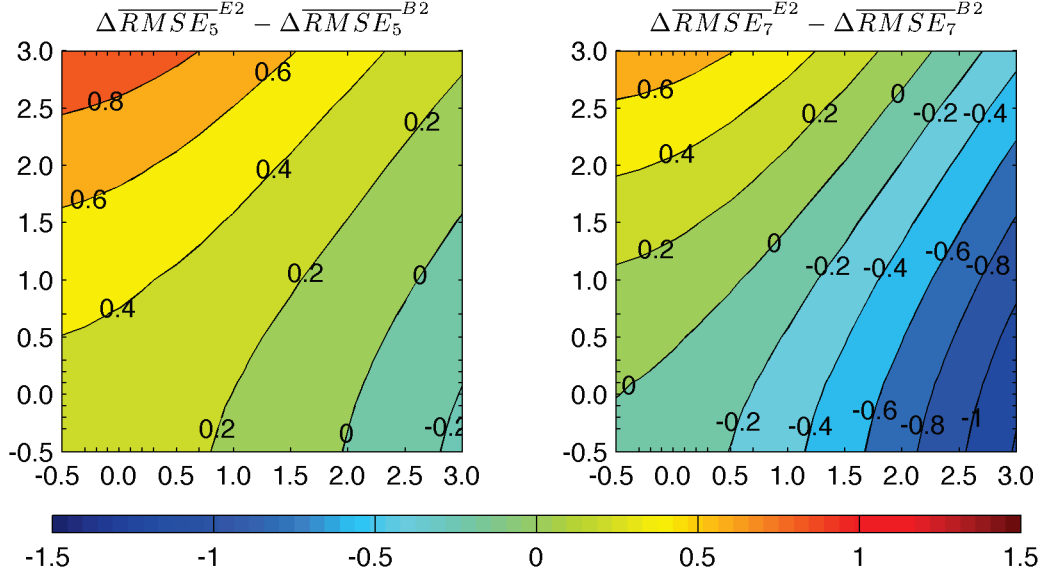


Figure 4.12 Color-filled contour plots of $\overline{\Delta RMSE}_5^{E2} - \overline{\Delta RMSE}_5^{B2}$ and $\overline{\Delta RMSE}_7^{E2} - \overline{\Delta RMSE}_7^{B2}$, where the superscript *E2* denotes Experiment 2 and the superscript *B2* denotes the benchmark experiment. Both experiments use the same erroneous precipitation data with the Type-II errors. The meanings of the horizontal and vertical axes are the same as in Figure 4.9.

In order to further evaluate the effectiveness of the MKS-based framework in recovering the magnitudes of the precipitation data associated with the Type-II errors, $\overline{\Delta RMSE}_j$ of Experiment 2 and $\overline{\Delta RMSE}_j$ of the benchmark experiment are also compared. Figure 4.12 shows that the MKS-based framework is superior to the conventional data fusion method at scale 5 for almost all of the combinations except when the bias levels at scale 7 are much higher than those at scale 5. At scale 7, the MKS-based data framework is superior to the conventional method only for the combinations when the bias levels at scale 5 are much higher than those at scale 7. This indicates a need of enhancing the performance of the MKS-based framework for the finer resolution, where there is a much larger bias in the data, when recovering the magnitudes of the synthetic precipitation data.

Table 4.3 A list of various $Corr$ and $RMSE$ values for Experiment 1 and Experiment 2 for an individual storm occurring at 9:00 AM of September 22, 2003.

	$Corr_5^-$	$Corr_5^+$	$Corr_7^-$	$Corr_7^+$	$RMSE_5^-$	$RMSE_5^+$	$RMSE_7^-$	$RMSE_7^+$
Experiment 1	0.33	0.91	0.40	0.58	3.75	2.18	3.75	2.81
Experiment 2	0.50	0.92	0.45	0.64	4.74	3.48	4.97	4.04

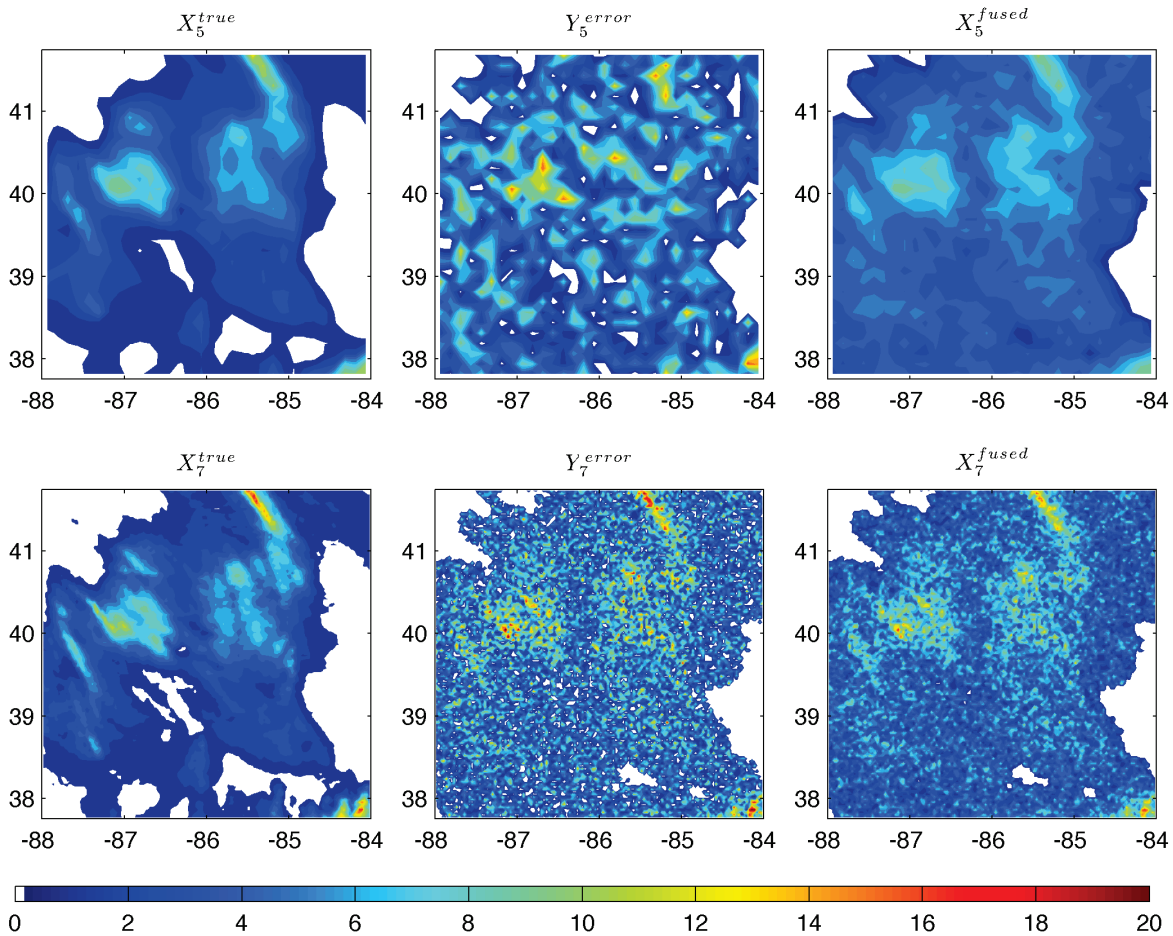


Figure 4.13 Comparison of the images among the true, erroneous, and fused precipitation for an individual storm occurred at 9:00 am of September 22, 2003. X_j^{true} , Y_j^{error} and X_j^{fused} ($j = 5$ and 7) denoted the true, synthetic, and fused precipitation images at scales 5 (upper panel) and 7 (lower panel), respectively. The synthetic precipitation data are generated with the Type-I errors in which the noise levels are $x_0 = 2.0$ for both scales 5 and 7. The horizontal and vertical axes in each plot represent, respectively, the longitudes and latitudes of our study area.

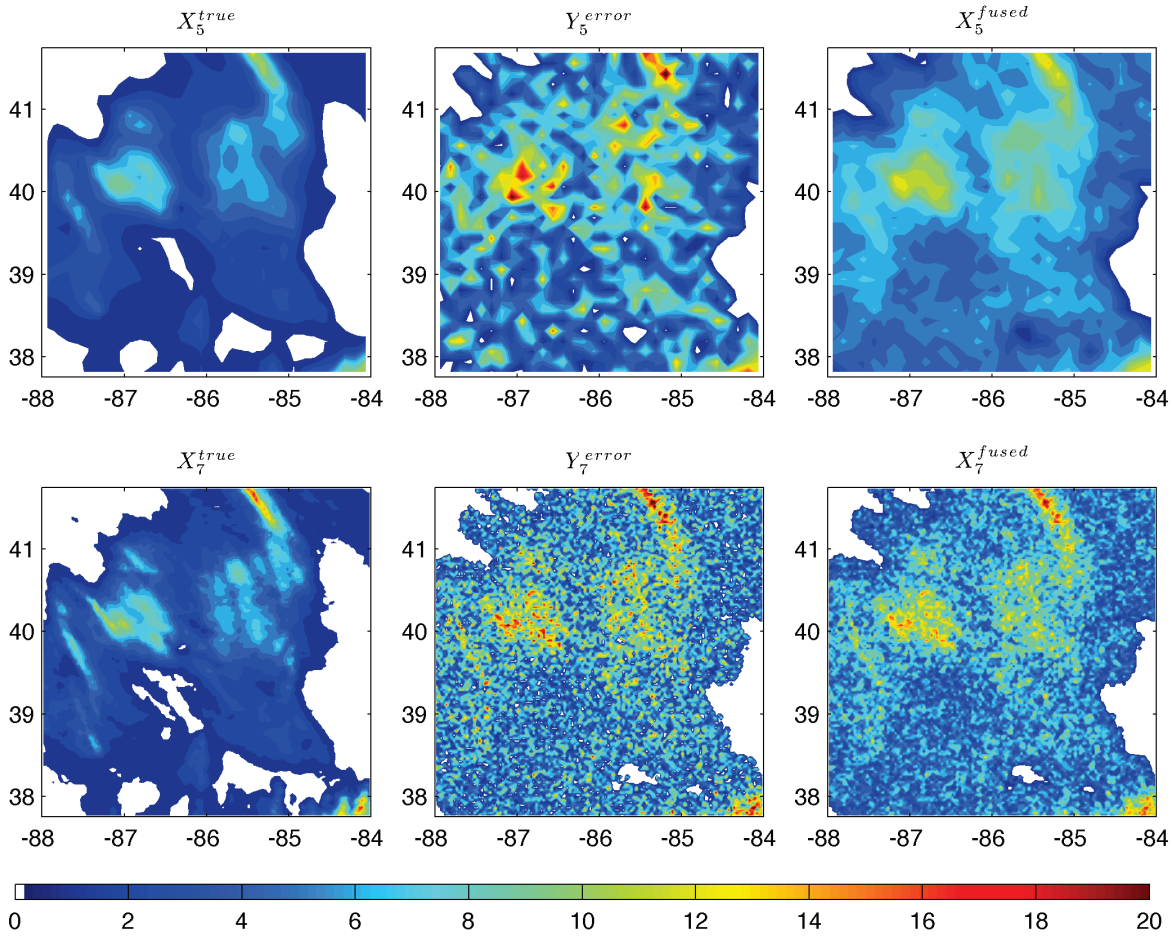


Figure 4.14 Comparison of the images among the true, erroneous, and fused precipitation for an individual storm occurred at 9:00 am of September 22, 2003. X_j^{true} , Y_j^{error} and X_j^{fused} ($j = 5$ and 7) denoted the true, synthetic, and fused precipitation images at scales 5 (upper panel) and 7 (lower panel), respectively. The synthetic precipitation data are generated with the Type-II errors in which the noise levels are $x_9 = 2.0$ and the bias levels are $y_{10} = 1.0$, respectively, for both scales 5 and 7. The horizontal and vertical axes of each plot have the same meanings as in Figure 4.13.

Analyses so far have been focused on evaluating the MKS-based framework in terms of statistical metrics over 2246 hourly precipitation images. Examples of the data fusion results at individual hours are also provided in this study. Figure 4.13 and Figure 4.14 illustrate the true,

the synthetic and the fused precipitation images at 9:00 am on 09/22/2003 for both scales 5 and 7, respectively. Figure 4.13 is for the situation in which the synthetic precipitation data include the Type-I errors (i.e., Experiment 1) and Figure 4.14 is for Experiment 2 in which the synthetic precipitation data include the Type-II errors. Both of the noise levels at scales 5 and 7 are 2.0 in Figure 4.13, while in Figure 4.14 the bias levels at both scales are 1.0 and the noise levels at both spatial scales are 2.0. Table 4.3 lists the correlation and RMSE of the two examples before and after the data fusion using the MKS-based framework. As expected, performance of these individual scenarios measured by the two metrics is consistent with the findings discussed in Section 4.4.2. Through inspections, Figure 4.13 and Figure 4.14 clearly show the significant improvements of the fused precipitation data in both of the spatial patterns and magnitudes at scales 5 and 7, respectively.

4.5 CONCLUSIONS

In this study, we systematically investigated the effectiveness of the MKS-based framework in removing the Type-I errors (white noise) and the Type-II errors (bias and noise together) associated with precipitation data. Hypothetical experiments are conducted using synthetic precipitation data, which are generated at scale 5 (1/8 degree resolution) and scale 7 (1/32 degree resolution), respectively. The mean of correlation and the mean of root mean square error are used in evaluation. In addition, results of the MKS-based framework are compared to those of a conventional data fusion method. Our main findings are summarized as follows.

1. For the Type-I errors, the MKS-based framework can significantly improve the spatial patterns and the magnitudes of the synthetic precipitation data at scale 5 (the coarser resolution) when the scale 7 (the finer resolution) data are fused with the scale 5 data. Exception occurs when the data at scale 5 are already pretty good and the data at scale 7 are very noisy. Results of Experiment 1 also suggest that the MKS-based framework is good at improving spatial patterns of the data at the coarser resolution, even if the finer resolution data may have larger Type-I errors. In other words, these results demonstrate the important value of the high-resolution data in multiscale data fusion using the MKS-based framework, even if the high-resolution data are noisier.
2. When the precipitation data at scale 5 are fused with the data at scale 7, improvements at scale 7 can still be achieved on both the spatial patterns and the magnitudes. But the improvements at the finer resolution are smaller than those at the coarser resolution because the coarser resolution data usually contain less information compared with the finer resolution data. The largest improvement comes with the combination of the less noisy data at scale 5 fused with the noisier data at scale 7. Slight deterioration occurs when the very noisy data at scale 5 are fused with the much less noisy data at scale 7
3. For the Type-II errors, results show that the influence of both the bias and the white noise portions of the Type-II errors can be simultaneously and effectively removed through the MKS-based framework. The improvements at both scales on the spatial patterns are close to those of the counterparts with the same noise level in Experiment 1. This demonstrates the value of the D term (see Eq. 3) in our MKS-based framework. The improvements at both scales on the magnitudes of the precipitation depend on the bias levels at scales 5 and 7. The

magnitudes at one scale may be deteriorated if the bias at this scale is small but the bias at the other scale is much larger.

4. Comparing the results of Experiments 1 and 2 to those of the benchmark experiments, the MKS-based framework is significantly superior to the conventional data fusion method in improving the spatial patterns and the magnitudes of the synthetic precipitation data at scale 5. This is especially true for the combinations when the precipitation data at scale 5 are much noisier than the precipitation data at scale 7. For improvements of the spatial patterns at scale 7, the MKS-based framework is mostly superior to the conventional data fusion method while for improvements of the magnitudes at scale 7, the MKS-based framework is superior only if the precipitation data at scale 5 are noisier to those at scale 7.
5. A limitation of the EM algorithm included in the MKS-based framework is found in this study. Because the number of measurements at the finer resolution (i.e., scale 7) is much larger (e.g., 16 times in this study) than that at the coarser resolution (i.e., scale 5), the EM algorithm over emphasizes the importance of the finer resolution data. Therefore, the MKS-based framework may not perform well when the finer resolution data are much noisier than the coarser resolution data.

In summary, the MKS-based framework is effective in recovering both spatial patterns and magnitudes of the synthetic precipitation data by removing the Type-I and the Type-II errors, which are associated with the precipitation data at multiple scales. This study provides not only new insights of the performance of the MKS-based framework, but also a guideline for the optimal fusion of the precipitation data at different resolutions. However, there are also two main limitations. The first is that an additive Gaussian error model is used in generating the synthetic

precipitation data. Thus, conclusions of this study may not apply to situations when a multiplicative error model is assumed for the precipitation data. The second limitation is that the synthetic precipitation data assume the errors are spatially independent. Thus, the effectiveness of the data fusion algorithms, including both the MKS-based framework and the conventional method, may be less when applied to real precipitation data with spatially correlated errors. In addition, the random errors added to each grid of a synthetic precipitation image follow the same distribution. In the future, we will evaluate a more complicated error model and compare its results to those obtained in this study. In addition, we will conduct further investigations to improve estimations of the variance parameters using the EM algorithm.

5.0 ASSESSMENT OF PRECIPITATION DATA FUSION ON HYDROLOGICAL SIMULATIONS

5.1 INTRODUCTION

Precipitation is an essential input for hydrological models and land surface models (LSMs) to simulate the water and energy budget in land surface processes. In reality, precipitation is the only natural water input to the hydrological cycling at watershed scale. It provides water demanded by runoff generation, evapotranspiration and soil moisture evaluation. Precipitation has two features, the total amount and the spatial pattern. In the distributed simulation of watershed hydrology, it is not enough to know the total amount and intensity of precipitation. The spatial pattern, which describes the spatial distribution of precipitation, is also important in simulating the variability of hydrological processes.

In general, hydrological simulations include streamflow simulation, evapotranspiration simulation and soil moisture simulation. Both hydrological models and land surface models can be used in hydrological simulations. However, LSMs, such as Noah model (Chen et al. 1996; Chen et al. 1997; Chen and Dudhia 2001; Ek et al. 2003), VIC model (Liang et al. 1994; Liang and Xie 2001; Liang and Xie 2003) and CLM model (Dai et al. 2004; Lawrence et al. 2010; Bonan et al. 2011), depict land surface processes with much more physics compared with

hydrological models. Typical LSMs simulate the water budget and energy budget of hydrological processes simultaneously while most hydrological models just focus on the water balance itself. In order to evaluate the influences of precipitation on hydrological simulation on a physical basis, the following discussion will mainly base on the theories of LSMs. Meanwhile, some widely-used conceptual hydrological models, such as TOPMODEL (Beven 1997; Beven and Freer 2001), SAC-SMC model (Vrugt et al. 2006) and Xinanjiang model (Zhao 1992), are also covered more or less. In particular, the influences of precipitation on hydrological simulations will be discussed separately from the aspects of streamflow, evapotranspiration and soil moisture.

In both LSMs and hydrological models, the water of streamflow comes from two sources: surface runoff and subsurface runoff. Surface runoff can be further categorized into infiltration excess runoff (Horton type) and saturation excess runoff (Dunne type). On the one hand, if the intensity of precipitation exceeds the infiltration rate of soil column, infiltration excess runoff will occur. On the other hand, if the total amount of precipitation exceeds the infiltration capacity of soil column, saturation excess runoff will occur. Thus, either the total amount or the intensity of precipitation has direct influences on the simulation of surface runoff. In respect of subsurface runoff simulation, conceptual hydrological models may relate the subsurface runoff linearly to the total soil water in soil column (layers), such as SAC-SMC model and Xinanjiang model, which use a linear reservoir approximation. Conceptual hydrological models may also relate subsurface runoff nonlinearly to the total soil water in soil column, for example TOPMODEL. In LSMs, subsurface flow is basically described with physical laws, such as Richards' equation or Darcy's law. For example, Noah model and VIC model simulate baseflow as the gravitational

drainage at the bottom boundary of soil column. The amount of baseflow is directly related to the soil moisture in the bottom layer of soil column. Precipitation changes soil moisture through infiltration, whose rate is usually a function of the amount and the intensity of precipitation and antecedent soil moisture. Therefore, precipitation also has influences on baseflow simulation. Considering that precipitation is the main recharge source of soil moisture, the influence of precipitation on baseflow simulation should be significant.

In physics-based LSMs and conceptual hydrological models, soil column is typically divided into layers to describe the evolution of soil moistures from the top to the bottom of soil column. The surface soil layer directly accepts the infiltrated water from precipitation, and then redistributes the accepted water to underneath layers through gravitational flow and diffusion processes. For all soil layers, the input water comes from infiltration and the output water goes to gravitational flow, diffusion fluxes and evapotranspiration. The recharge of soil moistures is a discrete process of short duration while the discharge of soil moistures is a continuous process of very long duration. When precipitation occurs, infiltration process significantly changes soil moistures in a short time. Meanwhile, antecedent soil moisture also influences infiltration rate. For example, the amount of infiltrated water is a function of the total precipitation amount in the simulation time step and the antecedent total soil water in soil column. However, precipitation is the positive factor of infiltration processes. It has the dominant influence on infiltration rate for most of the time. Therefore, precipitation is also one of the controlling forces for the evolution of soil moistures. This conclusion is consistent with field observations and the descriptions of soil moisture dynamics in LSMs and conceptual hydrological models as well.

In hydrological simulations, evapotranspiration is a compound term including multiple components. For most LSMs and the conceptual hydrological models, evapotranspiration is a sum of the evaporation from the water intercepted by the canopy of vegetation, direct evaporation from bare soil, and transpiration from vegetation. Actually, the water of the last two components comes from soil moisture in soil layers. For all kinds of models, the amount of intercepted water by vegetation canopy is a function of the amount of precipitation and the interception capacity of vegetation canopy. Therefore, precipitation has direct influences on the amount of intercepted water and the evaporation of the intercepted water. Once again, for most models, evapotranspiration from the root zone of soil layers and the direct evaporation from bare soil are functions of potential evapotranspiration (PET) and saturation degree of soil moistures. PET is usually specified as an input for conceptual models (e.g. SAC-SMC model, TOPMODEL and Xinanjiang Model) or calculated according to atmosphere conditions using Penman-Monteith equation in LSMs, such as Noah model and VIC model. The saturation degree, however, is calculated based on soil moisture contents, which helps to scale PET to actual evapotranspiration and actual evaporation directly from bare soil. Through the influence on soil moisture, precipitation also has significant impacts on the last two components of evapotranspiration.

Based on the analysis above, precipitation has significant influences on hydrological simulations, no matter whether such influences are direct or indirect. The reliability of hydrological simulations heavily relies on the accuracy of precipitation data. If the quality of precipitation data is improved, it can be expected that the reliability of hydrological simulation will be improved correspondingly.

From the viewpoint of hydrological simulations, there are no perfect precipitation data that not only accurately record the amount but also the spatial pattern of precipitation. The first reason for this problem is that precipitation measurements usually have limitations. Rain gauge, weather radar and weather satellite are the three conventional measurements of precipitation. Rain gauge directly measures precipitation at discrete points. Among these three types of measurements, rain gauge is the most reliable one but it is poor to describe the spatial pattern of precipitation. Even in the continental United States, rain gauge network is not dense enough to capture precipitation over space. Otherwise, there would be no need to develop and deploy Next-Generation Radar (NEXRAD) network by National Weather Service (NWS) from the perspective of hydrology. NEXRAD network continuously measures precipitation over space at a relatively high spatial resolution, i.e. closely 4 km. Satellite radar may carry either microwave imager or infrared imager. NEXRAD precipitation data are only widely available in the U.S. while weather satellites provide precipitation measurements at a global scale. Near-earth orbiting satellites usually carry microwave imager, such as the Spatial Sensor Microwave/Imager (SSM/I) and the Tropical Rainfall Measuring Mission (TRMM), but geostationary satellites usually carry infrared imager. Compared with near-earth orbiting satellites, geostationary satellites measure precipitation at coarser spatial resolutions but finer temporal resolutions over wider spatial areas. All precipitation data of weather radars and weather satellites are indirect measurements, which suffer from biases and uncertainties caused by inverse computation and parameter calibration. Another limitation comes from the multiscale of precipitation data. First of all, precipitation phenomenon is very complex and explicitly has multiscale features of statistics. For example, the mean of precipitation changes for different locations of measurements and different extents of measurements. In other words, precipitation phenomenon is nonstationary over space. Similarly,

precipitation is also nonstationary over time. Therefore, precipitation data are associated with the spatial and the temporal scales of the measurements. For the same precipitation event, the amount and the spatial pattern of precipitation data are different if the measurement scales are different. In addition, the applications of precipitation data are also conducted at specific temporal and spatial scales, which are not necessarily the same as those of precipitation data. Therefore, it is common to upscale or downscale the precipitation data before application.

However, the advantages of different types of precipitation data are usually complementary. For example, rain-gauge-based precipitation data are usually good at the total amount while weather-radar-based data are usually good at the spatial pattern. More reliable precipitation datasets can be derived for hydrological simulations if the rain-gauge-based precipitation data and the weather-radar-based precipitation data can be effectively fused together. Considering the multiscale characteristic of precipitation, the data fusion method should be able to deal with measurements or data at multiple spatial resolutions. Multiscale Kalman Smoother (MKS) (Basseville et al. 1992; Chou et al. 1993; Willsky 2002) is an algorithm designed to process signals of different spatial or temporal resolutions. For the cases of processing two-dimensional data, the MKS algorithm has demonstrated its strength in fusing multiscale data in the studies of soil moisture data assimilation (Parada and Liang 2004; Parada and Liang 2008), altimetry data fusion (Slatton et al. 2001; Slatton et al. 2002) and precipitation data fusion (Gorenburg et al. 2001; Gupta et al. 2006; Bocchiola 2007; de Vyver and Roulin 2009). According to the systematic evaluation by (Wang et al. 2011), the MKS algorithm can effectively remove noise in precipitation data, especially at coarse resolutions. Therefore, the MKS algorithm is the right tool for multiscale precipitation data fusion.

In this study, we first fuse NLDAS-2 and NEXRAD MPE precipitation data products with the MKS algorithm and then assess the improvements of hydrological simulations with derived precipitation data products. NLDAS-2 precipitation data are part of phase-2 forcing data of the North American Data Assimilation System (NLDAS) (LDAS 2011). NLDAS-2 precipitation data are developed based on CPC (Climate Prediction Center) daily CONUS (Continental United State) gauge data with topographical adjustment, CPC hourly CONUS/Mexico gauge data, hourly Doppler Stage II radar precipitation data, half-hourly CMORPH data and 3-hourly NARR precipitation data. Hourly NLDAS-2 precipitation is derived by temporally disaggregating the daily gauge products with the Doppler radar, CMORPH products, or hourly rain gauge products. NLDAS-2 precipitation data are believed to have reliable representation of the total amount of precipitation because of the backbone of CPC daily gauge data. However, NLDAS-2 precipitation data also have obvious limitations. The spatial pattern of NLDAS-2 precipitation data is mainly derived from interpolating of CPC daily gauge data. In addition, NLDAS-2 precipitation data are at a relatively coarse resolution, i.e. 1/8 degree. NEXRAD MPE data are derived from measurements of the Next Generation Weather Radar with the Multisensor Precipitation Estimation (MPE) algorithm (Nelson et al. 2006). NEXRAD MPE hourly data are at a spatial resolution of 4 km, so the spatial pattern of precipitation can be well captured. Compared with the previous version of NEXRAD precipitation data product, Stage III data product, NEXRAD MPE precipitation product is better in agreement with gauge observations (Wang et al. 2008). However, NEXRAD MPE data product also has considerable biases and uncertainties compared with rain gauge measurements (Habib et al. 2009). In this study, we derive three series of precipitation products based on NLDAS-2 precipitation data (called NLDAS-2 data for abbreviation) and NEXRAD MPE

precipitation data (call RADAR data for abbreviation). Assessments of the derived precipitation data will be conducted with Noah LSM in hydrological simulation. Fourteen watersheds in the Ohio River basin are selected to assess the influences of precipitation data fusion on hydrological simulations.

In the rest of this chapter, we will introduce the method of precipitation data fusion in section 5.2 and then introduce experimental watershed and analyze NLDAS-2 and RADAR data in section 5.3. Section 5.4 will describe three settings of data fusion. In section 5.5, we will assess the influence of precipitation fusion on the simulations of streamflow, soil moisture and evapotranspiration in the fourteen experimental watersheds. At last, a summary of this study will be given in section 5.6.

5.2 METHOD FOR PRECIPITATION DATA FUSION

In this study, Multiscale Kalman Smoother (MKS) algorithm and Expectation-Maximization (EM) algorithm are used together to fused precipitation data at multiple measurements. The MKS algorithm is a data fusion algorithm designed to deal with measurements at different spatial resolutions. As Figure 5.1 shows, multiscale measurements are organized into a multiscale tree. The computation of the MKS algorithm is conducted along the multiscale tree through two steps, upward sweep and downward sweep. Upward sweep is a Kalman filtering by scale from finer resolutions to coarser resolutions. It passes information from measurements at finer resolutions to estimates, the state variables and their associated error covariance, at coarser resolutions. Downward sweep is a Kalman smoothing from coarser

resolutions to finer resolutions. It passes information from measurements at coarser resolutions to estimates at finer resolutions. The MKS algorithm has a number of parameters, which will be optimally estimated with the EM algorithm based on measurements.

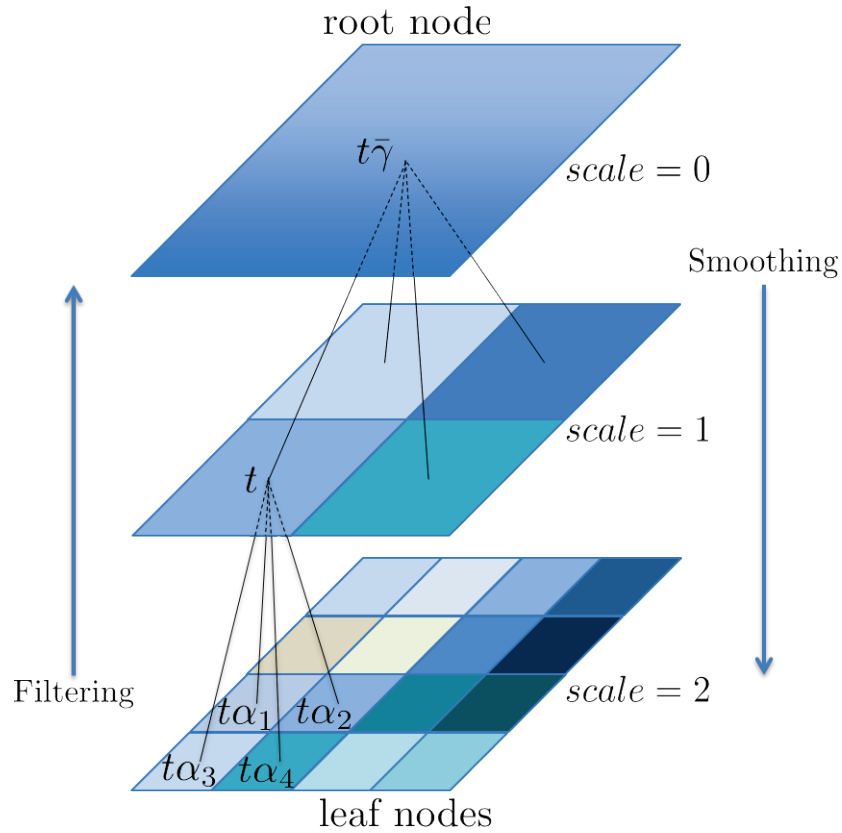


Figure 5.1 Schematic representation of Multiscale Kalman Smoother (MKS) algorithm. The three images, denoted as $scale = 0$, $scale = 1$ and $scale = 3$ respectively, represent measurements of the same region from the coarsest resolution to the finest resolution. The varying colors in these images represent different values of measurements. Each pixel of image is called a node. All nodes are organized into a tree shape, called multiscale tree while the node and the nodes at the coarsest resolution and the finest resolution are called root node and leaf nodes, respectively.

In the MKS algorithm, there are four kinds of estimates for state variables and their error covariance: (1) unconditional estimate, denoted as $\hat{x}(t| -)$ and $P(t| -)$; (2) estimate conditioned on measurements at descendent nodes of current node, denoted as $\hat{x}(t| +)$ and $P(t| t+)$; (3)

estimate conditioned on measurements at descendent nodes of the current node and the current node itself, denoted as $\hat{x}(t|t)$ and $P(t|t)$; and (4) estimate conditioned on measurements at the whole multiscale tree, $\hat{x}_s(t)$ and $P_s(t)$. $\hat{x}(t|-)$ and $P(t|-)$ are prior estimates computed in the initialization of the MKS algorithm. $\hat{x}(t|+)$ and $P(t|+)$ are predicted from the measurements at the descendent nodes of node t . $\hat{x}(t|t)$ and $P(t|t)$ are updated estimates of $\hat{x}(t|+)$ and $P(t|+)$ with the measurements at node t . $\hat{x}_s(t)$ and $P_s(t)$ are the outputs of the MKS algorithm and they are also called smoothed estimates because they are computed in the Kalman smoothing step.

Initialization is from the root node to the leaf nodes of the multiscale tree. Given the areal estimate at the root node, $\bar{X}(0)$, and its error variances $\Sigma(0)$, the state variables and their error covariances at the nodes of the multiscale tree can be initialized with

$$\hat{x}(t|-) = A(t)\hat{x}(t\bar{\gamma}|-) + w(t) \quad (5-1)$$

$$P(t|-) = A(t)P(t\bar{\gamma}|-)A^T(t) \quad (5-2)$$

where $w(t)$ is the process error following $\mathcal{N}(0, Q(t))$; $Q(t)$ is the covariance of $w(t)$; $t\bar{\gamma}$ represents the parent node of t .

Upward sweep includes measurement update and fine-to-coarse prediction. These two steps follow each other from the leaf nodes to the root nodes of the multiscale tree. For all leaf nodes, $\hat{x}(t|+) = \hat{x}(t|-)$ and $P(t|+) = P(t|-)$ since there are no descendent nodes for them. If there are measurements available for node t , denoted as $y(t)$, $\hat{x}(t|+)$ is updated into $\hat{x}(t|t)$ as

$$\hat{x}(t|t) = \hat{x}(t|+) + K(t) [y(t) - C(t)\hat{x}(t|+) - D(t)] \quad (5-3)$$

$$P(t|t) = [I - K(t)C(t)]P(t|+) \quad (5-4)$$

$$K(t) = P(t|+)C^T(t) [C(t)P(t|+)C^T(t) + R(t)]^{-1} \quad (5-5)$$

where $R(t)$ is the covariance of measurement errors at node t and $D(t)$ is a term of compensation for the biases between measurements. With the $D(t)$ term, the MKS algorithm just deals with the fluctuation of measurements relative to the estimate of areal mean, $\bar{X}(0)$.

Suppose the mean of the measurements at the scale of node t is \bar{Y}_s , then we calculate $D(t) = \bar{Y}_s - C(t)\bar{X}(0)$. If no measurements are available, set $\hat{x}(t|t) = \hat{x}(t|+)$ and $P(t|t) = P(t|+)$.

The fine-to-coarse prediction is next to the measurement update. For node t , $t\alpha_i$ is one of its child nodes and the fine-to-coarse prediction from $t\alpha_i$ to t is described as

$$\hat{x}(t|t\alpha_i) = F(t\alpha_i)\hat{x}(t\alpha_i|t\alpha_i) \quad (5-6)$$

$$P(t|t\alpha_i) = F(t\alpha_i)P(t\alpha_i|t\alpha_i)F^T(t\alpha_i) + \bar{Q}(t\alpha_i) \quad (5-7)$$

where

$$F(t\alpha_i) = P(t|-)A^T(t)P^{-1}(t\alpha_i|-) \quad (5-8)$$

$$\bar{Q}(t\alpha_i) = P(t|-) - P(t|-)A^T(t\alpha_i)P^{-1}(t\alpha_i|-)A(t\alpha_i)P(t|-). \quad (5-9)$$

All predictions of node t from its child nodes are then merged to get

$$\hat{x}(t|+) = P(t|+) \sum_{i=1}^{N_c(t)} P^{-1}(t|t\alpha_i)\hat{x}(t|t\alpha_i) \quad (5-10)$$

$$P(t|+) = \left[(1 - N_c(t))P^{-1}(t|-) + \sum_{i=1}^{N_c(t)} P^{-1}(t|t\alpha_i) \right]^{-1} \quad (5-11)$$

where $N_c(t)$ represents the number of child nodes.

The upward sweep stops once it proceeds to the root node of the multiscale tree. Information in the measurements at the whole multiscale tree has been incorporated into the updated estimates of state variables and their error covariance. Therefore, the last step of the upward sweep is to set $\hat{x}_s(0) = \hat{x}(0|0)$ and $P_s(0) = P(0|0)$. Starting from the root node, the downward sweep includes Kalman smoothing steps from coarser resolution to finer resolution. Except the root node, smoothed estimates at rest nodes of the multiscale tree are calculated as

$$\hat{x}_s(t) = \hat{x}(t|t) + J(t) [\hat{x}_s(t\bar{\gamma}) - \hat{x}(t\bar{\gamma}|t)] \quad (5-12)$$

$$P_s(t) = P(t|t) + J(t) [P_s(t\bar{\gamma}) - P(t\bar{\gamma}|t)] J^T(t) \quad (5-13)$$

where

$$J(t) = P(t|t) F^T(t) P^{-1}(t\bar{\gamma}|t) \quad (5-14)$$

Through the downward sweep, information in the measurements at coarser resolution is merged with the updated estimates ($\hat{x}(t|t)$ and $P(t|t)$) into the smoothed estimates ($\hat{x}_s(t)$ and $P_s(t)$) that are conditioned on measurements at the whole multiscale tree.

In addition to the computation steps introduced above, to conduct multiscale data fusion, we still need to specify parameters of the MKS algorithm, $A(t)$, $C(t)$, $Q(t)$, $R(t)$, $t \in \mathcal{T}$. \mathcal{T} is the set of nodes in the multiscale tree. Considering that all data are already the magnitudes of precipitation (NLDAS-2 data and RADAR data) in our precipitation data fusion experiments, we

set $A(t) = 1$ and $C(t) = 1$. However, if the data are not the magnitudes of state variable, $A(t)$ and $C(t)$ should be specified according to the characteristics of data. In order to reduce the complexity and difficulty of parameter estimation, we assume the error covariance terms $Q(t)$ and $R(t)$ to be scale homogeneous. In other words, $Q(t)$ or $R(t)$ takes the same value for all the nodes at the same scale. Supposing that the prediction errors are independent of all nodes and similar for the measurement errors, the log-likelihood function of all measurements, denoted as Y , given $Q(t)$ and $R(t)$ can be formulated as

$$\begin{aligned} \mathcal{L}[Y, Q(t), R(t)] = & - \sum_{t \in \mathcal{T}_c} \left\{ \log |Q(t)| + [\hat{x}_s(t) - A(t)\hat{x}_s(t\bar{\gamma})]^T Q^{-1}(t) [\hat{x}_s(t) - A(t)\hat{x}_s(t\bar{\gamma})] \right\} \\ & - \sum_{t \in \mathcal{T}_c} \left\{ \log |R(t)| + [y(t) - c(t)\hat{x}_s(t) - D(t)]^T R^{-1}(t) [y(t) - c(t)\hat{x}_s(t) - D(t)] \right\} \quad (5-15) \\ & + \text{constant} \end{aligned}$$

where \mathcal{T}_c is the set of nodes in the multiscale tree except the root node and \mathcal{T}_m is the set of nodes of the multiscale tree with measurements. We use the EM algorithm to estimate $Q(t)$ and $R(t)$. The EM algorithm includes two steps: Expectation step (E-step) and Maximization step (M-step). Particularly, the E-step is actually the upward sweep plus the downward sweep and it computes the smoothed estimates of state variables, i.e. $\hat{x}_s(t)$. The M-step is to estimate $Q(t)$ and $R(t)$ by maximizing equation (5-15). In this study, the maximization is conducted with Newton's method. Optimal parameters are obtained by iterating the E-step and the M-step for given numbers.

In addition to parameters, we also need to determine the areal mean of state variables and their prior error covariance, namely $\bar{X}(0)$ and $\Sigma(0)$, before precipitation data fusion. $\bar{X}(0)$ is the most important parameter of the MKS algorithm. It controls mean magnitudes of fused data at all

scales. The estimate of $\bar{X}(0)$ totally depends on the understanding of data and intensions of precipitation data fusion. Three settings for estimating $\bar{X}(0)$ will be given in the section 5.4 while the prior error covariance is estimated as $\Sigma(0) = [\hat{x}_s(0) - \bar{X}(0)][\hat{x}_s(0) - \bar{X}(0)]^T$. In the description of this section, we use vector notations for all variables. However, all the equations are also valid for scalar variables.

5.3 EXPERIMENTAL WATERSHEDS AND DATA ANALYSIS

5.3.1 Experimental watersheds

We select 14 experimental watersheds to assess the influences of precipitation data fusion on hydrological simulations. As shown in Figure 5.2, these watersheds scatter in the Ohio River Basin. The areas, elevation ranges and descriptions of these 14 watersheds are summarized in Table 5.1. Considering the strong association of precipitation with topography, four types of typical topographies are discussed in this study. Among the 14 watersheds, CLAI2, CRWI3 and FDYO1 have flat topographies; ALPI3, BAKI3, DBVO1, NHSO1 and SERI3 watersheds have mild topographies; BSNK2, CYCK2 and KINT1 watersheds have relatively steep topographies; ALDW2, ELRP1 and PSNW2 have steep topographies. Digital elevation model (DEM) data of these watersheds can be found in Figure 5.8 to Figure 5.21 respectively. In addition, these 14 watersheds distribute from the north to the south. This means that the selection of these experimental watersheds considers the association of precipitation with temperature, which varies with latitudes. Due to the comprehensive consideration of precipitation, topography and

temperature, conclusions drawn from this study are expected to be applicable over the entire Ohio River Basin.

There are no or minor human regulations in these watersheds. Therefore, observed streamflow data of these 14 watersheds, which can basically reflect the natural rainfall-runoff relationships, can be directly used in the parameter calibration of Noah LSM and its flow routing scheme.

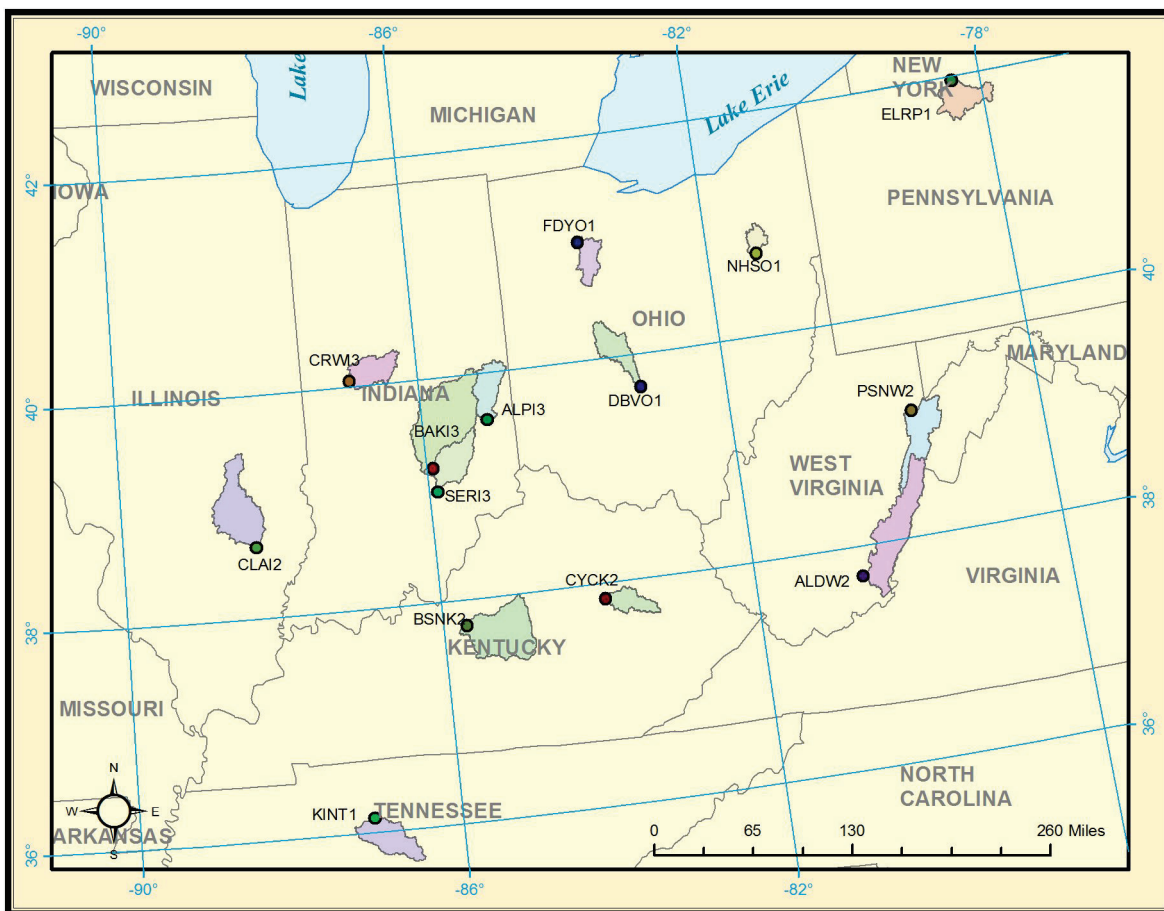


Figure 5.2 Maps of the 14 Experimental watersheds in the Ohio River Basin. For each watershed, the circle represents the location of outlet. SERI3 also includes the area of BAKI3 since the latter is a sub-watershed of the former.

5.3.2 Data analysis

NLDAS-2 precipitation data are in longitude-latitude coordinate system at 1/8 degree resolution over CONUS. NEXRAD MPE precipitation data are in a coordinate system of HRAP (Hydrologic Rainfall Analysis Project) at a resolution of 4 km. To unify the coordinate system of data, NEXRAD MPE precipitation data have been projected into a longitude-latitude coordinate system and resampled to 1/32 degree resolution, which is approximately 4 km in the region of the Ohio River Basin. In the following analysis, we call the projected and resampled NEXRAD MPE data as RADAR data for abbreviation.

The purpose of the data analysis is to reveal the differences between NLDAS-2 and RADAR data. Even though the two precipitation data describe precipitation over the same area, data fusion is valuable only if there are considerable differences between them. Comparison between NLDAS-2 and RADAR data are conducted separately in these 14 experimental watersheds. Particularly, three statistics related to precipitation are considered. The first is about recording the occurrences of precipitation. Precipitation data may or may not record a precipitation event. We use relative missing number (RMN) to evaluate the recording of occurrence. RMN is defined as the total number of situations that one precipitation data miss a precipitation event but the other data record it. Larger RMN indicates that the precipitation data are more probable to miss precipitation events compared with the other data. The second statistics is the correlation between the two precipitation data. Correlation is an indicator of the agreement between the spatial patterns of two precipitation images, which is formulated as the following

$$CORR(X_1, X_2) = \frac{E[(X_1 - \mu_{X_1})(X_2 - \mu_{X_2})]}{\sigma_{X_1}\sigma_{X_2}} \quad (5-16)$$

where X_1 and X_2 represent the amount of precipitation data in the pixels of precipitation images within precipitation-covered region Ω . σ_{X_1} and σ_{X_2} are variances of X_1 and X_2 . Ω is defined as the union of precipitation-covered pixels of precipitation image 1 and 2. The third statistics is the average magnitudes of precipitation images. The differences between the spatial averages of NLDAS-2 data and the spatial averages of RADAR data, namely $mean(NLDAS-2) - mean(RADAR)$, are used to compare the average magnitudes. In order to compute these three statistics, RADAR data have been aggregated into the same spatial resolution of NLDAS-2 data, namely 1/8 degree. This means that the spatial pattern and the variability of RADAR data have been significantly reduced. The actual differences between NLDAS-2 and RADAR data (at 1/32 degree resolution) should be larger than the differences shown at 1/8 degree resolution.

To be consistent with the section 5.4, in which the influence of precipitation data fusion on hydrological simulation was assessed in the period from 01/01/2003 to 12/31/2005, we analyze NLDAS-2 and RADAR precipitation data in the same period in section 5.3. In addition, data are analyzed by year to show the possible multiyear trend of differences between the two data.

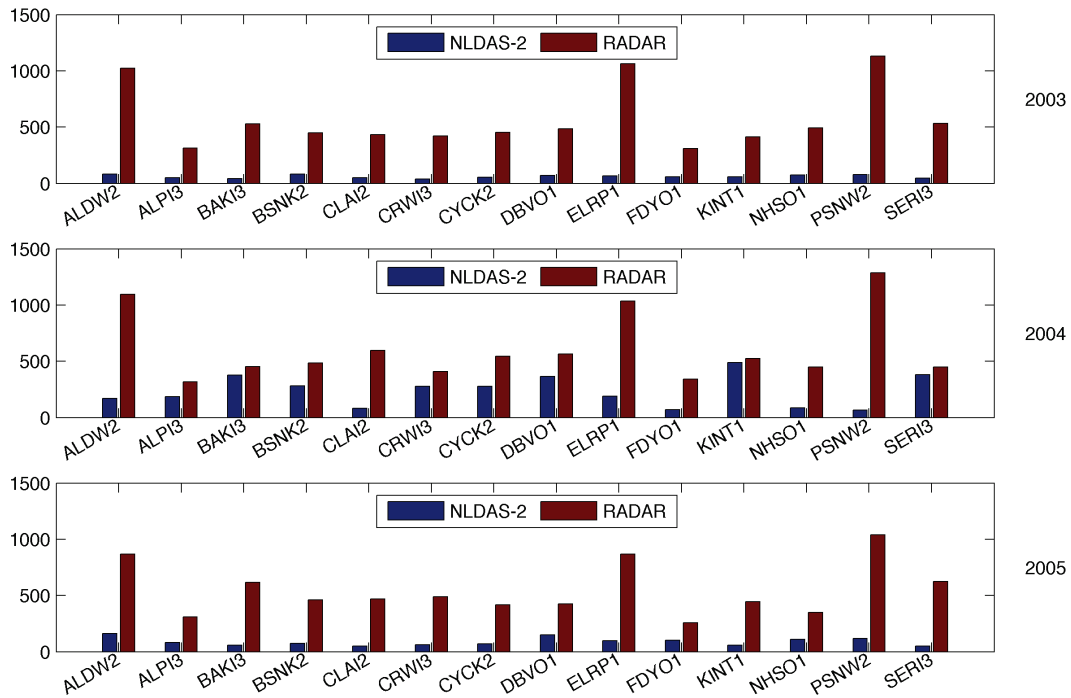


Figure 5.3 Relative missing numbers in the 14 experimental watersheds in the calibration period (2003, 2004 and 2005).

Figure 5.3 uses bar plots to show the RMNs of NLDAS-2 and RADAR data for year 2003, 2004 and 2005. First of all, both NLDAS-2 and RADAR data have nonzero RMN for these three years, which means that either of these two datasets has chances of missing the occurrences of precipitation events. Secondly, the RMNs of RADAR data are significantly larger than those of NLDAS data for all watersheds, especially in year 2003 and 2005. It indicates that RADAR data have much more chances to miss precipitation events compared with NLDAS-2 data. Thirdly, the RMNs of RADAR in the three watersheds with steep topographies, i.e. ALDW2, ELRP1 and PSNW2, are much larger than the RMNs of RADAR data in other watersheds. While the RMNs of NLDAS-2 data in the three watersheds are at the same level of those in other watersheds. In other words, the ability to record the occurrence of precipitation is

significantly affected by the topographies of watersheds for RADAR data but not for NLDAS-2 data. Fourthly, the RMNs of NLDAS-2 data in most of the experimental watersheds in 2004 are obviously larger than the corresponding ones in 2003 and 2005. While the RMNs of RADAR data in most of experimental watersheds in 2005 are smaller than the corresponding ones in 2003 and 2004. Such difference indicates that the qualities of NLDAS-2 and RADAR data may change annually. This point should be noticed in precipitation data fusion.

Figure 5.4 shows the distributions of correlation between all hourly precipitation images of NLDAS-2 and RADAR data in 2003, 2004 and 2005. For each watershed, the boxplot gives the 25th, 50th and 75th percentiles of the distribution. In addition, the means of correlations are also plotted. Three findings can be found from Figure 5.4. First, the means of correlations over all of the 14 watersheds are smaller than 0.5 for the three years, especially for ALDW2, ELRP1 and PSNW2, the watersheds with steep topographies. Except ALPI3 in the three years, BAKI3 in 2003, CYCK2 in 2003, KINT1 in 2003, SERI3 in 2003, the medians (50th percentiles) of other watersheds in the rest of years are almost equal to or less than 0.5. This indicates that at least a half of precipitation images of the two data have correlations no more than 0.5. Second, the 25th percentiles of all watersheds are equal to zero. This is because a big number of precipitation images have zero correlations due to the relative missing of precipitation occurrences. This result also indicates that at least 25% of the precipitation images have correlations no more than zero for the three years in all experimental watersheds. Third, the correlations in most of the 14 watersheds in 2004 are smaller than the corresponding ones in 2003 and 2005. This result is consistent with the results shown in Figure 5.3. That is to say that NLDAS-2 and RADAR data have poorer consistency in 2004. As mentioned earlier, the correlations between NLDAS-2 data

and RADAR data are computed at 1/8 degree resolution. It is reasonable to expect that correlations between the two data should be even smaller at 1/32 degree, the resolution of RADRA data, which will be fused.

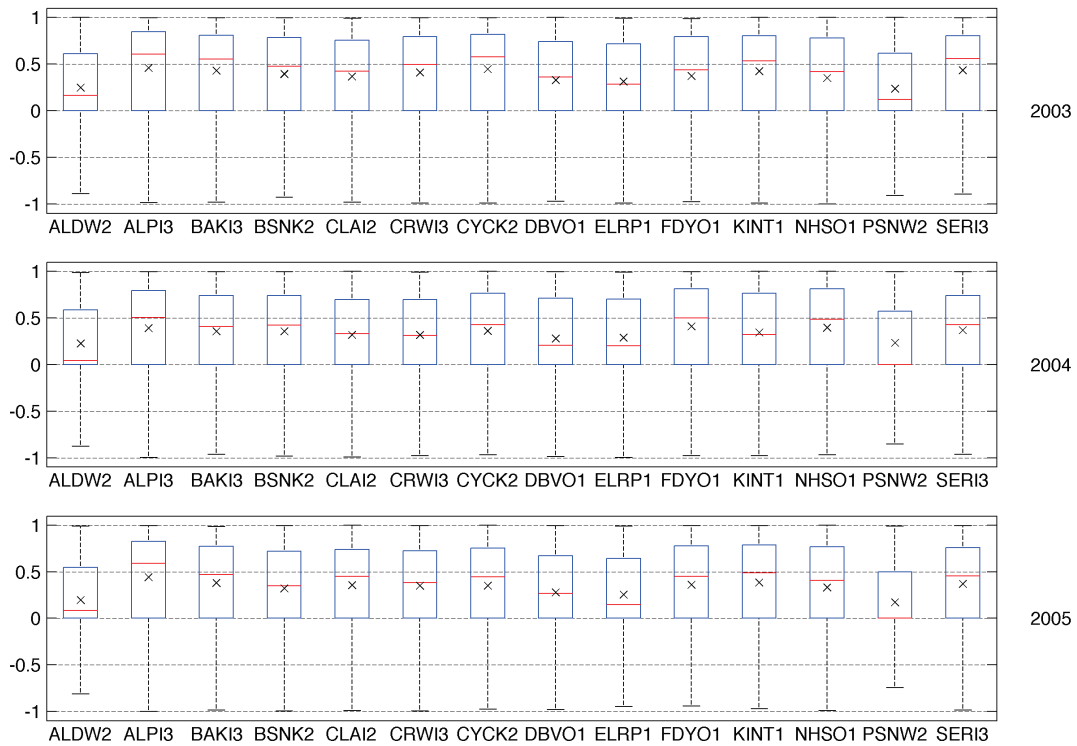


Figure 5.4 Boxplots of correlation between hourly NLDAS-2 and RADAR precipitation data over the 14 experimental watersheds in the three years of the calibration period (2003, 2004, and 2005). Marker “x” represents the mean of correlations.

Figure 5.5, Figure 5.6 and Figure 5.7 respectively illustrate the distributions of $mean(NLDAS-2) - mean(RADAR)$ for the 14 watersheds in year 2003, 2004 and 2005. The 10th, 25th, 50th, 75th, 90th percentiles of the distributions are also plotted along the x-axis of each histogram. From these three figures, we can firstly find that most of the differences are distributed between -1.0 to 1.0. For all watersheds over the three years, more than 50% of

precipitation images have differences ranging from -0.5 to 0.5. However, for most of watersheds, there also more than 20% precipitation images have differences, whose absolute values are beyond 0.5. Taking the precipitation-covered area into account, differences of the total amount of precipitation between the two data are not small at all, which may significantly impact the simulation of hydrological processes. The vertical green line in each histogram represents the annual mean of the difference. It can be seen that the annual mean of NLDAS-2 data is larger than that of RADAR data in most of watersheds over the three years, especially in ALDW2, PSNW2 and BSNK2, whose topographies are steep or relatively steep. Even the annual mean of RADAR data also has chances to be larger than that of NLDAS-2 data, for example SERI3 in 2004, DBVO1 in 2005 and FDYO1 in 2005, but the absolute magnitudes are very small. In this study, precipitation data fusion and hydrological simulations are conducted at hourly time step, which means all the hourly differences between two data will be taken into account even though the annual means of the two data are close.

In this section, we have analyzed the differences between NLDAS-2 data and RADAR data by year. We found considerable differences in terms of recording the occurrences of precipitation events, agreements between the spatial patterns, and average hourly precipitation. These differences indicate the possibility of deriving more reliable precipitation data through fusing these two products.

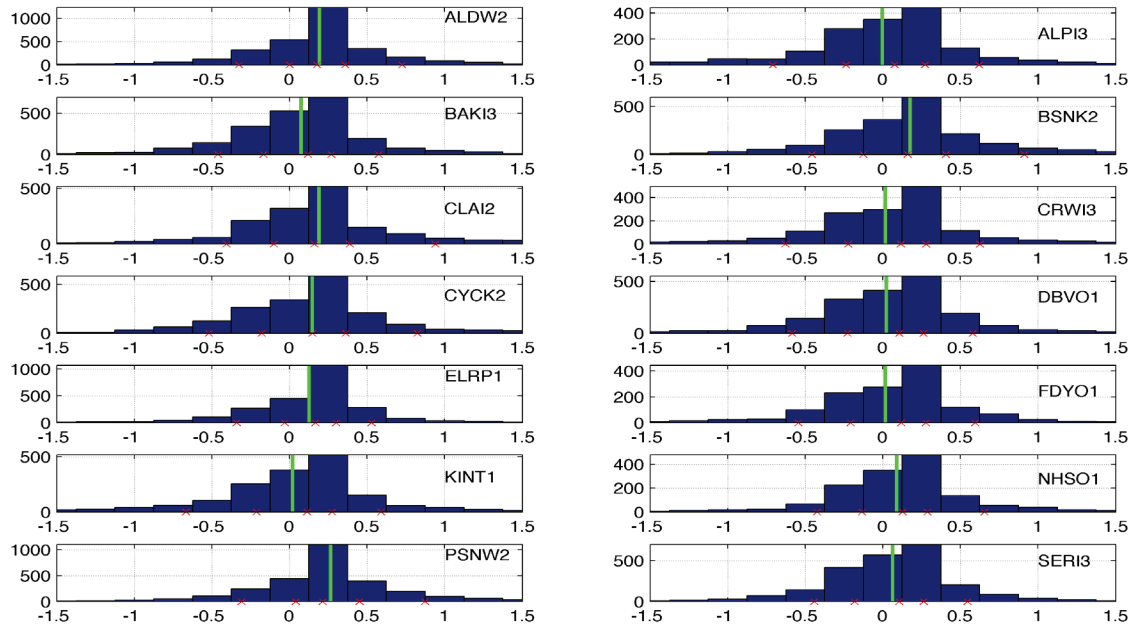


Figure 5.5 Histograms of $mean(NLDAS-2) - mean(RADAR)$ in the 14 experimental watersheds in 2003.

From left to right, the five red “x” markers in each plot represent the 10th, 25th, 50th, 75th and 90th percentiles. The green line represents the mean of data.

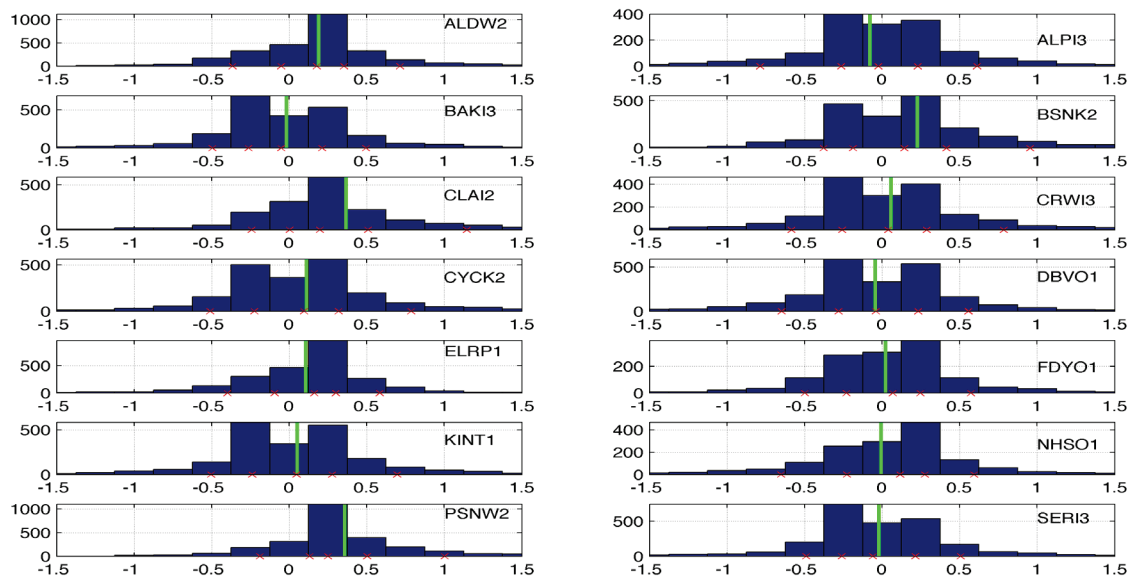


Figure 5.6 Histograms of $mean(NLDAS-2) - mean(RADAR)$ in the 14 experimental watersheds in 2004.

From left to right, the five red “x” markers in each plot represent the 10th, 25th, 50th, 75th and 90th percentiles. The green line represents the mean of data.

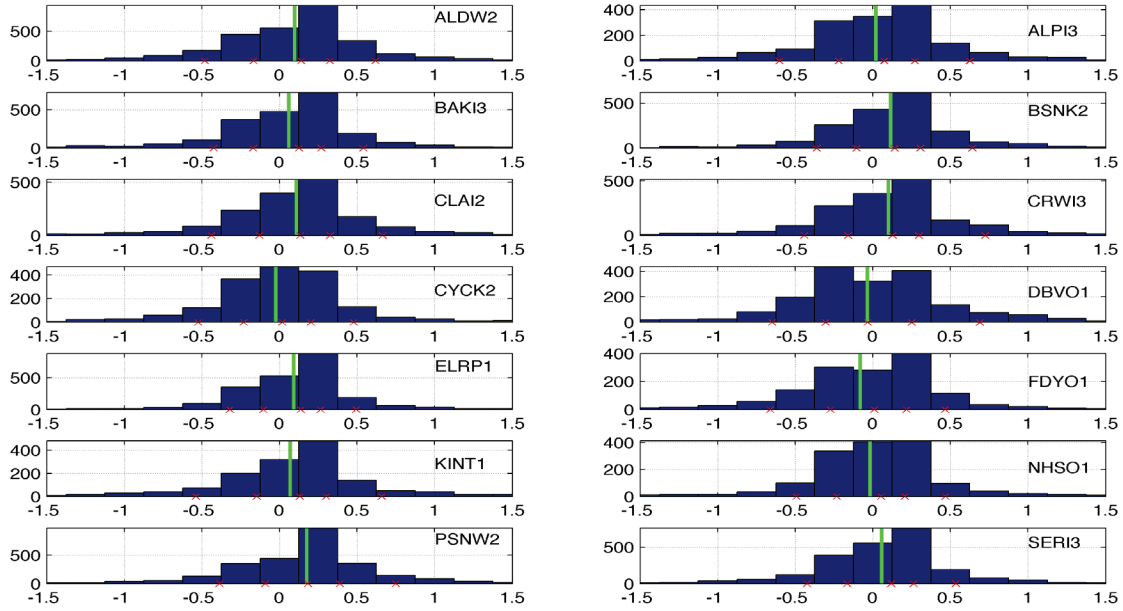


Figure 5.7 Histograms of $mean(NLDAS - 2) - mean(RADAR)$ in the 14 experimental watersheds in 2005.

From left to right, the five red “x” markers in each plot represent the 10th, 25th, 50th, 75th and 90th percentiles. The green line represents the mean of data.

5.4 SETTINGS OF PRECIPITATION DATA FUSION

As mentioned in section 5.2, $\bar{X}(0)$ is the most important parameter of the MKS algorithm. In the content of the precipitation data fusion, $\bar{X}(0)$ represents the areal mean of precipitation over the area of data fusion. Once $\bar{X}(0)$ is set, the means of fused precipitation data at all scales are equal to it. Therefore, $\bar{X}(0)$ has a decisive influence on the magnitude of fused precipitation. $\bar{X}(0)$ cannot be determined automatically using optimization algorithms or statistical inference algorithms. Instead, it can only be determined according to a user’s

judgment. There are two references for determining $\bar{X}(0)$. One is the understanding of the data to be fused. The other is the expectation of the fused precipitation data.

In this study, we have three settings for $\bar{X}(0)$. In the first setting, we set

$$\bar{X}(0) = 0.5 \times [\text{mean}(\text{NLDAS-2}) + \text{mean}(\text{RADAR})]. \quad (5-17)$$

This setting, called FUSED-1 hereafter, is based on the understanding that NLDAS-2 data and RADAR data are equally reliable in terms of the average magnitude. Fused precipitation data of this setting are expected to have the average of $\text{mean}(\text{NLDAS-2})$ and $\text{mean}(\text{RADAR})$ as mean magnitude. In the second setting, we set

$$\bar{X}(0) = \max[\text{mean}(\text{NLDAS-2}), \text{mean}(\text{RADAR})]. \quad (5-18)$$

This setting, called FUSED-2 hereafter, is based on the understanding that both NLDAS-2 data and RADAR data may underestimate precipitation. Fused precipitation data of this setting are expected to have the maximum of $\text{mean}(\text{NLDAS-2})$ and $\text{mean}(\text{RADAR})$ as mean magnitude.

In the third setting, we set

$$\bar{X}(0) = \text{mean}(\text{NLDAS-2}). \quad (5-19)$$

This setting, called FUSED-3 hereafter, is based on the understanding that NLDAS-2 data are more reliable than RADAR precipitation data. Fused precipitation data of this setting are expected to have the same mean magnitude as NLDAS-2 data.

In the settings FUSED-1 and FUSED-2, both the spatial pattern and the magnitude of NLDAS-2 and RADAR data will contribute to the fused precipitation data. However, in the setting FUSED-3, RADAR data only contribute spatial pattern to the fused precipitation data.

Because RADAR data are at a much finer resolution than that of NLDAS-2 data, RADAR data, therefore, will play much more significant roles in determining the spatial pattern of the fused precipitation data than NLDAS-2 data.

In the precipitation data fusion with the MKS algorithm, fused data can be at all scales of the multiscale tree built for the input data. For example, when doing data fusion in SERI3 site (a square envelope of SERI3 watershed with the size of $2^{\circ} \times 2^{\circ}$), there are 7 scales of the multiscale tree ranging from 0 to 6. NLDAS-2 data and RADAR data are at scale 4 and scale 6 of the multiscale tree respectively. The fused precipitation data can be at 1/32, 1/16, 1/8, 1/4, 1/2, 1, and 2 degree resolutions. In this study, we just output fused precipitation data at 1/8 and 1/32 degree resolutions for the assessments with hydrological simulations. The fused data at 1/8 degree resolution can be regarded as the improved version of NLDAS-2 data by incorporating information in RADAR data at 1/32 degree resolution. Similarly, the fused data at 1/32 degree resolution can be regarded as the improved version of RADAR data by incorporating information in NLDAS-2 data at 1/8 degree resolution.

5.5 ASSESSMENT OF FUSED PRECIPITATION DATA

5.5.1 Assessment with streamflow simulations

Streamflow is the most important hydrological forecast. If fused precipitation data can improve the accuracy of simulated streamflow, hydrological forecast will be improved, too. In addition, streamflow observations are much more reliable than the observations of soil moisture

and evapotranspiration. Therefore, this study first assesses precipitation data fusion based on streamflow.

The assessment is conducted by comparing simulated streamflows with the three fused precipitation datasets (FUSED-1, FUSED-2 and FUSED-3) and two input precipitation datasets (NLDAS-2 and RADAR). Without special note, the streamflow simulated with the fused precipitation data of setting FUSED-1 are abbreviated as FUSED-1 in later analysis, and similarly for FUSED-2, FUSED-3, NLDAS-2 and RADAR. Streamflows are simulated using Noah LSM at 1/8 degree resolution. The flow routing scheme described in chapter 2.0 is used to route the surface runoff and baseflow simulated by Noah LSM into streamflow series at the outlet of watershed. For the 14 experimental watershed, DEM data, 1/8 degree computational grids, and flow networks are given in Figure 5.8 to Figure 5.21. As the input parameter information of Noah model, hybrid STATSGO/FAO topsoil texture data and USGS 24-category vegetation (land use) data have been processed into 1/8 degree resolution from 30-second resolution using majority resampling method. The maps of soil types and land use types of the 14 watersheds are also given in Figure 5.8 to Figure 5.21. Parameters of Noah LSM and its routing scheme are calibrated simultaneously with NLDAS-2, RADAR, FUSED-1, FUSED-2 and FUSED-3 precipitation data using the parameter calibration scheme described in chapter 3.0 . The parameter calibration period is from 01/01/2003 to 12/31/2005 while Noah LSM runs from 01/01/2000. The three years of 2000, 2001 and 2002 are the spin-up period for Noah LSM to remove the influences of initial conditions. Only one set of parameters is calibrated for the five precipitation inputs. In the assessment, this set of parameters will work with the five precipitation

inputs to simulate streamflow series. In order to simply focus on the influences of precipitation input on simulated streamflow, assessment is conducted in the calibration period (2003-2005).

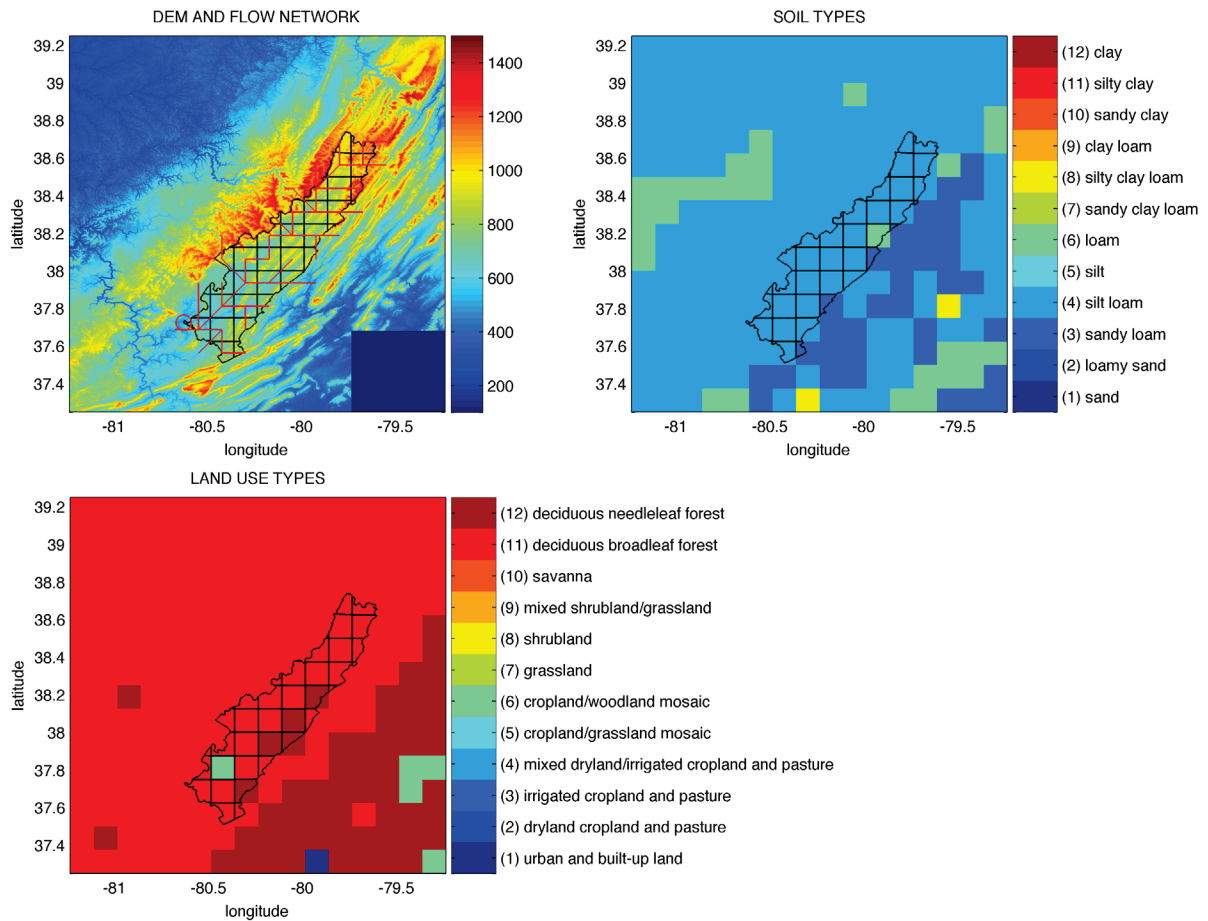


Figure 5.8 DEM, flow network, soil types, and land use types in ALDW2 site. Except DEM is at 1/2048 degree resolution, all other data are at 1/8 degree resolution. Gridded region is the ALDW2 watershed, whose outlet is marked with the red circle.

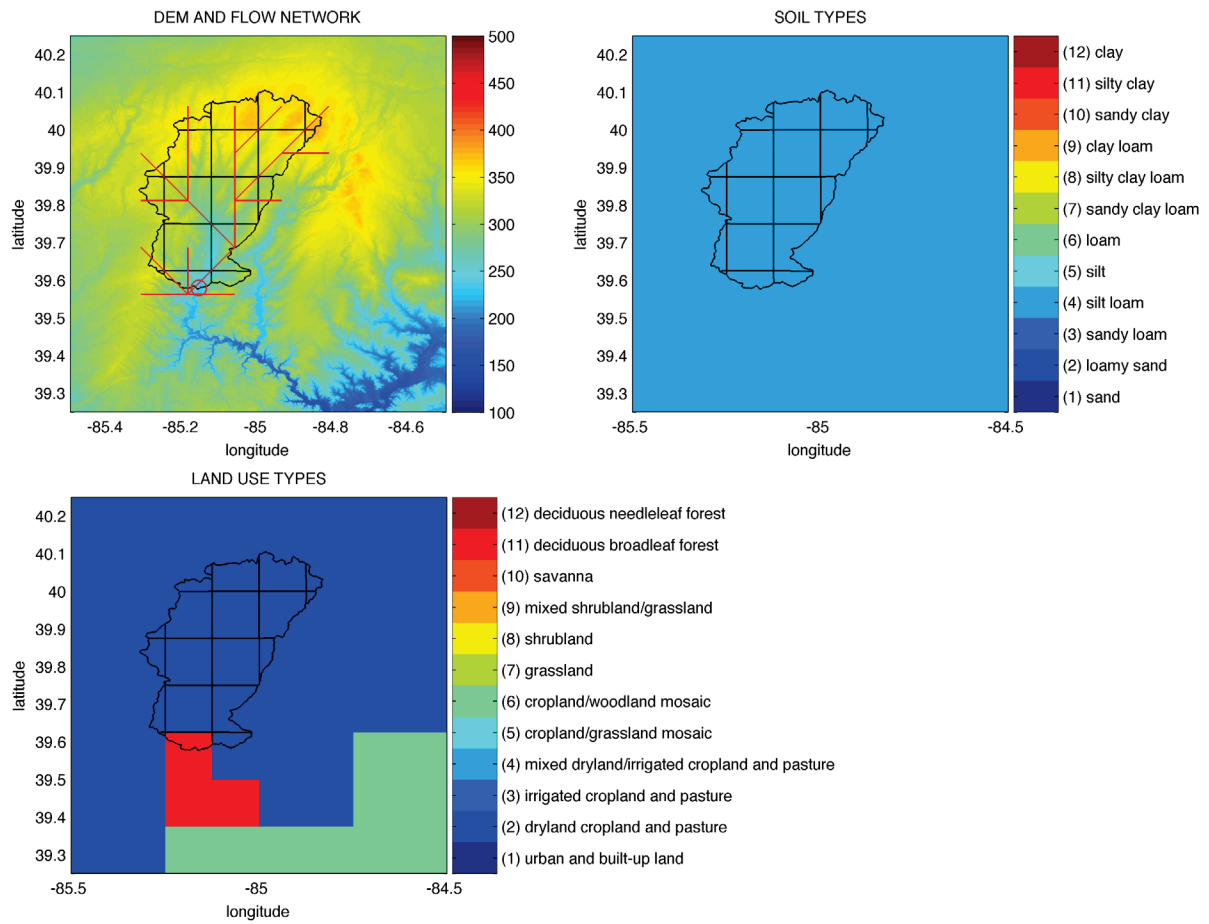


Figure 5.9 DEM, flow network, soil types, and land use types in ALPI3 site. Except DEM is at 1/2048 degree resolution, all other data are at 1/8 degree resolution. Gridded region is the ALPI3 watershed, whose outlet is marked with the red circle.

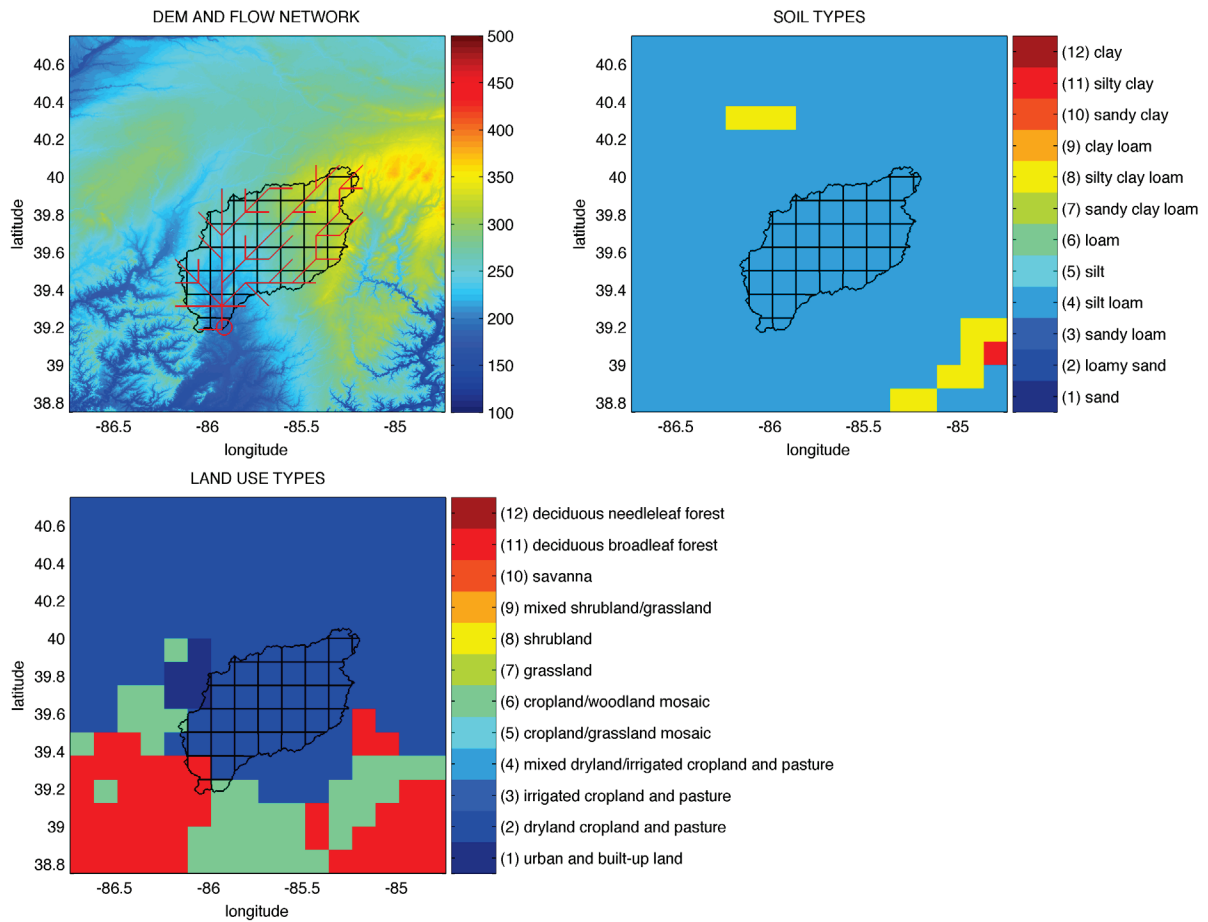


Figure 5.10 DEM, flow network, soil types, and land use types in BAKI3 site. Except DEM is at 1/2048 degree resolution, all other data are at 1/8 degree resolution. Gridded region is the BAKI3 watershed, whose outlet is marked with the red circle.

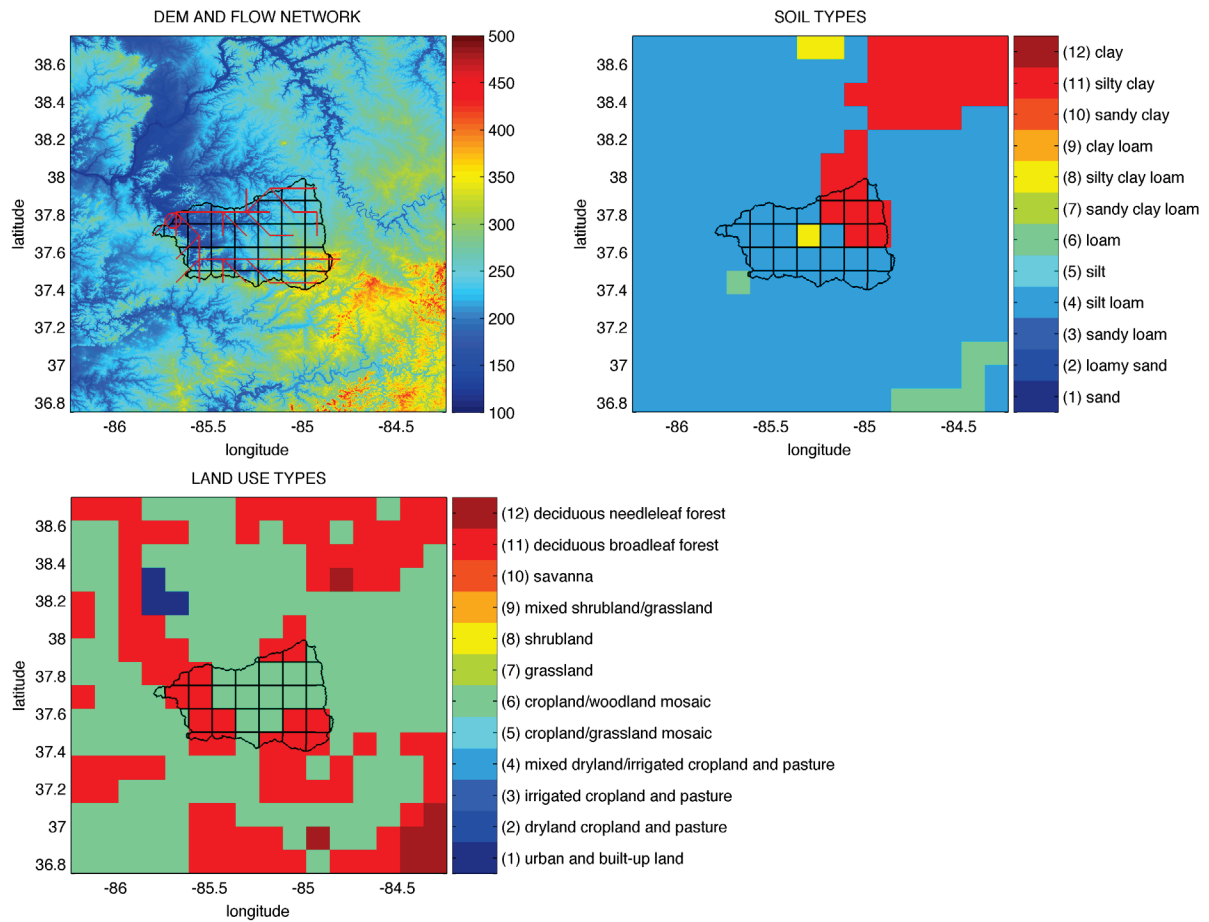


Figure 5.11 DEM, flow network, soil types, and land use types in BSNK2 site. Except DEM is at 1/2048 degree resolution, all other data are at 1/8 degree resolution. Gridded region is the BSNK2 watershed, whose outlet is marked with the red circle.

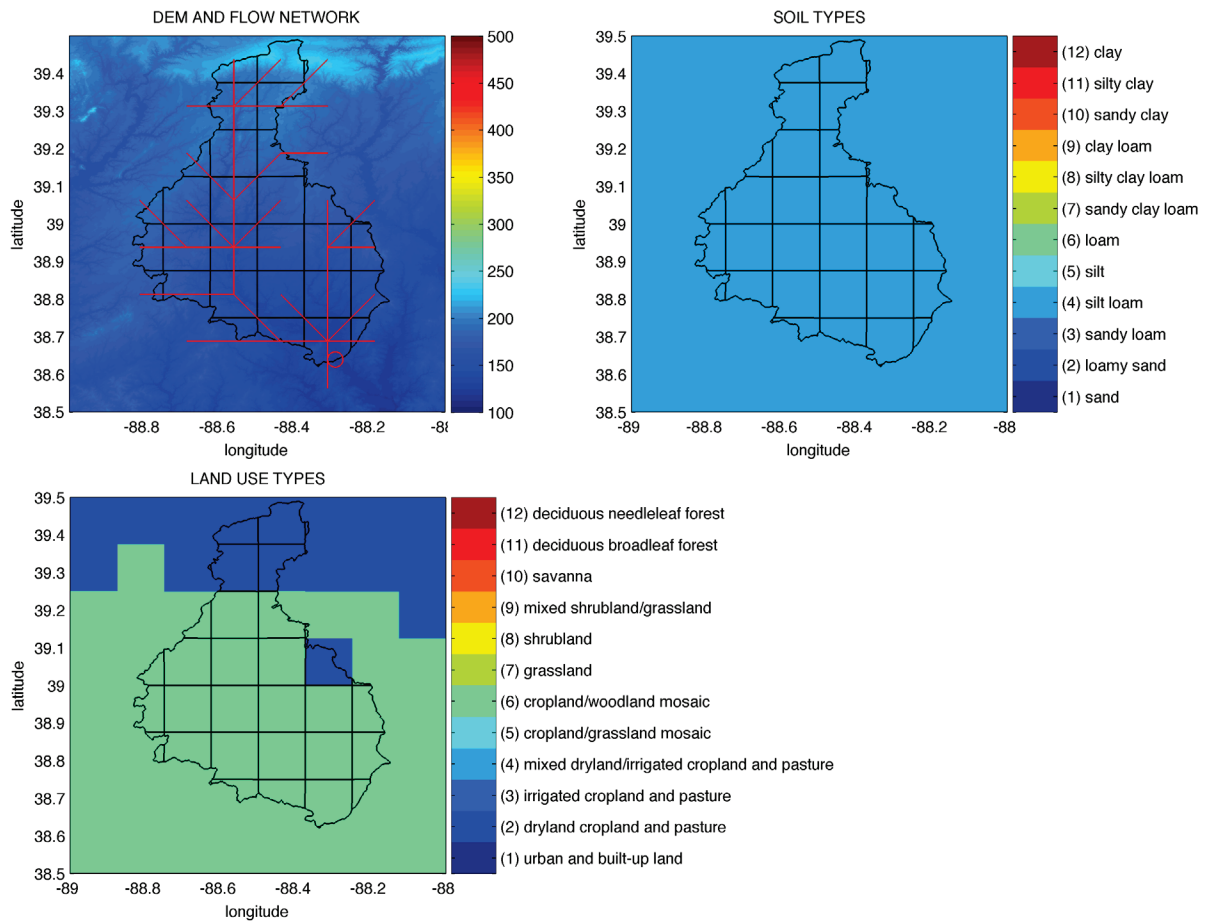


Figure 5.12 DEM, flow network, soil types, and land use types in CLAI2 site. Except DEM is at 1/2048 degree resolution, all other data are at 1/8 degree resolution. Gridded region is the CLAI2 watershed, whose outlet is marked with the red circle.

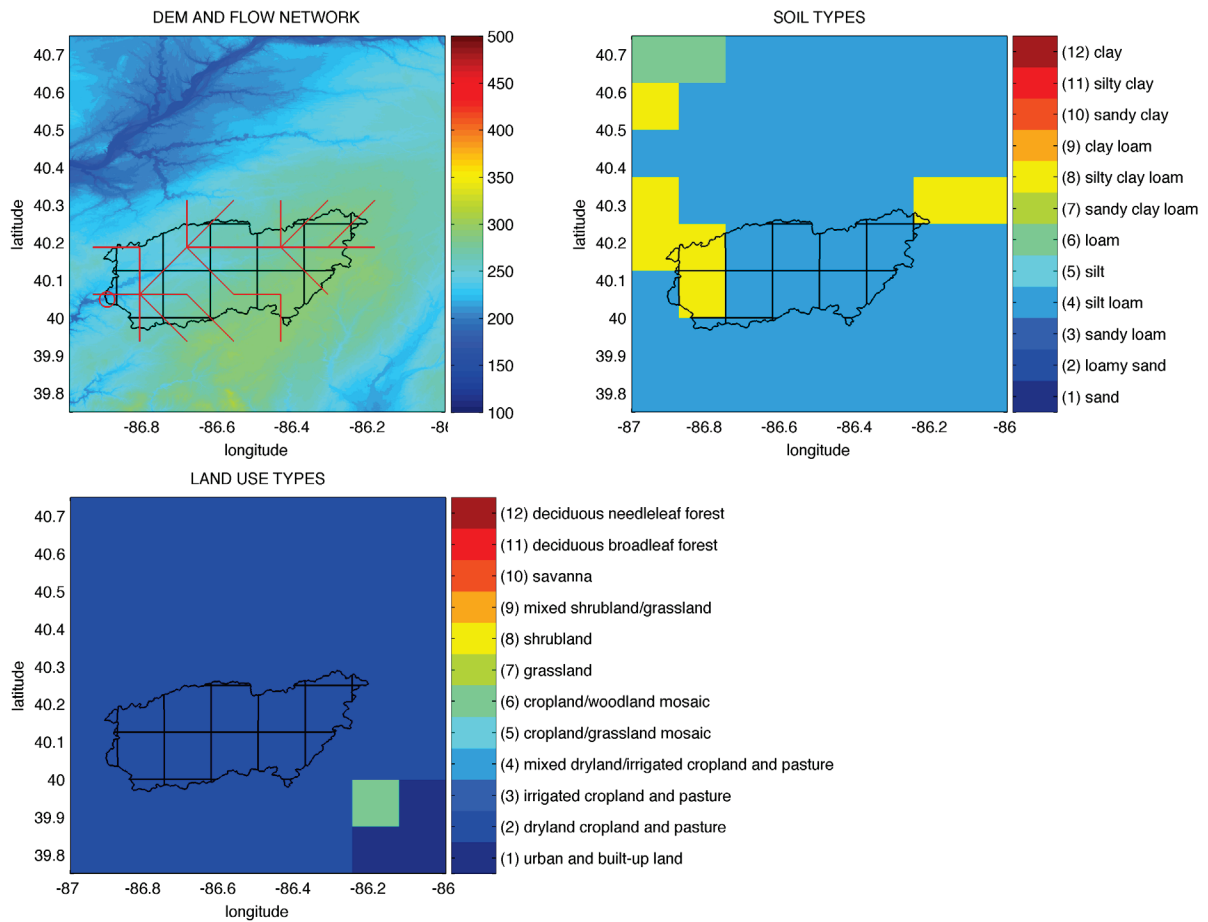


Figure 5.13 DEM, flow network, soil types, and land use types in CRWI3 site. Except DEM is at 1/2048 degree resolution, all other data are at 1/8 degree resolution. Gridded region is the CRWI3 watershed, whose outlet is marked with the red circle.

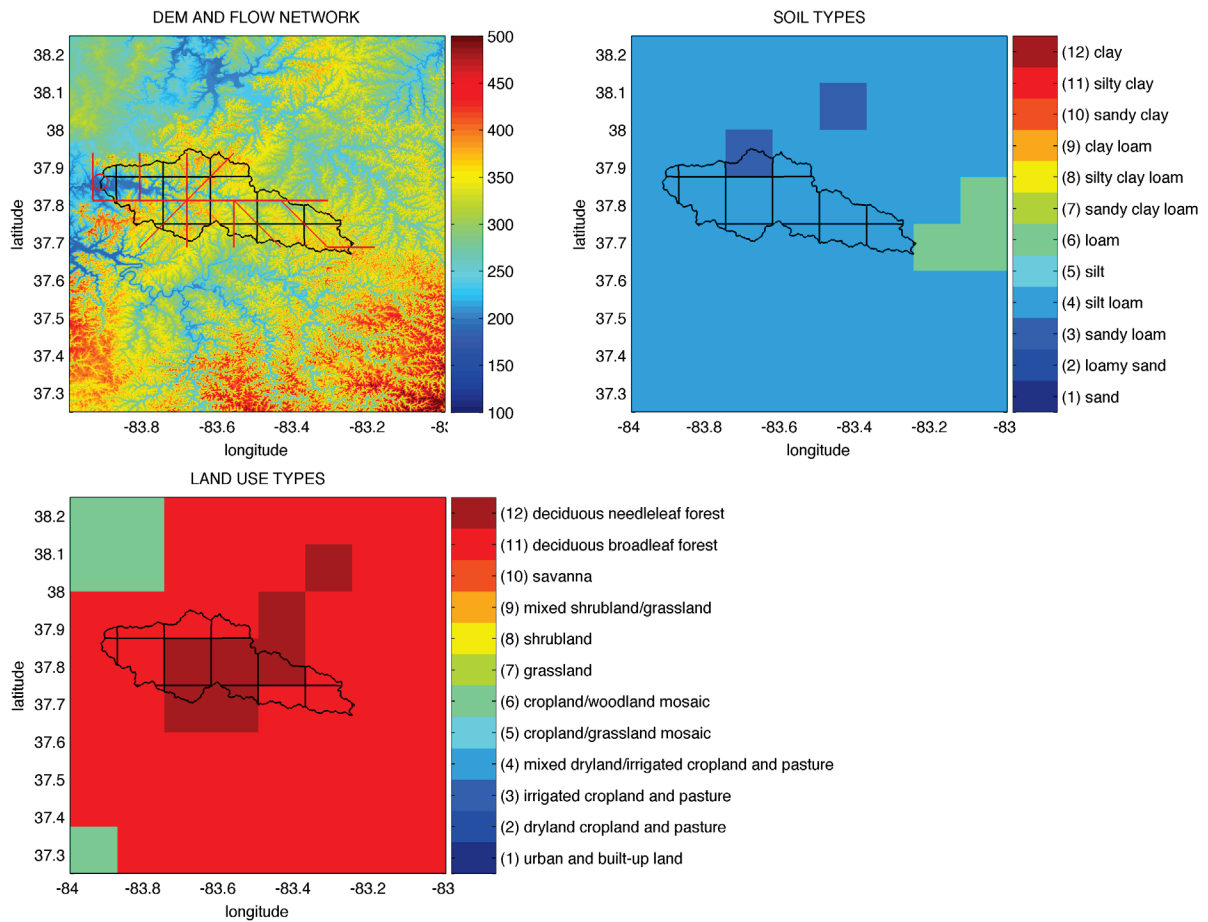


Figure 5.14 DEM, flow network, soil types, and land use types in CYCK2 site. Except DEM is at 1/2048 degree resolution, all other data are at 1/8 degree resolution. Gridded region is the CYCK2 watershed, whose outlet is marked with the red circle.

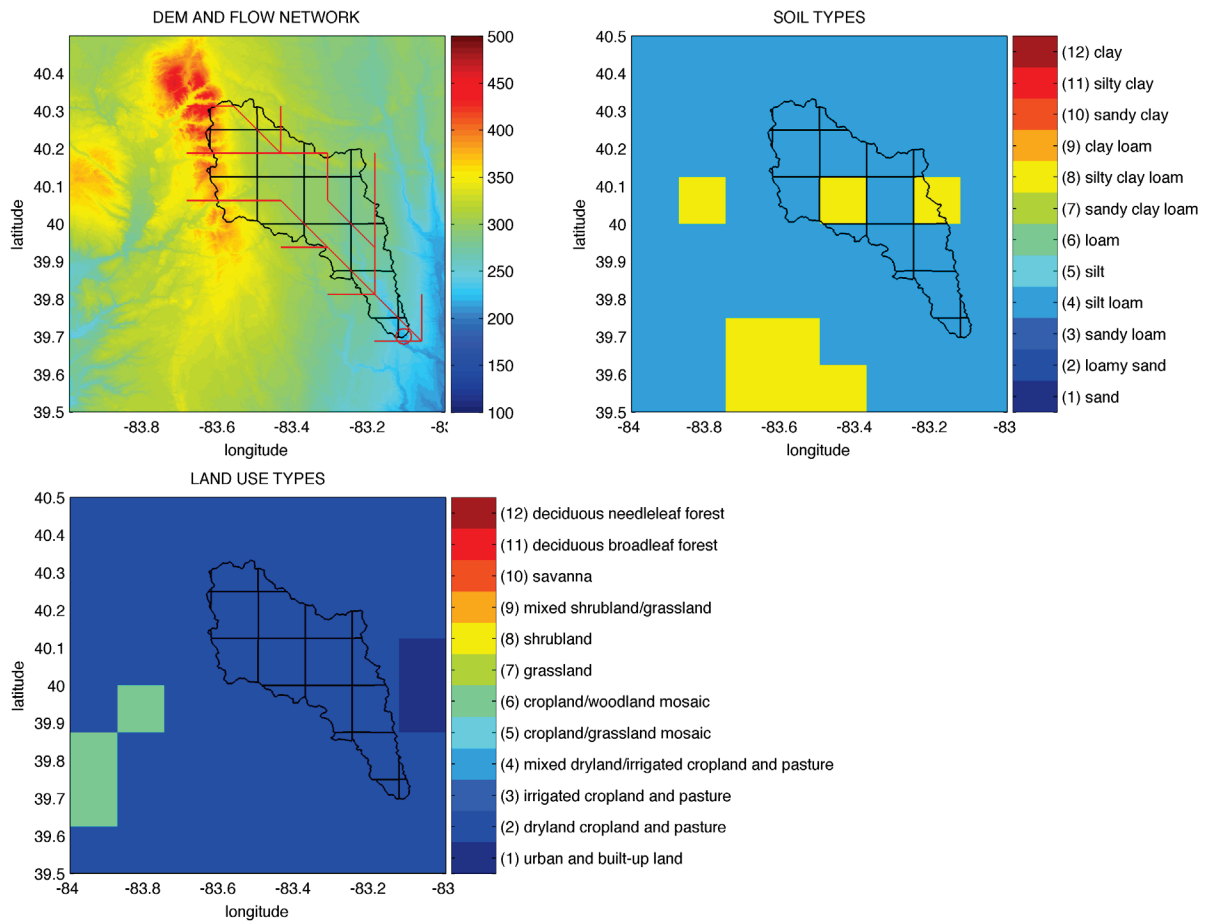


Figure 5.15 DEM, flow network, soil types, and land use types in DBVO1 site. Except DEM is at 1/2048 degree resolution, all other data are at 1/8 degree resolution. Gridded region is the DBVO1 watershed, whose outlet is marked with the red circle.

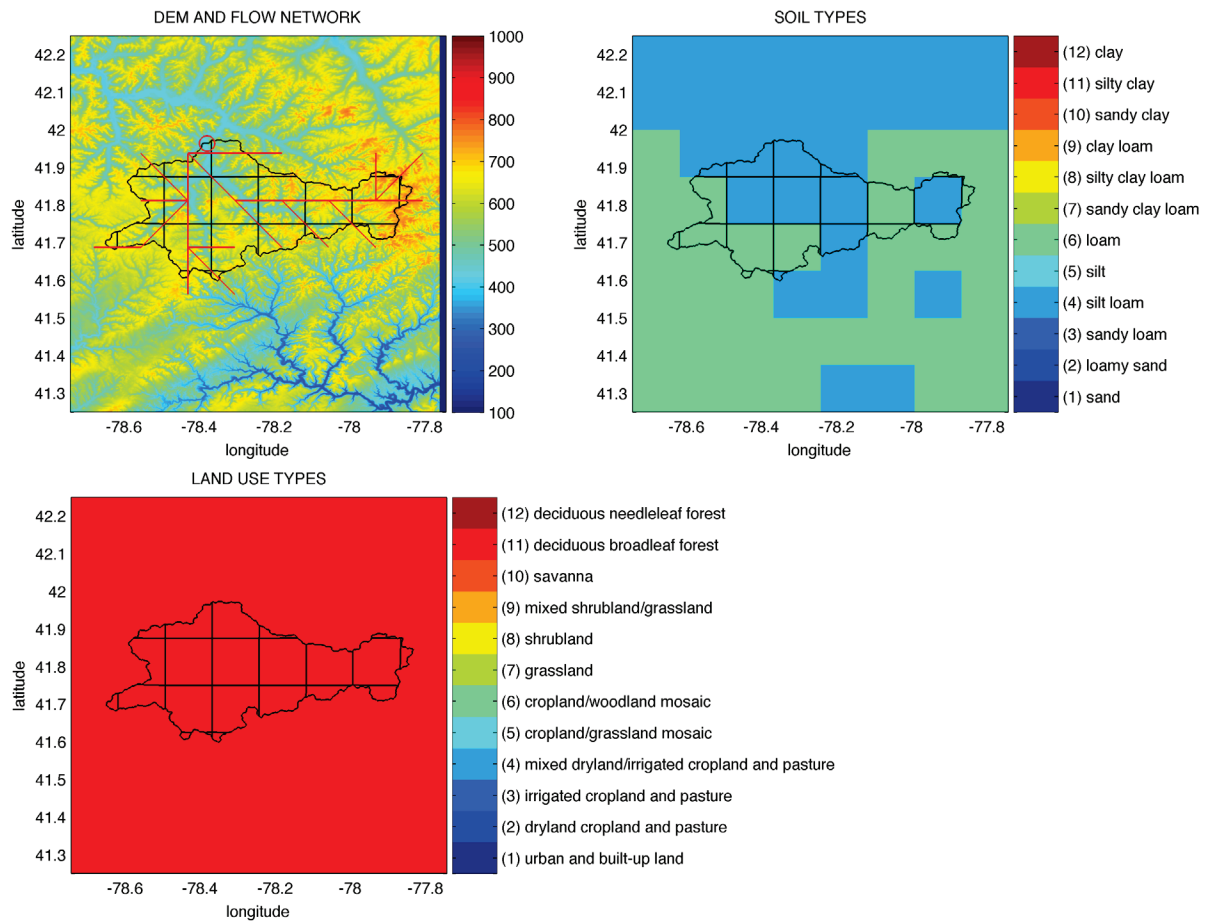


Figure 5.16 DEM, flow network, soil types, and land use types in ELRP1 site. Except DEM is at 1/2048 degree resolution, all other data are at 1/8 degree resolution. Gridded region is the ELRP1 watershed, whose outlet is marked with the red circle.

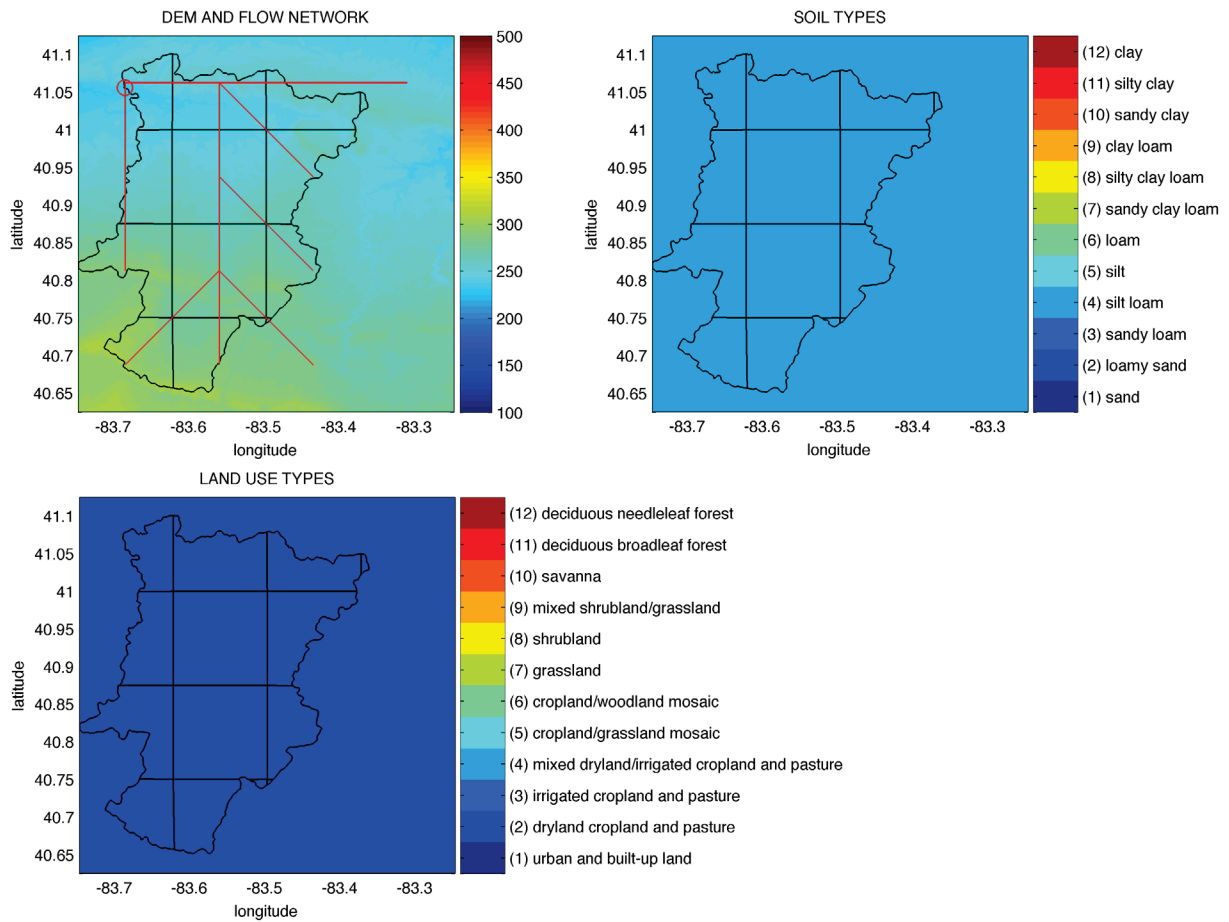


Figure 5.17 DEM, flow network, soil types, and land use types in FDYO1 site. Except DEM is at 1/2048 degree resolution, all other data are at 1/8 degree resolution. Gridded region is the FDYO1 watershed, whose outlet is marked with the red circle.

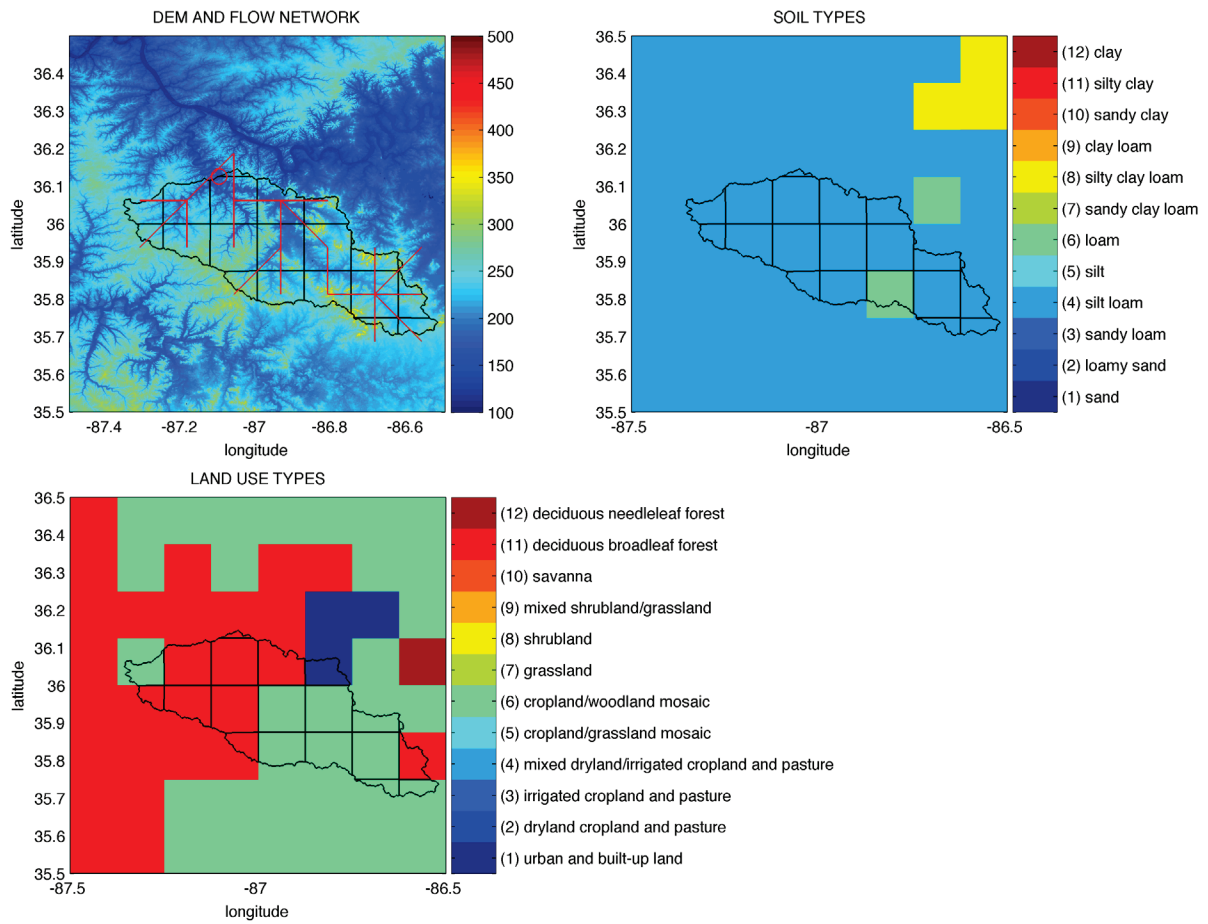


Figure 5.18 DEM, flow network, soil types, and land use types in KINT1 site. Except DEM is at 1/2048 degree resolution, all other data are at 1/8 degree resolution. Gridded region is the KINT1 watershed, whose outlet is marked with the red circle.

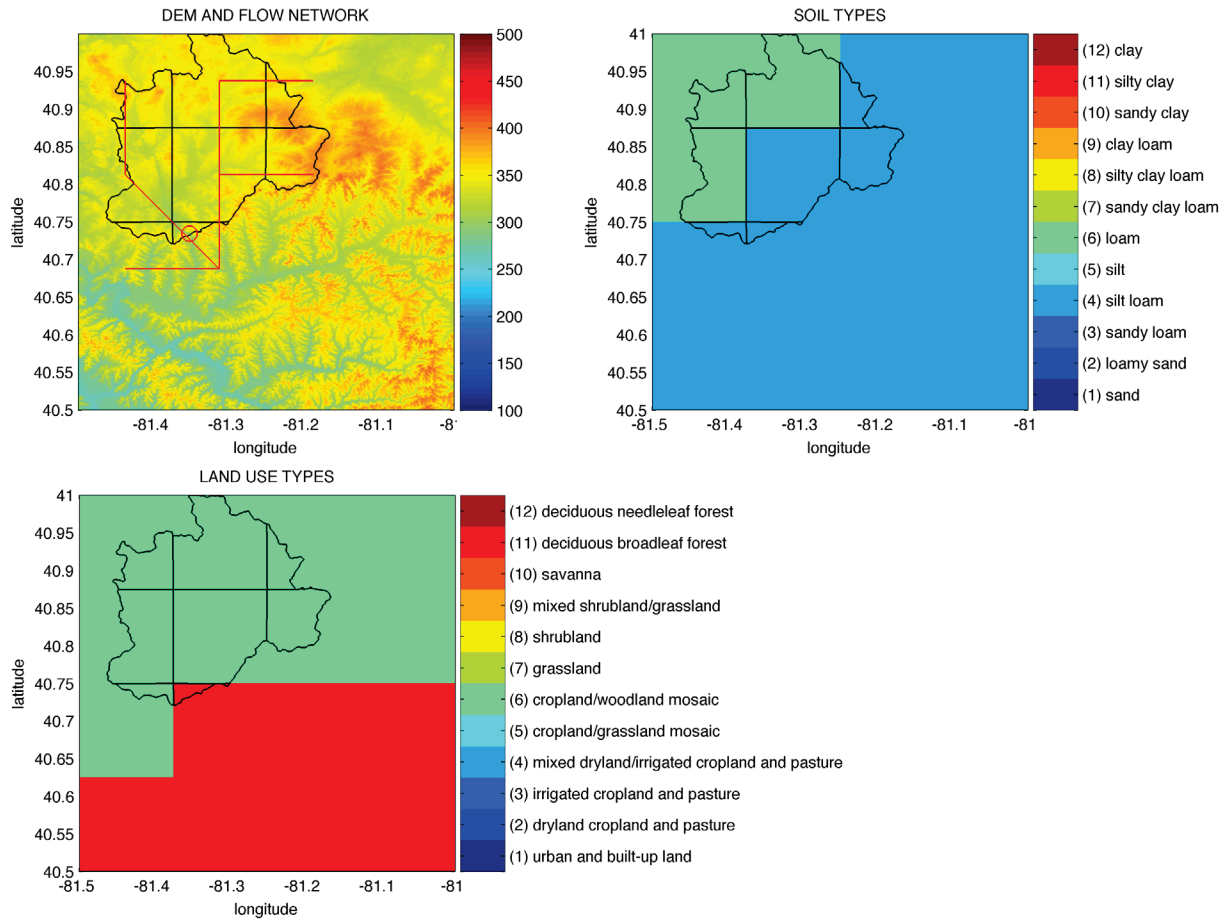


Figure 5.19 DEM, flow network, soil types, and land use types in NHSO1 site. Except DEM is at 1/2048 degree resolution, all other data are at 1/8 degree resolution. Gridded region is the NHSO1 watershed, whose outlet is marked with the red circle.

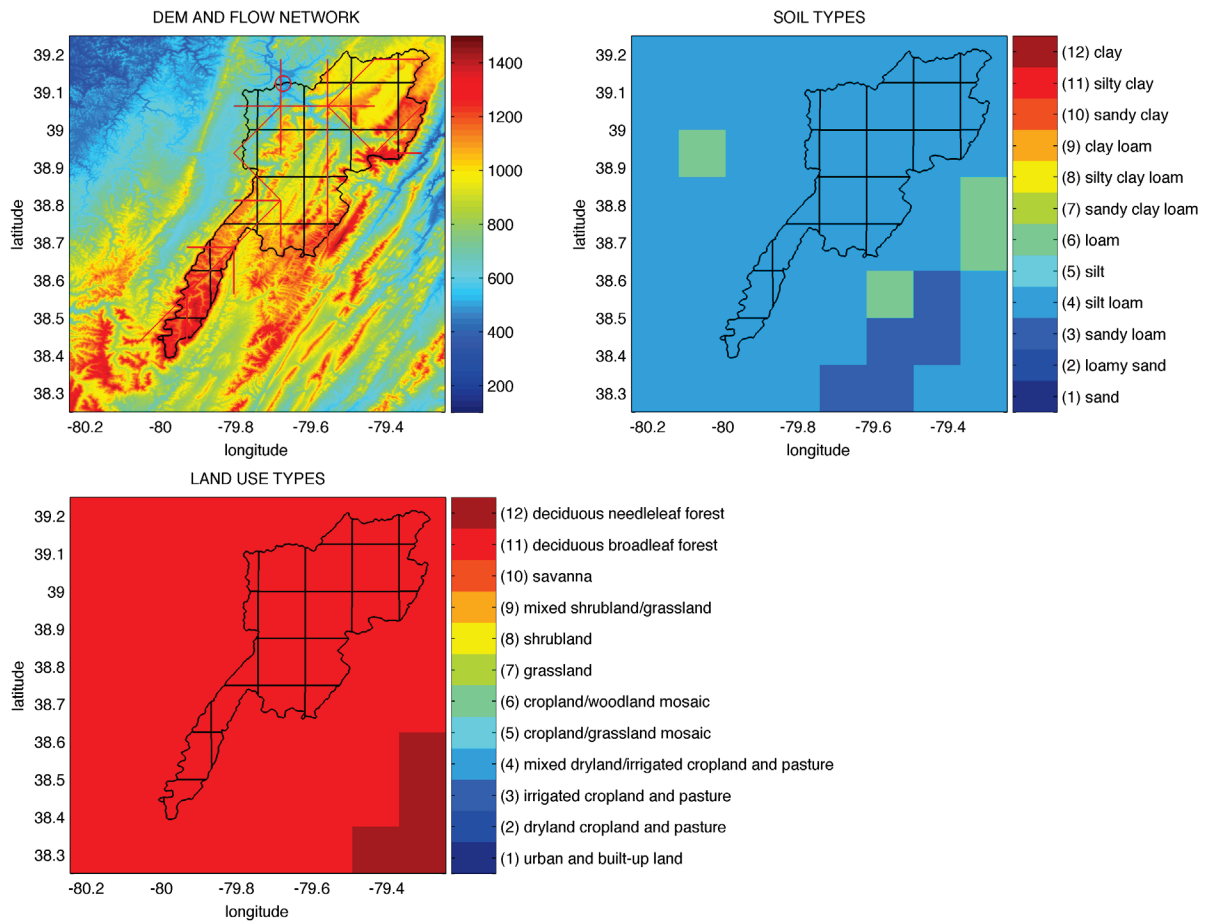


Figure 5.20 DEM, flow network, soil types, and land use types in PSNW2 site. Except DEM is at 1/2048 degree resolution, all other data are at 1/8 degree resolution. Gridded region is the PSNW2 watershed, whose outlet is marked with the red circle.

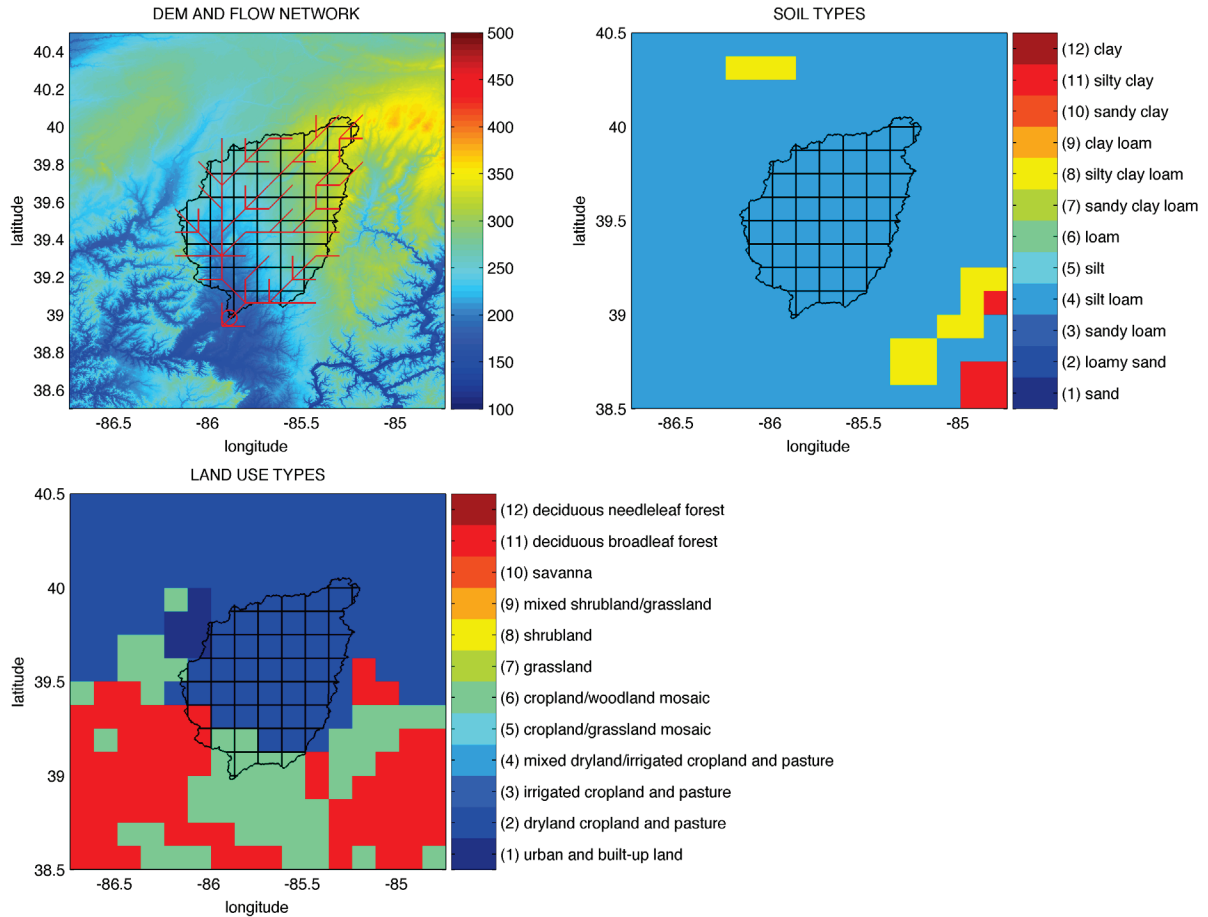


Figure 5.21 DEM, flow network, soil types, and land use types in SERI3 site. Except DEM is at 1/2048 degree resolution, all other data are at 1/8 degree resolution. Gridded region is the SERI3 watershed, whose outlet is marked with the red circle.

The assessment in terms of streamflow simulation is discussed below by watersheds. Hydrographs and Nash-Sutcliffe Efficiency (NSE) are used as the standards to evaluate the reliability of precipitation inputs. NSE can range from $-\infty$ to 1. An NSE of 1 corresponds a perfect match of the simulated streamflow to the observed streamflow. An NSE of 0 indicates that the model simulation is as accurate as the mean of the observed streamflow, whereas an NSE less than 0 occurs when the mean of observed streamflow is a better predictor than simulated streamflow. Therefore, it is expected that the streamflow simulated with fused

precipitation data has larger NSE than that of streamflow simulated with NLDAS-2 or RADAR precipitation data. In the following, the assessments of precipitation data fusion are conducted in terms of simulated streamflow by watershed.

Table 5.1 Areas, elevation ranges and descriptions of the 14 experimental watersheds

NAME	AREA (km ²)	MIN_E (m)	MAX_E (m)	TOPOGRAPHY	USGS station name
ALDW2	3533	469	1478	steep	Greenbrier River at Alderson, WV
ALPI3	1352	232	381	mild	Whitewater River near Alpine, IN
BAKI3	4421	182	363	mild	East fork White River at Columbus, IN
BSNK2	3364	127	447	relatively steep	Rolling Fork near Boston, KY
CLAI2	2929	124	237	flat	Little Wabash River below Clay city, IL
CRWI3	1318	202	298	flat	Sugar Creek at Crawfordsville, IN
CYCK2	938	189	444	relatively steep	Red River at Clay city, KY
DBVO1	1383	219	454	mild	Big Darby Creek at Darbyville, OH
ELRP1	1424	433	788	steep	Allegheny River at Eldred, PA
FDYO1	896	231	315	flat	Blanchard River near Findlay, OH
KINT1	1764	146	390	relatively steep	Harpeth River near Kingston Springs, TN
NHSO1	453	298	403	mild	Nimishillen Creek at North Industry, OH
PSNW2	1870	488	1477	very steep	Cheat River near Parsons, WV
SERI3	6063	170	363	mild	East fork White River near Seymour, IN

ALDW2 watershed. ALDW2 is a mountainous watershed in West Virginia with steep topography. The hydrographs of the observed and the five simulated streamflow series are plotted in Figure 5.22 by years and corresponding NSEs are listed in Table 5.2. Findings in ALDW2 watershed include:

- 1) FUSED-2 data have best performances in 2003, 2004, and 2005. This indicates that both NLDAS-2 and RADAR data underestimate precipitation in these years. As shown in Figure 5.22, the peaks simulated with NLDAS-2 data and RADAR data are below the observed peaks. Even the peaks simulated with FUSED-2 data may slightly above the observed peaks sometimes; but the hydrographs of FUSED-2 data fit the observed hydrographs much better than those of other precipitation data. This means that the average magnitude of the two input precipitation data makes positive contribution to the fused precipitation data.
- 2) FUSED-3 data have better performances than NLDAS-2 data since FUSED-3 data keeps the mean magnitudes of NLDAS-2 data. The difference between these two data is that the spatial patterns of RADAR data have been fused into FUSED-3 data. This finding indicates that the spatial patterns of RADAR data make some positive contribution to the fused precipitation data. Even though the NSEs of RADAR data are significantly smaller than the corresponding ones of NLDAS-2 data, the spatial patterns of RADAR data (at 1/32 degree resolution) are still valuable for precipitation data fusion.
- 3) FUSED-1 data have poorer performances than NLDAS-2 data because the average magnitudes of RADAR data have been introduced into FUSED-1 data. This finding indicates that the fused precipitation data may have poor reliability than input data if the areal mean of precipitation ($\bar{X}(0)$) is not properly estimated. In addition, spatial pattern takes the second place in influencing the streamflow simulation compared with the average magnitudes of precipitation in ALDW2 watershed.
- 4) In the snowing season of ALDW2 watershed, i.e. December to May, simulations of flow peaks are poor for the five precipitation inputs. A possible reason is that Noah LSM doesn't describe snow accumulation and melting processes well.

5) Overall, streamflow simulation can be substantially improved using fused precipitation data, such as FUSED-2.

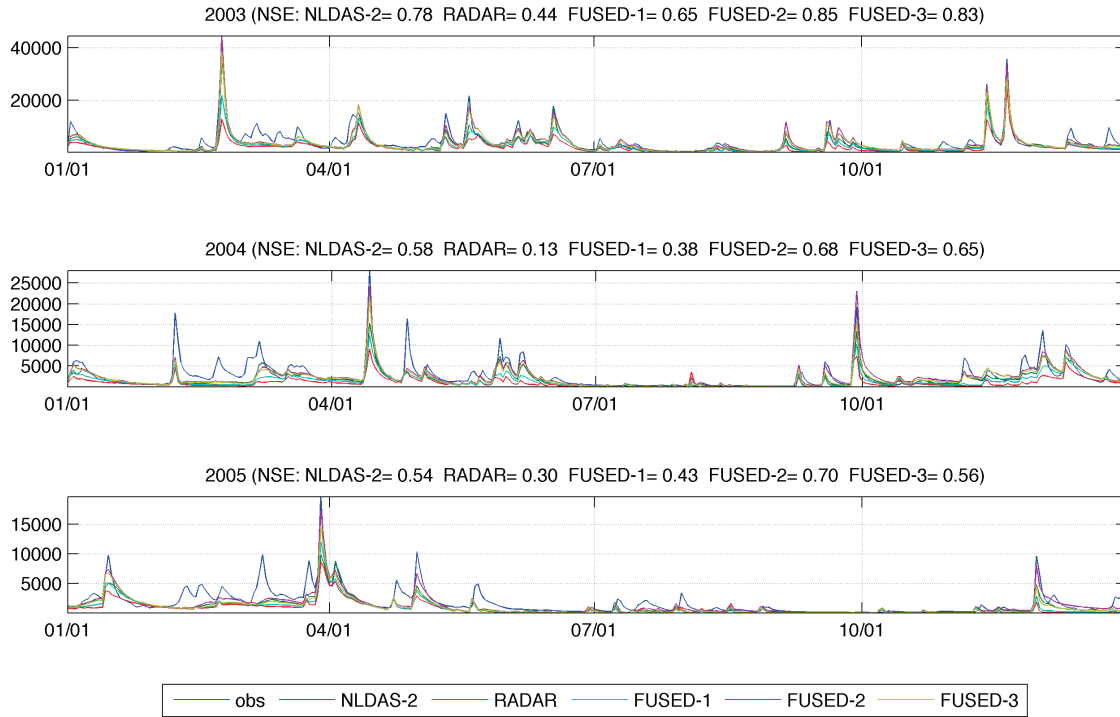


Figure 5.22 Observed streamflow and simulated streamflow with NLDAS-2, RADAR, FUSED-1, FUSED-2 and FUSED-3 precipitation data in calibration period (2003, 2004 and 2005) in ALDW2 watershed. The unit of streamflow is cubic feet per second (cft/s). Corresponding Nash-Sutcliffe Efficiencies (NSE) are given in the titles of plots.

Table 5.2 Nash-Sutcliffe Efficiencies (NSEs) corresponding to the five precipitation inputs in ALDS2 watershed

	NLDAS-2	RADAR	FUSED-1	FUSED-2	FUSED-3
2003	0.776	0.440	0.650	0.849	0.826
2004	0.582	0.131	0.378	0.680	0.650
2005	0.543	0.300	0.433	0.698	0.557

ALPI3 watershed. ALPI3 is a watershed in Indiana with mild topography. The hydrographs of the observed and the five simulated streamflow series are plotted in Figure 5.23 by years and the corresponding NSEs are listed in Table 5.3. Findings in ALPI3 watershed include:

- 1) FUSED-2 data have best performances in 2003, 2004 and 2005. This means that both NLDAS-2 and RADAR data have chances of underestimating precipitation. From the hydrographs in Figure 5.23, we can also have the same finding. For the three years, the peaks of streamflow simulated with NLDAS-2 and RADAR data are below the observed peaks. Even though the hydrographs of FUSED-2 may be slightly above the observed peaks, they have much better fit to the observed hydrographs than those of NLDAS-2 and RADAR data, especially in 2004 and 2005.
- 2) In 2003, the reliability of NLDAS-2 data is very poor, i.e. $NSE=0.366$ and the reliability of RADAR data is a little bit better, i.e. $NSE=0.492$, while the NSE of FUSED-2 data is 0.562, which is almost over 0.2 than that of NLDAS-2 data. In 2005, the NSEs of NLDAS-2 and RADAR data are 0.504 and 0.559 respectively, while the NSE of FUSED-2 data is 0.833, which is over 0.3 than that of NLDAS-2 data. These results indicate that even the RADAR data have poor reliability; they also can be used to improve NLDAS-2 data through data fusion.
- 3) FUSED-3 data have NSEs slightly larger than the corresponding ones of NLDAS-2 in the three years. This spatial pattern of RADAR data doesn't help much to improve the reliability of NLDAS-2 data through data fusion in ALPI3 watershed.

- 4) In the March and April of 2003, poor streamflow simulations with the five precipitation inputs may be because Noah LSM doesn't describe snow accumulation and melting processes well.
- 5) Overall, streamflow simulation can be improved significantly in ALPI3 watershed, especially for 2003 and 2005.

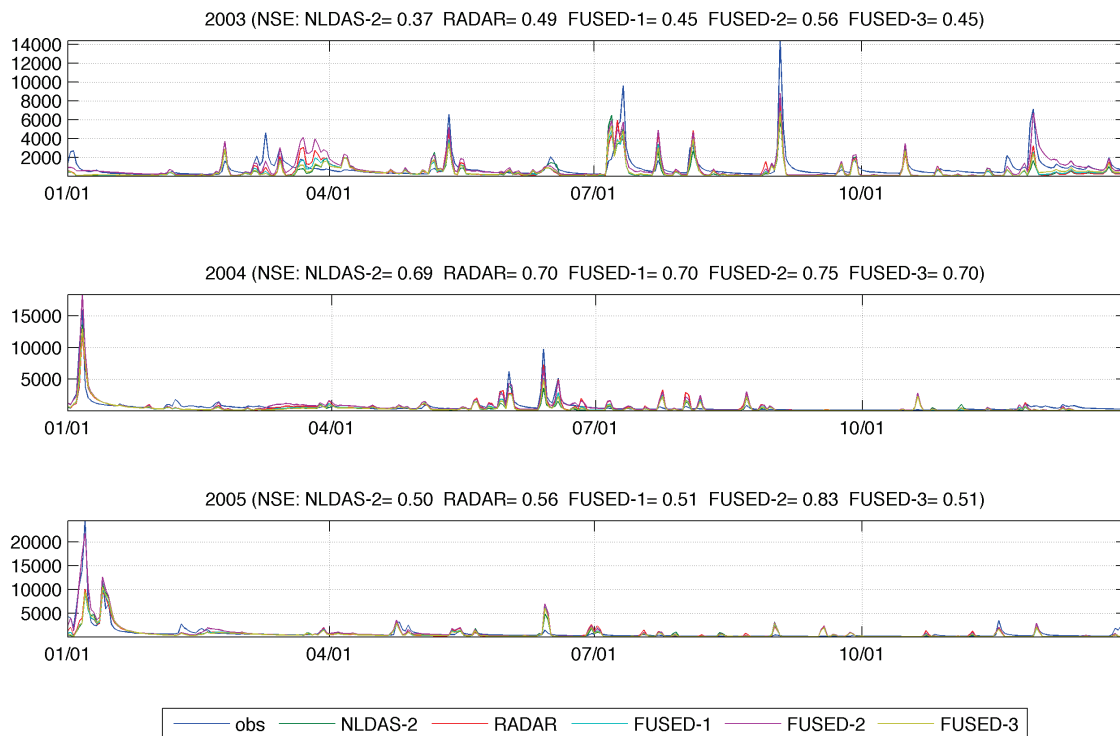


Figure 5.23 Observed streamflow and simulated streamflow with NLDAS-2, RADAR, FUSED-1, FUSED-2 and FUSED-3 precipitation data in calibration period (2003, 2004 and 2005) in ALPI3 watershed. The unit of streamflow is cubic feet per second (cft/s). Corresponding Nash-Sutcliffe Efficiencies (NSE) are given in the titles of plots.

Table 5.3 Nash-Sutcliffe Efficiencies (NSEs) corresponding to the five precipitation inputs in ALPI2 watershed

	NLDAS-2	RADAR	FUSED-1	FUSED-2	FUSED-3
2003	0.366	0.493	0.455	0.562	0.455
2004	0.695	0.696	0.702	0.755	0.703
2005	0.504	0.559	0.507	0.833	0.511

BAKI3 watershed. BAKI3 is a watershed in Indiana with mild topography. The hydrographs of the observed and the five simulated streamflows are plotted in Figure 5.24 by years and the corresponding NSEs are listed in Table 5.4. Findings in BAKI3 watershed are:

- 1) In 2003, both NLDAS-2 and RADAR data have poor reliability. NSEs of all fused precipitation data are smaller than the NSE of NLDAS-2 data, which means that it is possible that RADAR data deteriorate NLDAS-2 data through precipitation data fusion if RADAR data are poor. It can be seen from the observed and simulated hydrographs in 2003 that the simulated hydrographs are even worse in cold season than those in warm season. Therefore, there are two possible reasons for the poor simulations of streamflow in 2003. One is that there were more precipitation events in the cold season of 2003 and both NLDAS-2 and RADAR data didn't well record these events. The other reason is that Noah LSM didn't properly describe snow accumulation and melting processes in the cold season. The second reason is more possible because the peak of simulated streamflow is behind the peak of the observed streamflow. This timing difference may indicate that the snow melting process simulated by Noah LSM is slower than the real process in March and April of 2003.

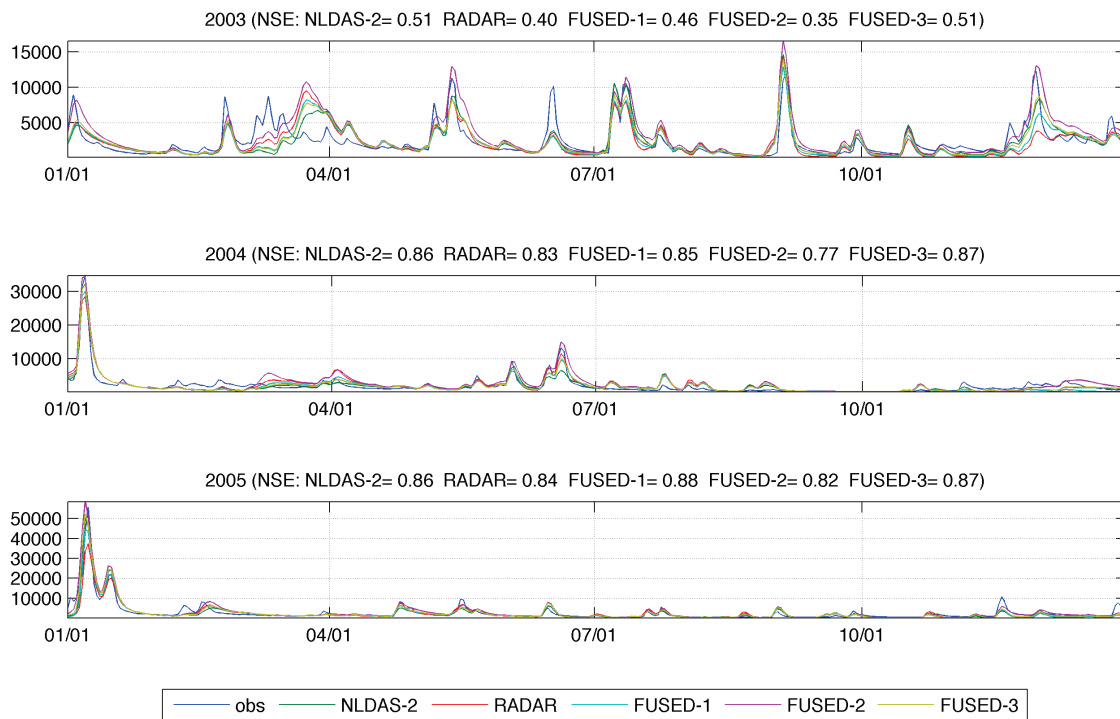


Figure 5.24 Observed streamflow and simulated streamflow with NLDAS-2, RADAR, FUSED-1, FUSED-2 and FUSED-3 precipitation data in calibration period (2003, 2004 and 2005) in BAKI3 watershed. The unit of streamflow is cubic feet per second (cft/s). Corresponding Nash-Sutcliffe Efficiencies (NSE) are given in the titles of plots.

Table 5.4 Nash-Sutcliffe Efficiencies (NSEs) corresponding to the five precipitation inputs in BAKI3 watershed

	NLDAS-2	RADAR	FUSED-1	FUSED-2	FUSED-3
2003	0.513	0.401	0.461	0.352	0.510
2004	0.857	0.827	0.854	0.775	0.875
2005	0.864	0.837	0.877	0.822	0.866

- 2) In 2004, both NLDAS-2 and RADAR data have good reliability, i.e. NSE=0.857 and 0.827 respectively. As Figure 5.24 shows, the hydrographs of simulated streamflows with NLDAS-2 and RADAR data have good fits to the hydrographs of observed streamflow. The NSE of FUSED-3 data is slightly larger than that of NLDAS-2 data, which reflects the minor contribution from the spatial patterns of RADAR data at 1/32 degree resolution.
- 3) In 2005, both NLDAS-2 and RADAR data have good reliability, i.e. NSE=0.864 and NSE=0.837. The NSE of FUSED-1 data is slightly higher than that of NLDAS-2 data, which indicates that the real average magnitude of precipitation falls between those of NLDAS-2 and RADAR data.
- 4) Overall, no essential improvements of streamflow simulations have been made through precipitation data fusion. For year 2003, it is because both NLDAS-2 data and RADAR data have poor reliabilities; for year 2004 and 2005, it is because both NLDAS-2 data already have good reliability and there is no big room for further improvement.

Table 5.5 Nash-Sutcliffe Efficiencies (NSEs) corresponding to the five precipitation inputs in BSNK2 watershed

	NLDAS-2	RADAR	FUSED-1	FUSED-2	FUSED-3
2003	0.717	0.588	0.656	0.745	0.735
2004	0.813	0.410	0.634	0.813	0.753
2005	0.776	0.712	0.779	0.834	0.791

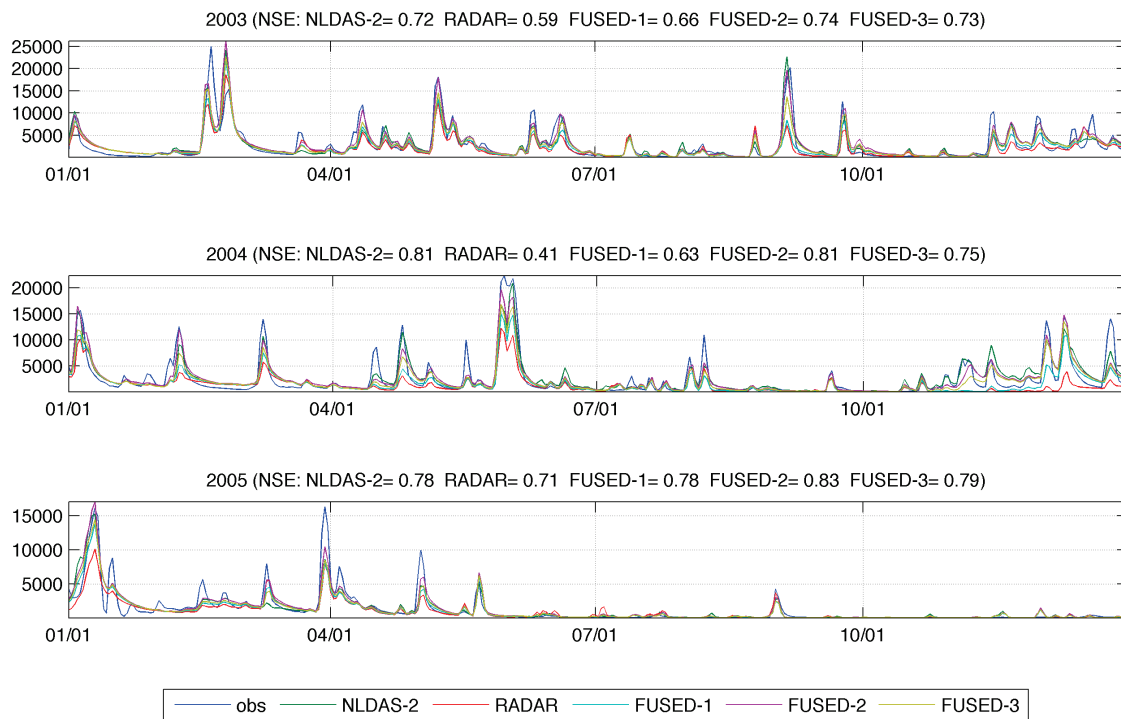


Figure 5.25 Observed streamflow and simulated streamflow with NLDAS-2, RADAR, FUSED-1, FUSED-2 and FUSED-3 precipitation data in calibration period (2003, 2004 and 2005) in BSNK2 watershed. The unit of streamflow is cubic feet per second (cft/s). Corresponding Nash-Sutcliffe Efficiencies (NSE) are given in the titles of plots.

BSNK2 watershed. BSNK2 is a watershed in Kentucky with relatively steep topography. The hydrographs of the observed and the five simulated streamflows are plotted in **Figure 5.25** and the corresponding NSEs are listed in Table 5.5. Findings in BSNK2 watershed include:

- 1) In 2003, the NSEs of FUSED-2 and FUSED-3 data are slightly larger than the NSE of NLDAS-2. In this year, both NLDAS-2 and RADAR underestimate precipitation in flooding period, which can be seen from the observed hydrograph and the simulated hydrographs with

NLDAS-2 and RADAR data. This is the reason why FUSED-1 data have smaller NSE, which falls between the NSEs of NLDAS-2 and RADAR data.

- 2) In 2004, the NSE of FUSED-2 data have the same NSE as NLDAS-2 data, while the NSEs of FUSED-1 and FUSED-3 data are smaller than the NSE of NLDAS-2 data. From the plot of the observed hydrograph and the simulated hydrographs with NLDAS-2 data and RADAR data, we can see that both data underestimate precipitation but the underestimation of RADAR data is more severe. Correspondingly, the NSE of RADAR data (0.410) is much smaller than that of NLDAS-2 data (0.813). That is why FUSED-1 data have smaller NSE than NLDAS-2 data. FUSED-2 and NLDAS-2 data have the same NSE is because FUSED-2 data takes the average magnitude of NLDAS-2 data. Because the NSE of FUSED-3 data is smaller than the NSE of NLDAS-2 data, it can be inferred that the RADAR data (at 1/32 degree resolution) didn't well capture the spatial pattern of precipitation in this year.
- 3) In 2005, all NSEs of FUSED-1, FUSED-2 and FUSED-3 data, especially FUSED-2 data, are larger than the NSE of NLDAS-2 data. This is mainly due to RADAR data have relatively good reliability, i.e. NSE=0.712. Meanwhile, this finding indicates that both NLDAS-2 and RADAR data also underestimate precipitation in flooding periods of 2005.
- 4) Overall, considerable improvements of streamflow simulations have been made through precipitation data fusion in year 2003 and 2005. When RADAR data have higher reliability, there are larger improvements.

CLAI2 watershed. CLAI2 is a watershed in Illinois with flat topography. The hydrographs of the observed and the five simulated streamflow series are plotted in Figure 5.26 and the corresponding NSEs are listed in Table 5.6. Findings in CLAI2 watershed include:

- 1) In 2003, both NLDAS-2 and RADAR data are not very reliable, i.e. $NSE=0.605$ and $NSE=0.487$ respectively. The NSEs of FUSED-1, FUSED-2 and FUSED-3 data are smaller than the NSE of NLDAS-2 data. This is mainly due to the poor qualities of these two data. As shown in the first panel of Figure 5.26, the hydrographs simulated with NLDAS-2 and RADAR data have very poor fits to the observed hydrograph in the period from February to August. As a result, the fused precipitation data also generate poor hydrographs in this period.
- 2) In 2004, NLDAS-2 data are relative reliable, i.e. $NSE=0.739$. The hydrograph simulated with NLDAS-2 data basically captures the shape of observed hydrograph. RADAR data have very poor reliability, i.e. $NSE=0.236$. As indicated by hydrographs, RADAR data significantly underestimate precipitation in this year. The NSE of FUSED-2 data is slightly larger than the NSE of NLDAS-2 data. Because the RADAR data are very unreliable, the improvement made through precipitation data fusion is very slight.
- 3) In 2005, NLDAS-2 data are very reliable, i.e. $NSE=0.896$ while RADAR data are very unreliable, i.e. $NSE=0.387$. The NSEs of FUSED-2 and FUSED-3 data are slightly larger than the NSE of NLDAS-2 data. Due to the low reliabilities of NLDAS-2 and RADAR data, improvements of streamflow simulation are hard to made through precipitation data fusion.
- 4) Overall, no improvements of streamflow simulations are made through precipitation data fusion in 2003 since both NLDAS-2 and RADAR data are not reliable in this year. There are very slight improvements of streamflow simulation made through precipitation data fusion in 2004 and 2005.

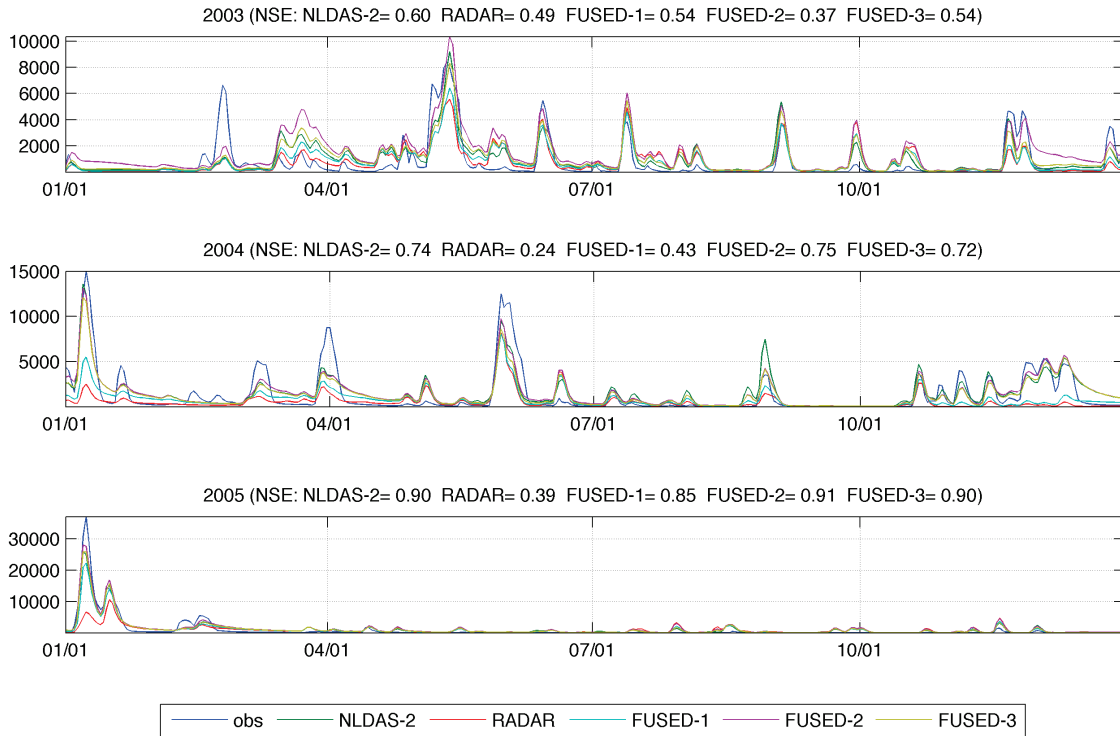


Figure 5.26 Observed streamflow and simulated streamflow with NLDAS-2, RADAR, FUSED-1, FUSED-2 and FUSED-3 precipitation data in calibration period (2003, 2004 and 2005) in CLAI2 watershed. The unit of streamflow is cubic feet per second (cft/s). Corresponding Nash-Sutcliffe Efficiencies (NSE) are given in the titles of plots.

Table 5.6 Nash-Sutcliffe Efficiencies (NSEs) corresponding to the five precipitation inputs in CLAI2 watershed

	NLDAS-2	RADAR	FUSED-1	FUSED-2	FUSED-3
2003	0.604	0.487	0.535	0.367	0.544
2004	0.739	0.238	0.431	0.750	0.719
2005	0.896	0.387	0.847	0.907	0.904

CRWI3 watershed. CRWI3 is a watershed in Indiana with flat topography. The hydrographs of the observed and the five simulated streamflow series are plotted in Figure 5.27 and the corresponding NSEs are listed in Table 5.7. Findings of CRWI3 watershed include:

- 1) In 2003, RADAR data have good reliability, i.e. $NSE=0.789$, while the NSEs of FUSED-1, FUSED-2 and FUSED-3 data are significantly larger than the NSE of NLDAS-2 data but are slightly smaller than the NSE of RADAR data. Particularly, the NSE of FUSED-3 data is 0.1 more than the NSE of NLDAS-2 data, which means that the spatial pattern of RADAR data (at 1/32 degree resolution) can improve the NLDAS-2 data significantly. But the mean magnitudes of RADAR data don't help much because the NSEs of FUSED-1 and FUSED-2 data are just slightly larger than the NSE of FUSED-3.
- 2) In 2004, NLDAS-2 data have poor reliability, i.e. $NSE=0.585$ while RADAR data have relative better reliability, i.e. $NSE=0.669$. The NSEs of FUSED-1 and FUSED-3 data are significantly larger than the NSE of NLDAS-2 data. Meanwhile, the NSEs of FUSED-1 and FUSED-3 data are very close, which indicates that the mean magnitudes of NLDAS-2 and RADAR data are close. The improvements of simulated streamflows with FUSED-1 and FUSED-3 are essentially attributed to the spatial patterns of RADAR data (at 1/32 degree resolution) on the fused precipitation data. The smaller NSE of FUSED-2 data is because FUSED-2 data overestimate precipitation in this year, which is indicated by the hydrographs in the second panel of Figure 5.27. In addition, the results in 2004 also indicate that NLDAS-2 and RADAR have different timing, since it has been already inferred that the mean magnitudes of NLDAS-2 and RADAR are close but the FUSED-2 data overestimate precipitation.

- 3) In 2005, NLDAS-2 data have good reliability, i.e. $NSE=0.795$ while RADAR data have relatively good reliability, i.e. $NSE=0.667$. The NSEs of FUSED-1 and FUSED-2 data are slightly larger than that the NSE of NLDAS-2 data, which is mainly due to the contribution of the spatial patterns in RADAR data (at 1/32 degree resolution).
- 4) Overall, NLDAS-2 data can be improved significantly in 2003 and 2004 and be improved slightly in 2005. The improvements mainly come from the spatial patterns in RADAR data at 1/32 degree resolution.

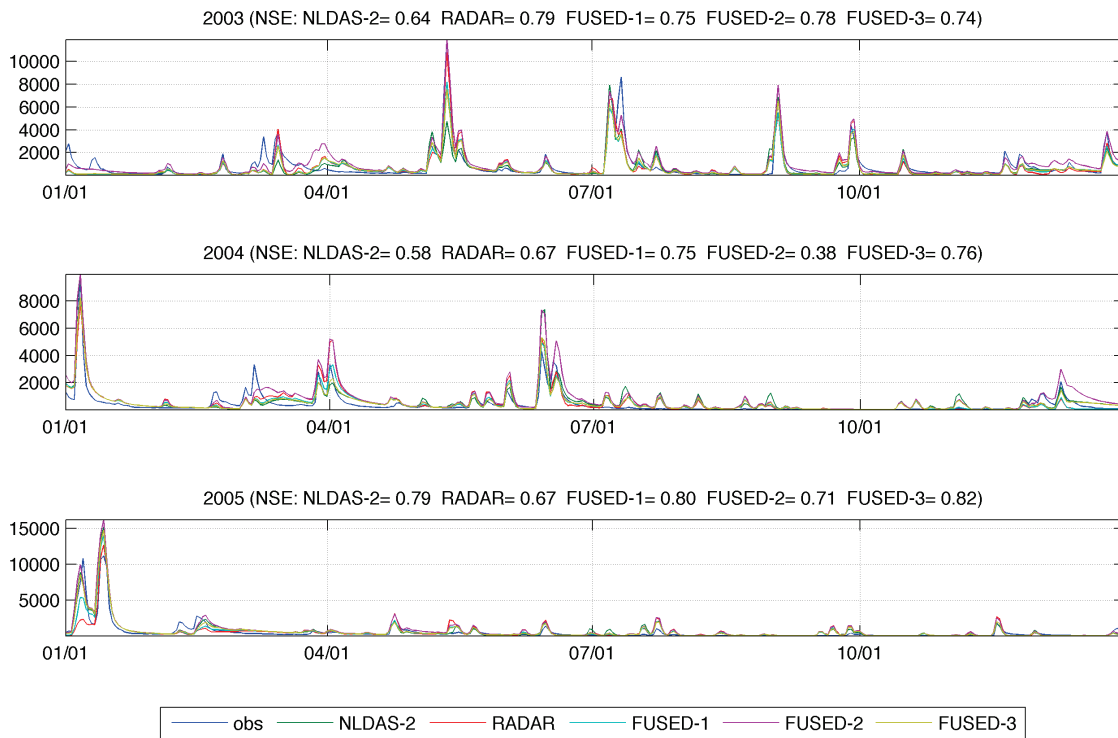


Figure 5.27 Observed streamflow and simulated streamflow with NLDAS-2, RADAR, FUSED-1, FUSED-2 and FUSED-3 precipitation data in calibration period (2003, 2004 and 2005) in CRW13 watershed. The unit of streamflow is cubic feet per second (cft/s). Corresponding Nash-Sutcliffe Efficiencies (NSE) are given in the titles of plots

Table 5.7 Nash-Sutcliffe Efficiencies (NSEs) corresponding to the five precipitation inputs in CRWI3 watershed

	NLDAS-2	RADAR	FUSED-1	FUSED-2	FUSED-3
2003	0.636	0.789	0.749	0.784	0.739
2004	0.585	0.669	0.751	0.375	0.759
2005	0.795	0.667	0.804	0.706	0.817

CYCK2 watershed. CYCK2 is a watershed in Kentucky with relatively steep topography. The hydrographs of the observed and the five simulated streamflow series are plotted in Figure 5.28 and the corresponding NSEs are listed in Table 5.8. Findings in CYCK2 watershed include:

- 1) In 2003, both NLDAS-2 and RADAR data have very poor reliability, i.e. $NSE=0.154$ and $NSE=0.146$ respectively. It is mainly reflected in the simulated hydrographs for the peak in February, as shown in Figure 5.28. No matter magnitude or timing, the simulated hydrographs are significantly different from the observed hydrograph. Even though the NSEs of FUSED-1 and FUSED-3 data are slightly larger than the NSE of NLDAS-2 data, but there are no essential improvements made through data fusion. There are two possible reasons for the poor streamflow simulations. One is that both NLDAS-2 and RADAR data didn't well record the precipitation (very possible snow) in February. The other is that Noah LSM fails to properly describe snow accumulation and melting processes, or both.
- 2) In 2004, NLDAS-2 data have good reliability, i.e. $NSE=0.786$, and RADAR data have relatively good reliability, i.e. $NSE=0.710$. For the fused precipitation data, the NSEs of FUSED-1 and FUSED-2 data are close to the NSE of NLDAS-2 data while the NSE of FUSED-2 data, i.e. 0.891, is significantly larger than the NSE of NLDAS-2 data. This

indicates that the improvements made through precipitation data fusion is mainly due to the mean magnitudes instead of the spatial patterns of RADAR data.

- 3) In 2005, both NLDAS-2 and RADAR data have relatively poor reliability, i.e. $NSE=0.656$ and $NSE=0.631$ respectively. Similar to the results in 2004, the NSE of FUSED-2 data is significantly larger than that of NLDAS-2 data while the NSEs of FUSED-1 and FUSED-3 data are close to the NSE of NLDAS-2 data. These results in this year are the same as those in 2004.
- 4) Overall, no essential improvements of streamflow simulation are made through precipitation data fusion in 2003 but there are significant improvements made in 2004 and 2005.

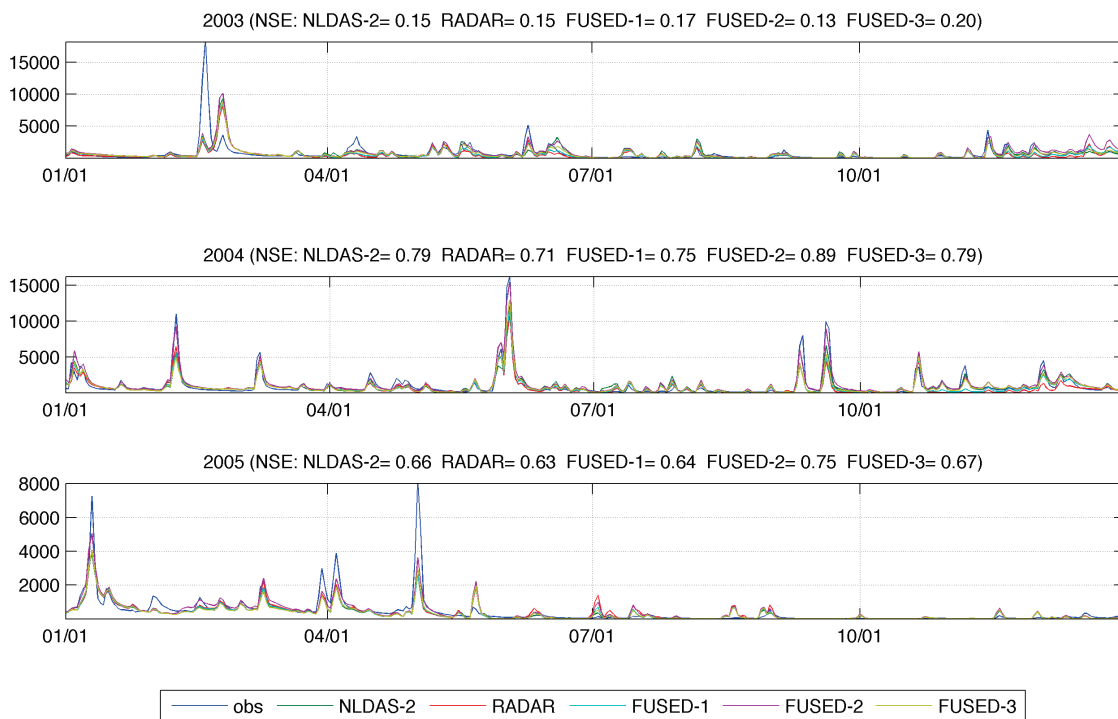


Figure 5.28 Observed streamflow and simulated streamflow with NLDAS-2, RADAR, FUSED-1, FUSED-2 and FUSED-3 precipitation data in calibration period (2003, 2004 and 2005) in CYCK2 watershed. The unit of streamflow is cubic feet per second (cft/s). Corresponding Nash-Sutcliffe Efficiencies (NSE) are given in the titles of plots.

Table 5.8 Nash-Sutcliffe Efficiencies (NSEs) corresponding to the five precipitation inputs in CYCK2 watershed

	NLDAS-2	RADAR	FUSED-1	FUSED-2	FUSED-3
2003	0.154	0.146	0.170	0.133	0.199
2004	0.786	0.710	0.751	0.891	0.786
2005	0.656	0.631	0.644	0.746	0.669

DBVO1 watershed. DBVO1 is a watershed in Ohio with mild topography. The hydrographs of the observed and the simulated stream flow series are plotted in Figure 5.29 and the corresponding NSEs are listed in Table 5.9. Findings in DBVO1 watershed include:

- 1) In 2003, both NLDAS-2 and RADAR data are very unreliable, i.e. NSE=0.369 and NSE=0.295 respectively, while the NSE of FUSED-2 data is slightly larger than that of NLDAS-2 data. As shown in the first panel of Figure 5.29, the simulated hydrographs in March and April are especially poor. This is either because NLDAS-2 and RADAR data have poor qualities in these two months or because Noah LSM fails to properly describe snow accumulation and melting processes in this period.
- 2) In 2004, NLDAS-2 data have relatively good reliability (NSE=0.748) while RADAR data have relatively poor reliability (NSE=0.580). The NSE of FUSED-2 data is significantly larger than that of NLDAS-2 data while the NSE of FUSED-3 data is close to that of NLDAS-2 data. This indicates that the improvements of streamflow simulation made through precipitation are mainly due to the mean magnitudes instead of the spatial patterns of RADAR data (at 1/32 degree resolution).
- 3) In 2005, NLDAS-2 data have relatively poor reliability, i.e. NSE=0.642 while RADAR data have relatively good reliability, i.e. NSE=0.766. NSEs of FUSED-1, FUSED-2 and FUSED-3 data, especially that of FUSED-2 data (i.e. 0.888), are all larger than the NSE of NLDAS-2

data. This indicates that very significant improvements of streamflow simulation have been made through precipitation data fusion. Both the spatial patterns and the mean magnitudes of RADAR data (at 1/32 degree resolution) contribute to the improvements but the mean magnitudes play a more important role.

- 4) Overall, no essential improvements of streamflow stimulation are made through precipitation data fusion in 2003. But significant improvements are made through precipitation data fusion in 2004 and 2005.

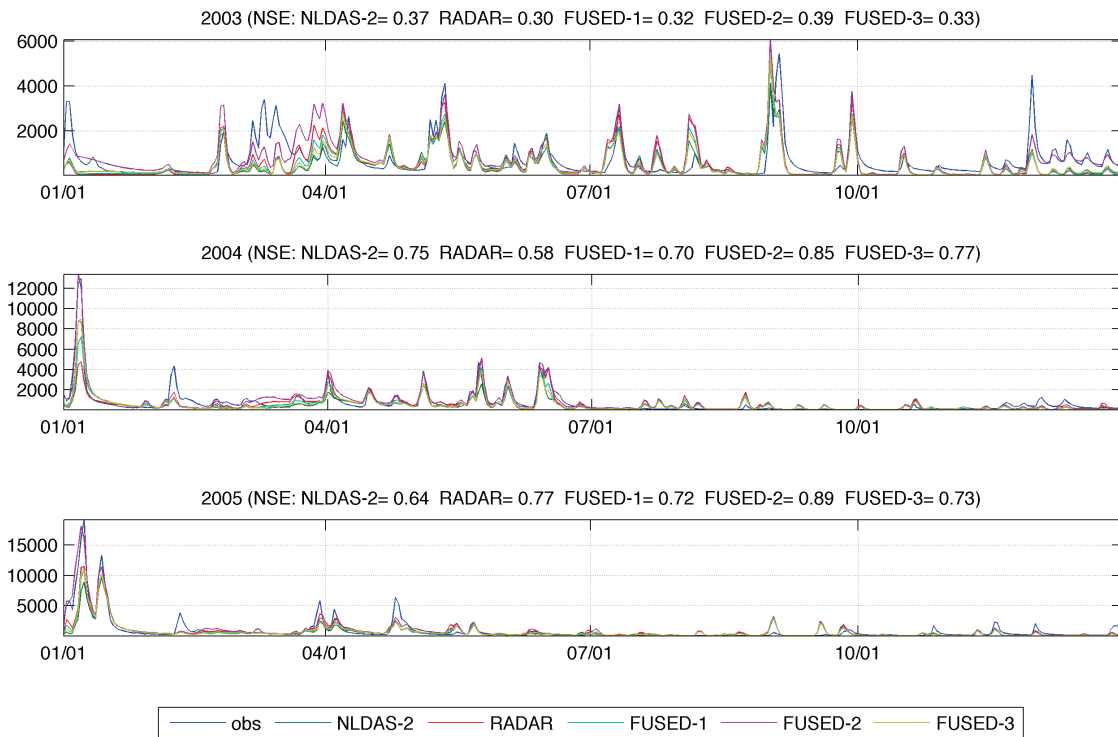


Figure 5.29 Observed streamflow and simulated streamflow with NLDAS-2, RADAR, FUSED-1, FUSED-2 and FUSED-3 precipitation data in calibration period (2003, 2004 and 2005) in DBVO1 watershed. The unit of streamflow is cubic feet per second (cft/s). Corresponding Nash-Sutcliffe Efficiencies (NSE) are given in the titles of plots.

Table 5.9 Nash-Sutcliffe Efficiencies (NSEs) corresponding to the five precipitation inputs in DBVO1 watershed

	NLDAS-2	RADAR	FUSED-1	FUSED-2	FUSED-3
2003	0.369	0.295	0.319	0.392	0.335
2004	0.748	0.580	0.701	0.852	0.766
2005	0.642	0.766	0.721	0.888	0.729

ELRP1 watershed. ELRP1 is a mountainous watershed in Pennsylvania with steep topography. The hydrographs of the observed and the five simulated streamflow series are plotted in Figure 5.30 and the corresponding NSEs are listed in Table 5.10. Findings in ELRP1 watershed include:

- 1) In the three years, both NLDAS-2 and RADAR data have poor reliability, i.e. all $NSE < 0.5$, especially RADAR data. For each year, the NSE of FUSED-2 data are at least 0.1 larger than that of NLDAS-2 data. Meanwhile, the NSE of FUSED-3 data is slightly larger than the corresponding NSE of NLDAS-2 data. This means that NLDAS-2 data can be improved through precipitation data fusion even RADAR data have worse qualities. The improvements are mainly due to the mean magnitudes instead of the spatial patterns of RADAR data (at 1/32 degree resolution).
- 2) As shown in Figure 5.30, the simulated hydrographs have worse fits to the observed hydrographs for cold seasons of the three years. This is either because both NLDAS-2 data or RADAR data have poorer reliability in cold seasons or because Noah LSM has poor performance in describing the snow accumulation and snow melting processes.
- 3) Overall, there are significant improvements of streamflow simulation are made through precipitation fusion for the three years.

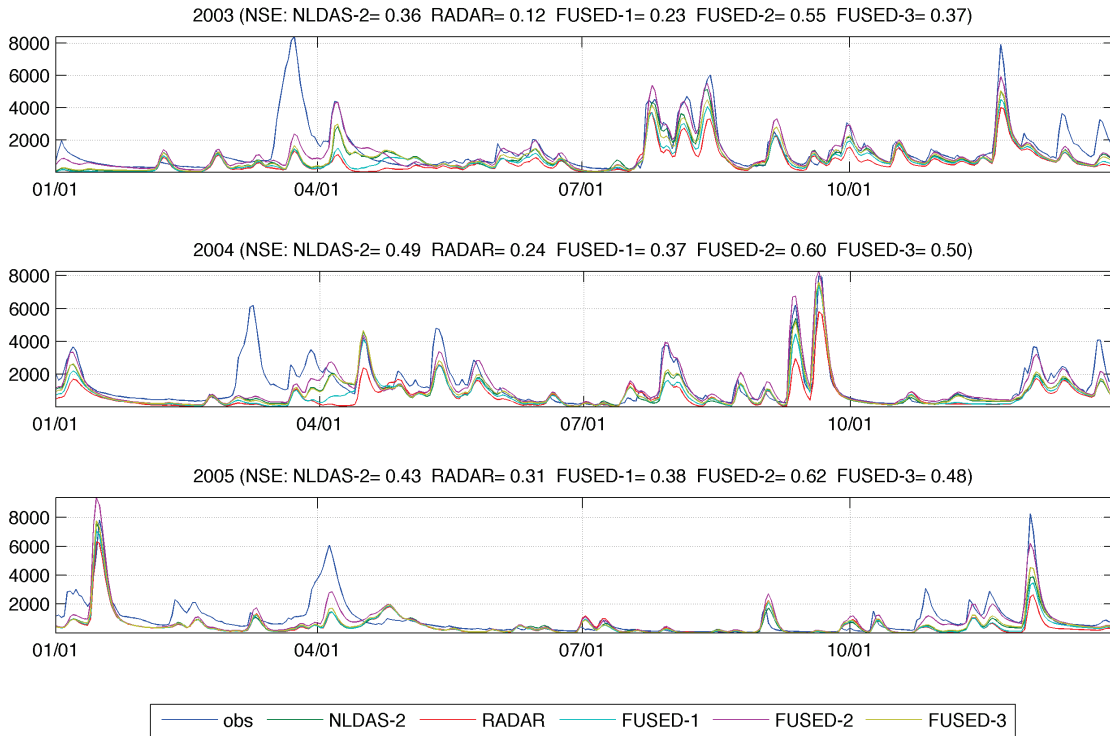


Figure 5.30 Observed streamflow and simulated streamflow with NLDAS-2, RADAR, FUSED-1, FUSED-2 and FUSED-3 precipitation data in calibration period (2003, 2004 and 2005) in ELRP1 watershed. The unit of streamflow is cubic feet per second (cft/s). Corresponding Nash-Sutcliffe Efficiencies (NSE) are given in the titles of plots.

Table 5.10 Nash-Sutcliffe Efficiencies (NSEs) corresponding to the five precipitation inputs in ELRP1 watershed

	NLDAS-2	RADAR	FUSED-1	FUSED-2	FUSED-3
2003	0.362	0.122	0.235	0.548	0.374
2004	0.492	0.235	0.365	0.598	0.500
2005	0.434	0.308	0.380	0.616	0.482

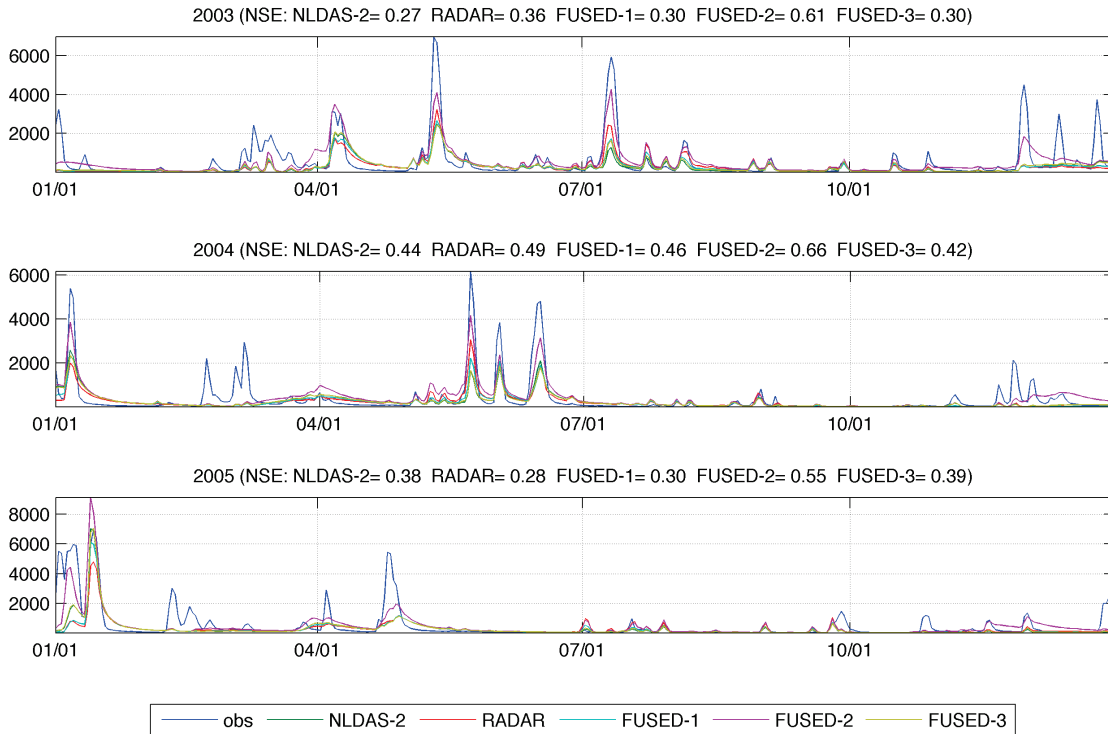


Figure 5.31 Observed streamflow and simulated streamflow with NLDAS-2, RADAR, FUSED-1, FUSED-2 and FUSED-3 precipitation data in calibration period (2003, 2004 and 2005) in FDYO1 watershed. The unit of streamflow is cubic feet per second (cft/s). Corresponding Nash-Sutcliffe Efficiencies (NSE) are given in the titles of plots.

FDYO1 watershed. FDYO1 is a watershed in Ohio with a flat topography. The hydrographs of the observed and the five simulated streamflow series are plotted in Figure 5.31 and corresponding NSEs are listed in Table 5.11. Findings in FDYO1 watershed include:

- 1) In the three years, both NLDAS-2 and RADAR data have poor reliability, i.e. all $NSE < 0.5$.

As shown in Figure 5.31, the hydrographs simulated with NLDAS-2 data and RADAR data are significantly below the observed hydrograph in flood period. This means that these two data commonly underestimate precipitation in the three years. The NSE of FUSED-2 data are significantly larger than the NSE of NLDAS-2 data in each of these three years.

- 2) Overall, significant improvements of streamflow simulation are made through precipitation data fusion. The improvements are mainly due to the mean magnitudes of RADAR data (at 1/32 degree resolution).

Table 5.11 Nash-Sutcliffe Efficiencies (NSEs) corresponding to the five precipitation inputs in FDYO1 watershed

	NLDAS-2	RADAR	FUSED-1	FUSED-2	FUSED-3
2003	0.270	0.361	0.298	0.606	0.296
2004	0.437	0.491	0.458	0.661	0.418
2005	0.384	0.281	0.298	0.548	0.392

KINT1 watershed. KINT1 is a watershed in Tennessee with relatively steep topography. The hydrographs of the observed and the five simulated streamflow series are plotted in Figure 5.32 and the corresponding NSEs are listed in Table 5.12. Findings in KINT1 watershed include:

- 1) In 2003, both NLDAS-2 and RADAR data have very good reliability, i.e. NSE=0.932 and NSE=0.938 respectively. As shown in Figure 5.32, the simulated hydrographs with these two data reproduce the observed hydrograph very well. The NSE of FUSED-1 data is slightly larger than that of NLDAS-2 data.
- 2) In 2004 and 2005, both NLDAS-2 and RADAR data have good reliability. The NSEs of FUSED-1 and FUSED-2 data slightly larger than the NSE of NLDAS-2 data in each of these two years.
- 3) Overall, there are no essential improvements of streamflow simulation made through precipitation data fusion. Both of NLDAS-2 and RADAR data have good reliability in these three years. There is very limited room for improvements.

Table 5.12 Nash-Sutcliffe Efficiencies (NSEs) corresponding to the five precipitation inputs in KINT1 watershed

	NLDAS-2	RADAR	FUSED-1	FUSED-2	FUSED-3
2003	0.932	0.938	0.942	0.860	0.913
2004	0.843	0.815	0.854	0.734	0.851
2005	0.809	0.786	0.816	0.776	0.833

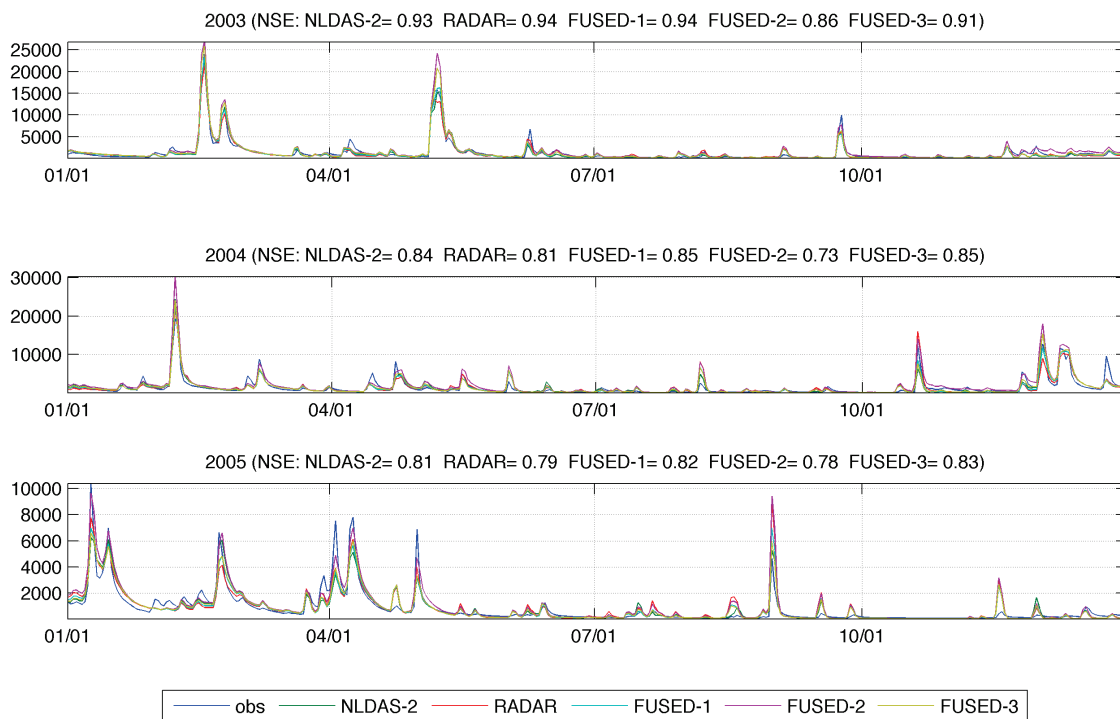


Figure 5.32 Observed streamflow and simulated streamflow with NLDAS-2, RADAR, FUSED-1, FUSED-2 and FUSED-3 precipitation data in calibration period (2003, 2004 and 2005) in KINT1 watershed. The unit of streamflow is cubic feet per second (cft/s). Corresponding Nash-Sutcliffe Efficiencies (NSE) are given in the titles of plots.

NHSO1 watershed. NHSO1 is a watershed in Ohio with mild topography. The hydrographs of the observed and the five simulated streamflow series are plotted in Figure 5.33 and the corresponding NSEs are listed in Table 5.13. Findings in NHSO1 watershed include:

- 1) In 2003 and 2004, NLDAS-2 data have poor reliability, i.e. $NSE < 0.6$, while the reliability of NLDAS-2 data is a little bit better. All NSEs of FUSED-1, FUSED-2 and FUSED-3 data are significantly higher than the NSE of NLDAS-2 data, especially the NSEs of FUSED-2 data, which are significantly larger than the corresponding NSEs of NLDAS-2 data. This indicates that both the mean magnitudes and the spatial patterns of RADAR data (at 1/32 degree resolution) contribute to the improvements obtained by fused precipitation data while the mean magnitudes plays a bigger role.
- 2) In 2005, both NLDAS-2 and RADAR data have relatively good reliability. Even though the NSE of FUSED-2 data is slightly larger than that of NLDAS-2 data, all NSEs of fused data are very close to the NSE of NLDAS-2 data.
- 3) Overall, there are significant improvements of streamflow simulation made through precipitation data fusion in 2003 and 2004. However, no essential improvements are made in 2005.

Table 5.13 Nash-Sutcliffe Efficiencies (NSEs) corresponding to the five precipitation inputs in NHSO1 watershed

	NLDAS-2	RADAR	FUSED-1	FUSED-2	FUSED-3
2003	0.583	0.677	0.695	0.801	0.751
2004	0.447	0.560	0.494	0.729	0.493
2005	0.716	0.689	0.716	0.718	0.716

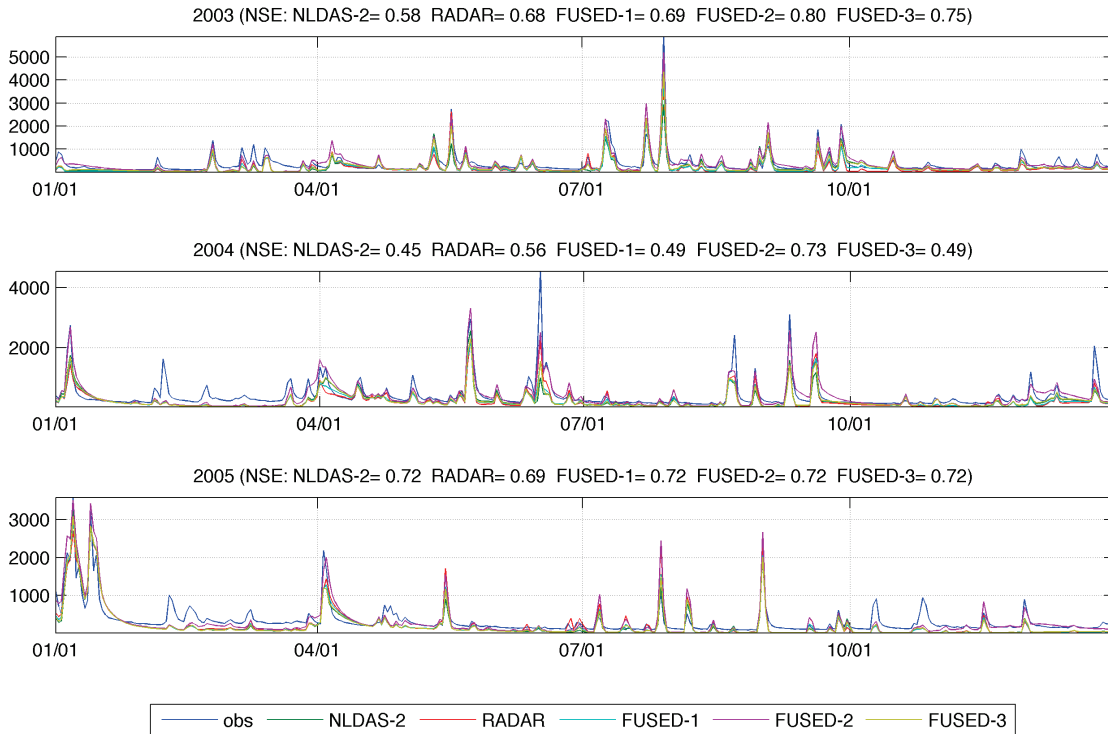


Figure 5.33 Observed streamflow and simulated streamflow with NLDAS-2, RADAR, FUSED-1, FUSED-2 and FUSED-3 precipitation data in calibration period (2003, 2004 and 2005) in NHSO1 watershed. The unit of streamflow is cubic feet per second (cft/s). Corresponding Nash-Sutcliffe Efficiencies (NSE) are given in the titles of plots.

PSNW2 watershed. PSNW2 is a mountainous watershed in West Virginia with very steep topography. The hydrographs of the observed and the five simulated streamflow series are plotted in Figure 5.34 and the corresponding NSEs are listed in Table 5.14. Findings in PSNW2 watershed include:

- 1) In 2003 and 2005, NLDAS-2 data have relatively poor reliability, i.e. $NSE=0.664$ and $NSE=0.523$ respectively, while RADAR data have very poor reliability, i.e. $NSE=0.173$ and $NSE=-0.074$ respectively. In 2003, the NSE of FUSED-2 data is slightly larger than that of NLDAS-2 data while the NSEs of FUSED-1 and FUSED-3 data are smaller than that of

NLDAS-2 data. In 2005, the NSE of FUSED-2 data significantly larger than that of NLDAS-2 data while the NSEs of FUSED-1 and FUSED-3 data are smaller than that of NLDAS-2 data. This means that both NLDAS-2 and RADAR data underestimate precipitation in these two years, which can be seen the hydrographs in Figure 5.34. In addition, the spatial patterns of NLDAS-2 data cannot help to improve streamflow simulation with fused precipitation data.

- 2) In 2004, NLDAS-2 data have relatively poor reliability, i.e. $NSE=0.548$, while RADAR data have extremely poor reliability, i.e. $NSE=-0.457$. No NSEs of fused precipitation data are larger than the NSE of NLDAS-2 data. This means that the fused data may have worse reliability than all input datasets if one of input datasets has very bad quality.
- 3) Overall, data assimilation has different performance in the three years. In 2003, very slight improvements are made. Significant deteriorations occur in 2004. However, significant improvements are made in 2005.

Table 5.14 Nash-Sutcliffe Efficiencies (NSEs) corresponding to the five precipitation inputs in PSNW2 watershed.

	NLDAS-2	RADAR	FUSED-1	FUSED-2	FUSED-3
2003	0.664	0.173	0.463	0.681	0.648
2004	0.548	-0.457	-0.051	0.393	0.368
2005	0.523	-0.074	0.214	0.641	0.487

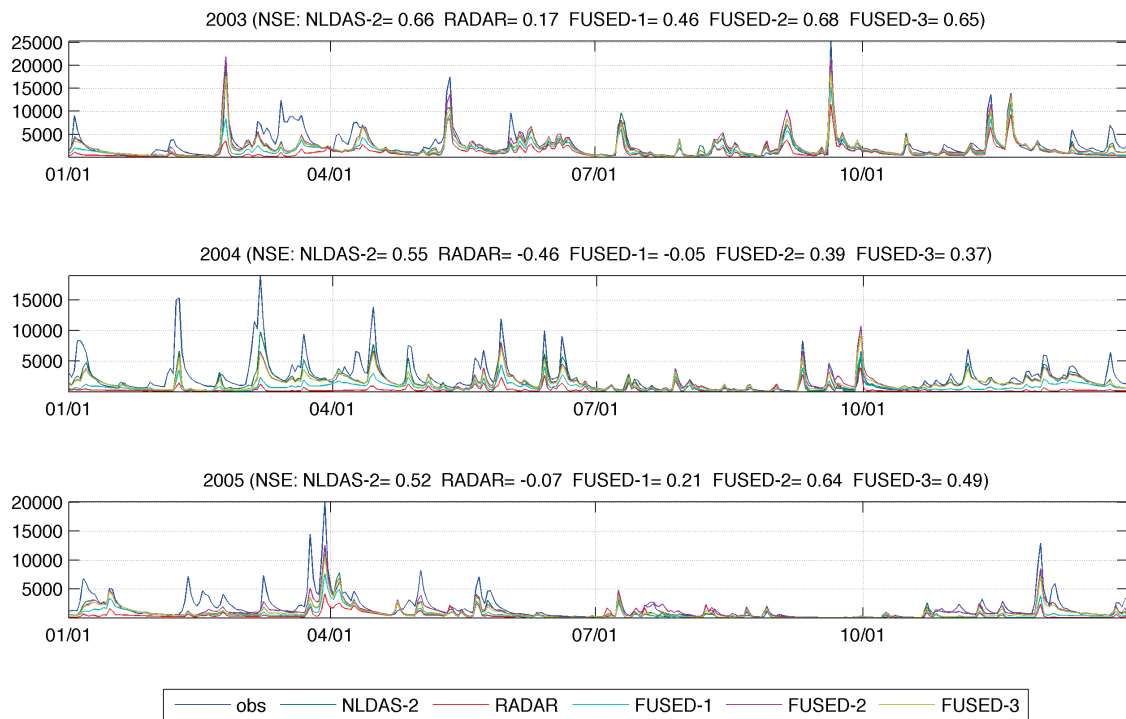


Figure 5.34 Observed streamflow and simulated streamflow with NLDAS-2, RADAR, FUSED-1, FUSED-2 and FUSED-3 precipitation data in calibration period (2003, 2004 and 2005) in PSNW2 watershed. The unit of streamflow is cubic feet per second (cft/s). Corresponding Nash-Sutcliffe Efficiencies (NSE) are given in the titles of plots.

SERI3 watershed. SERI3 is a watershed in Indiana with mild topography. The hydrographs of the observed and the five simulated streamflow series are plotted in Figure 5.35 and the corresponding NSEs are listed in Table 5.15. Findings in SERI3 watershed include:

- 1) In 2003, both NLDAS-2 and RADAR data have poor reliability, i.e. $NSE < 0.5$. The NSE of FUSED-3 data is slightly larger than that of NLDAS-2 data while the NSEs of FUSED-1 and FUSED-2 data are smaller than that of NLDAS-2 data. This means that the spatial patterns of RADAR data (at 1/32 degree resolution) slightly help to improve the streamflow simulation with FUSED-3 data but the magnitudes do not help in this year.

- 2) In 2004 and 2005, both NLDAS-2 data and RADAR data are very reliable, i.e. $NSE > 0.85$. Except the NSE of FUSED-2 data in 2004, all NSEs of fused data are close to the corresponding NSEs of NLDAS-2 data. No essential improvements are made through precipitation data fusion even though the NSEs of FUSED-1 and FUSED-3 data are lightly larger than the NSE of NLDAS-2 data in 2005.
- 3) Overall, no essential improvements are made through precipitation data fusion in these three years.

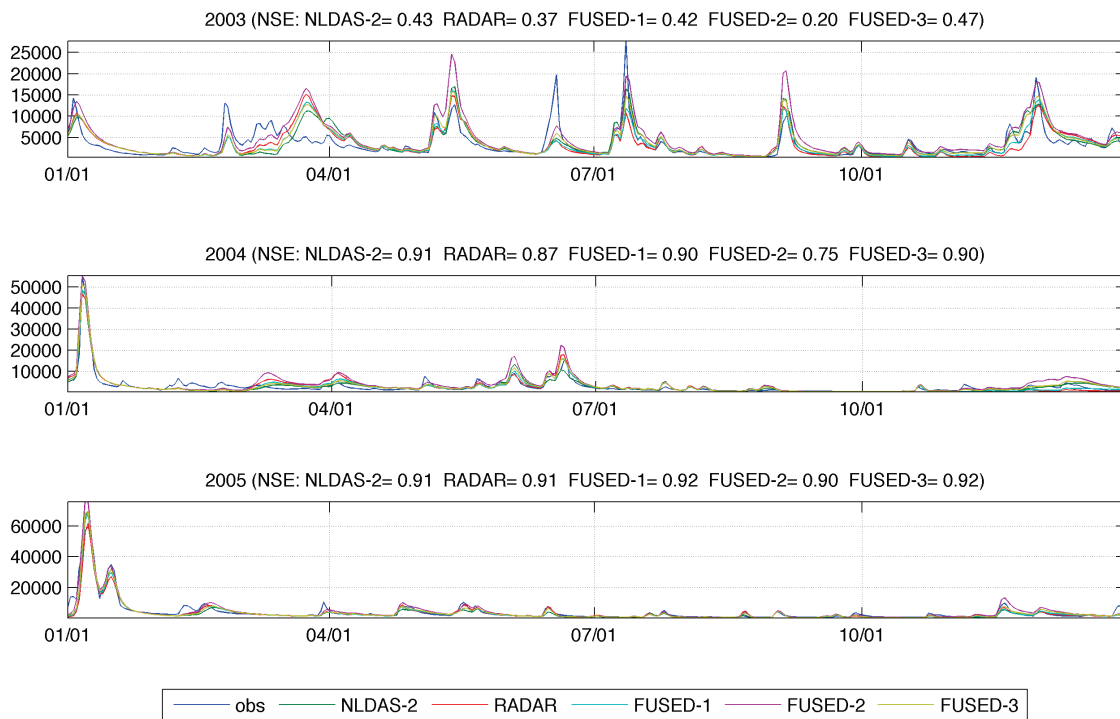


Figure 5.35 Observed streamflow and simulated streamflow with NLDAS-2, RADAR, FUSED-1, FUSED-2 and FUSED-3 precipitation data in calibration period (2003, 2004 and 2005) in SERI3 watershed. The unit of streamflow is cubic feet per second (cft/s). Corresponding Nash-Sutcliffe Efficiencies (NSE) are given in the titles of plots.

Table 5.15 Nash-Sutcliffe Efficiencies (NSEs) corresponding to the five precipitation inputs in SERI3 watershed

	NLDAS-2	RADAR	FUSED-1	FUSED-2	FUSED-3
2003	0.434	0.373	0.420	0.197	0.473
2004	0.905	0.866	0.902	0.750	0.903
2005	0.911	0.905	0.918	0.904	0.920

Table 5.16 Flags of essential improvement (Y), negligible change (=) and deterioration (N) for the 14 experimental watersheds over 2003, 2004 and 2005

	2003	2004	2005
ALDW2	Y	Y	Y
ALPI3	Y	Y	Y
BAKI3	=	=	=
BSNK2	=	=	Y
CLAI2	N	=	=
CRWI3	Y	Y	=
CYCK2	=	Y	Y
DBVO1	=	Y	Y
ELRP1	Y	Y	Y
FDYO1	Y	Y	Y
KINT1	=	=	=
NHSO1	Y	Y	=
PSNW2	=	N	Y
SERI3	=	=	=

To summarize the assessments of precipitation data fusion in terms of streamflow simulation, we can define three qualitative categories: essential improvement, negligible change, and deterioration. If the maximum NSE of the three fused precipitation data is at least 0.05 larger than the NSE of NLDAS-2 data, we say that essential improvement is made, whereas we say that deterioration happens if the maximum NSE of the three fused precipitation data is at least 0.05 smaller than the NSE of NLDAS-2 data. If the maximum NSE of the three fused precipitation data falls between the NSEs of essential improvement and deterioration, we say the change made by precipitation data fusion is negligible. Table 5.16 listed the flags of essential improvement, negligible change and determination. Over the 42 watershed/year, 21 of them have essential improvements, 19 of them have negligible changes and only 2 of them have deteriorations. Such results indicate that it is likely that the fused precipitation data can simulate better hydrographs of streamflow. Therefore, we can conclude that precipitation data fusion is an effective approach to improve the reliability of precipitation data.

5.5.2 Assessment with soil moisture simulations

The assessment of precipitation data fusion on soil moisture simulation is conducted along with streamflow simulation. We don't use measurements to directly validate soil moisture simulation. Instead, the goodness of simulated streamflow is regarded as the indicator of reliability for simulated soil moistures. Given precipitation inputs, it is reasonable to infer that soil moisture contents (SMCs) are simulated properly if streamflow simulation is good. In the following assessment, we will focus on the differences between simulated SMCs with NLDAS-2, RADAR, FUSED-1, FUSED-2 and FUSED-3 data. Particularly, the assessment is conducted from two aspects. One is to show the difference over time and the other is to show the

differences over space. To investigate the temporal differences, the simulated SMCs of the four soil layers of Noah LSM are plotted in Figure 5.36 to Figure 5.49 for all of the 14 experimental watersheds. To investigate the spatial differences, land surface simulations are conducted with the fused precipitation data at 1/32 degree resolution. No matter whether over time or over space, the simulated SMCs corresponding to larger NSE are regarded as the better simulation.

Specifically, the simulated SMCs with the five precipitation inputs in 2004 are analyzed individually for the 14 experimental watersheds. Differences between averaged SMCs of each watershed will be first described. And then, common features of these differences also will be summarized.

In ADLDW watershed (Figure 5.36), we have the following findings:

- 1) In rain period (January to June, September to December), there are considerable differences between the simulated SMCs of the 1st and the 2nd layers in short periods after precipitation events.
- 2) In dry period (July to August), there are significant differences between the simulated SMCs of the 3rd and the 4th layers.
- 3) In the transition time of dry period and rain period (September and October), the differences of simulated SMCs in the 1st, the 2nd, and the 3rd layers vanish quickly while the differences in the 4th layer vanish slowly.
- 4) In four layers, SMCs simulated with FUSED-2 data are always higher than those simulated with other precipitation inputs.

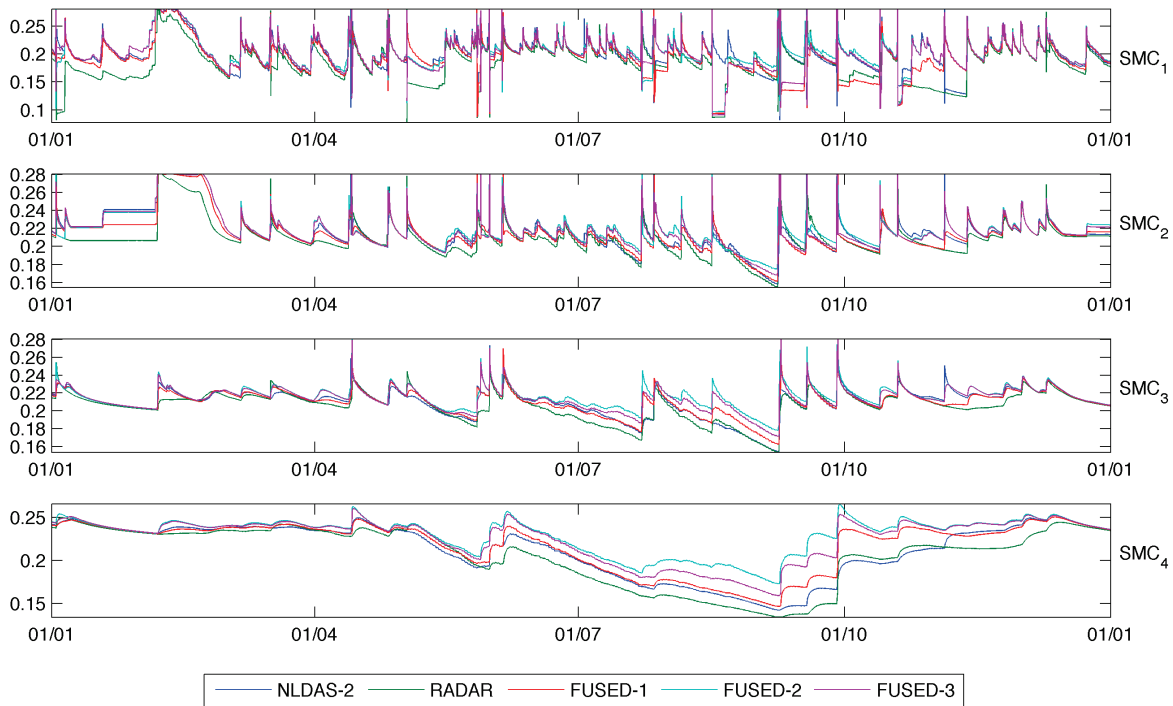


Figure 5.36 Spatial average of simulated soil moisture contents of the 1st, 2nd, 3rd and 4th layer (SMC₁, SMC₂, SMC₃ and SMC₄) over ALDW2 watershed in 2004 with NLDAS-2, RADAR, FUSED-1, FUSED-2 and FUSED-3 precipitation inputs. The unit of soil moisture is volumetric ratio (m^3/m^3).

In ALPI3 watershed (Figure 5.37), we have the following findings:

- 1) From July to the end of the year, there were no heavy precipitation events to form flood peaks. There are considerable differences between simulated SMCs in four layers.
- 2) Especially, the SMCs simulated with NLDAS-2 data are significantly higher than those simulated with other precipitation data.

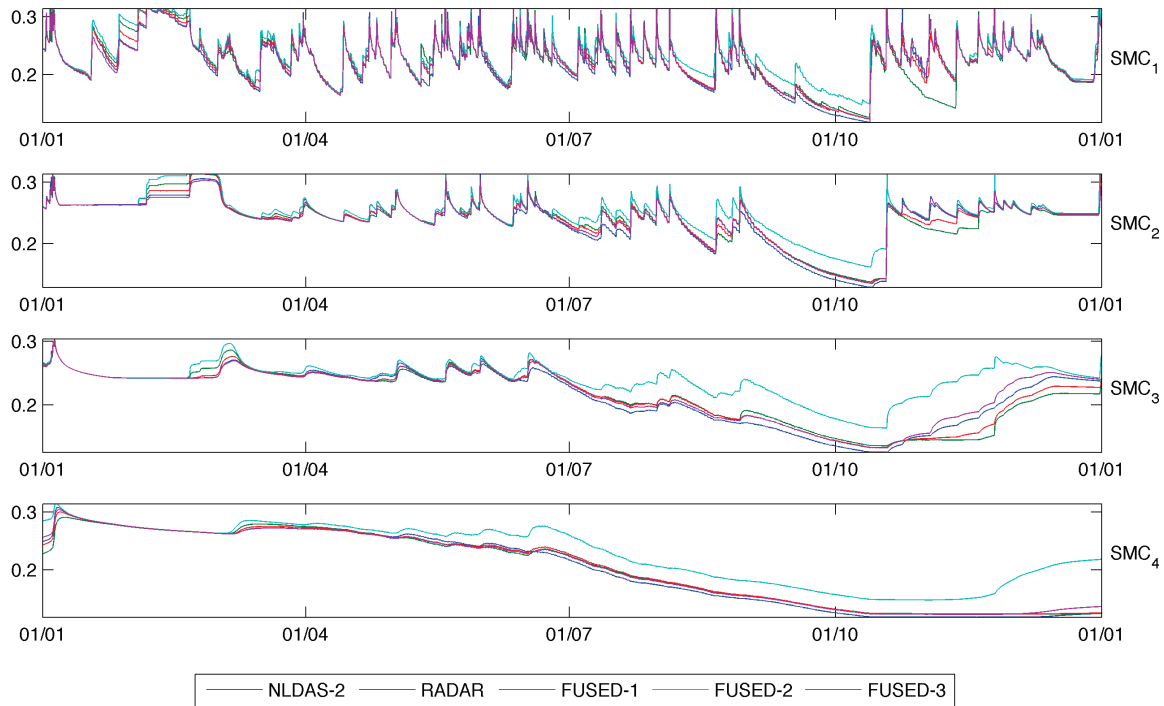


Figure 5.37 Spatial average of simulated soil moisture contents of the 1st, 2nd, 3rd and 4th layer (SMC₁, SMC₂, SMC₃ and SMC₄) over ALPI3 watershed in 2004 with NLDAS-2, RADAR, FUSED-1, FUSED-2 and FUSED-3 precipitation inputs. The unit of soil moisture is volumetric ratio (m^3/m^3).

In BAKI3 watershed (Figure 5.38), we have the following findings:

- 1) From July to September is the dry period of 2004. The differences between simulated hydrographs are very small. But considerable differences between simulated SMCs can be found in the 3rd layer.
- 2) In November and December, the time period that the 3rd and the 4th layers are getting wet, there are significant differences between the simulated SMCs in these two layers.

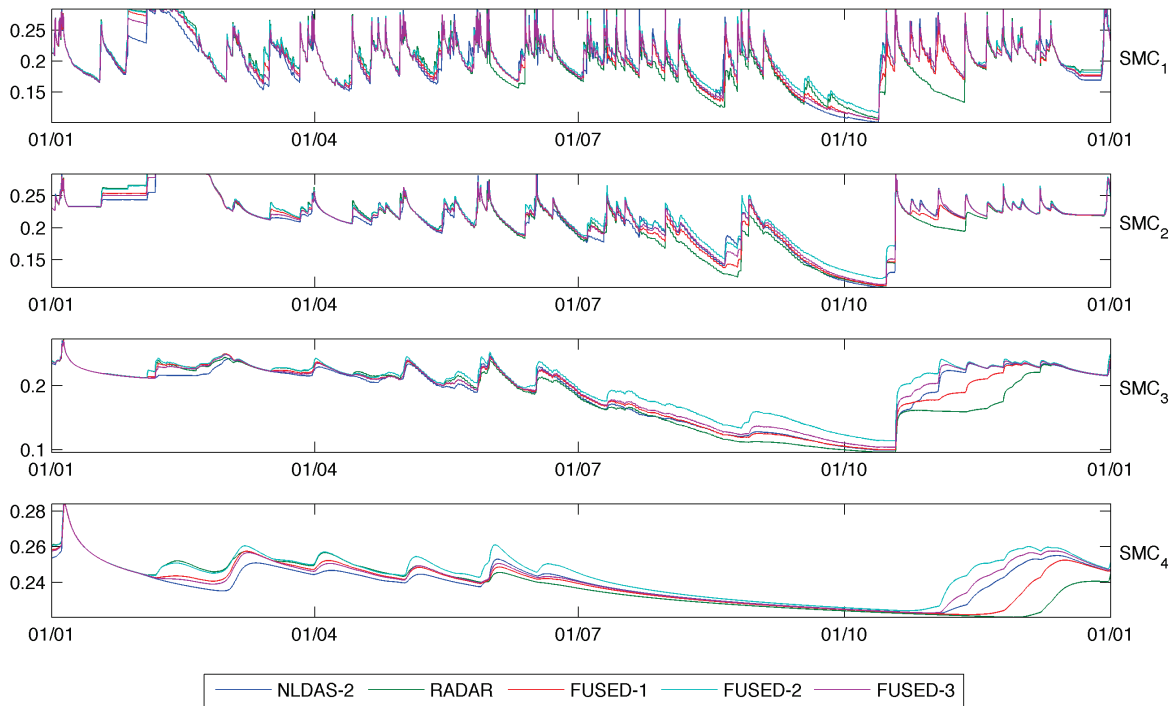


Figure 5.38 Spatial average of simulated soil moisture contents of the 1st, 2nd, 3rd and 4th layer (SMC₁, SMC₂, SMC₃ and SMC₄) over BAKI3 watershed in 2004 with NLDAS-2, RADAR, FUSED-1, FUSED-2 and FUSED-3 precipitation inputs. The unit of soil moisture is volumetric ratio (m^3/m^3).

In BSNK2 watershed (Figure 5.39), we have the following findings:

- 1) August and September are the dry period of 2004. There are significant differences between the SMCs in four layers, especially in the 3rd and the 4th layer.
- 2) From October to December, the 3rd and the 4th layer are getting wet. There are significantly differences between simulated SMCs.

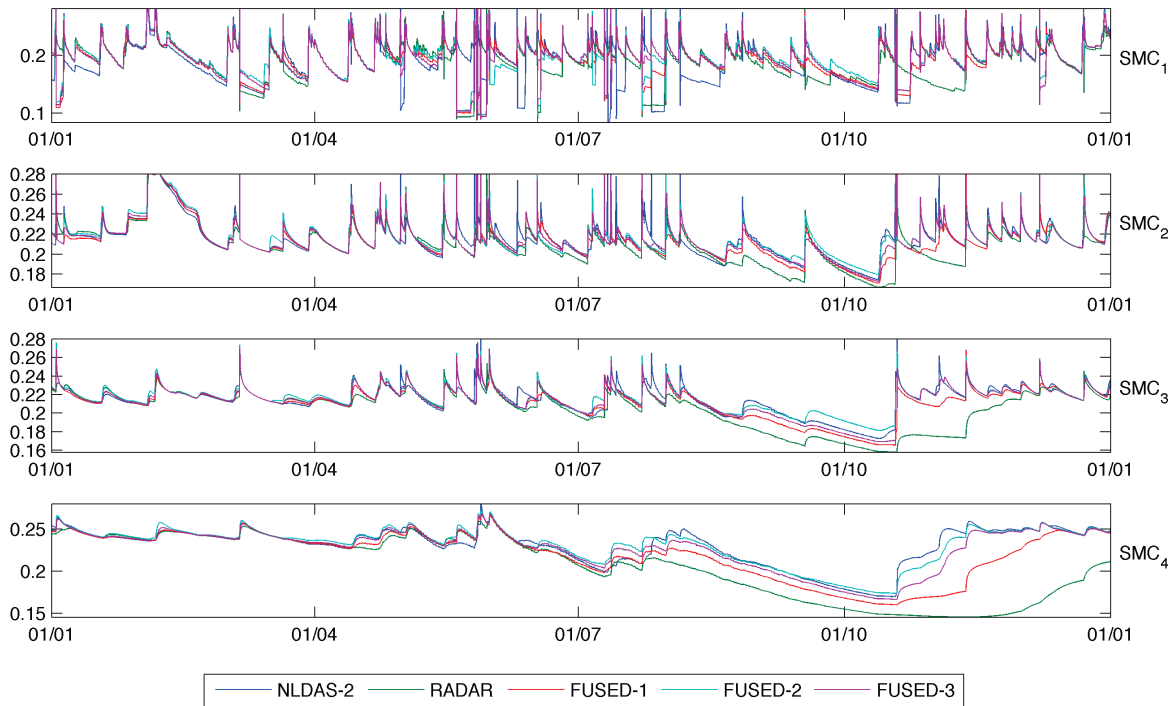


Figure 5.39 Spatial average of simulated soil moisture contents of the 1st, 2nd, 3rd and 4th layer (SMC₁, SMC₂, SMC₃ and SMC₄) over BSNK2 watershed in 2004 with NLDAS-2, RADAR, FUSED-1, FUSED-2 and FUSED-3 precipitation inputs. The unit of soil moisture is volumetric ratio (m³/m³).

In CLAI2 watershed (Figure 5.40), we have the following findings:

- 1) There are significant differences between the simulated SMCs in the 1st, the 2nd and the 3rd layer. Even though NLDAS-2, FUSED-2 and FUSED-3 data have close NSEs in 2004, differences of SMCs simulated with them are still considerable.
- 2) The differences of SMCs are more significant in dry down period of soil moistures.

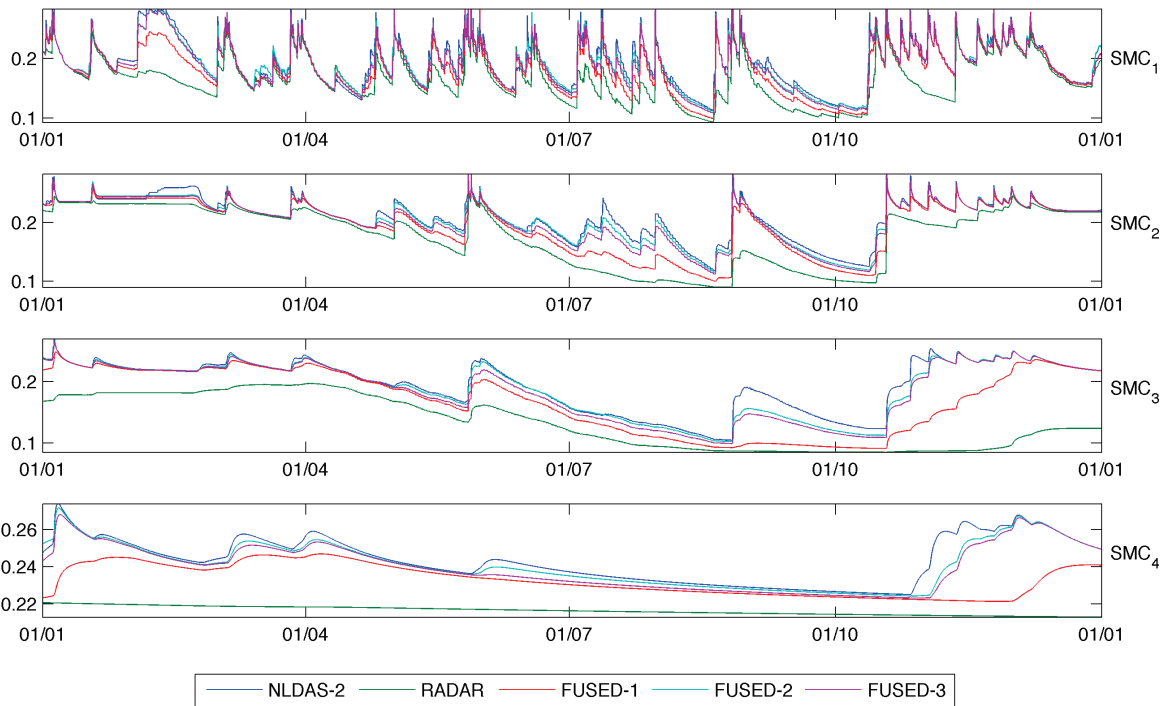


Figure 5.40 Spatial average of simulated soil moisture contents of the 1st, 2nd, 3rd and 4th layer (SMC₁, SMC₂, SMC₃ and SMC₄) over CLAI2 watershed in 2004 with NLDAS-2, RADAR, FUSED-1, FUSED-2 and FUSED-3 precipitation inputs. The unit of soil moisture is volumetric ratio (m^3/m^3).

In CRWI3 watershed (Figure 5.41), we have the following findings:

- 1) Significant differences between simulated SMCs can be found in the 1st and the 2nd layer during the dry down periods of soil moisture, e.g. September.
- 2) Significant differences between simulated SMCs can be found in the 3rd and 4th layer during the wetting period of soil moisture, e.g. November and December.

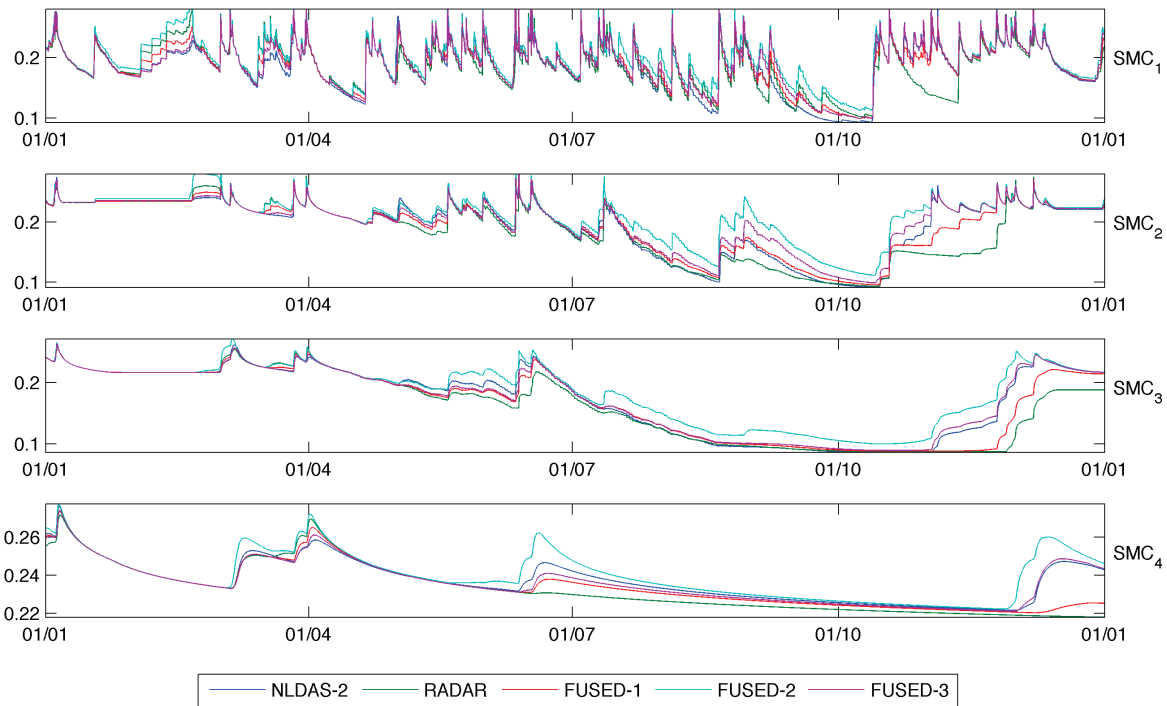


Figure 5.41 Spatial average of simulated soil moisture contents of the 1st, 2nd, 3rd and 4th layer (SMC₁, SMC₂, SMC₃ and SMC₄) over CRWI3 watershed in 2004 with NLDAS-2, RADAR, FUSED-1, FUSED-2 and FUSED-3 precipitation inputs. The unit of soil moisture is volumetric ratio (m^3/m^3).

In CYCK2 watershed (Figure 5.42), we have the following findings:

- 1) Significant differences between simulated SMCs can be found in the 1st, 2nd, 3rd, and 4th layers, especially in the 3rd and 4th layer during the period of July, August and September.
- 2) In particular, the simulated SMCs in the 4th layer with FUSED-2 data are significantly higher than others during the period from July to November.

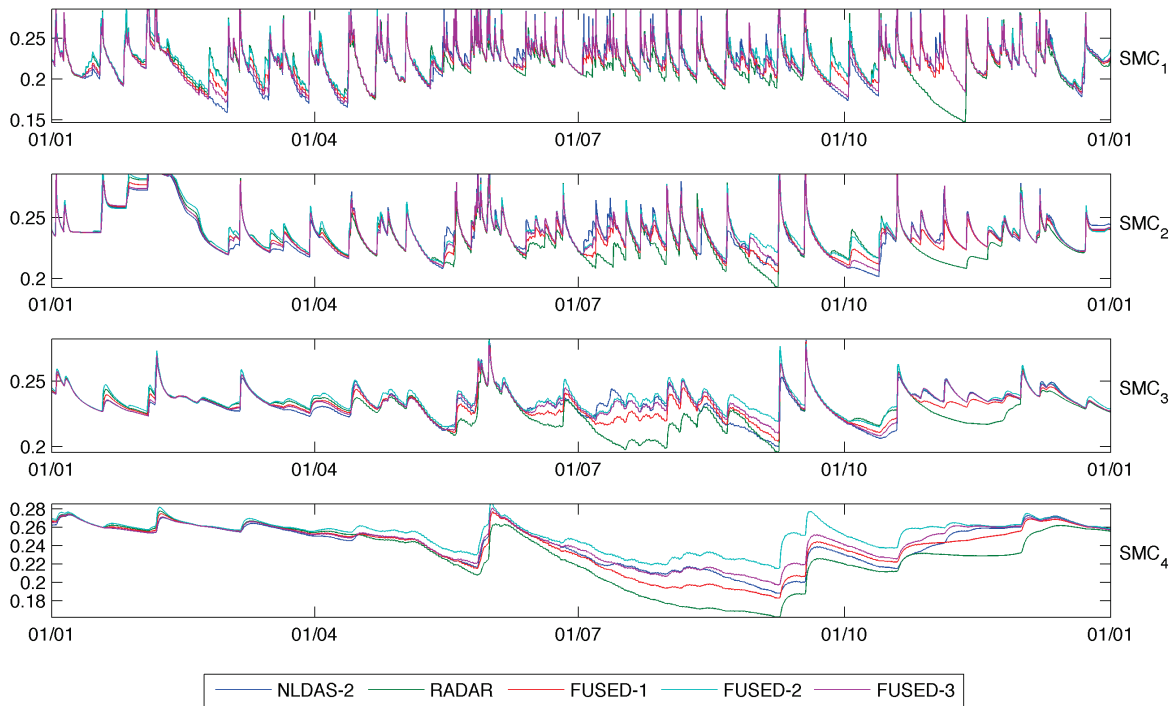


Figure 5.42 Spatial average of simulated soil moisture contents of the 1st, 2nd, 3rd and 4th layer (SMC₁, SMC₂, SMC₃ and SMC₄) over CYCK2 watershed in 2004 with NLDAS-2, RADAR, FUSED-1, FUSED-2 and FUSED-3 precipitation inputs. The unit of soil moisture is volumetric ratio (m³/m³).

In DBVO1 watershed (Figure 5.43), we have the following findings:

- 1) Significant differences between simulated SMCs can be found in the 1st, the 2nd, the 3rd and the 4th layers, especially during the period from July to December.
- 2) For most of the time, the SMCs simulated with FUSED-2 data are considerably higher than others, especially in the 3rd layer.

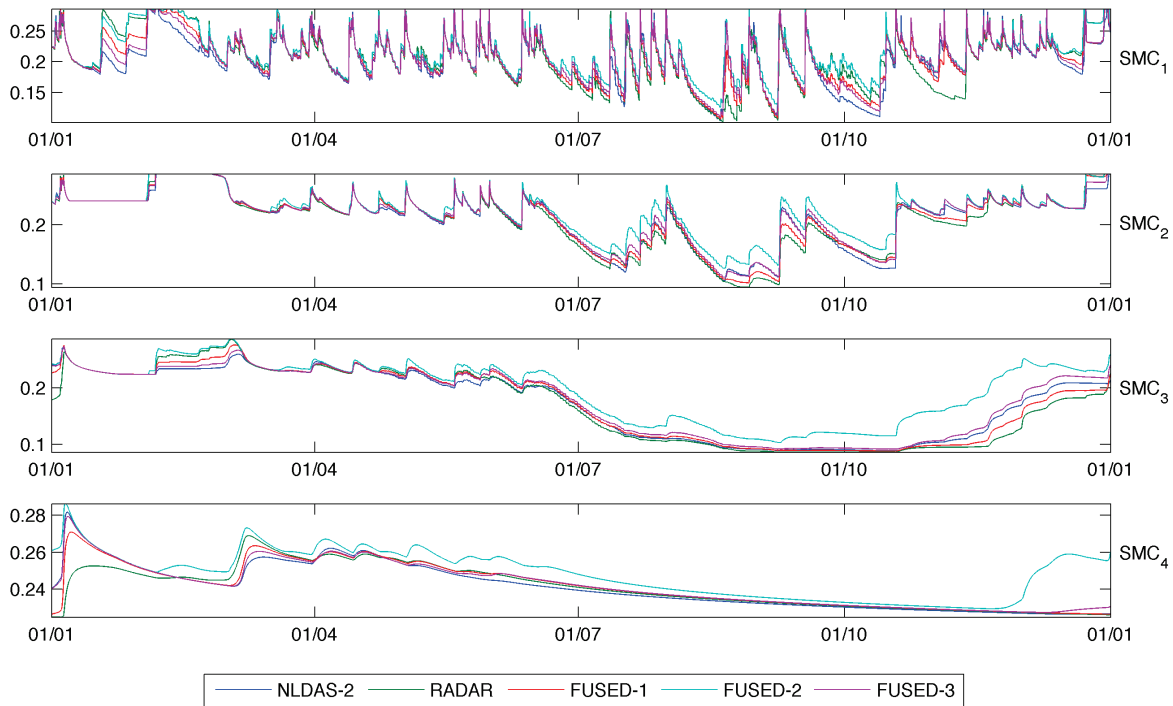


Figure 5.43 Spatial average of simulated soil moisture contents of the 1st, 2nd, 3rd and 4th layer (SMC₁, SMC₂, SMC₃ and SMC₄) over DBVO1 watershed in 2004 with NLDAS-2, RADAR, FUSED-1, FUSED-2 and FUSED-3 precipitation inputs. The unit of soil moisture is volumetric ratio (m^3/m^3).

In ELRP1 watershed (Figure 5.44), we have the following findings:

- 1) Significant differences between simulated SMCs can be found in the 1st, the 2nd, the 3rd and the 4th layers, especially the 3rd and the 4th layers.
- 2) In the 3rd and the 4th layers, simulated SMCs with FUSED-2 data are significantly higher than others in the wetting periods of soil moisture.

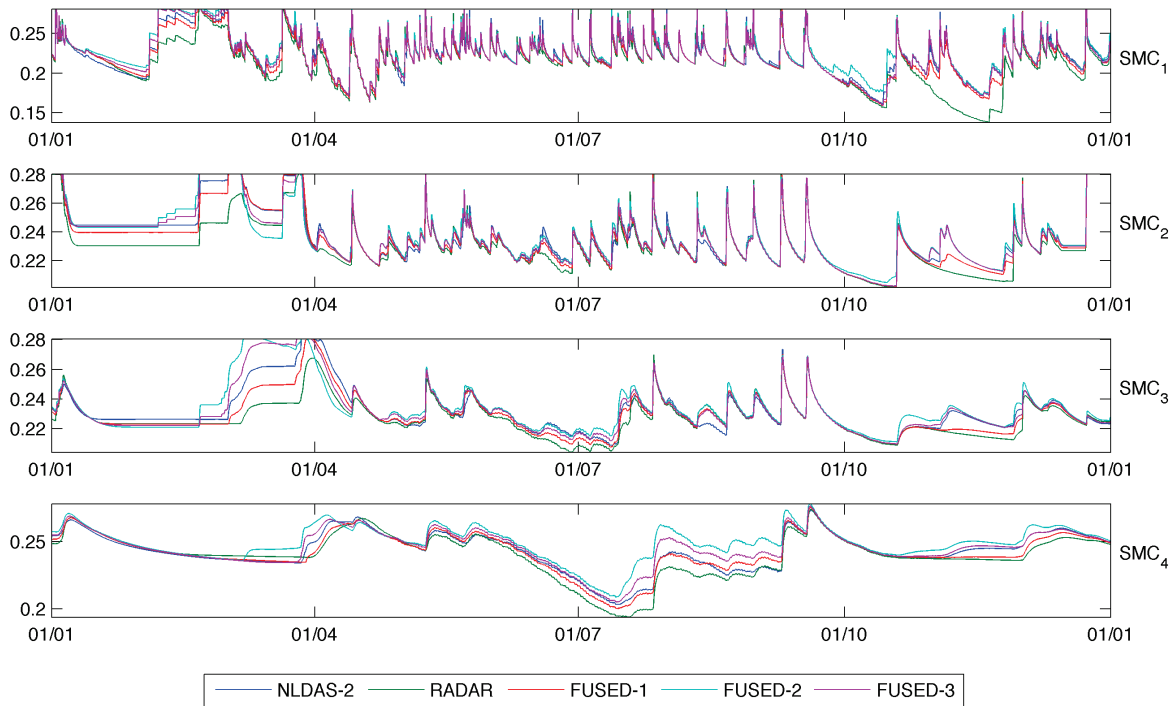


Figure 5.44 Spatial average of simulated soil moisture contents of the 1st, 2nd, 3rd and 4th layer (SMC₁, SMC₂, SMC₃ and SMC₄) over ELRP1 watershed in 2004 with NLDAS-2, RADAR, FUSED-1, FUSED-2 and FUSED-3 precipitation inputs. The unit of soil moisture is volumetric ratio (m^3/m^3).

In FDYO1 watershed (Figure 5.45), we have the following findings:

- 1) Significant differences between simulated SMCs can be found in the 1st, the 2nd, the 3rd and the 4th layers, especially the 2nd, the 3rd and the 4th layers.
- 2) In the 2nd and the 3rd layers, SMCs simulated with FUSED-2 data are significantly higher than others in the dry down periods of soil moisture. In the 4th layer, SMCs simulated with FUSED-2 data are significantly higher than others in the wetting period of soil moisture, e.g. December.

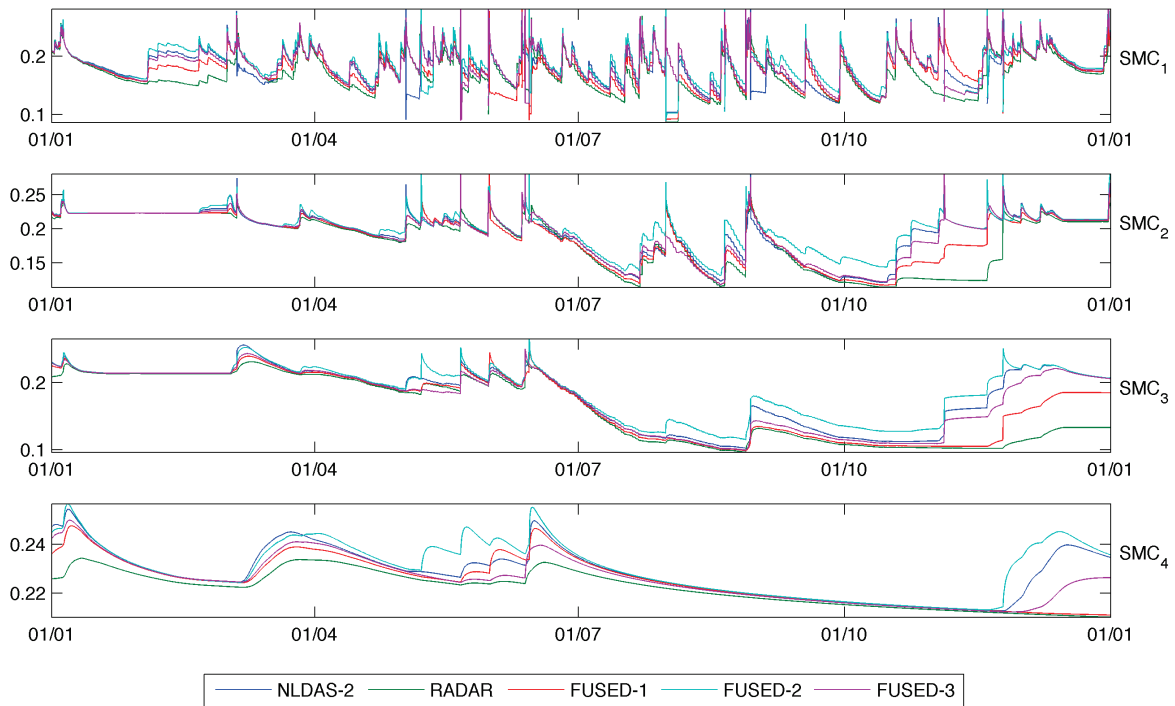


Figure 5.45 Spatial average of simulated soil moisture contents of the 1st, 2nd, 3rd and 4th layer (SMC₁, SMC₂, SMC₃ and SMC₄) over FDYO1 watershed in 2004 with NLDAS-2, RADAR, FUSED-1, FUSED-2 and FUSED-3 precipitation inputs. The unit of soil moisture is volumetric ratio (m³/m³).

In KINT1 watershed (Figure 5.46), we have the following findings:

- 1) Even though the simulated hydrographs with NLDAS-2, RADAR, FUSED-1 and FUSED-3 are very close, considerable differences still exist between SMCs simulated with these five precipitation inputs, especially during the period from July to November.

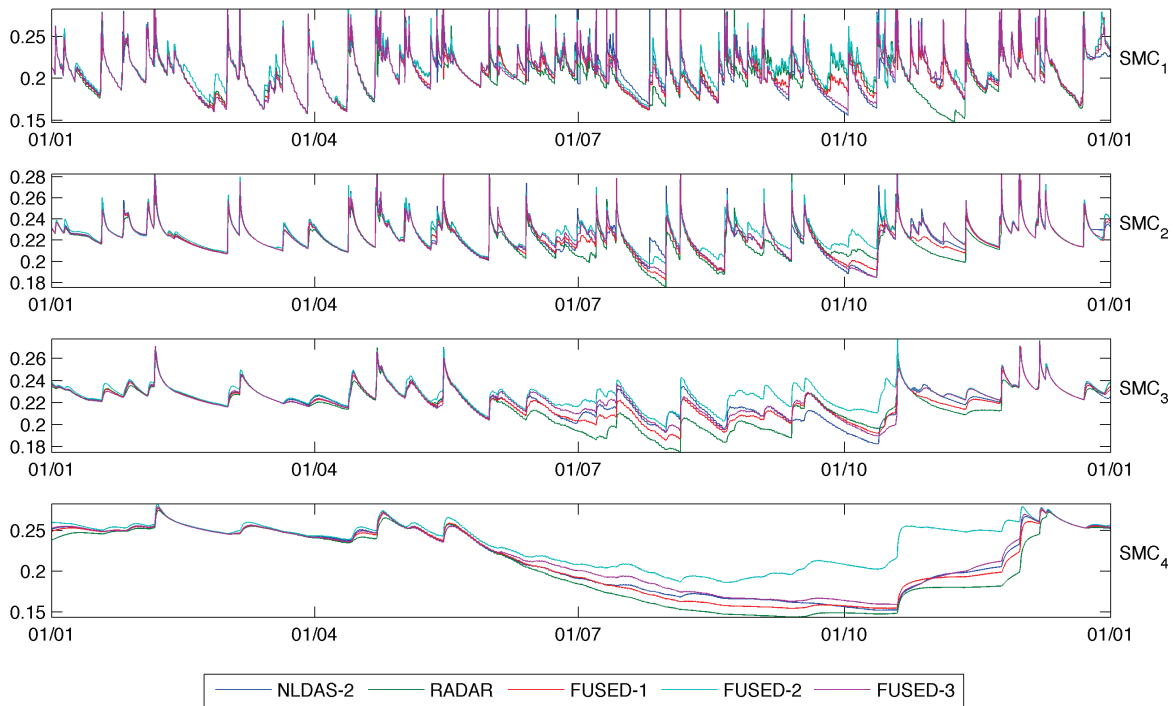


Figure 5.46 Spatial average of simulated soil moisture contents of the 1st, 2nd, 3rd and 4th layer (SMC₁, SMC₂, SMC₃ and SMC₄) over KINT1 watershed in 2004 with NLDAS-2, RADAR, FUSED-1, FUSED-2 and FUSED-3 precipitation inputs. The unit of soil moisture is volumetric ratio (m³/m³).

In NHSO1 watershed (Figure 5.47), we have the following findings:

- 1) Significant differences between simulated SMCs can be found in the 1st, the 2nd, the 3rd and the 4th layers, especially the 3rd and the 4th layers.
- 2) In the 4th layer, SMCs simulated with FUSED-2 data are higher than others during most time of the year.

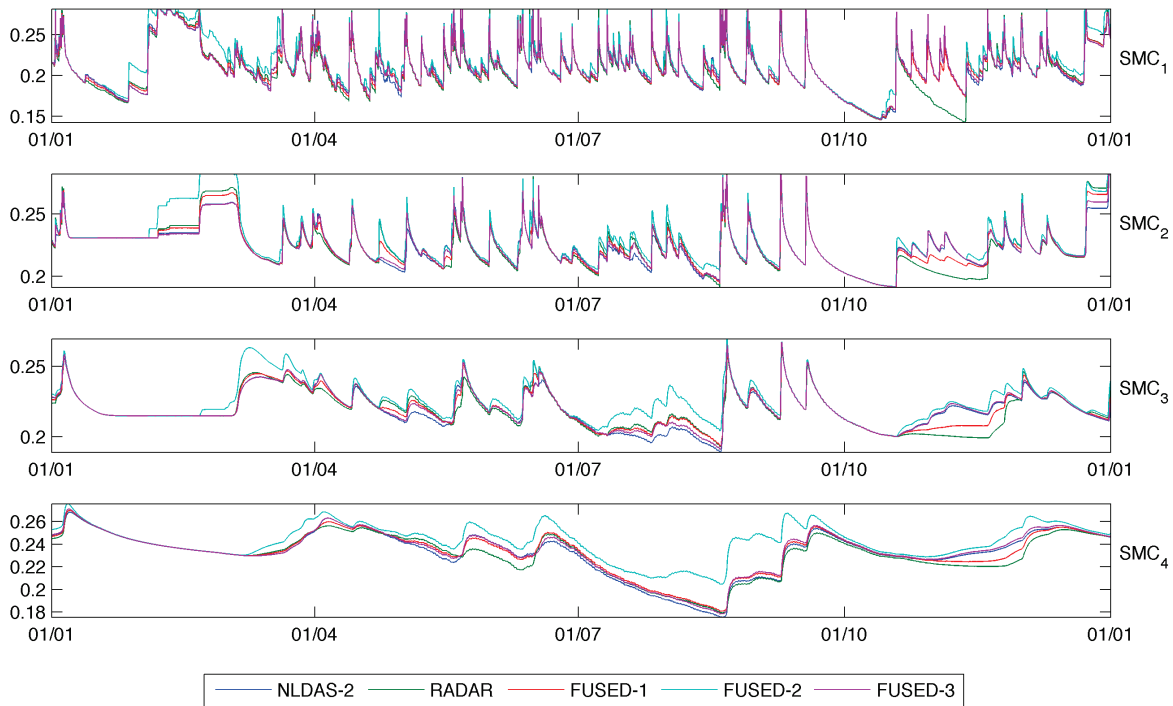


Figure 5.47 Spatial average of simulated soil moisture contents of the 1st, 2nd, 3rd and 4th layer (SMC₁, SMC₂, SMC₃ and SMC₄) over NHSO1 watershed in 2004 with NLDAS-2, RADAR, FUSED-1, FUSED-2 and FUSED-3 precipitation inputs. The unit of soil moisture is volumetric ratio (m^3/m^3).

In PSNW2 watershed (Figure 5.48), we have the following findings:

- 1) The SMCs simulated with RADAR data are significantly lower than others in the 4 layers during most time of the year. No more analyses are needed in this watershed since fused precipitation data have poor reliability than NLDAS-2 data and RADAR severely underestimates precipitation.

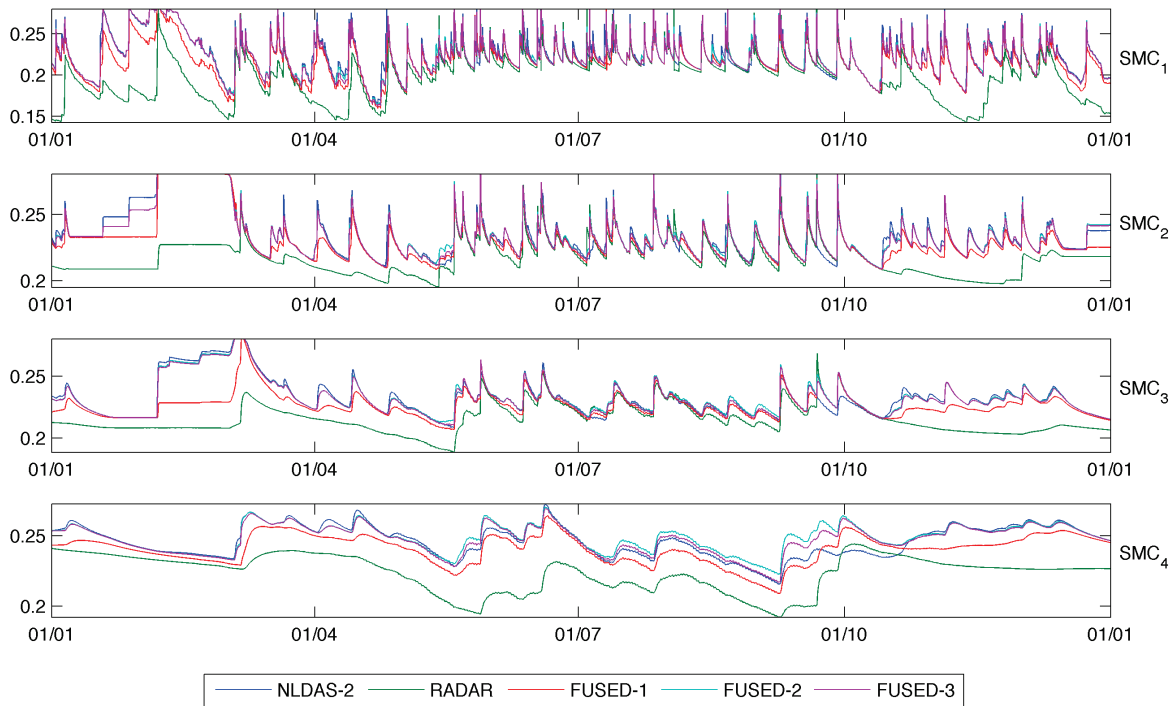


Figure 5.48 Spatial average of simulated soil moisture contents of the 1st, 2nd, 3rd and 4th layer (SMC₁, SMC₂, SMC₃ and SMC₄) over PSNW2 watershed in 2004 with NLDAS-2, RADAR, FUSED-1, FUSED-2 and FUSED-3 precipitation inputs. The unit of soil moisture is volumetric ratio (m^3/m^3).

In SERI3 watershed (Figure 5.49), we have the following findings:

- 1) Considerable differences between SMCs simulated with NLDAS-2, RADAR, FUSED-1 and FUSED-3 data can be found in four layers even though the simulated hydrographs with these four precipitation inputs are equally good.

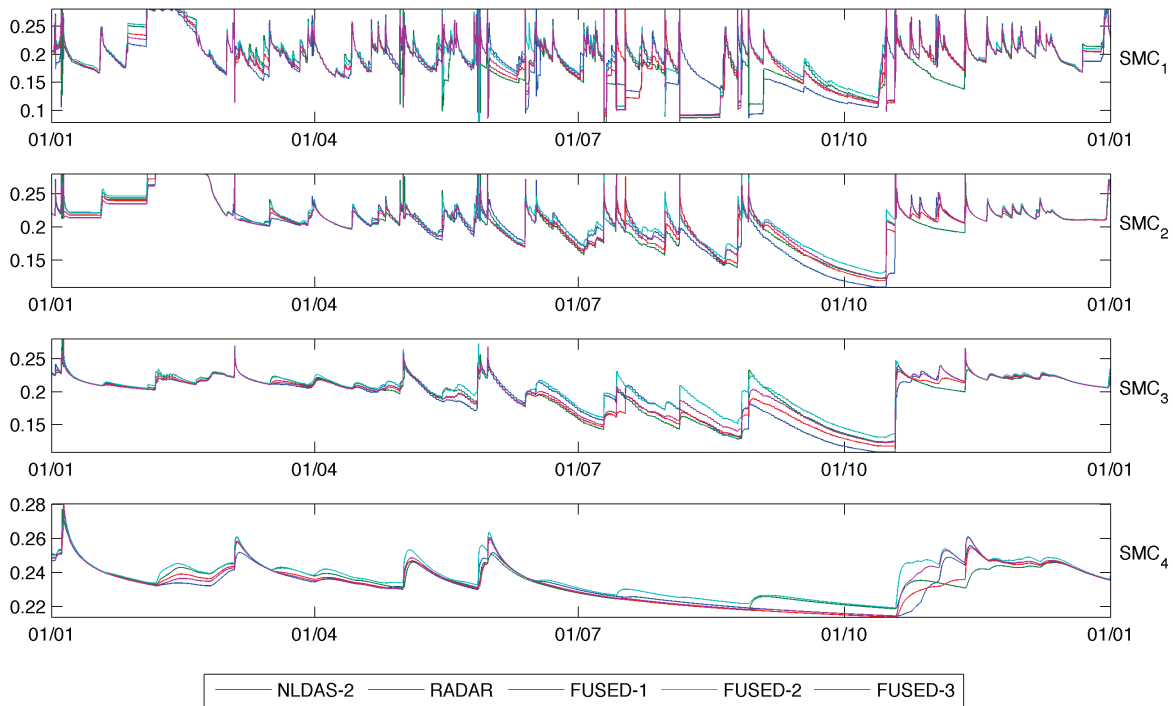


Figure 5.49 Spatial average of simulated soil moisture contents of the 1st, 2nd, 3rd and 4th layer (SMC₁, SMC₂, SMC₃ and SMC₄) over SERI3 watershed in 2004 with NLDAS-2, RADAR, FUSED-1, FUSED-2 and FUSED-3 precipitation inputs. The unit of soil moisture is volumetric ratio (m^3/m^3).

Despite the differences obtained at each watershed, common features of simulated SMCs can be found in all watersheds. For different soil layers, the influences of precipitation data fusion on simulated SMCs vary at different time scales. For the 1st layer, most influences are just kept in the dry-down period of SMC. However, for the other three layers, most differences from precipitation data fusion are getting smaller in the dry-down period and those differences will vanish once all simulated SMCs reach to the wilting point of soil. Precipitation event may also sweep out the differences made by precipitation data fusion. If precipitation is heavy enough to make the 1st soil layer saturated, the differences of simulated SMCs will vanish too. For deeper layers, the time scales of influences are getting longer. This is because impacts of precipitation

data fusion can be accumulated in deeper layers. Therefore, seasonal patterns are shown in the differences of SMC in the 4th layer.

As shown in Table 5.16, in terms of streamflow simulation, precipitation data fusion makes essential changes in some experimental watersheds but makes negligible changes in some other experimental watersheds. ALDW2 watershed and SERI3 watershed are selected as the representatives of watersheds with essential changes and negligible changes. Figure 5.50 and Figure 5.51 show snapshots of the simulated SMCs in the four layers of Noah LSM with the five precipitation inputs in these two watersheds. The time of the two snapshots is 08/01/2004 17:00 (UTC). For both watersheds, there are a long dry-down periods before this time. Therefore, the spatial patterns of simulated SMCs have smaller differences than average levels. For ALDW2 watershed, differences between spatial patterns can be seen from simulated SMCs of the four layers. The differences are getting larger from the top layer to the bottom layer. In addition, it also clearly shows that the spatial patterns of SMCs simulated with NLDAS-2 data and RADAR data have been mingled into the spatial patterns of SMCs simulated with fused precipitation data. For SERI3 watershed, the differences are smaller than those in ALDW2 watershed, but are still noticeable. The findings from Figure 5.50 and Figure 5.51 indicate that the spatial pattern and the average magnitude of RADAR data also can be improved through fusing NLDAS-2 precipitation data.

In summary, we include that significant differences of simulated SMCs can be obtained with fused precipitation data compared with those simulated with NLDAS-2 data or RADAR data. In other words, we can improve SMC simulations if the corresponding NSEs of fused precipitation data are higher than the NSE of NLDAS-2 or RADAR data.

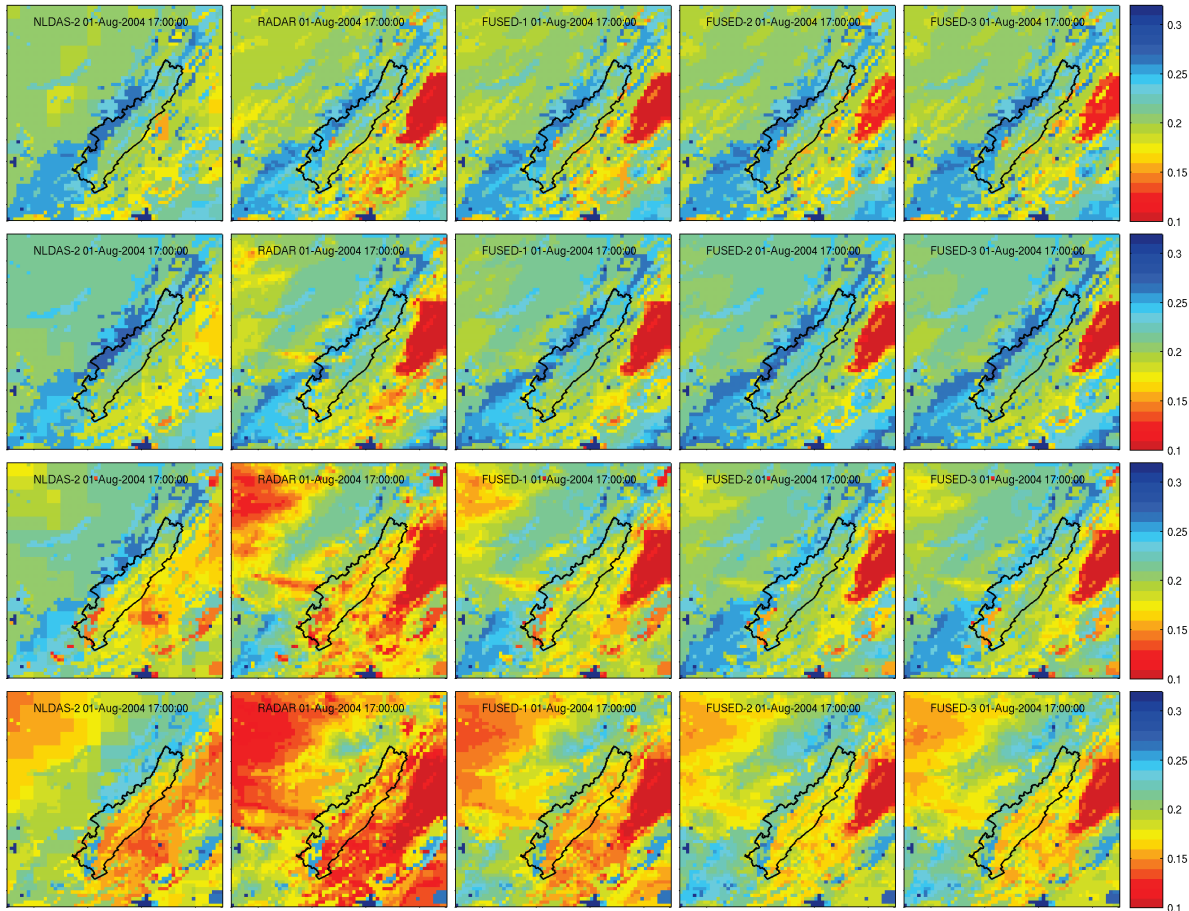


Figure 5.50 Simulated soil moisture contents of the 1st, 2nd, 3rd and 4th layer of Noah LSM in ALDW2 watershed at 08/01/2004 17:00:00 (UTC time) with NLDAS-2, RADAR, FUSED-1, FUSED-2 and FUSED-3 precipitation inputs. From top to bottom, the four rows are corresponding to the four layers; from left to right, the five columns are corresponding to the five precipitation inputs.

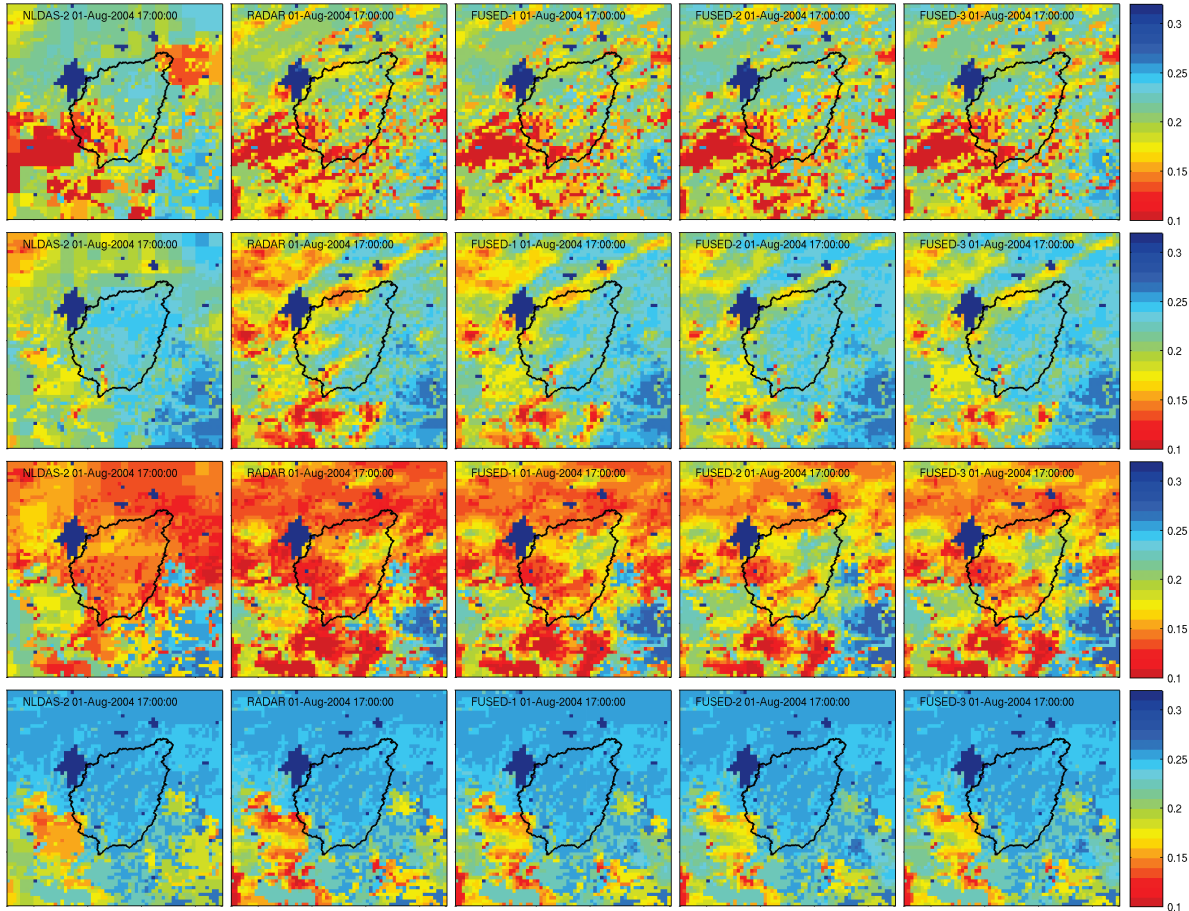


Figure 5.51 Simulated soil moisture contents of the 1st, 2nd, 3rd and 4th layer of Noah LSM in SERI3 watershed at 08/01/2004 17:00:00 (UTC time) with NLDAS-2, RADAR, FUSED-1, FUSED-2 and FUSED-3 precipitation inputs. From top to bottom, the four rows are corresponding to the four layers; from left to right, the five columns are corresponding to the five precipitation inputs.

5.5.3 Assessment with evapotranspiration simulations

The assessment of precipitation data fusion with evapotranspiration simulation is conducted using the same assessment strategy for soil moisture simulation. Noah LSM simulates a number of evaporation and transpiration terms, including evaporation from the intercepted water by canopy, sublimation of snow, direct evaporation from bare soil, and transpirations from

soil layers of root zone. In this section, we will assess the actual evapotranspiration (ETA), which is the sum of all the above-mentioned terms. If there are considerable differences between simulated ETAs, either over time or over space, we believe that the precipitation data with the highest NSE make effective improvements in ETA compared with other precipitation data.

The differences between simulated ETA over time is demonstrated in Figure 5.52 to Figure 5.65, which plot the spatial average of daily ETA series over the 14 experimental watersheds during the time of February, May, August, and November of 2004. Generally, considerable differences of simulated ETA can be found in each of the 14 plots. For the EAT series in May and August, the differences are seem to be small in most of plots. However, the differences are actually larger than the differences in February and November because the ranges of the Y-axes in the subplots of May and August are much lager than those in the subplots of February and November. In conclusion, considerable differences between simulated ETA series can be found in all of the 14 experimental watersheds including those with negligible streamflow improvements made through precipitation data fusion.

Once again, as the representatives of watersheds with essential improvements in streamflow simulation and watersheds with negligible improvements in streamflow simulation, ALDW2 watershed and SERI3 watershed are selected to run Noah LSM at 1/32 degree resolution. Simulations are conducted in square regions, which enclose these two watersheds respectively. Snapshots of simulated ETA on 08/17/2004 are given in Figure 5.66 and Figure 5.67 for ALDS2 site and SERI3 site respectively. The times marked on the snapshots are UTC time while the daylight saving time of these two sites are four hours after UTC times.

Considerable differences can be found between the spatial patterns of simulated ETA in both watersheds. For both sites, there are no precipitation events since at least 24 hours ahead 08/17/2004. This means that the differences between the spatial patterns of simulated ETA is caused by the differences of simulated SMCs due to precipitation fusion. In other words, there are always differences between simulated ETAs if simulated SMCs are different. Due to the long memory of soil moisture contents on precipitation inputs, the differences between precipitation data also have long-time influences on simulated ETA.

In summary, considerable differences have been found in simulated ETA time series over the 14 experimental watersheds and in the spatial patterns of ETA snapshots over space in ALDW2 and SERI3 watersheds. Based on these findings, it is reasonable to infer that effective improvements of ETA simulation can be made through precipitation data fusion.

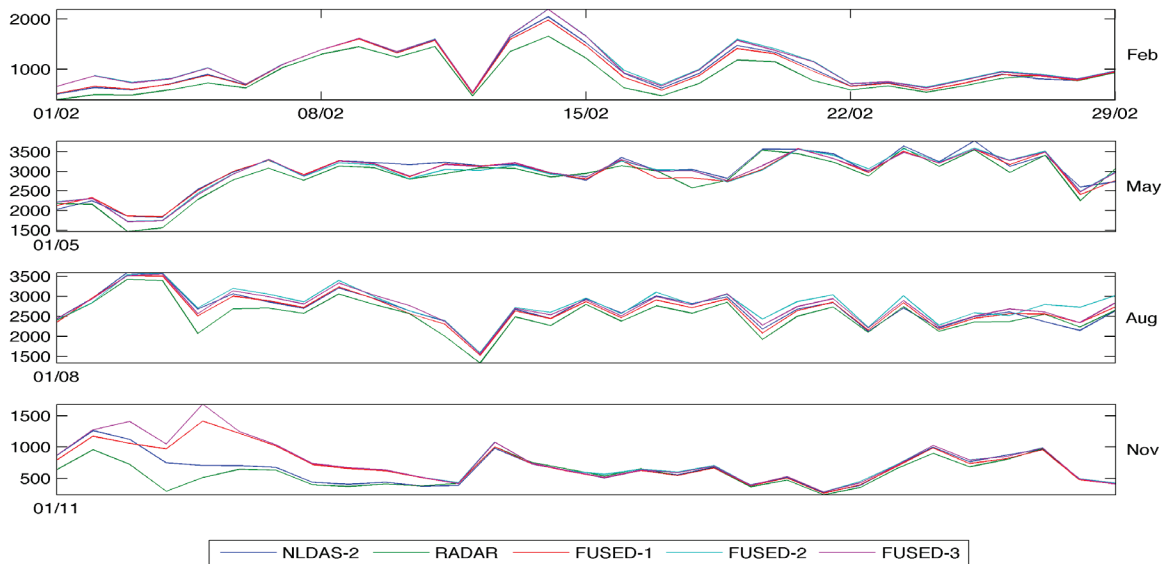


Figure 5.52 Spatial average of daily total evapotranspiration simulated by Noah LSM with NLDAS-2, RADAR, FUSED-1, FUSED-2 and FUSED-3 precipitation inputs over ALDW2 watershed during February, May, August and November of 2004. The Unit is W/m^3 .

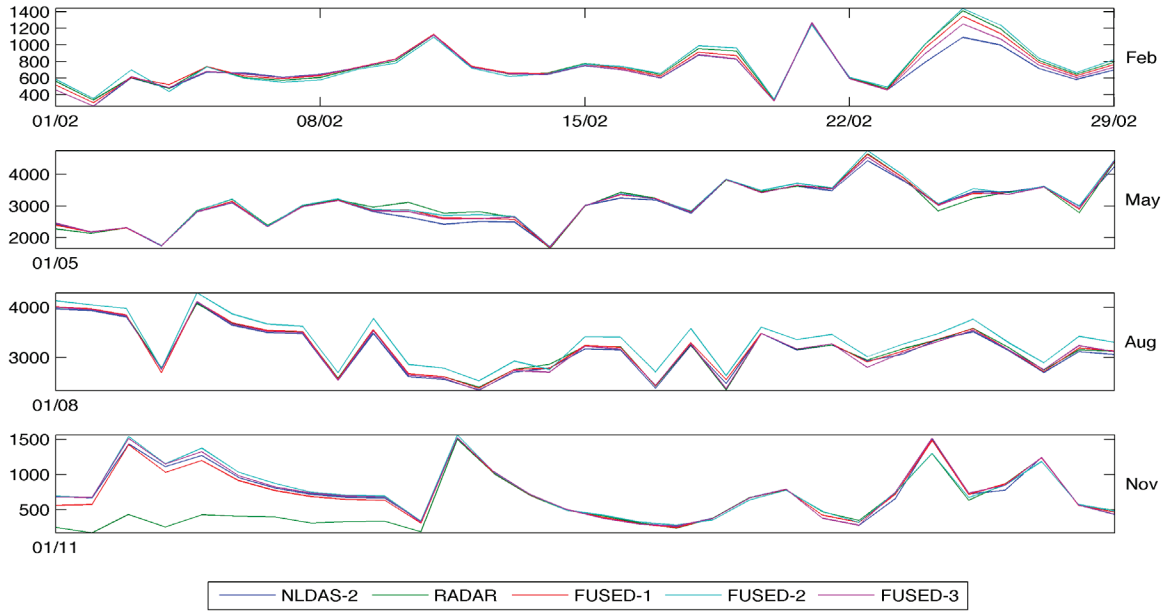


Figure 5.53 Spatial average of daily total evapotranspiration simulated by Noah LSM with NLDAS-2, RADAR, FUSED-1, FUSED-2 and FUSED-3 precipitation inputs over ALPI3 watershed during February, May, August and November of 2004. The Unit is W/m^3 .

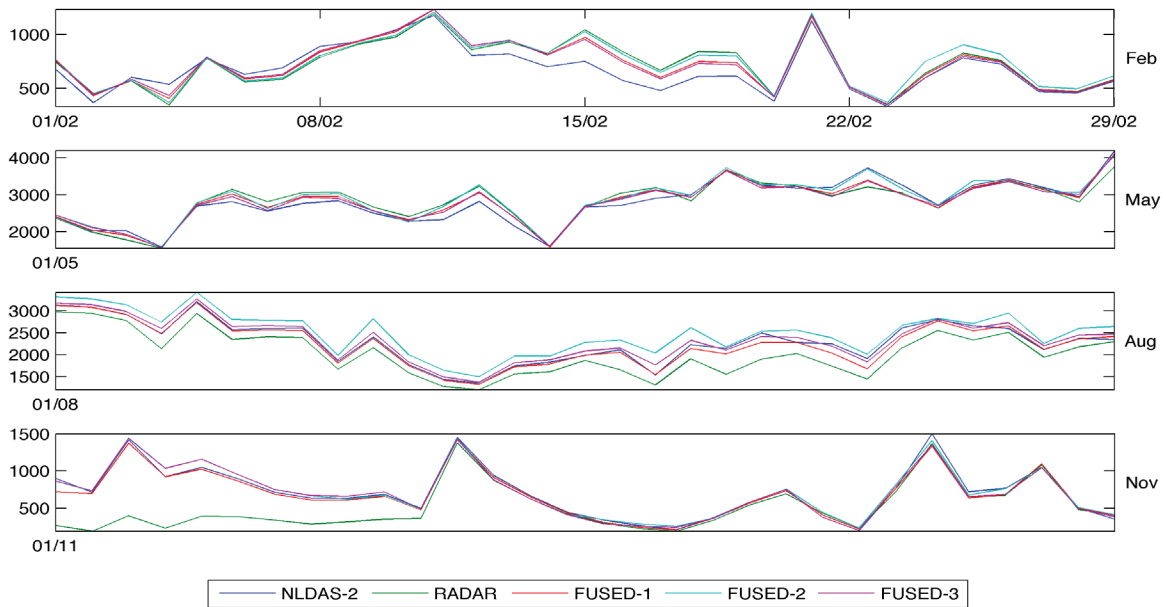


Figure 5.54 Spatial average of daily total evapotranspiration simulated by Noah LSM with NLDAS-2, RADAR, FUSED-1, FUSED-2 and FUSED-3 precipitation inputs over BAKI3 watershed during February, May, August and November of 2004. The Unit is W/m^3 .

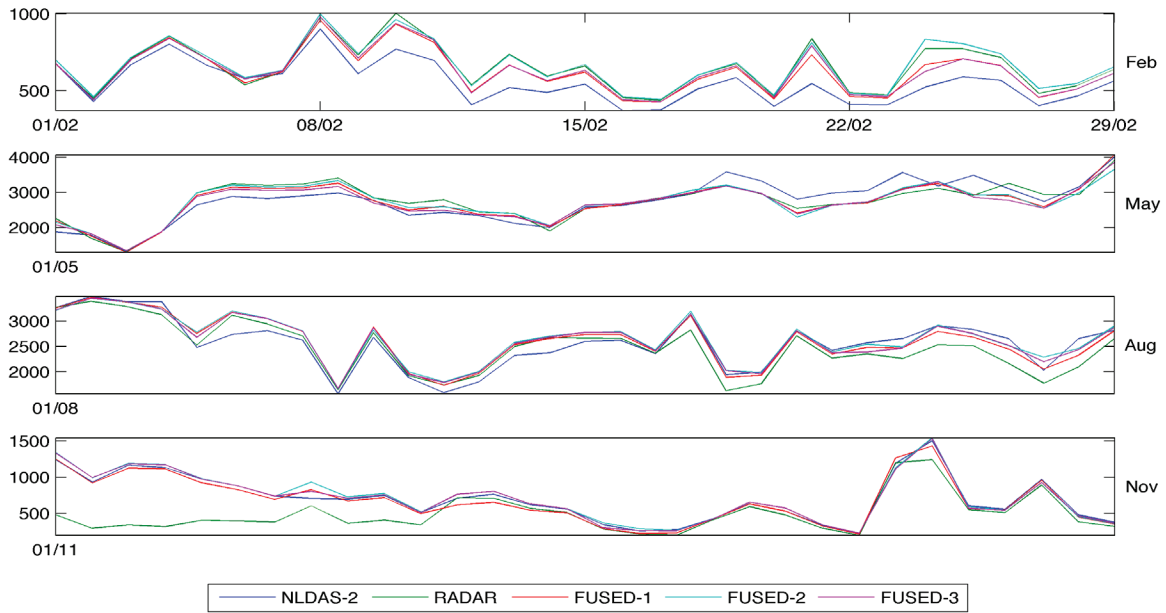


Figure 5.55 Spatial average of daily total evapotranspiration simulated by Noah LSM with NLDAS-2, RADAR, FUSED-1, FUSED-2 and FUSED-3 precipitation inputs over BSNK2 watershed during February, May, August and November of 2004. The Unit is W/m^3 .

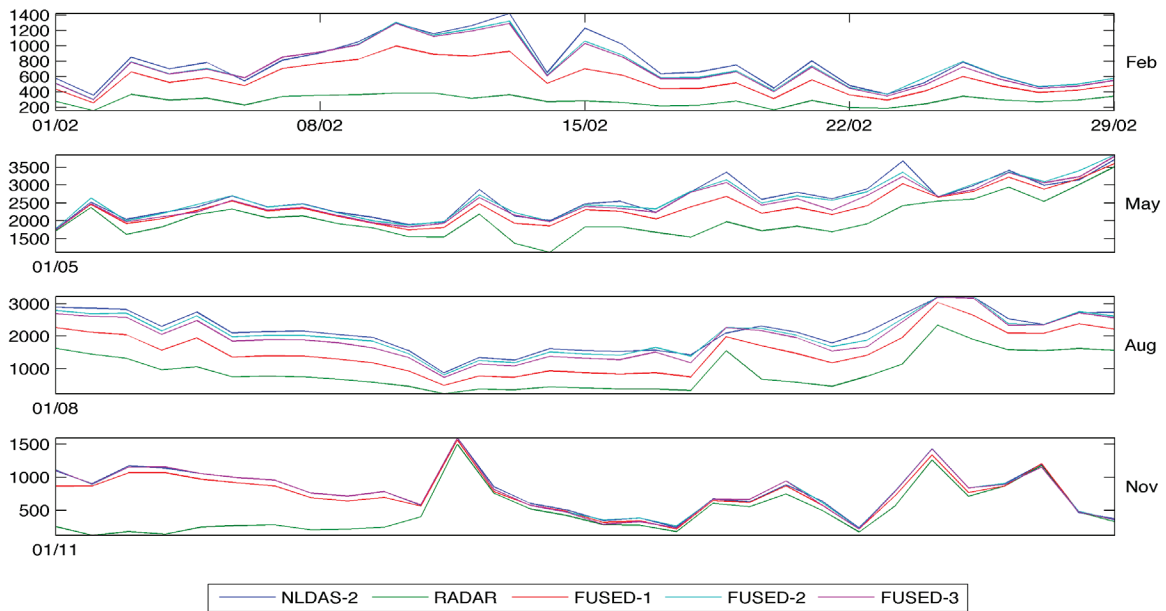


Figure 5.56 Spatial average of daily total evapotranspiration simulated by Noah LSM with NLDAS-2, RADAR, FUSED-1, FUSED-2 and FUSED-3 precipitation inputs over CLAI2 watershed during February, May, August and November of 2004. The Unit is W/m^3 .

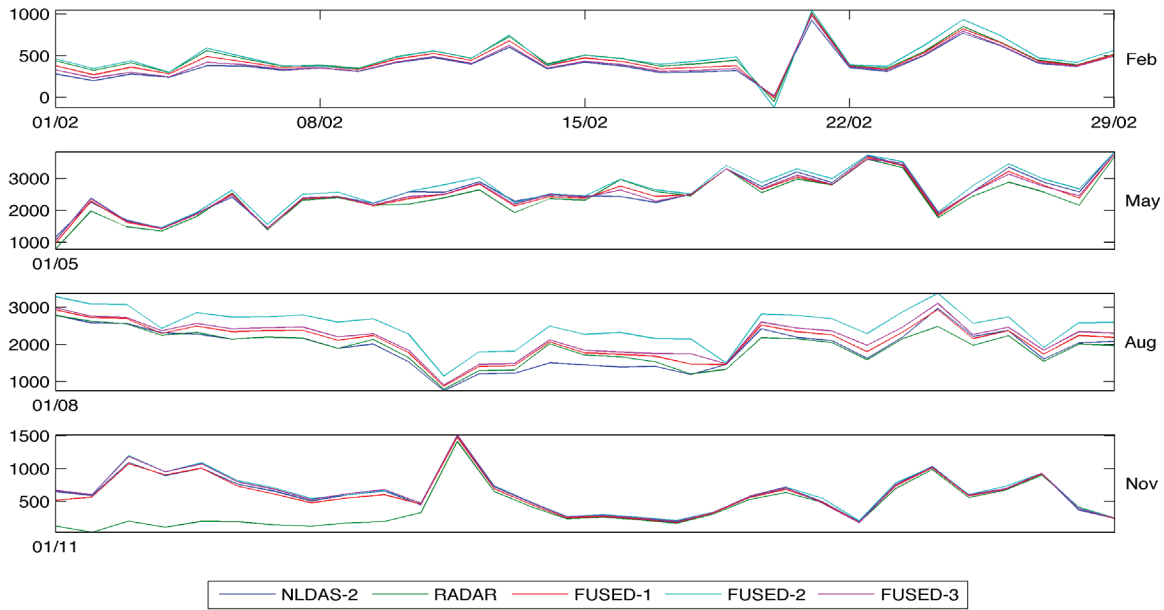


Figure 5.57 Spatial average of daily total evapotranspiration simulated by Noah LSM with NLDAS-2, RADAR, FUSED-1, FUSED-2 and FUSED-3 precipitation inputs over CRWI3 watershed during February, May, August and November of 2004. The Unit is W/m^3 .

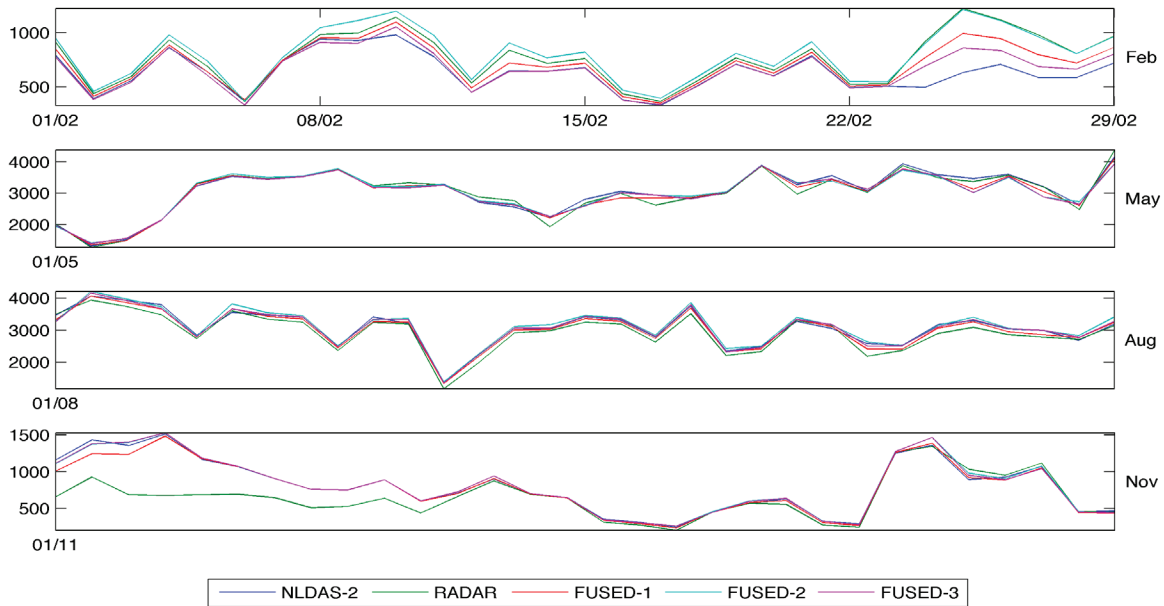


Figure 5.58 Spatial average of daily total evapotranspiration simulated by Noah LSM with NLDAS-2, RADAR, FUSED-1, FUSED-2 and FUSED-3 precipitation inputs over CYCK2 watershed during February, May, August and November of 2004. The Unit is W/m^3 .

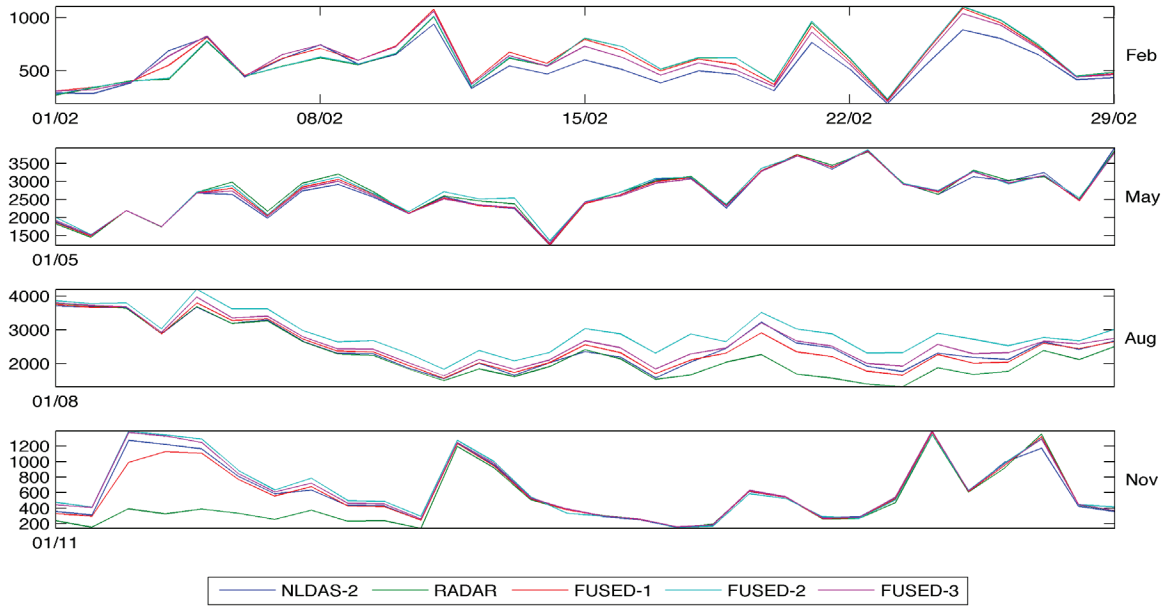


Figure 5.59 Spatial average of daily total evapotranspiration simulated by Noah LSM with NLDAS-2, RADAR, FUSED-1, FUSED-2 and FUSED-3 precipitation inputs over DBO1 watershed during February, May, August and November of 2004. The Unit is W/m^3 .

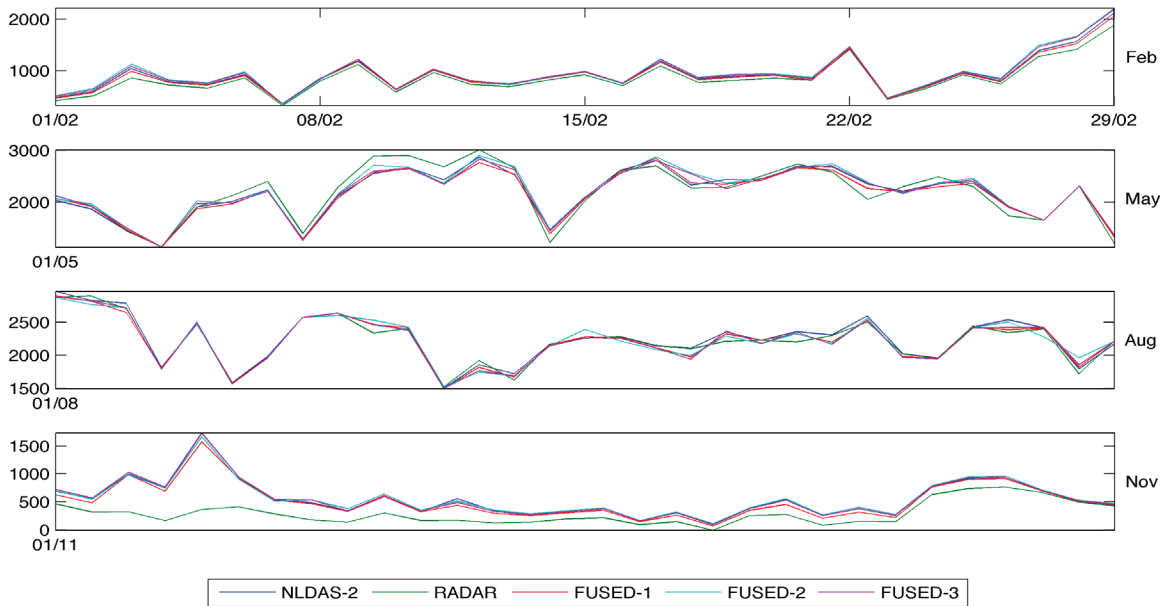


Figure 5.60 Spatial average of daily total evapotranspiration simulated by Noah LSM with NLDAS-2, RADAR, FUSED-1, FUSED-2 and FUSED-3 precipitation inputs over ELRP1 watershed during February, May, August and November of 2004. The Unit is W/m^3 .

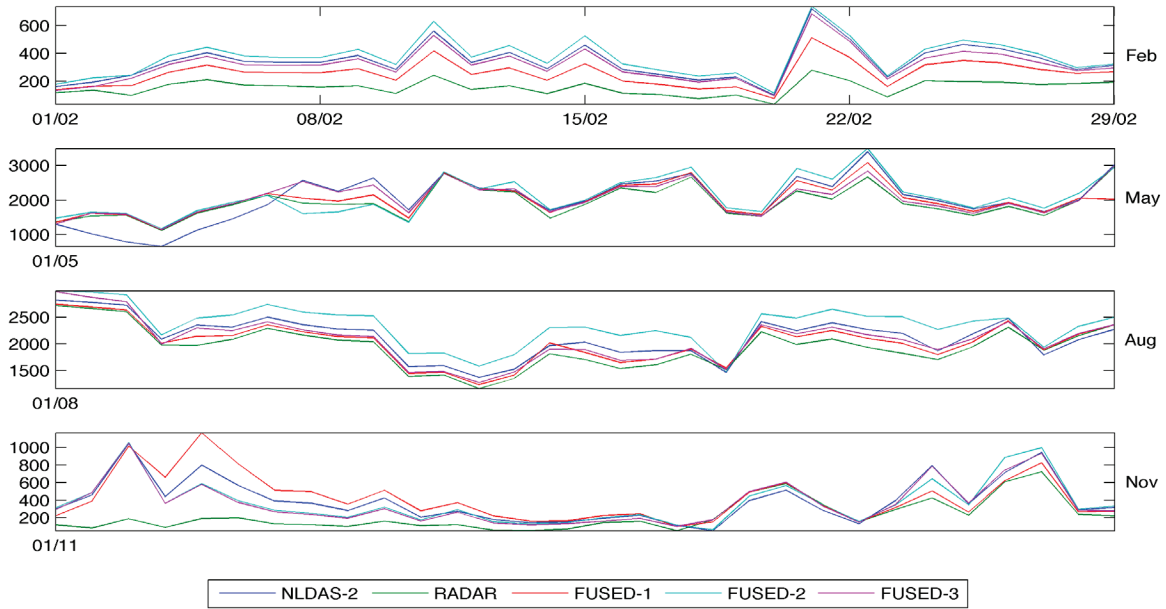


Figure 5.61 Spatial average of daily total evapotranspiration simulated by Noah LSM with NLDAS-2, RADAR, FUSED-1, FUSED-2 and FUSED-3 precipitation inputs over FDYO1 watershed during February, May, August and November of 2004. The Unit is W/m^3 .

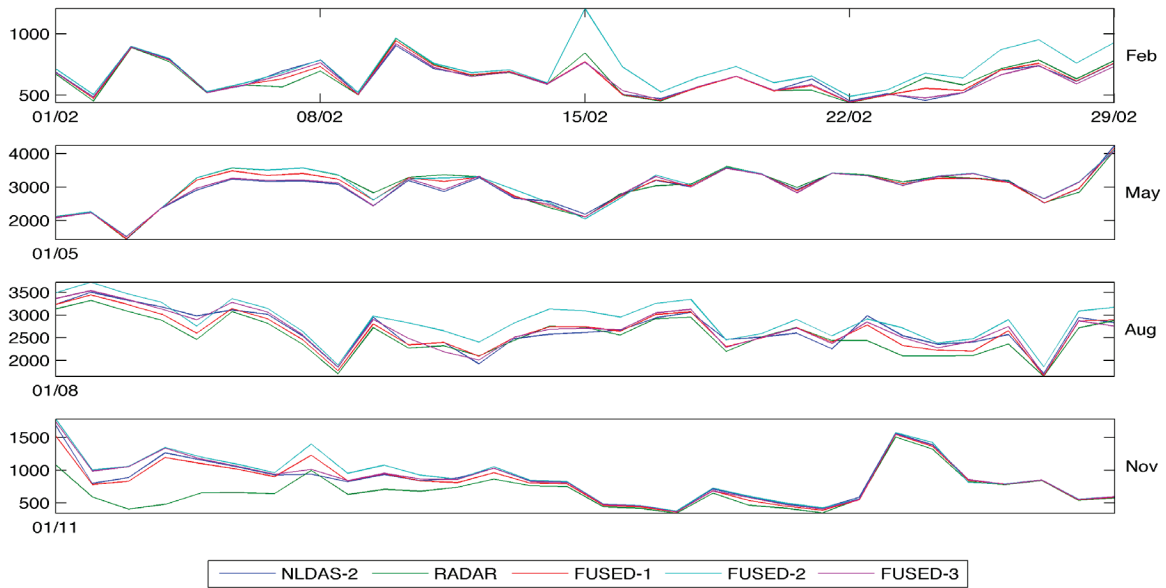


Figure 5.62 Spatial average of daily total evapotranspiration simulated by Noah LSM with NLDAS-2, RADAR, FUSED-1, FUSED-2 and FUSED-3 precipitation inputs over KINT1 watershed during February, May, August and November of 2004. The Unit is W/m^3 .

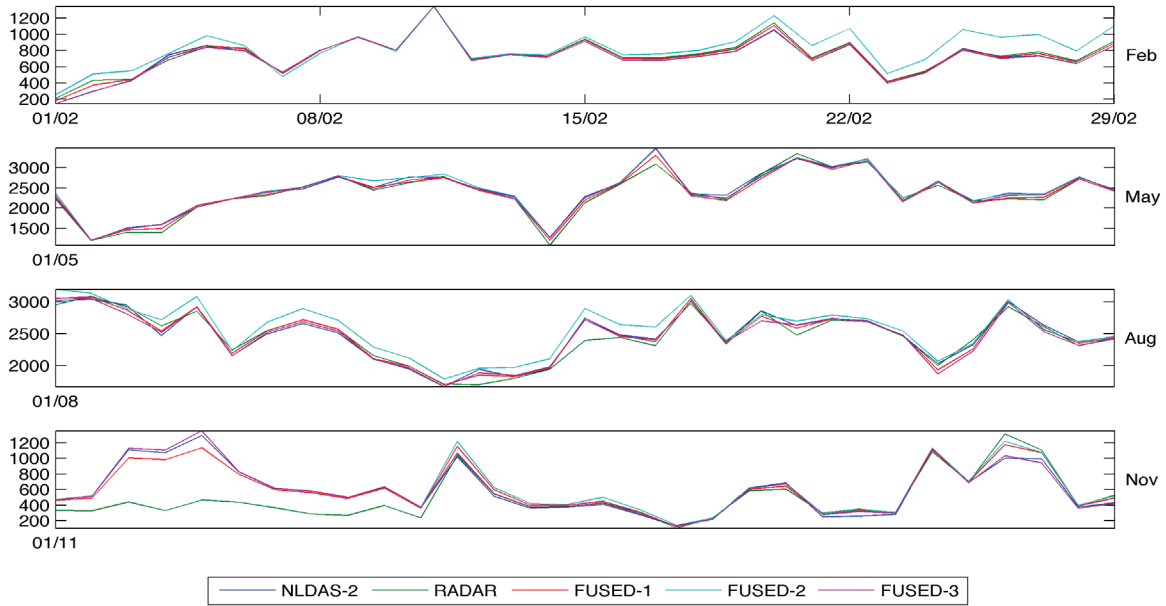


Figure 5.63 Spatial average of daily total evapotranspiration simulated by Noah LSM with NLDAS-2, RADAR, FUSED-1, FUSED-2 and FUSED-3 precipitation inputs over NHSO1 watershed during February, May, August and November of 2004. The Unit is W/m^3 .

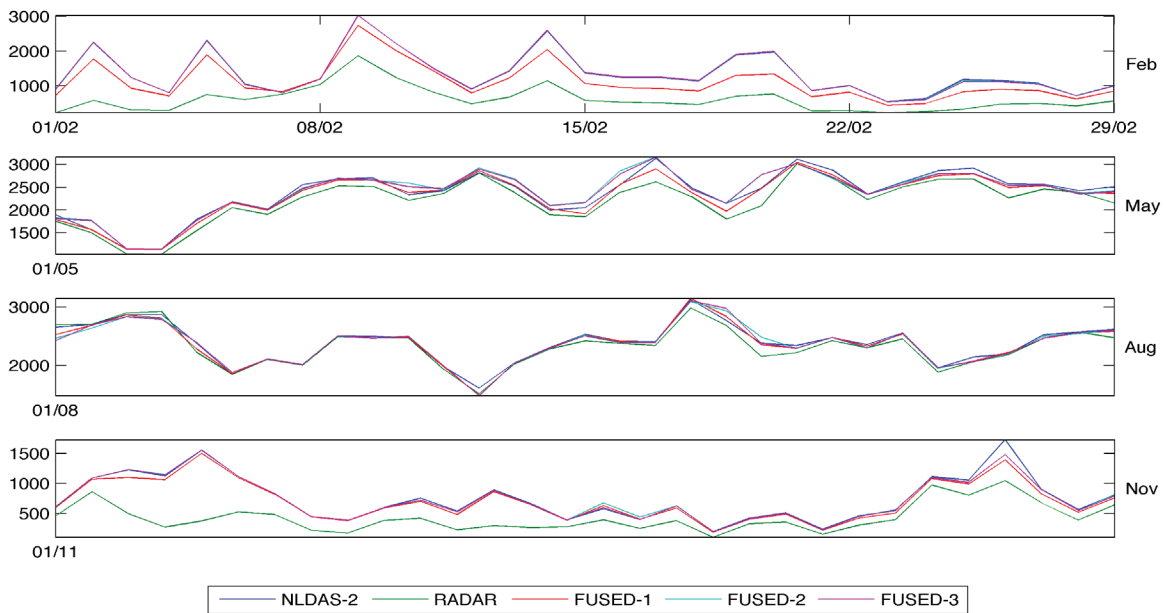


Figure 5.64 Spatial average of daily total evapotranspiration simulated by Noah LSM with NLDAS-2, RADAR, FUSED-1, FUSED-2 and FUSED-3 precipitation inputs over PSNW2 watershed during February, May, August and November of 2004. The Unit is W/m^3 .

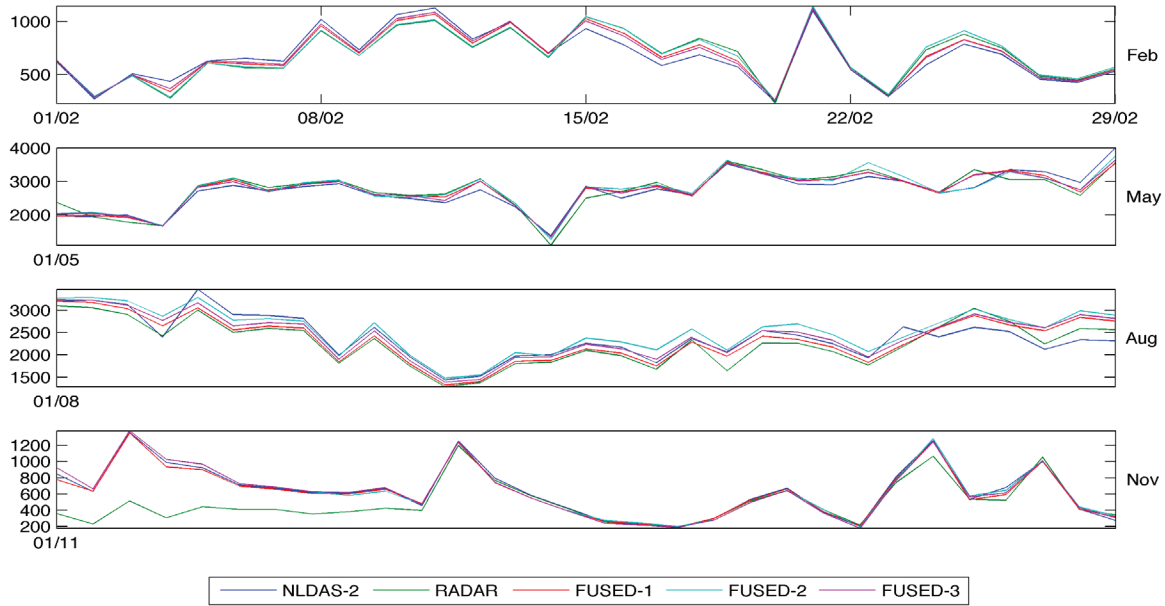


Figure 5.65 Spatial average of daily total evapotranspiration simulated by Noah LSM with NLDAS-2, RADAR, FUSED-1, FUSED-2 and FUSED-3 precipitation inputs over SERI3 watershed during February, May, August and November of 2004. The Unit is W/m^3 .

5.6 SUMMARY AND CONCLUSIONS

Precipitation is the most important input for hydrological simulation. The reliability of hydrological simulations is directly related to the quality of precipitation data. In this study, we have extensively assessed the improvements made by precipitation data fusion in hydrological simulations of 14 experimental watersheds in Ohio River Basins with Noah LSM. Due to the features of total amount and spatial pattern, NLDAS-2 data (at 1/8 degree resolution) and NEXRAD MPE data (at 4km resolution and resampled into 1/32 degree resolution, called RADAR data) are fused to derive three precipitation data products. Moreover, Multiscale

Kalman Smoother (MKS) is used in precipitation data fusion because it is good at dealing with multi-resolution data.

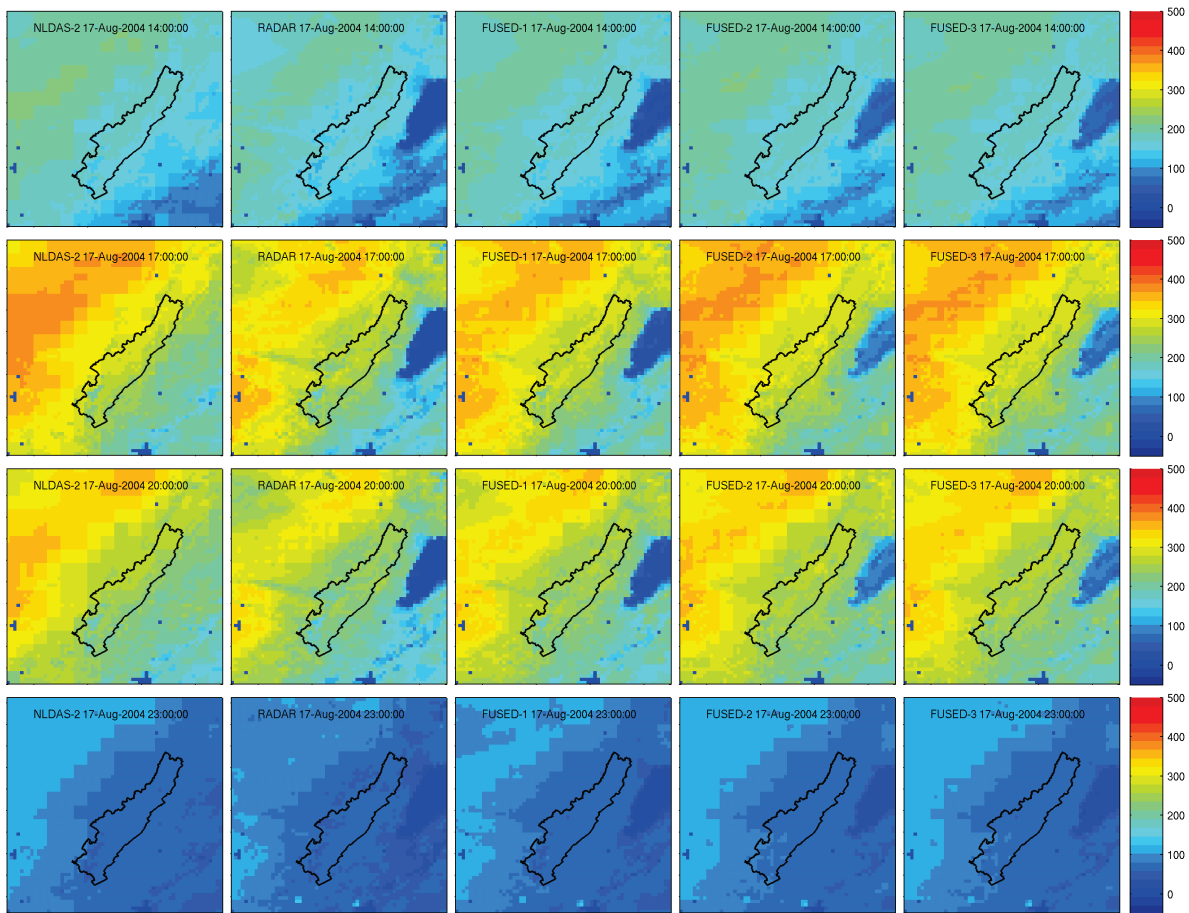


Figure 5.66 Simulated hourly total evapotranspiration by Noah LSM with NLDAS-2, RADAR, FUSED-1, FUSED-2 and FUSED-3 precipitation inputs in ALDW2 site at 14:00, 17:00, 20:00 and 23:00 of 08/17/2004 (UTC time).

Considerable differences have been found between NLDAS-2 data and RADAR data in terms of the recording of precipitation events, spatial patterns and mean magnitudes of precipitation. To be more specific, essential improvements of streamflow simulation have been made through precipitation data fusion in 21 watershed/year over 42 watershed/year. In improving NLDAS-2 data with RADAR data (at 1/32 degree resolution), the mean amount of RADAR data plays a bigger role than the spatial pattern. In addition, 19 watershed/year have

negligible changes in the streamflow simulation using fused precipitation data. There are two main reasons for negligible changes. One is that NLDAS-2 data and/or RADAR data are already very good. There is very limited room for further improvements. For example, BAKI3 in 2004 and 2005, KINT1 in 2003, 2004, and 2005, and SERI3 in 2004 and 2005 belong to this category. The other reason is that NLDAS-2 data and/or RADAR data have poor quality. For example, BAKI3 in 2003, CLAI2 in 2004 and 2005, CYCK2 in 2003 and SERI3 in 2003. There are only two watershed/year that have deteriorations. The watershed/year of CLAI2 in 2003 has slight deterioration, which is probably resulted from the poor reliability of RADAR data. The watershed/year of PSNW2 in 2005 has significant deterioration because of the very poor reliability of RADAR data. According to these findings, it can be concluded that precipitation data fusion is a statistically effective method to improve streamflow simulation.

The assessments with soil moisture simulation and evapotranspiration simulation are conducted with the same strategy. With the five precipitation inputs, simulated SMCs and ETAs have been compared **over time** (e.g. the spatial average SMC and ETA **over** the 14 experimental watersheds) and over spaces (e.g. ALDW2 site and SERI3 site). Considerable differences can be found between simulated SMCs and ETA both in terms of time series and spatial patterns. Under the assumption that once a precipitation input generates better hydrographs (i.e. larger NSEs), the SMCs and ETA simulated with this precipitation input are better than those simulated with other precipitation inputs, improvements of SMCs and ETA simulations can also be made by precipitation data fusion.

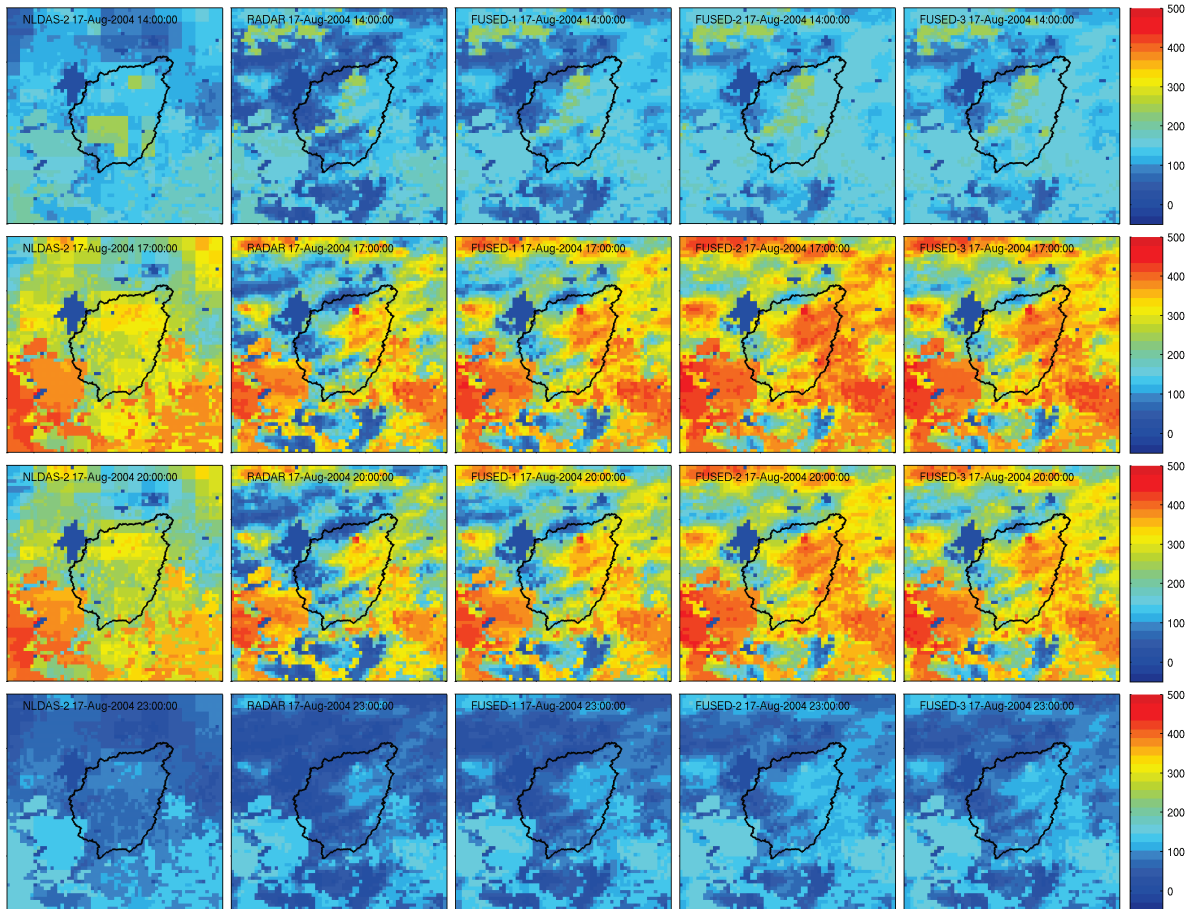


Figure 5.67 Simulated hourly total evapotranspiration by Noah LSM with NLDAS-2, RADAR, FUSED-1, FUSED-2 and FUSED-3 precipitation inputs in SERI3 site at 14:00, 17:00, 20:00 and 23:00 of 08/16/2004 (UTC time)

In general, this study shows that precipitation data fusion is a statistically effective approach to improve hydrological simulation. There are good chances that the simulations of streamflow, soil moisture and evapotranspiration can be improved by using fused precipitation data, especially for the watersheds in which either NLDAS-2 data or RADAR data are not very reliable. However, this study has the following two limitations. First, assessments with soil moistures and evapotranspiration have not been conducted with direct measurements. Future work is needed when accurate spatial measurements of soil moisture contents and

evapotranspiration are available. Second, Noah LSM may have relatively poor performance in simulating the accumulation or melting of snow since it affects the assessments of precipitation data fusion in cold season, especially for watersheds with relatively steep and very steep topographies. In the future, we may either improve the description of snow process in Noah LSM or use other LSMs with better description of snow process to assess the effectiveness of precipitation data fusion in hydrological simulations.

6.0 ASSESSMENT OF SOIL MOISTURE DATA ASSIMILATION ON HYDROLOGICAL SIMULATIONS

6.1 INTRODUCTION

At watershed scale, hydrological cycle includes the movements of water in atmosphere, vegetation, soil and river channels. These movements are interconnected by soil hydrology. Basically, soil hydrology includes the descriptions of water and heat fluxes within soil column and related boundary and initial conditions. In most of hydrological models and land surface models (LSMs), soil columns are typically divided into a number of layers, which are designed to give quick and slow responses of soil columns to atmospheric inputs. There are many state variables related to soil layers, such as soil moisture contents (SMCs) and soil layer temperatures. However, SMCs are the most important state variables, which impact runoff generation, infiltration, and evapotranspiration. Taking Noah LSM (Chen et al. 1996; Chen et al. 1997; Koren et al. 1999; Chen and Dudhia 2001; Ek et al. 2003) as an example, surface runoff and infiltration are functions of precipitation and total SMC in soil column. Baseflow is a function of the SMC of the bottom layer of soil column. Given atmospheric inputs, evapotranspiration is also a function of SMCs in soil layers of root zone. In addition, SMCs of the current time step also have influences on the SMCs and other state variables of the next time step. Therefore, SMCs are

important states of hydrological system. The accuracy of simulated SMCs directly influences other hydrological simulations.

For hydrological simulations conducted with LSMs, the accuracy of SMCs is under influence. Firstly, atmospheric inputs, especially precipitation, have significant influences on the simulation of SMCs. Results of Chapter 5.0 show that precipitation affects not only the magnitudes of simulated SMCs but also the spatial patterns of simulated SMCs. Because errors and uncertainties are unavoidable in the measurements made by meteorological stations, weather radars and weather satellites, atmospheric data are usually erroneous, which directly introduces errors in simulated SMCs with LSMs. The second aspect is the structure and the parameters of LSMs. For example, Richards' equation governs soil hydrology in most of LSMs. In order to solve the equation, LSMs need to formulate the relationship between SMC and soil water potential. There are many empirical parameterization of this relationship, such as a Brooks-Corey equation (Brooks and Corey 1966) and van Genuchten's equation (van Genuchten 1980). Such parameterization brings a considerable number of parameters to LSMs. Even though some of them can be associated with physical attributes of soil types (Cosby et al. 1984), it is still hard to accurately estimate their values due to the third factor, the heterogeneity of land surface characteristics within the computational unit of LSM, which is usually called a grid. Generally, LSMs associate land surface characteristics with soil types and vegetation types. For example, LSMs, e.g. Noah LSM and VIC LSM (Liang et al. 1994; Liang and Xie 2001; Liang and Xie 2003), assume that there is only one soil type within a grid. Because of the large size of LSM grid, it is impossible to have only one soil type over such a big area. Therefore, the soil type of the LSM grid is a kind of effective soil type or the dominant soil type in the grid. No matter what

the situation is, the parameters associated with the soil type are hard to effectively describe the heterogeneity related to soil. Due to such simplification of LSMs and the heterogeneity of land surface characteristics within LSM grid, errors are unavoidable when using SMCs simulated with LSMs to represent the average status of soil moisture at the scale of LSM grid. To sum up, errors and uncertainties exist in simulated SMCs because of these three reasons. The magnitudes of these errors and uncertainties are related to the errors in atmospheric data, model structures, model parameters, and the heterogeneity of land surface characteristics within LSM grid. In order to obtain more reliable hydrological simulations, simulation of SMCs should be first improved.

In recent years, more and more satellite derived soil moisture datasets, such as SSM/I data (Drusch et al. 1999), TMI data (Cashion et al. 2005) and AMSR-E data (Crow et al. 2001), are becoming available for hydrological applications. These data are indirect measurement of near surface SMC. The magnitudes of SMCs are derived based on the empirical relationships between satellite-measured brightness temperatures and SMC in the near-surface soil layer. Satellites measure near surface soil moisture over a large spatial area, which provides new insights about the magnitudes and the spatial patterns of SMC. However, there are also a number of limitations of satellite-derived data. The first is uncertainties in the data, which particularly come from empirical relationships used in data derivation. In addition, there are also uncertainties caused by unmodeled reflection, scattering and absorption of microwave by atmosphere and vegetation. The second is the shallow depth of satellite measurements, which usually ranges from 0 to 5 cm. To date, no satellite detects soil moisture contents in deep layers. The third is the coarse spatial resolution of satellite measurements. For examples, SSM/I has a

resolution of $69 \times 43 \text{ km}^2$ at 19 GHz; TMI has a resolution of $63 \times 37 \text{ km}^2$ at 10.65 GHz; and AMSR-E has a resolution of $75 \times 43 \text{ km}^2$ at 6.925 GHz (C-band). These resolutions are usually larger than those of hydrological simulations. Due to these limitations, satellite data are not ready to be directly applied as inputs of hydrological simulation.

Data assimilation is a technique to improve model simulation with measurements directly or indirectly related to state variables. Both the model simulation and the measurements are allowable to come with errors and uncertainties. Typically, data assimilation has two consecutive steps. The first step is data fusion, which derives more reliable estimates of model states based on model-simulated state variables and related measurements. The second step is model simulation with the fused estimates of model states as initial conditions. Through these two steps, model simulation can be improved by assimilating measurements. Data assimilation technique, therefore, provides a chance to improve hydrological simulations with satellite-derived soil moisture data.

Sequential data assimilation is a simple and effective data assimilation method, which improves model simulation by sequentially assimilating measurements. Kalman Filter (KF) derived algorithms, such as Extended Kalman Filter (EKF) and Ensemble Kalman Filter (EnKF), are algorithms that are widely used in sequential data assimilation (Reichle et al. 2002; Aubert et al. 2003; Francois et al. 2003; Reichle and Koster 2003). Especially, EnKF algorithm has been extensively used in soil moisture data assimilation due to its strength of dealing with the nonlinearity of model prediction (Zhou et al. 2006; Montaldo et al. 2007). Essentially, KF, EKF and EnKF are data fusion algorithms requiring model simulations and measurements at the same

spatial resolution. If measurements are not at the spatial resolution of model simulation, measurements should be resampled into the spatial resolution of model simulation, which introduces extra errors and uncertainties. Multiscale Kalman Smoother (MKS) is another kind of data fusion algorithm specializing at fusing data of multiple spatial resolutions (Chou et al. 1993; Chou et al. 1994; Willsky 2002). Due to this feature, MKS algorithm has been extensively used in many fields, for example, signal processing (Nounou 2006), altimetry data fusion (Slatton et al. 2001; Slatton et al. 2002), precipitation data fusion (Gorenburg et al. 2001; de Vyver and Roulin 2009), and data assimilation (Parada and Liang 2004; Parada and Liang 2008). In terms of soil moisture data assimilation, if the spatial resolutions of measurement and model simulation are different, MKS algorithm is a good choice to avoid errors and uncertainties brought by data resampling.

With respect to applications in hydrological simulation, soil moisture data assimilation is at the starting phase. Most of existing studies focus on the changes of simulated water and energy fluxes made by data assimilation at single points (Parada and Liang 2004; Zhou et al. 2006; Huang et al. 2008). Very few studies have directly investigated the impacts of data assimilation on streamflow simulation. For the purpose of improving hydrological forecast, it is necessary to systematically investigate the impacts of soil moisture data assimilation on hydrological simulation at watershed scale, especially for the streamflow simulation. To increase the significance of the operational hydrological forecast, such investigations should be conducted in multiple watersheds with operational LSM, widely-used forcing data and satellite-measure soil moisture data.

In this study, we first assimilate AMSR-E near surface soil moisture data hydrological simulation with Noah LSM and then assess the impacts of soil moisture data assimilation on hydrological simulation through multiple experiments in 14 watersheds. The AMSR-E data are provided by Goddard Earth Sciences Data and Information Services Center. They are averaged daily soil moisture contents in near surface soil layer, which roughly corresponds to the first layer of Noah LSM. In the assessment, we use NLDAS-2 forcing data, plus RADAR, FUSED-1, FUSED-2 and FUSED-3 precipitation data to simulate hydrological processes with Noah LSM. Hydrological simulations are conducted at 1/8 degree, which is the spatial resolution of atmospheric inputs. However, the spatial resolution of the AMSR-E data is 1/4 degree, which is different from model simulation. Instead of resampling AMSR-E data to 1/8 degree, we use MKS algorithm in the assessment.

In the rest of this chapter, we will describe experiment design in section 6.2. And then, features of the AMSR-E data are explored in section 6.3. The essential part of this study, assessments of soil moisture data assimilation, will be discussed in section 6.4. In the end, findings of this study will be summarized in section 6.5.

6.2 EXPERIMENT DESIGN

6.2.1 Experimental watersheds

Fourteen experimental watersheds are selected to assess the impact of soil moisture data assimilation on hydrological simulations. Locations of these watersheds are illustrated in **Figure 5.2**. Areas, elevation ranges, topographies and descriptions are listed in **Table 5.1**. These 14 experimental watersheds with flat, relatively steep, steep and very steep topographies are evenly distributed in the Ohio River Basin, which ensures the applicability of the findings of this study in the Ohio River Basin. More detailed descriptions of these experimental watersheds are provided in Chapter 5.0.

6.2.2 Data assimilation experiments

In this study, data assimilation includes two essential operations: model simulation and data fusion of measured and simulated near surface soil moisture content. Model simulations are conducted at hourly time step with Noah LSM and NLDAS-2 forcing data, plus RADAR, FUSED-1, FUSED-2 and FUSED-3 precipitation inputs. Totally, there are five precipitation inputs together with the precipitation data of NLDAS-2 forcing. As described in **Figure 3.1**, there are four soil layers in Noah model while the near surface layer has a thickness of 10 cm. For each watershed, there are five data assimilation experiments, which correspond to NLDAS-2, RADAR, FUSED-1, FUSED-2 and FUSED-3 precipitation inputs respectively. These five precipitation inputs represent different scenarios of precipitation data. Model simulations of all

experiments in this study use the same parameters and initial conditions of the study in chapter 5.0 , which makes the results of this study comparable to those of the study in chapter 5.0 .

Noah LSM simulates two kinds of soil moisture contents, namely SMC and SH2O. SMC is the total soil moisture content in a soil layer, which is the general concept of soil moisture content. SH2O is the liquid part of SMC. Because the dielectric constant of ice is close to the dielectric constant of soil, the AMSR-E data only recorded the liquid part of SMC. Therefore, data assimilation of near surface soil moisture actually just works on SH2O instead of SMC. In consideration of the considerable missing values in AMSR-E data (as shown in section 6.3), data assimilations are only conducted at the day when the missing percentage of the AMSR-E data is no more than 25%. Specifically, data assimilation includes the following six steps:

Step 1: Step 1 is to compute the daily average value of liquid soil moisture content ($\overline{SH2O^-}$) in the near surface layer.

$$\overline{SH2O^-} = \frac{1}{24} \sum_{n=0}^{23} SH2O_n^- \quad (6-1)$$

where $SH2O_n^-$ is the liquid soil moisture content in the near surface soil layer at the n^{th} hour of the day.

Step 2: Step 2 is to fuse $\overline{SH2O^-}$ with the daily AMSR-E near surface soil moisture data, while the fused soil moisture content is denoted as $\overline{SH2O^+}$. Data fusion is based on the MKS algorithm. Details of MKS algorithms are provided in chapter 5. As discussed in Chapter 4 and Chapter 5, the estimate of areal mean of state variables is essential to multiscale data fusion with the MKS algorithm. In the experiments of this study, we estimate the areal mean of SH2O in near surface layer as

$$\bar{X}(0) = 0.5 \times \left[\text{mean}(\overline{SH2O^-}) + \text{mean}(SH2O_{\text{AMSR-E}}) \right], \quad (6-2)$$

which indicates that the mean of fused SH2O in near surface soil layer will be the average of the mean of simulated daily SH2O and the mean of AMSR-E data.

Step 3: Step 3 is to compute update coefficient as

$$\text{Coef} = \frac{SH2O_{23}^-}{SH2O_{23}^+}. \quad (6-3)$$

Step 4: Step 4 is to update the liquid soil moisture content of the near surface soil layer

$$SH2O_{23}^+ = SH2O_{23}^- + \text{Coef} \times (\overline{SH2O^+} - \overline{SH2O^-}). \quad (6-4)$$

To ensure that $SH2O_{23}^+$ is in a proper range for Noah LSM, validation check of $SH2O_{23}^+$ is conducted for each grid. If $SH2O_{23}^+$ is larger than the porosity of soil type of the grid (θ_s), then we set $SH2O_{23}^+ = \theta_s$, whereas if $SH2O_{23}^+$ is smaller than the wilting point of the soil type of the grid (θ_w), we set $SH2O_{23}^+ = \theta_w$.

Step 5: Step 5 is to update the total soil moisture content (SMC) of near surface layer. SH2O is part of SMC. Once SH2O is updated, SMC is updated correspondingly

$$SMC_{23}^+ = SMC_{23}^- + (SH2O_{23}^+ - SH2O_{23}^-) \quad (6-5)$$

Like step 4, validation check is also conducted for SMC_{23}^+ .

Step 6: Step 6 is to proceed the model simulation to the hour 0 of the next day while SMC_{23}^+ and $SH2O_{23}^+$ used as part of initial conditions.

Through these steps, the AMSR-E data are assimilated into the hourly simulations with Noah LSM. By revising one of initial conditions, AMSR-E data influence simulated soil moisture contents, evapotranspiration and runoffs. In above descriptions, SH2O and SMC represent the liquid soil moisture content and the total soil moisture content in the near surface layer. In the rest part of this chapter, we abbreviate liquid soil moisture content and total soil moisture content as SH2O and SMC for notational convenience. In addition, we use subscripts 1, 2, 3 and 4 to respectively represent the near surface, the second, the third and the bottom soil layer.

6.3 ANALYSIS OF AMSR-E DATA

6.3.1 Data missing and processing

Data missing is a serious problem of the AMSR-E data. Figure 6.1 shows the cumulative missing percentages of the AMSR-E data during the period of 2003 to 2005 over the 14 experimental watersheds. It can be seen that at least 20% of days have 75% - 100% missing values in AMSR-E data for all experimental watersheds. Data missing is especially serious in ALDW2, CYCK2, ELRP1 and PSNW2 watersheds, whose topographies are relatively steep, steep or very steep. Over a half of days have 50% to 100% missing in the AMSR-E data. Missing data are replaced with interpolated values before data assimilation. For a grid without valid value, if its neighboring grids have valid values at the same time, then the missing value of the grid is replaced by interpolating values of neighboring grids using inversed distances as weights. If all of its neighboring grids don't have valid values, then the missing value of the grid is

interpolated with the values of the grid at previous and next time steps. However, if the values of the grid at the previous and the next time steps are invalid, then use the average of valid values in the watershed to replace the missing values of the grid.

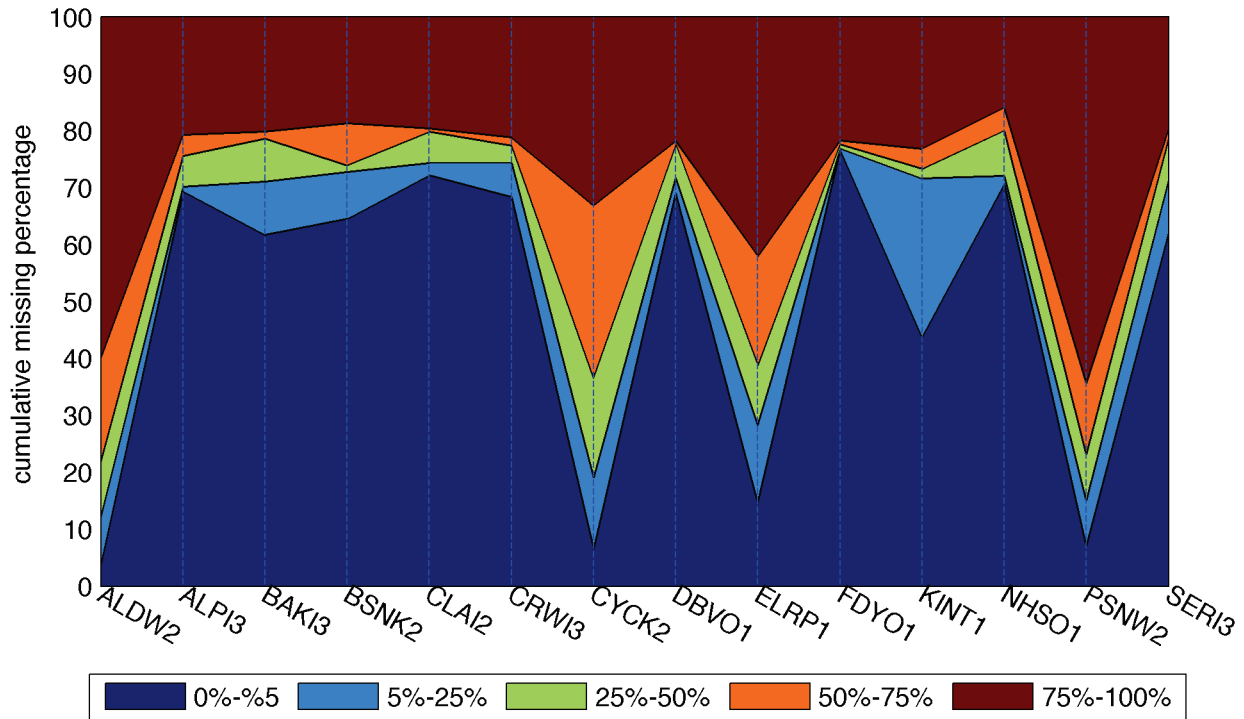


Figure 6.1 Cumulative missing percentage of AMSR-E data over the 14 experimental watersheds.

The problem of data missing has significantly influences on data assimilation. When data missing exceeds certain extent, there is very limited information that can be added to model simulation. Additionally, the interpolations for the missing values also introduce extra errors and uncertainties into the AMSR-E data. Therefore, we only assimilate data in days whose missing percentages of the AMSR-E data are no more than 25%. Thus, data assimilation is conducted in less than 20% of days in ALDW2, CYCK2 and PSNW2 watersheds and less than 30% of days in ELRP1 watershed. For the rest of watersheds, data assimilation is conducted in more than 70% of days in the period of 2003 to 2005.

6.3.2 Magnitudes of the AMSR-E data

In data assimilation, it is expected that some differences exist between the magnitudes of the AMSR-E data and model simulated SH2Os. Model simulations are improved if the AMSR-E data are more reliable than model simulations. Meanwhile, consistency is also expected between AMSR-E data and model simulated SH2Os since they describe the same status of near surface soil layer. If the differences between the AMSR-E data and model simulated SH2Os are too small, the impact of data assimilation on model simulation will be very limited. However, if the consistencies between the AMSR-E data and model simulated SH2Os are very poor, it may indicate that either the measurements or the model simulations are very unreliable.

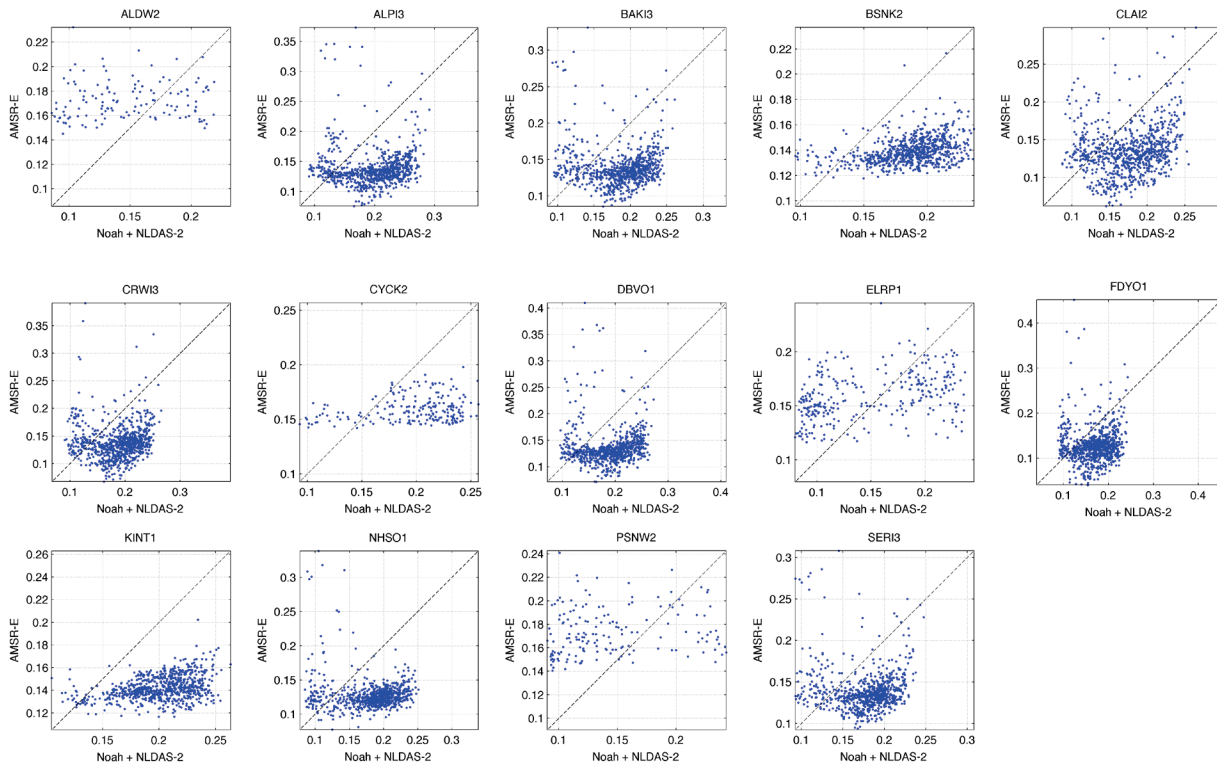


Figure 6.2 Scatter plots of the mean of AMSR-E data and the mean of daily liquid soil moisture data in near surface layer simulated by Noah LSM with NLDAS-2 precipitation data for the 14 experimental watersheds over the period of 2003 to 2005. In each plot, the dashed line is 1:1 line.

For analyzing the results of data assimilation, it is worthwhile investigating the relationship between the AMSR-E data and daily-averaged SH2Os simulated by Noah LSM with the five precipitation inputs. The scatter plots between the spatial average of the AMSR-E data and the spatial average of daily-averaged SH2O simulated with Noah LSM in the 14 experimental watersheds are given in Figure 6.2 to Figure 6.6, which are corresponding to NLDAS-2, RADAR, FUSED-1, FUSED-2 and FUSED-3 precipitation inputs. In addition, the correlations between the spatial average of the AMSR-E data and the spatial average of daily-averaged SH2O simulated with the five precipitation inputs are listed by year in Table 6.1 to Table 6.14 for the 14 experimental watersheds.

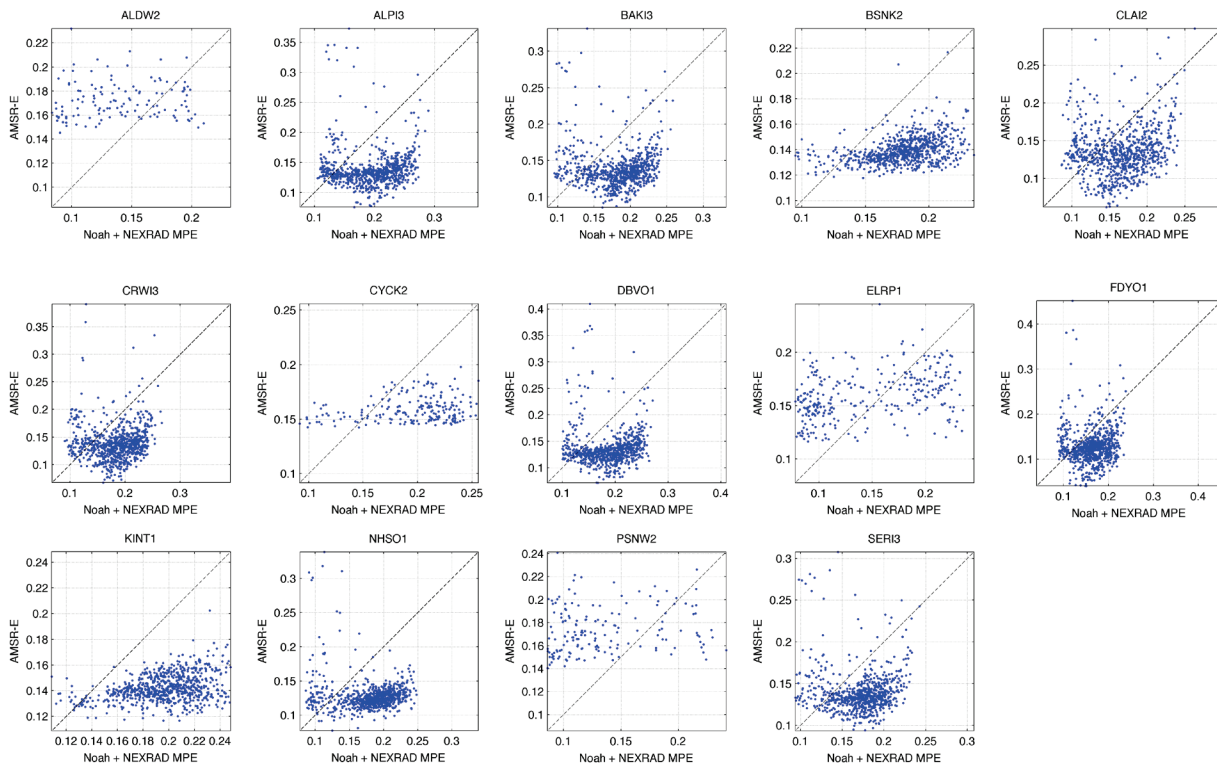


Figure 6.3 Scatter plots of the mean of AMSR-E data and the mean of daily liquid soil moisture data in near surface layer simulated by Noah LSM with RADAR precipitation data for the 14 experimental watersheds over the period of 2003 to 2005. In each plot, the dashed line is 1:1 line.

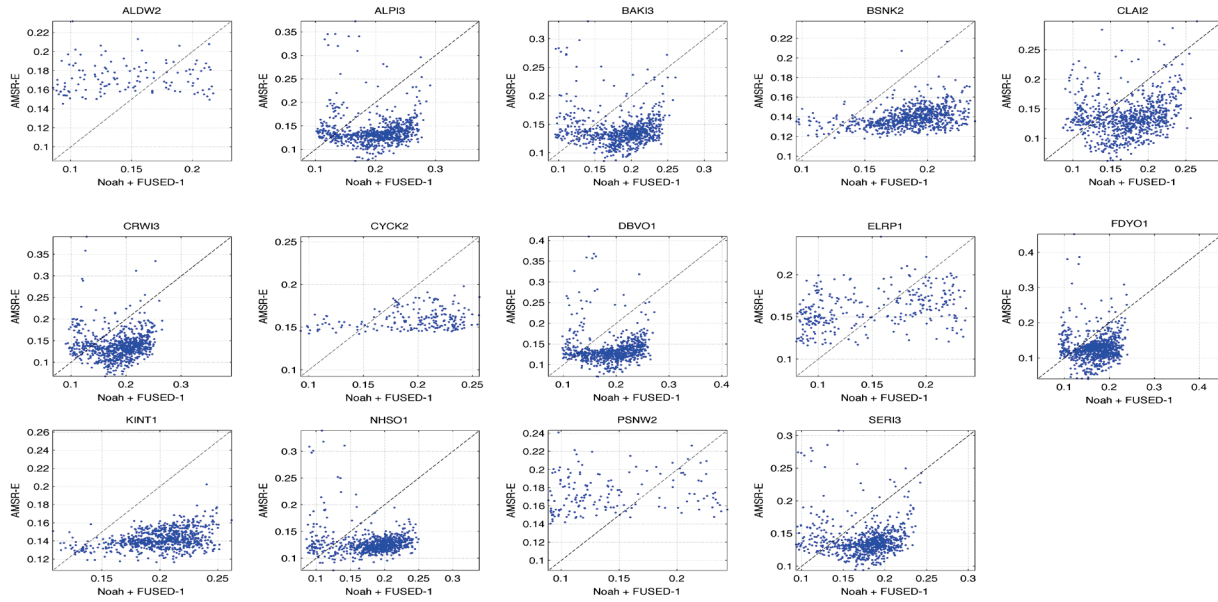


Figure 6.4 Scatter plots of the mean of AMSR-E data and the mean of daily liquid soil moisture data in near surface layer simulated by Noah LSM with FUSED-1 precipitation data for the 14 experimental watersheds over the period of 2003 to 2005. In each plot, the dashed line is 1:1 line.

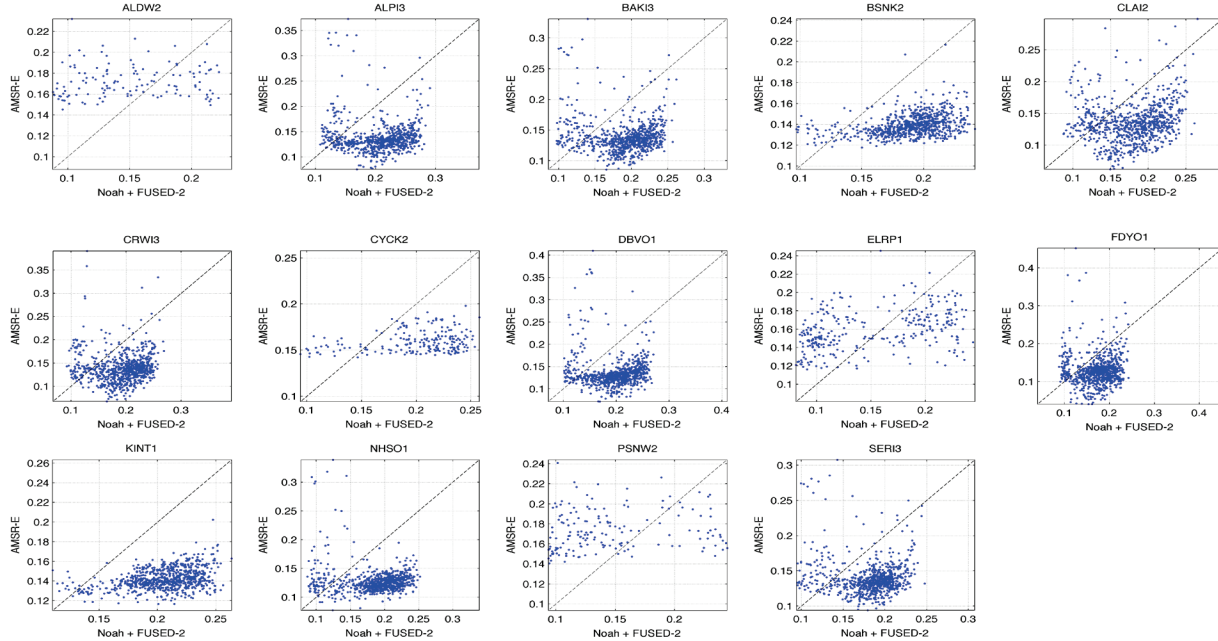


Figure 6.5 Scatter plots of the mean of AMSR-E data and the mean of daily liquid soil moisture data in near surface layer simulated by Noah LSM with FUSED-2 precipitation data for the 14 experimental watersheds over the period from 2003 to 2005. In each plot, the dashed line is 1:1 line.

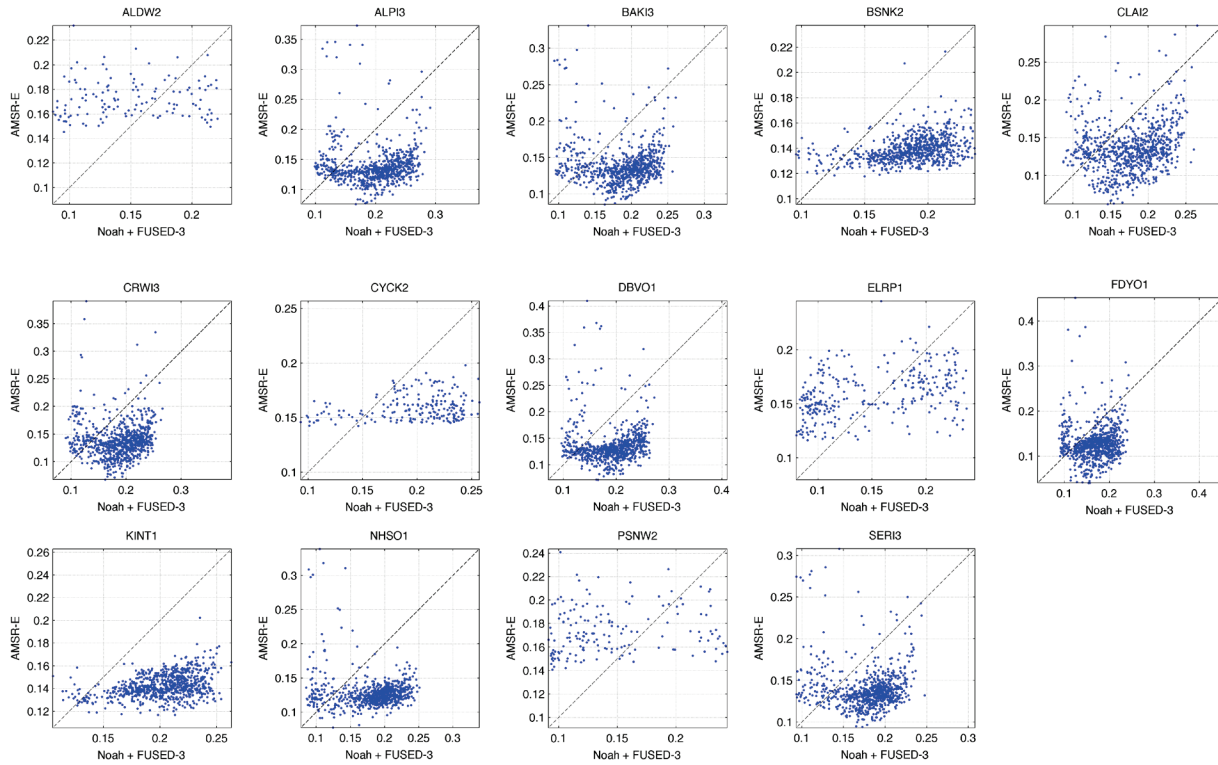


Figure 6.6 Scatter plots of the mean of AMSR-E data and the mean of daily liquid soil moisture data in near surface layer simulated by Noah LSM with FUSED-3 precipitation data for the 14 experimental watersheds over the period of 2003 to 2005. In each plot, the dashed line is 1:1 line.

Two main findings can be summarized based on Figure 6.2 to Figure 6.6 and Table 6.1 to Table 6.14. The first is that consistency between the AMSR-E data and model simulated SH₂O is very poor. Except ALDW2 in 2003 (correlations > 0.4), BSNK2 in 2005 (correlations > 0.5), ELRP1 in 2003 (correlations > 0.5), KINT1 in 2005 (correlations > 0.4) and PSNW2 in 2003 (correlations > 0.4), correlations in the rest experimental watersheds are far less than 0.5 for all the time and even a big number of them have correlations less than 0.0. This finding suggests that the AMSR-E data have poor agreements with Noah simulations in terms of average magnitudes of SH₂O in the near surface soil layer over time. The second finding is that the spatial averages of AMSR-E data are mostly smaller than the spatial averages of daily-averaged SH₂O simulated

with Noah LSM. As shown in Figure 6.2 to Figure 6.6, most scatter points are below the 1:1 line in most plots except those of ALDW2, ELRP1 and PSNW2 watersheds. This finding indicates that data assimilation may improve model simulation for experimental watersheds only if the precipitation data are larger than actual values. For ALDW2, ELRP1 and PSNW2 watersheds, the impacts of data assimilation are expected to be limited since there are small numbers of days with eligible satellite-measured soil moisture data.

Table 6.1 Correlations between the average AMSR-E and the mean of daily-averaged liquid soil moisture content of the near surface layer simulated by Noah LSM with NLDAS-2, RADAR, FUSED-1, FUSED-2 and FUSED-3 precipitation inputs in ALDW2 watershed.

	NLDAS-2	RADAR	FUSED-1	FUSED-2	FUSED-3	COUNT
2003	0.460	0.417	0.426	0.416	0.421	54
2004	-0.177	-0.165	-0.172	-0.180	-0.180	30
2005	-0.242	-0.229	-0.233	-0.221	-0.234	45
AVERAGE	0.014	0.008	0.007	0.005	0.002	

Table 6.2 Correlations between the average AMSR-E and the mean of daily-averaged liquid soil moisture content of the near surface layer simulated by Noah LSM with NLDAS-2, RADAR, FUSED-1, FUSED-2 and FUSED-3 precipitation inputs in ALPI3 watershed.

	NLDAS-2	RADAR	FUSED-1	FUSED-2	FUSED-3	COUNT
2003	0.006	0.015	-0.001	-0.058	-0.006	247
2004	-0.154	-0.176	-0.180	-0.235	-0.174	264
2005	0.303	0.299	0.294	0.247	0.291	251
AVERAGE	0.052	0.046	0.038	-0.015	0.037	

Table 6.3 Correlations between the average AMSR-E and the mean of daily-averaged liquid soil moisture content of the near surface layer simulated by Noah LSM with NLDAS-2, RADAR, FUSED-1, FUSED-2 and FUSED-3 precipitation inputs in BAKI3 watershed.

	NLDAS-2	RADAR	FUSED-1	FUSED-2	FUSED-3	COUNT
2003	0.143	0.162	0.145	0.113	0.132	251
2004	-0.325	-0.320	-0.335	-0.353	-0.338	265
2005	0.240	0.252	0.237	0.194	0.226	256
AVERAGE	0.019	0.032	0.016	-0.015	0.007	

Table 6.4 Correlations between the average AMSR-E and the mean of daily-averaged liquid soil moisture content of the near surface layer simulated by Noah LSM with NLDAS-2, RADAR, FUSED-1, FUSED-2 and FUSED-3 precipitation inputs in BSNK2 watershed.

	NLDAS-2	RADAR	FUSED-1	FUSED-2	FUSED-3	COUNT
2003	0.283	0.311	0.285	0.297	0.282	257
2004	0.262	0.315	0.257	0.241	0.248	265
2005	0.553	0.538	0.545	0.534	0.539	268
AVERAGE	0.366	0.388	0.363	0.357	0.356	

Table 6.5 Correlations between the average AMSR-E and the mean of daily-averaged liquid soil moisture content of the near surface layer simulated by Noah LSM with NLDAS-2, RADAR, FUSED-1, FUSED-2 and FUSED-3 precipitation inputs in CLAI2 watershed.

	NLDAS-2	RADAR	FUSED-1	FUSED-2	FUSED-3	COUNT
2003	0.293	0.330	0.313	0.292	0.295	265
2004	0.013	0.007	0.023	-0.010	0.015	278
2005	0.279	0.325	0.299	0.266	0.278	264
AVERAGE	0.195	0.221	0.212	0.183	0.196	

Table 6.6 Correlations between the average AMSR-E and the mean of daily-averaged liquid soil moisture content of the near surface layer simulated by Noah LSM with NLDAS-2, RADAR, FUSED-1, FUSED-2 and FUSED-3 precipitation inputs in CRWI3 watershed.

	NLDAS-2	RADAR	FUSED-1	FUSED-2	FUSED-3	COUNT
2003	0.291	0.328	0.303	0.266	0.283	262
2004	-0.142	-0.147	-0.147	-0.151	-0.142	279
2005	0.116	0.127	0.112	0.082	0.103	266
AVERAGE	0.089	0.103	0.089	0.065	0.081	

Table 6.7 Correlations between the average AMSR-E and the mean of daily-averaged liquid soil moisture content of the near surface layer simulated by Noah LSM with NLDAS-2, RADAR, FUSED-1, FUSED-2 and FUSED-3 precipitation inputs in CYCK2 watershed.

	NLDAS-2	RADAR	FUSED-1	FUSED-2	FUSED-3	COUNT
2003	0.365	0.303	0.341	0.363	0.366	73
2004	0.111	0.180	0.131	0.146	0.119	69
2005	0.167	0.162	0.169	0.187	0.172	64
AVERAGE	0.214	0.215	0.214	0.232	0.219	

Table 6.8 Correlations between the average AMSR-E and the mean of daily-averaged liquid soil moisture content of the near surface layer simulated by Noah LSM with NLDAS-2, RADAR, FUSED-1, FUSED-2 and FUSED-3 precipitation inputs in DBVO1 watershed.

	NLDAS-2	RADAR	FUSED-1	FUSED-2	FUSED-3	COUNT
2003	0.034	0.004	0.010	-0.054	0.017	255
2004	-0.078	-0.112	-0.110	-0.171	-0.096	268
2005	0.194	0.182	0.181	0.132	0.182	256
AVERAGE	0.050	0.025	0.027	-0.031	0.034	

Table 6.9 Correlations between the average AMSR-E and the mean of daily-averaged liquid soil moisture content of the near surface layer simulated by Noah LSM with NLDAS-2, RADAR, FUSED-1, FUSED-2 and FUSED-3 precipitation inputs in ELRP1 watershed.

	NLDAS-2	RADAR	FUSED-1	FUSED-2	FUSED-3	COUNT
2003	0.570	0.570	0.570	0.565	0.571	93
2004	0.219	0.200	0.204	0.226	0.221	110
2005	0.387	0.386	0.390	0.411	0.391	104
AVERAGE	0.392	0.385	0.388	0.401	0.394	

Table 6.10 Correlations between the average AMSR-E and the mean of daily-averaged liquid soil moisture content of the near surface layer simulated by Noah LSM with NLDAS-2, RADAR, FUSED-1, FUSED-2 and FUSED-3 precipitation inputs in FDYO1 watershed.

	NLDAS-2	RADAR	FUSED-1	FUSED-2	FUSED-3	COUNT
2003	0.186	0.165	0.181	0.124	0.193	275
2004	-0.147	-0.160	-0.182	-0.171	-0.155	284
2005	0.255	0.248	0.254	0.240	0.254	276
AVERAGE	0.098	0.084	0.084	0.064	0.097	

Table 6.11 Correlations between the average AMSR-E and the mean of daily-averaged liquid soil moisture content of the near surface layer simulated by Noah LSM with NLDAS-2, RADAR, FUSED-1, FUSED-2 and FUSED-3 precipitation inputs in KINT1 watershed.

	NLDAS-2	RADAR	FUSED-1	FUSED-2	FUSED-3	COUNT
2003	0.303	0.189	0.290	0.286	0.303	254
2004	0.310	0.345	0.322	0.305	0.309	259
2005	0.481	0.478	0.481	0.477	0.482	265
AVERAGE	0.365	0.337	0.364	0.356	0.365	

Table 6.12 Correlations between the average AMSR-E and the mean of daily-averaged liquid soil moisture content of the near surface layer simulated by Noah LSM with NLDAS-2, RADAR, FUSED-1, FUSED-2 and FUSED-3 precipitation inputs in NHSO1 watershed.

	NLDAS-2	RADAR	FUSED-1	FUSED-2	FUSED-3	COUNT
2003	0.127	0.143	0.133	0.113	0.126	257
2004	-0.324	-0.296	-0.324	-0.319	-0.325	263
2005	0.084	0.081	0.082	0.077	0.084	263
AVERAGE	-0.037	-0.024	-0.036	-0.043	-0.038	

Table 6.13 Correlations between the average AMSR-E and the mean of daily-averaged liquid soil moisture content of the near surface layer simulated by Noah LSM with NLDAS-2, RADAR, FUSED-1, FUSED-2 and FUSED-3 precipitation inputs in PSNW2 watershed.

	NLDAS-2	RADAR	FUSED-1	FUSED-2	FUSED-3	COUNT
2003	0.465	0.464	0.469	0.454	0.461	67
2004	-0.036	-0.043	-0.043	-0.041	-0.039	43
2005	-0.309	-0.290	-0.298	-0.299	-0.309	52
AVERAGE	0.040	0.044	0.043	0.038	0.038	

Table 6.14 Correlations between the average AMSR-E and the mean of daily-averaged liquid soil moisture content of the near surface layer simulated by Noah LSM with NLDAS-2, RADAR, FUSED-1, FUSED-2 and FUSED-3 precipitation inputs in SERI3 watershed.

	NLDAS-2	RADAR	FUSED-1	FUSED-2	FUSED-3	COUNT
2003	0.099	0.135	0.098	0.069	0.086	251
2004	-0.309	-0.290	-0.318	-0.336	-0.321	268
2005	0.285	0.311	0.282	0.239	0.266	255
AVERAGE	0.025	0.052	0.021	-0.009	0.010	

6.4 ASSESSMENTS OF SOIL MOISTURE DATA ASSIMILATION

Assessments of soil moisture data assimilation are conducted in the 14 experimental watersheds respectively. In terms of the impacts on the simulations of streamflow, soil moisture contents and evapotranspiration, assessments are discussed in the following three subsections. The same method of assessment is used for the three subsections, which is to compare the simulations with and without soil moisture data assimilation. Experiments in Chapter 5.0 are control experiments, i.e. experiments without data assimilation.

6.4.1 Assessment in the simulation of soil moisture contents

As state variables, soil moisture contents affects all outputs of LSM related to soil water, such as runoffs and evapotranspiration. Theoretically, the MKS algorithm based soil moisture data assimilation will definitely improve the simulation of SH2O if the following two criteria are satisfied. One criterion is model simulated and satellite-measured SH2Os are unbiased estimates of real soil moisture contents and the other criterion is the uncertainties associated with the measured and the simulated SH2Os are properly estimated. However, model simulated and satellite-measured SH2Os usually come with biases in reality. If biases are not well dealt, data assimilation may deteriorate simulations of SH2Os. In practical hydrological simulation, it is very hard to determine the biases in simulated SH2Os because there are too many possible influences. Thus, equation (6-2), which puts equal confidences on model simulation and satellite measurement, is the most robust way of dealing with biases for soil moisture data assimilation with the MKS algorithm.

In order to assess the impacts of assimilating the AMSR-E data on the simulation of SMCs, spatial averages of SMCs in the 1st, the 2nd, 3rd and 4th layers simulated by Noah LSM and NLDAS-2 forcing with and without data assimilation are plotted in Figure 6.7 to Figure 6.20, which are respectively corresponding to the 14 experimental watersheds in 2004. From these figures, firstly it can be seen that data assimilation has strong influences on simulated SMC in near surface soil layer (called SMC₁ hereafter) for all experimental watersheds except ALDW2 and PSNW2. The impacts of data assimilation on SMC₁ have clear seasonal feature. Except BSNK2 and KINT1, which are in area of relatively warm climate, data assimilation increases SMC₁ in cold months, e.g. December, January and February whereas data assimilation decreases SMC₁ in the rest months of the year. This is very possible that the AMSR-E data overestimate SH2O in cold months and underestimate SH2O in the rest of months. For ALDW2 and PSNW2 watershed, they are not much affected by data assimilation because only a few days have data assimilation. As shown in Table 6.1 and Table 6.13, there are only 30 and 43 days with the missing percentage of the AMSR-E data less than 25% in these two watersheds. In addition, another reason is, as shown in Figure 6.2 to Figure 6.6, the situation of underestimation in ALDW2, PSNW2 and ELRP1 is not as severe as the rest of experimental watersheds. For this reason, data assimilation also has very limited impacts on simulated SMC₁ in ELRP1 watershed except in the cold months. The second finding from Figure 6.7 to Figure 6.20 is that data assimilation not only affects the SMC in the near surface soil layer but also affect the SMCs in deeper layers, while the magnitudes of influences are getting smaller along soil depth. This means that the impacts of data assimilation for the near surface soil layer can be effectively propagated to deep layers through the soil hydrology of Noah LSM. This finding further indicates that data assimilation for near surface soil layer has effects on runoff generation and

evapotranspiration, which depend on SMCs in all soil layers. From Figure 6.7 to Figure 6.20, we can also have the third finding. The influences of data assimilation on SMCs exist at different time scales. For example, data assimilation has short-time influences on SMC_1 . The influences are mostly kept in inter-storm period. Once there is an effective precipitation event, the influences of data assimilation on SMC_1 will be swept out by infiltration. Data assimilation has longtime influences in deeper layers, especially in third layer and the bottom layer.

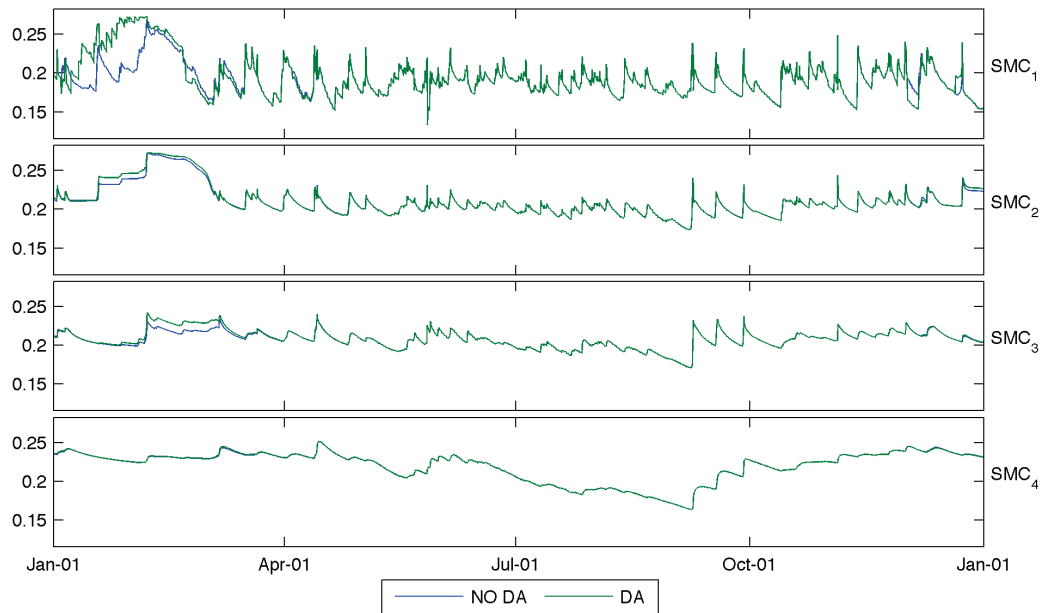


Figure 6.7 Spatial averages of simulated soil moisture contents (m^3/m^3) with and without data assimilation by Noah LSM and NLDAS-2 forcing data in ALDW2 watershed for 2004. SMC_1 , SMC_2 , SMC_3 and SMC_4 represent average soil moisture contents in layers 1, 2, 3, and 4.

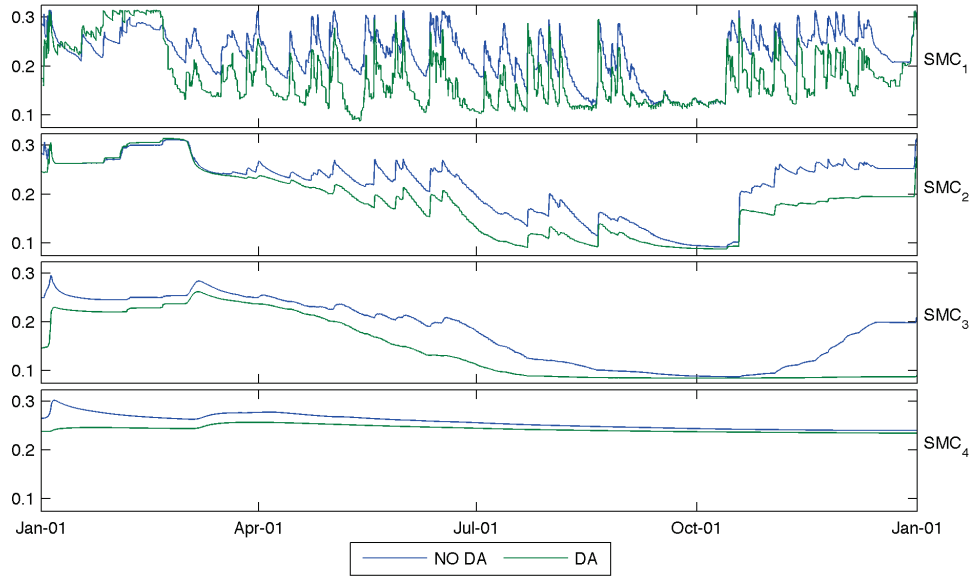


Figure 6.8 Spatial averages of simulated soil moisture contents (m^3/m^3) with and without data assimilation by Noah LSM and NLDAS-2 forcing data in ALPI3 watershed for 2004. SMC_1 , SMC_2 , SMC_3 and SMC_4 represent average soil moisture contents in layers 1, 2, 3, and 4.

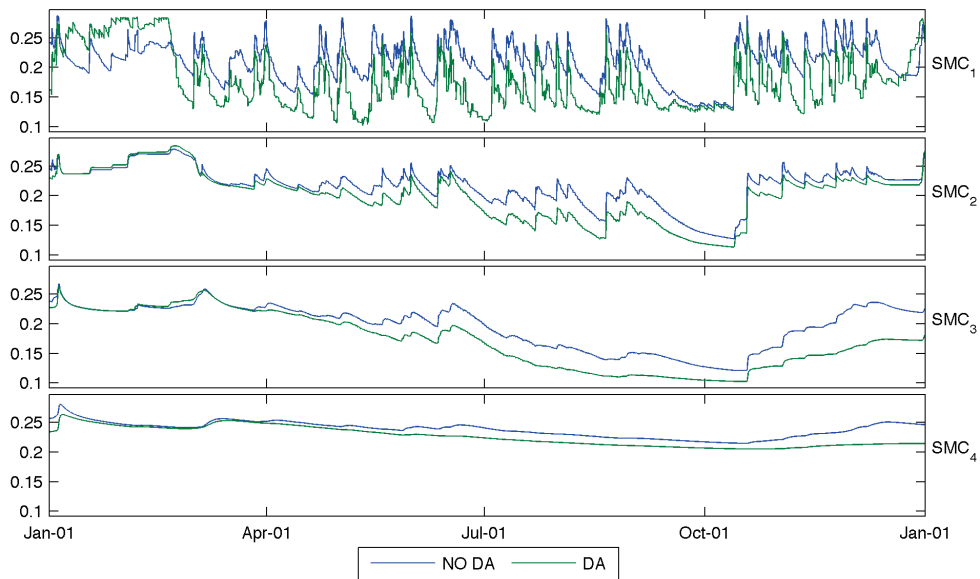


Figure 6.9 Spatial averages of simulated soil moisture contents (m^3/m^3) with and without data assimilation by Noah LSM and NLDAS-2 forcing data in BAKI3 watershed for 2004. SMC_1 , SMC_2 , SMC_3 and SMC_4 represent average soil moisture contents in layers 1, 2, 3, and 4.

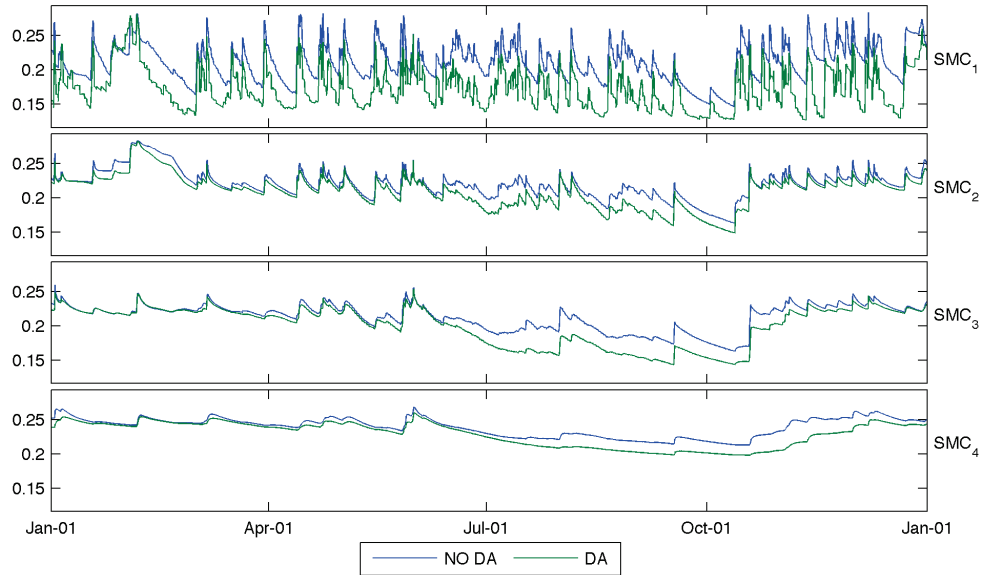


Figure 6.10 Spatial averages of simulated soil moisture contents (m^3/m^3) with and without data assimilation by Noah LSM and NLDAS-2 forcing data in BSNK2 watershed for 2004. SMC_1 , SMC_2 , SMC_3 and SMC_4 represent average soil moisture contents in layers 1, 2, 3, and 4.

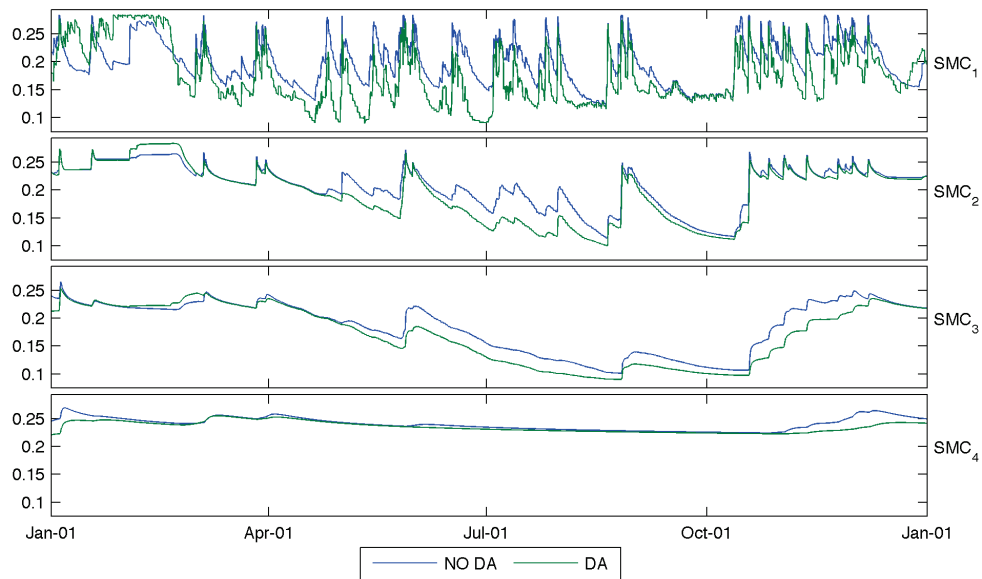


Figure 6.11 Spatial averages of simulated soil moisture contents (m^3/m^3) with and without data assimilation by Noah LSM and NLDAS-2 forcing data in CLAI2 watershed for 2004. SMC_1 , SMC_2 , SMC_3 and SMC_4 represent average soil moisture contents in layers 1, 2, 3, and 4.

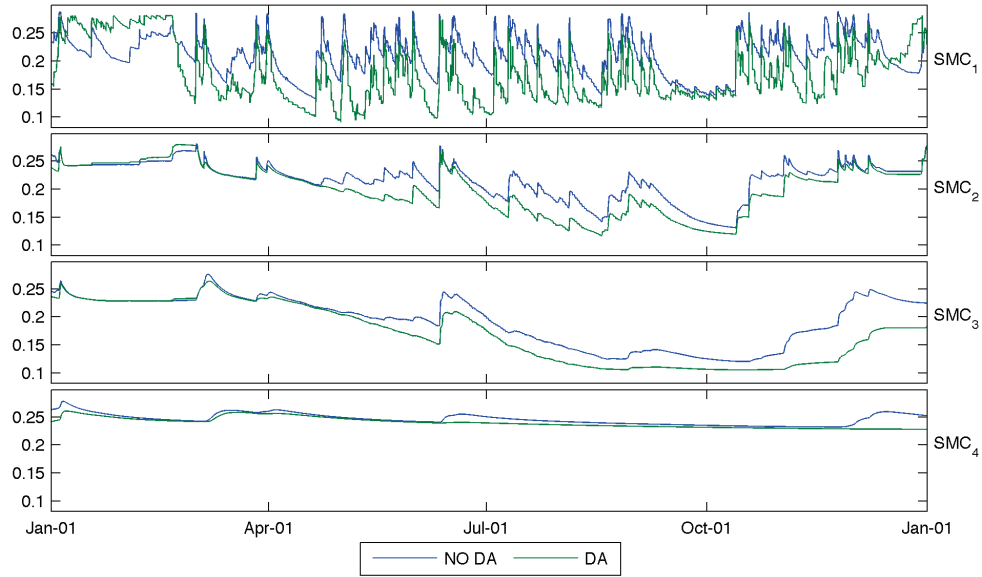


Figure 6.12 Spatial averages of simulated soil moisture contents (m^3/m^3) with and without data assimilation by Noah LSM and NLDAS-2 forcing data in CRWI3 watershed for 2004. SMC_1 , SMC_2 , SMC_3 and SMC_4 represent average soil moisture contents in layers 1, 2, 3, and 4.

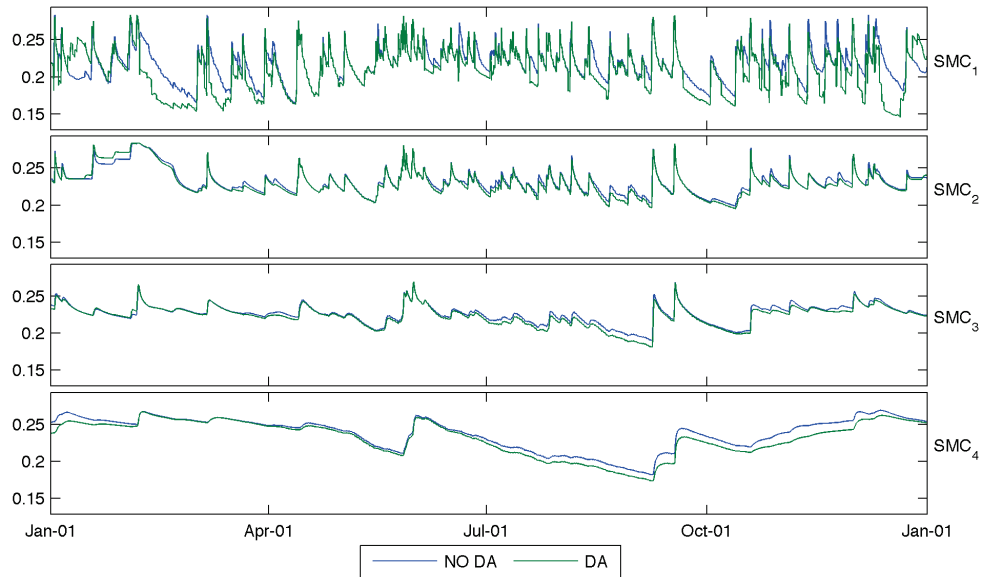


Figure 6.13 Spatial averages of simulated soil moisture contents (m^3/m^3) with and without data assimilation by Noah LSM and NLDAS-2 forcing data in CYCK2 watershed for 2004. SMC_1 , SMC_2 , SMC_3 and SMC_4 represent average soil moisture contents in layers 1, 2, 3, and 4.

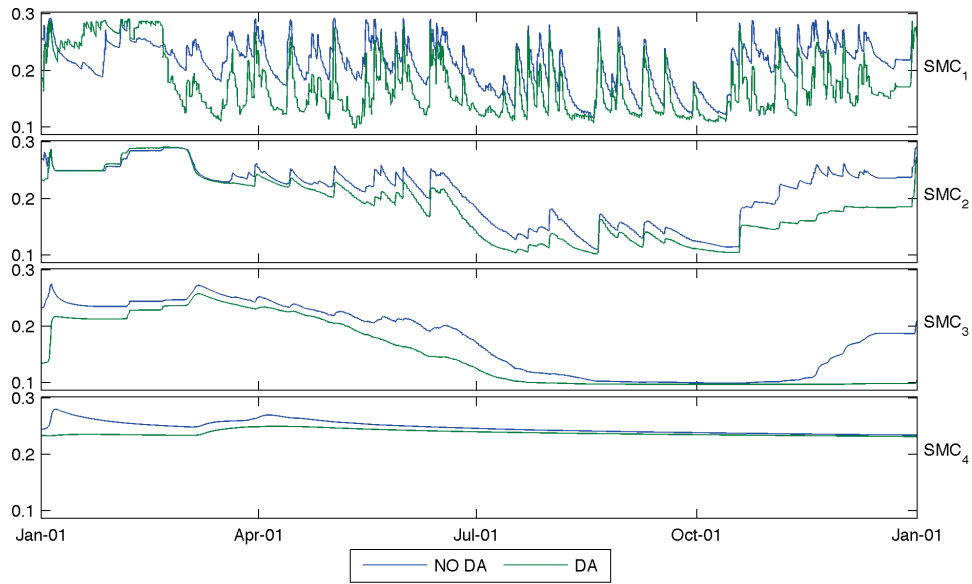


Figure 6.14 Spatial averages of simulated soil moisture contents (m^3/m^3) with and without data assimilation by Noah LSM and NLDAS-2 forcing data in DBVO1 watershed for 2004. SMC_1 , SMC_2 , SMC_3 and SMC_4 represent average soil moisture contents in layers 1, 2, 3, and 4.

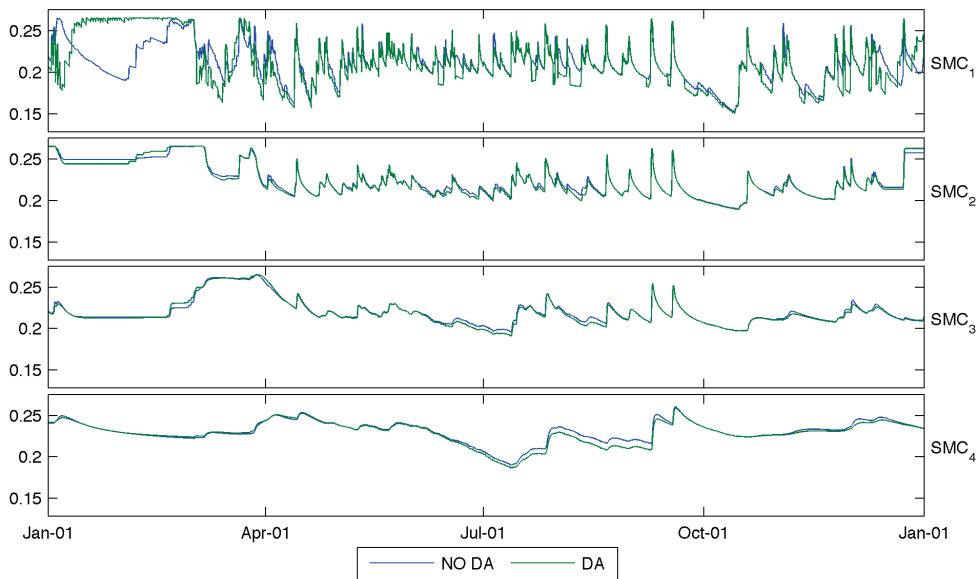


Figure 6.15 Spatial averages of simulated soil moisture contents (m^3/m^3) with and without data assimilation by Noah LSM and NLDAS-2 forcing data in ELRP1 watershed for 2004. SMC_1 , SMC_2 , SMC_3 and SMC_4 represent average soil moisture contents in layers 1, 2, 3, and 4.

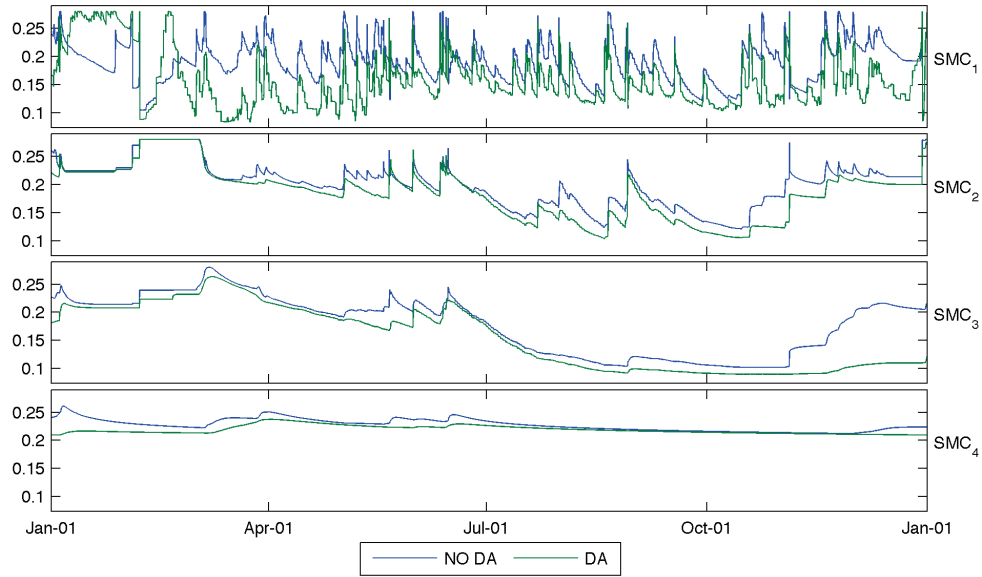


Figure 6.16 Spatial averages of simulated soil moisture contents (m^3/m^3) with and without data assimilation by Noah LSM and NLDAS-2 forcing data in FDYO1 watershed for 2004. SMC_1 , SMC_2 , SMC_3 and SMC_4 represent average soil moisture contents in layers 1, 2, 3, and 4.

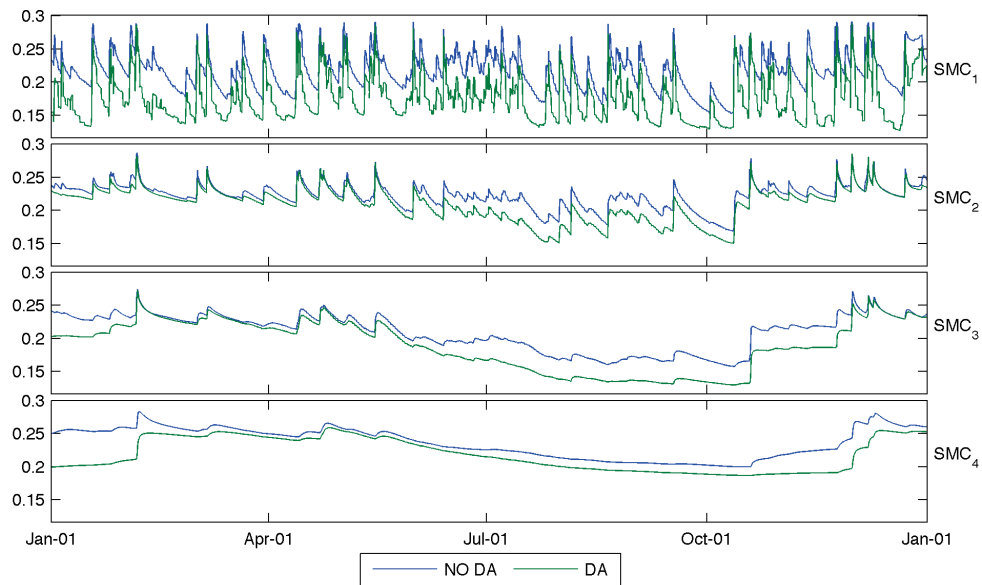


Figure 6.17 Spatial averages of simulated soil moisture contents (m^3/m^3) with and without data assimilation by Noah LSM and NLDAS-2 forcing data in KINT1 watershed for 2004. SMC_1 , SMC_2 , SMC_3 and SMC_4 represent average soil moisture contents in layers 1, 2, 3, and 4.

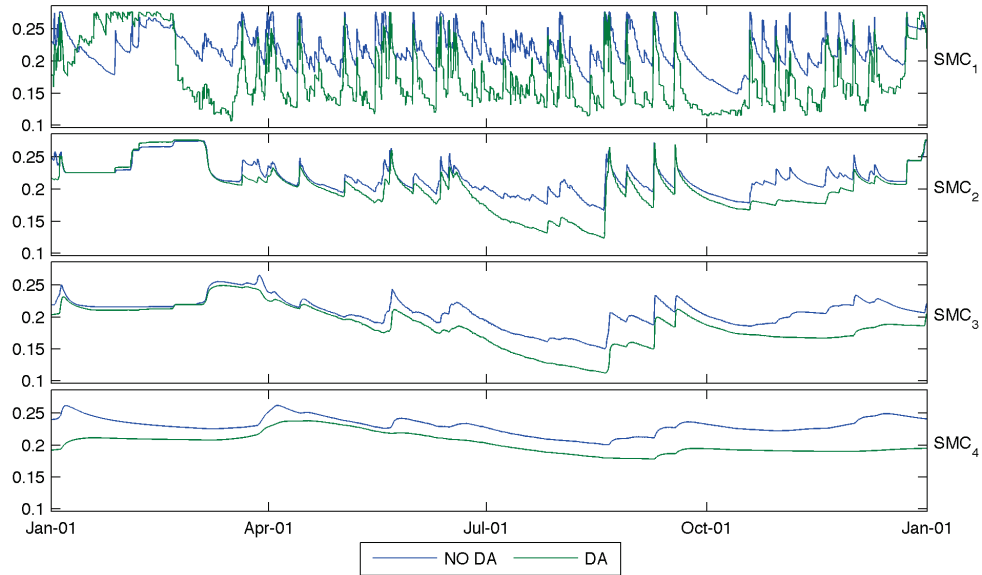


Figure 6.18 Spatial averages of simulated soil moisture contents (m^3/m^3) with and without data assimilation by Noah LSM and NLDAS-2 forcing data in NHSO1 watershed for 2004. SMC_1 , SMC_2 , SMC_3 and SMC_4 represent average soil moisture contents in layers 1, 2, 3, and 4.

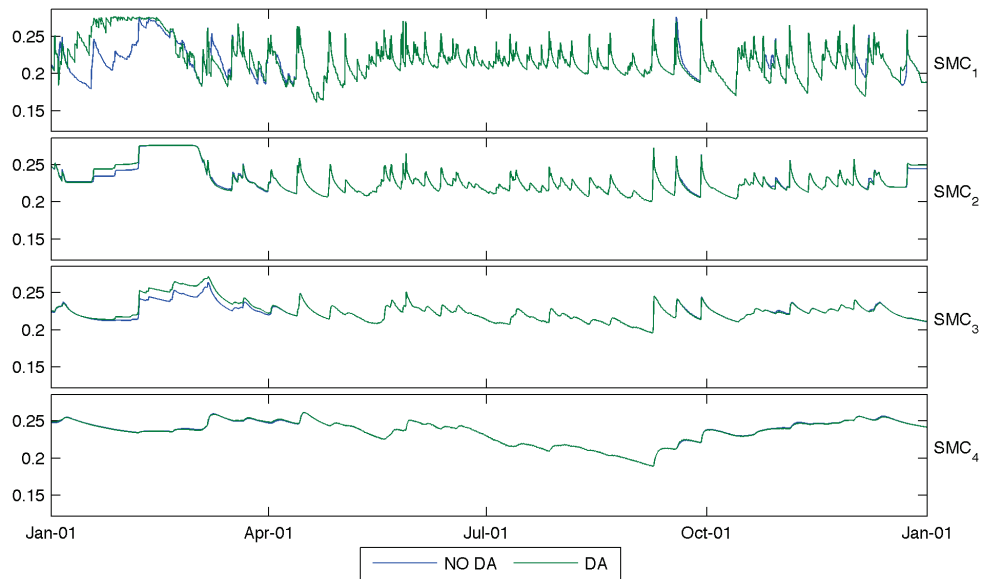


Figure 6.19 Spatial averages of simulated soil moisture contents (m^3/m^3) with and without data assimilation by Noah LSM and NLDAS-2 forcing data in PSNW2 watershed for 2004. SMC_1 , SMC_2 , SMC_3 and SMC_4 represent average soil moisture contents in layers 1, 2, 3, and 4.

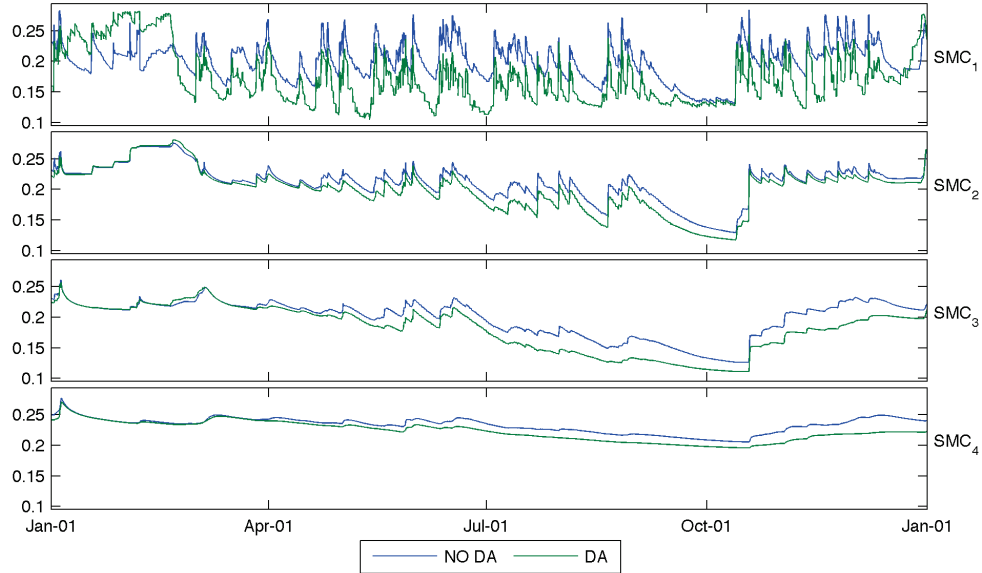


Figure 6.20 Spatial averages of simulated soil moisture contents (m^3/m^3) with and without data assimilation by Noah LSM and NLDAS-2 forcing data in SERI3 watershed for 2004. SMC_1 , SMC_2 , SMC_3 and SMC_4 represent average soil moisture contents in layers 1, 2, 3, and 4.

These findings can be explained by the data assimilation method and features of the AMSR-E data. Given land surface model, atmospheric inputs and parameters, the performance of data assimilation depends on data fusion method and the quality of satellite-measured soil moisture data. The features of the AMSR-E data have been analyzed in section 6.3. Except the problem of data missing, another important feature is that most of the AMSR-E data underestimate SH2O compared with simulated SH2Os with Noah LSM and any of NLDAS-2, RADAR, FUSED-1, FUSED-2 and FUSED-3 precipitation data, which is shown in Figure 6.2 to Figure 6.6. In terms of data fusion method, the areal mean of SH2O in near surface soil layer is determined by equation (6-2), which indicates that the mean of fused SH2O falls between the average of the mean of the AMSR-E data and the mean of daily-averaged SH2O simulated with Noah LSM. Therefore, if the average magnitudes of AMSR-E data are smaller than those of simulated SH2O, then the fused SH2O will be smaller than the simulated SH2O by average.

Correspondingly, simulated SH2O and SMC will be smaller once the fused SH2O replaces the simulated SH2O as the initial condition for the next step simulation. After iterations, the change of SMC_1 will propagate to SMCs in deeper layers through the soil hydrology of Noah LSM. Precipitation events can easily restore the SMC_1 to its highest value, i.e. the porosity of soil type, whereas the influences of precipitation events on SMCs in deeper layers are much weaker. Therefore, the influences of data assimilation in deeper soil layers will accumulate. That is why data assimilation, as shown in Figure 6.7 to Figure 6.20, has influences on SMC_3 and SMC_4 almost at seasonal time scales.

Based on the results, data assimilation significantly influences simulations of SMCs. In the soil hydrology of Noah LSM, SMCs have direct influences on runoff generation and evapotranspiration. Therefore, it is expected that data assimilation also have significant impact on simulations of streamflow and evapotranspiration.

6.4.2 Assessments in streamflow simulation

Assessments in streamflow simulation are mainly conducted by comparing the Nash-Sutcliffe Efficiencies (NSEs) of streamflows simulated with and without data assimilation. NSE can range from $-\infty$ to 1, which is defined in equation 3-23. An NSE of 1 corresponds a perfect match of simulated streamflow to the observed streamflow. An NSE of 0 indicates that the simulated streamflow is as accurate as the mean of the observed streamflow, whereas an NSE less than zero occurs when the mean of the observed streamflow is a better predictor than model simulation. If streamflow simulation can be improved by soil moisture data assimilation, then the NSE of streamflow simulated with data assimilation should be larger than the NSE of the

corresponding streamflow simulated without data assimilation. On the contrary, if soil moisture data assimilation deteriorates streamflow simulation, then the NSE of streamflow simulated with soil moisture data assimilation will be smaller than the NSE of streamflow simulated without soil moisture data assimilation.

The NSEs of streamflow simulated with and without data assimilation in 2004 and 2005 over the 14 experimental watersheds are presented in Figure 6.21 to Figure 6.25, which are respectively corresponding to the streamflows simulated by Noah LSM and NLDAS-2, RADAR, FUSED-1, FUSED-2 and FUSED-3 precipitation data. As shown in Figure 6.21, assimilating of the AMSR-E data significantly deteriorates streamflow simulation with NLDAS-2 data in most experimental watersheds except ALDW2, CYCK2, ELRP1 and PSNW2. Besides, data assimilation also doesn't deteriorate the NSE in CRWI3 in 2005. As shown in Figure 6.22, the impacts of data assimilation on NSE for the streamflows simulated with RADAR data are similar to the impacts on NSE for the streamflows simulated with NLDAS-2 data but the deteriorations are smaller than those shown in Figure 6.21. Similar finding of Figure 6.22 also can be found in Figure 6.23 and Figure 6.25, which shows that the NSEs of streamflows is simulated with FUSED-1 and FUSED-3 data. In Figure 6.24, even though data assimilation deteriorates the NSEs of simulated streamflows in most experimental watersheds, just like Figure 6.21, Figure 6.22, Figure 6.23 and Figure 6.25, there is a distinct difference in Figure 6.24 where considerable improvements of NSE are shown in SERI3 in 2004, KINT1 in 2004 and CRWI3 in 2004. This suggests that there are chances that data assimilation can help to improve streamflow simulation, even though data assimilation deteriorates streamflow simulations for most watersheds over most of the time.

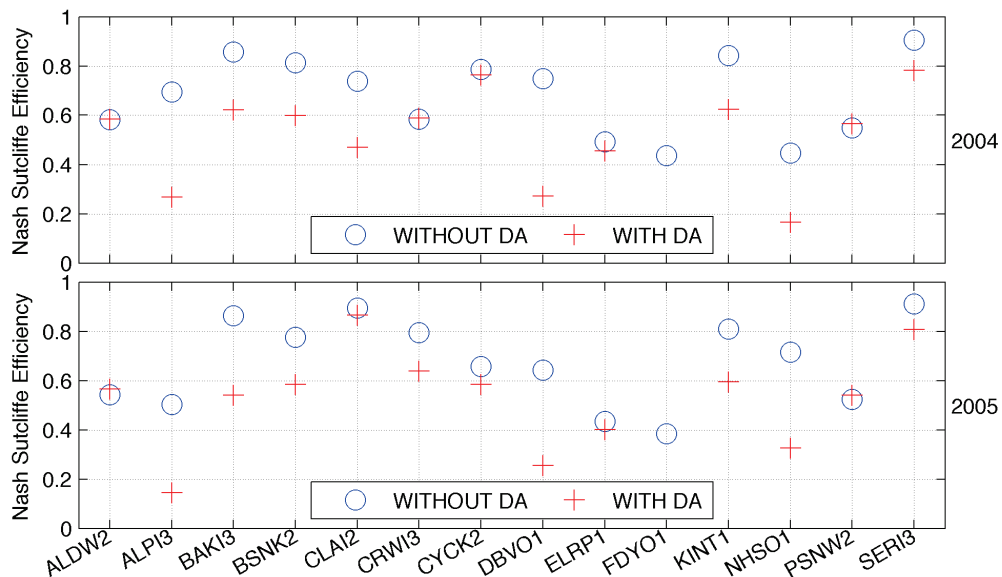


Figure 6.21 Nash-Sutcliffe Efficiencies with and without data assimilation in 2004 and 2005 over the 14 experimental watersheds. NLDAS-2 precipitation data are used in Noah LSM simulation.

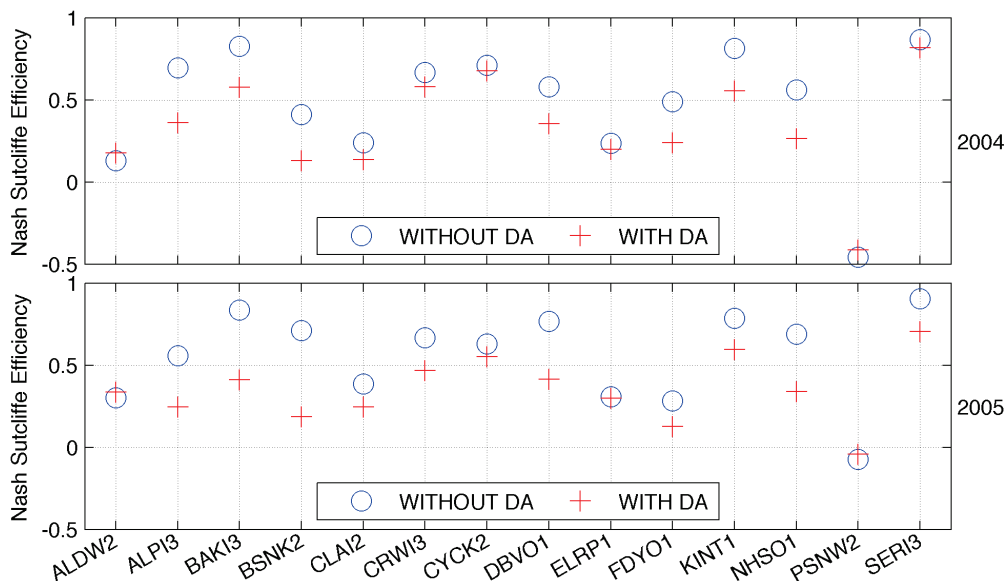


Figure 6.22 Nash-Sutcliffe Efficiencies with and without data assimilation in 2004 and 2005 over the 14 experimental watersheds. RADAR precipitation data are used in Noah LSM simulation.

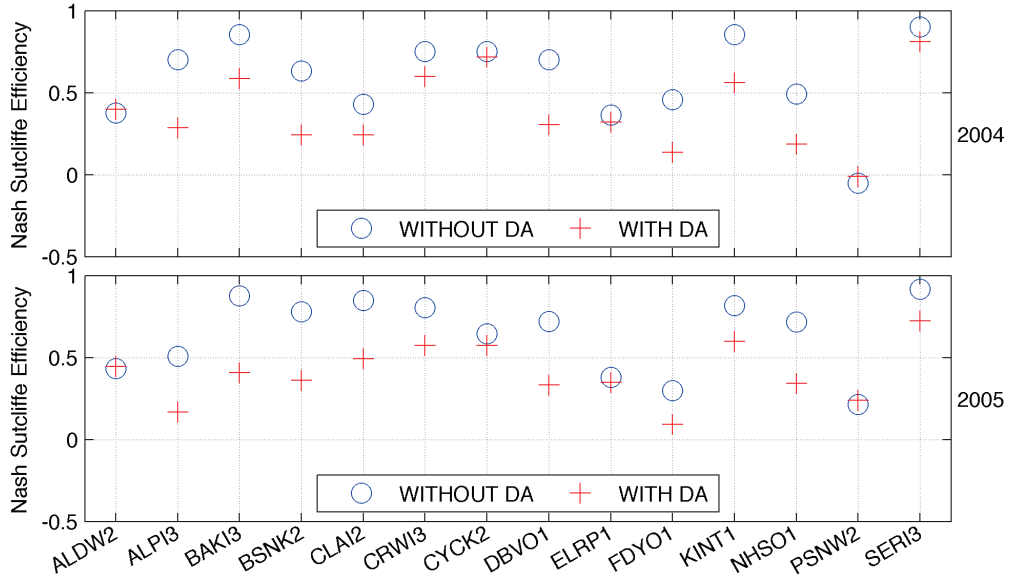


Figure 6.23 Nash-Sutcliffe Efficiencies with and without data assimilation in 2004 and 2005 over the 14 experimental watersheds. FUSED-1 precipitation data are used in Noah LSM simulation.

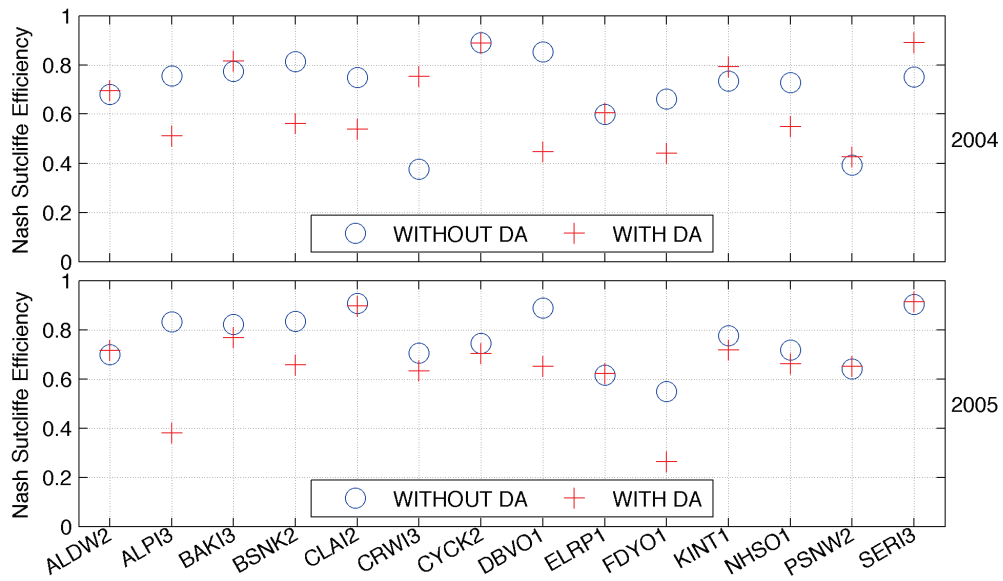


Figure 6.24 Nash-Sutcliffe Efficiencies with and without data assimilation in 2004 and 2005 over the 14 experimental watersheds. FUSED-2 precipitation data are used in Noah LSM simulation.

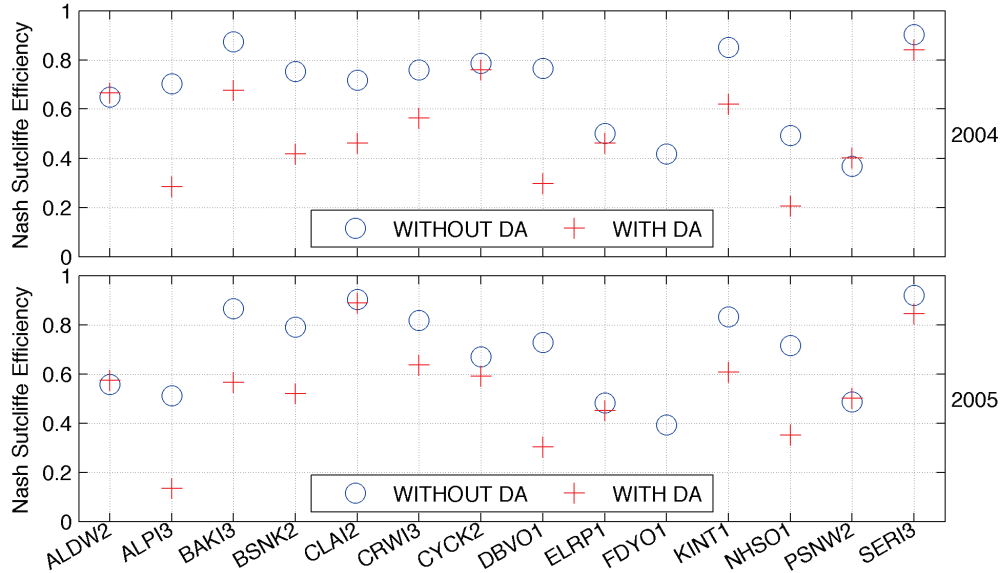


Figure 6.25 Nash-Sutcliffe Efficiencies with and without data assimilation in 2004 and 2005 over the 14 experimental watersheds. FUSED-3 precipitation data are used in Noah LSM simulation

In addition to NSE, hydrograph of streamflow series can also provide insights about the impacts of soil moisture data assimilation on streamflow simulations. Figure 6.26 to Figure 6.39 plot the observed streamflow and the streamflows simulated by Noah LSM and NLDAS-2 data with and without data assimilation in 2004 and 2005 for all of the 14 experimental watersheds. Except ALDW2, ELRP1 and PSNW2, the three watersheds with steep or very steep topographies, streamflows simulated with data assimilation are usually smaller than those simulated without data assimilation, which are usually smaller than observed streamflows. These findings indicate that simulations of Noah LSM and NLDAS-2 data already underestimate streamflows in most of watersheds, but data assimilation makes the simulation even severe. And then, the NSEs of streamflow are smaller after data assimilation.

Why data assimilation deteriorates streamflow simulations for some cases and improves streamflow simulations for some other cases? Streamflow simulation is impacted by data assimilation in terms of surface runoff generation and baseflow generation. For experimental watersheds except ALDW2, ELRP1 and PSNW2, data assimilation makes soil layers drier for the time except cold months. This means that the infiltration capacity of soil column is increased compared with the situation without data assimilation during the time. Then less surface runoff will be generated for given amount of precipitation. Meanwhile, baseflow is also decreased since the decrease of SMC in the bottom layer, namely SMC_4 . Due to the nonlinear relationship between gravitational drainage and SMC_4 , slight change of SMC_4 will cause considerable change of baseflow.

The impacts of data assimilation on runoff generations can explain the results shown in Figure 6.26 to Figure 6.39. According to the hydrographs, we can tell that the precipitation of NLDAS-2 data underestimate precipitation for most watersheds. After data assimilation, simulated SMCs are even smaller in the time except cold months because the AMSR-E data underestimate SH2O comparing simulated SH2O during the same time period. Sequentially, less surface runoff and baseflow are generated due to the decreases of SMCs caused by data assimilation. This is the reason why the NSEs of most experimental watersheds are smaller after data assimilation. However, there are also cases that NSEs are larger after data assimilation. This also can be explained by the impacts of data assimilation on runoff generation. As shown in Figure 5.27, Figure 5.32 and Figure 5.35 in chapter 5.0, FUSED-2 data obviously overestimate precipitation in CRWI3, KINT1, and SERI3 in 2004. There are peaks of hydrographs simulated with FUSED-2 data that are significantly larger than the observed peaks for these cases. Due to

the features of the AMSR-E data, data assimilation makes soil layers drier, which counteracts some of negative influences caused by the overestimation of precipitation. Therefore, streamflow simulations are improved for these cases. The impacts of data assimilation on runoff generation can also explain why the deteriorations of NSE in Figure 6.22 are smaller than those in Figure 6.21. It has been found in chapter 5.0, RADAR precipitation data usually have smaller magnitudes than NLDAS-2 data for most of experimental watersheds. In other words, the SMCs simulated with RADAR data are drier than those simulated with NLDAS-2 data. For this reason, the changes of SMCs made by data assimilation are smaller for the cases with RADAR data than the cases with NLDAS-2 data. Thus, it is reasonable that the deteriorations in Figure 6.22 are smaller than those in Figure 6.21.

In summary, streamflow simulations are not improved for most of the experimental watersheds by assimilating AMSR-E data into hydrological simulation with Noah LSMs and the five precipitation inputs. There are only very limited cases in which data assimilation makes improvements through firstly affecting soil moisture contents and then affecting runoff generation sequentially.

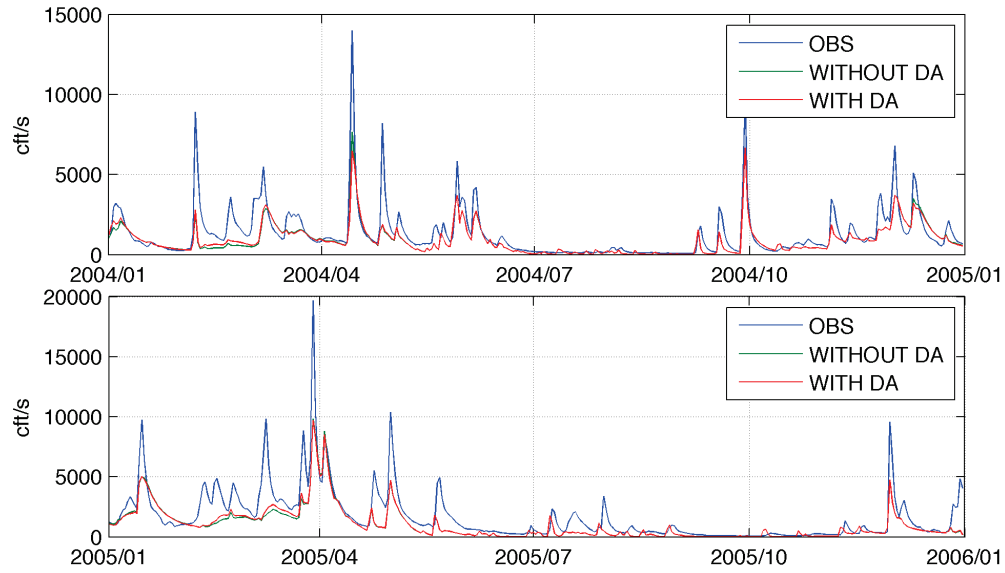


Figure 6.26 Observed streamflow series and simulated streamflow series with and without data assimilation by Noah LSM and NLDAS-2 forcing data in ALDW2 watershed for 2004 and 2005.

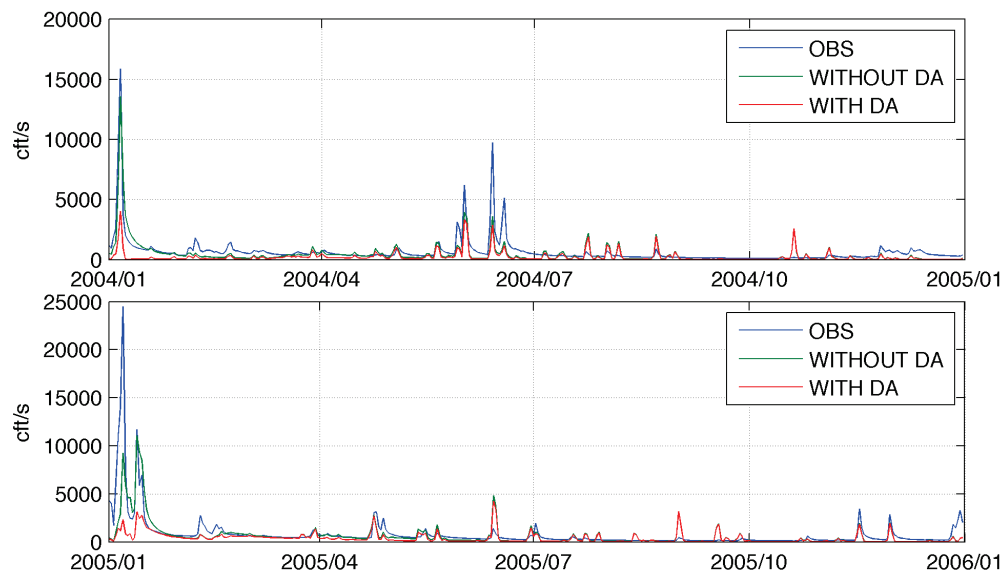


Figure 6.27 Observed streamflow series and simulated streamflow series with and without data assimilation by Noah LSM and NLDAS-2 forcing data in ALPI3 watershed for 2004 and 2005.

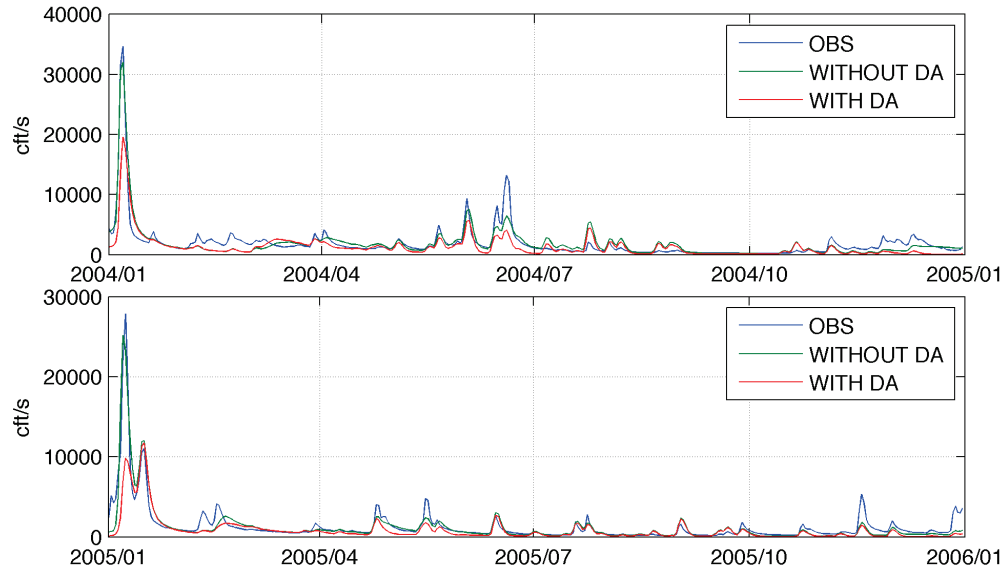


Figure 6.28 Observed streamflow series and simulated streamflow series with and without data assimilation by Noah LSM and NLDAS-2 forcing data in BAKI3 watershed for 2004 and 2005.

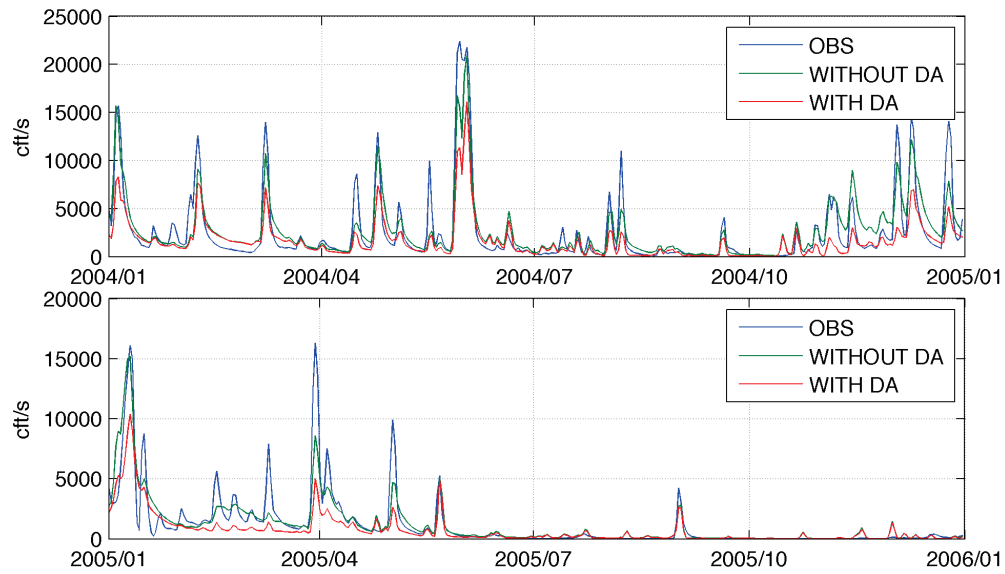


Figure 6.29 Observed streamflow series and simulated streamflow series with and without data assimilation by Noah LSM and NLDAS-2 forcing data in BSKN2 watershed for 2004 and 2005.

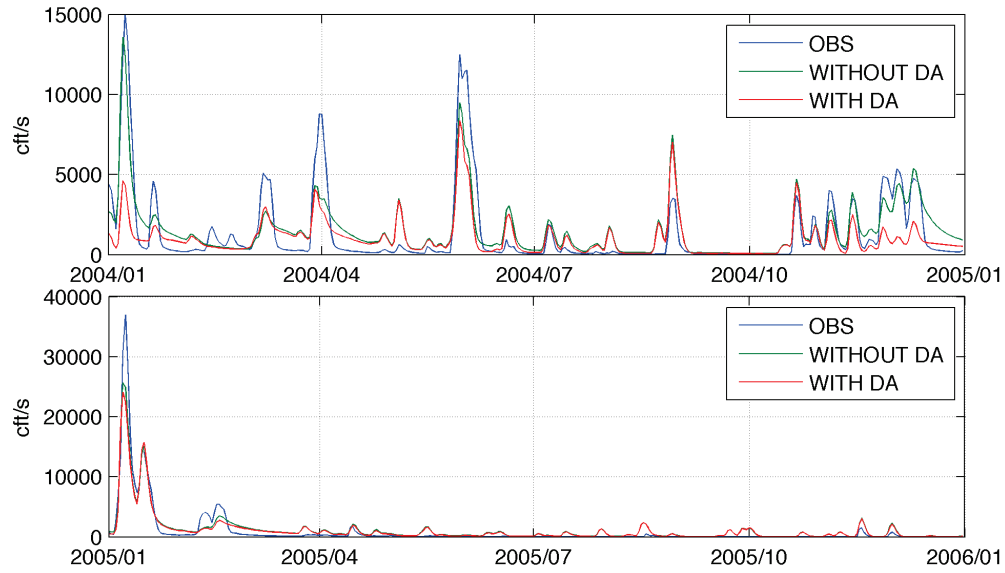


Figure 6.30 Observed streamflow series and simulated streamflow series with and without data assimilation by Noah LSM and NLDAS-2 forcing data in CLAI2 watershed for 2004 and 2005

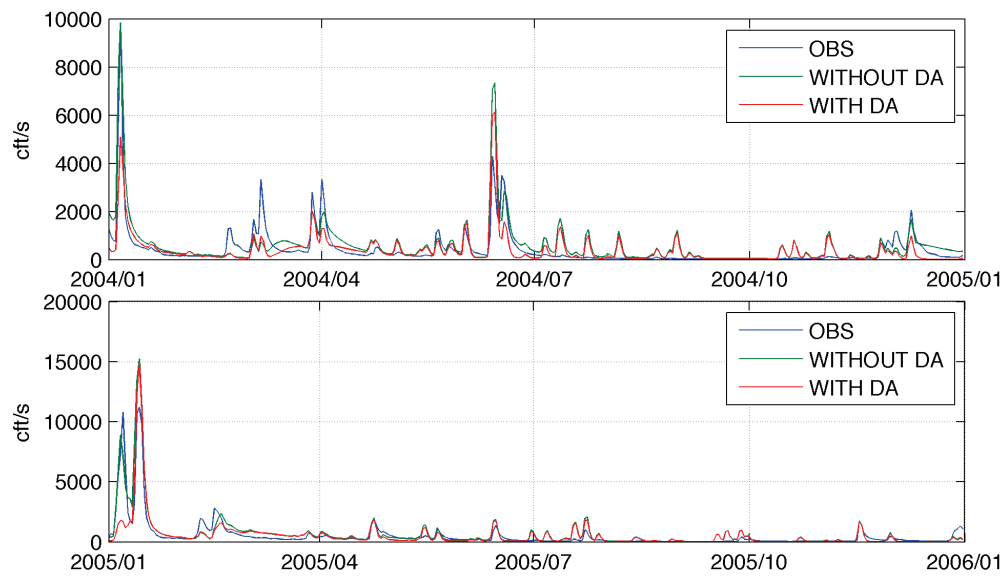


Figure 6.31 Observed streamflow series and simulated streamflow series with and without data assimilation by Noah LSM and NLDAS-2 forcing data in CRWI3 watershed for 2004 and 2005.

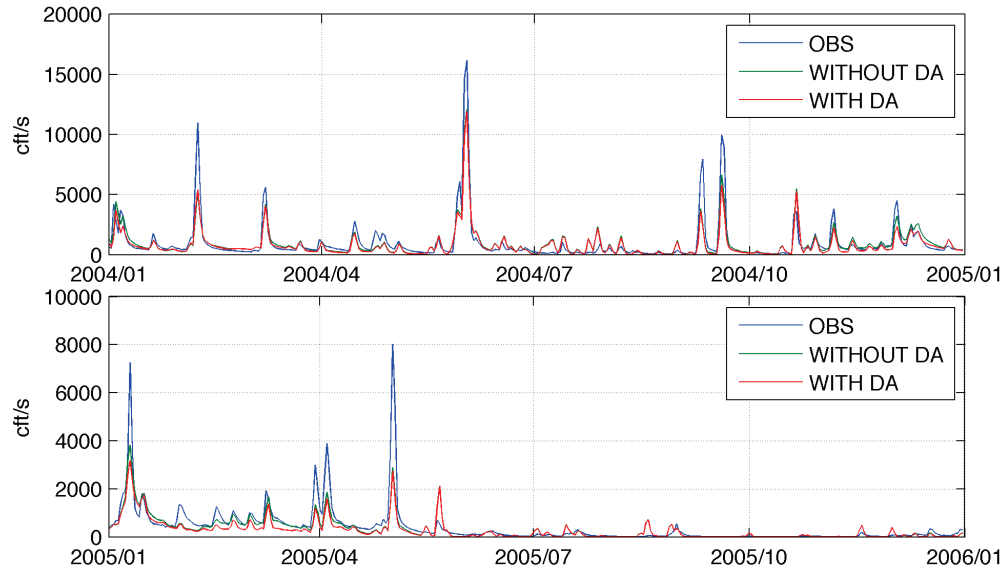


Figure 6.32 Observed streamflow series and simulated streamflow series with and without data assimilation by Noah LSM and NLDAS-2 forcing data in CYCK2 watershed for 2004 and 2005

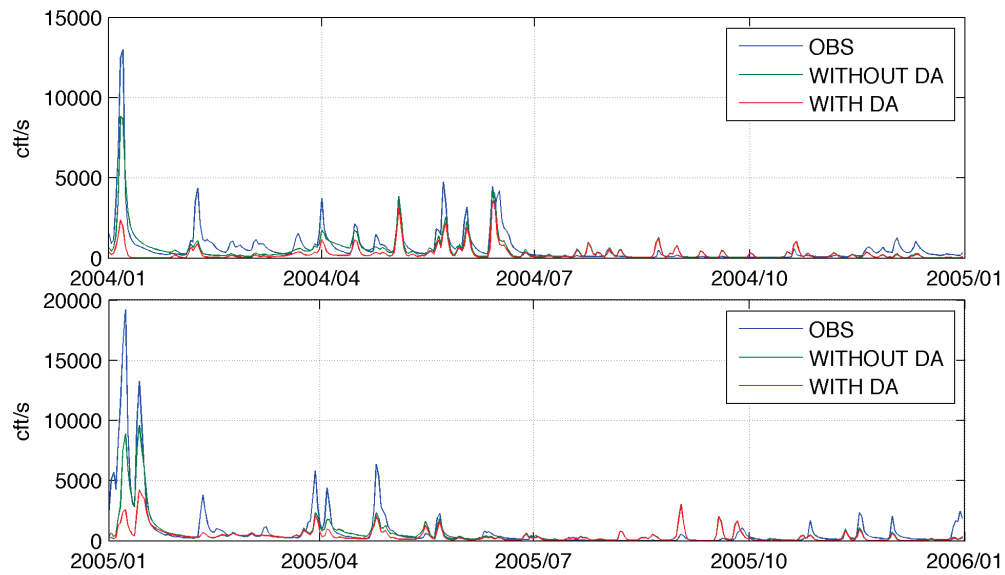


Figure 6.33 Observed streamflow series and simulated streamflow series with and without data assimilation by Noah LSM and NLDAS-2 forcing data in DBVO1 watershed for 2004 and 2005.

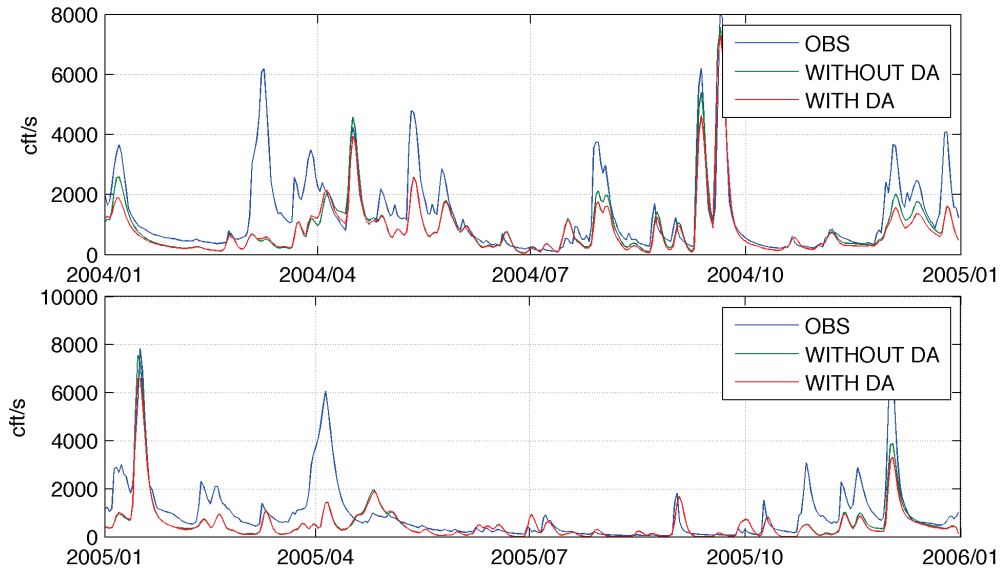


Figure 6.34 Observed streamflow series and simulated streamflow series with and without data assimilation by Noah LSM and NLDAS-2 forcing data in ELRP1 watershed for 2004 and 2005.

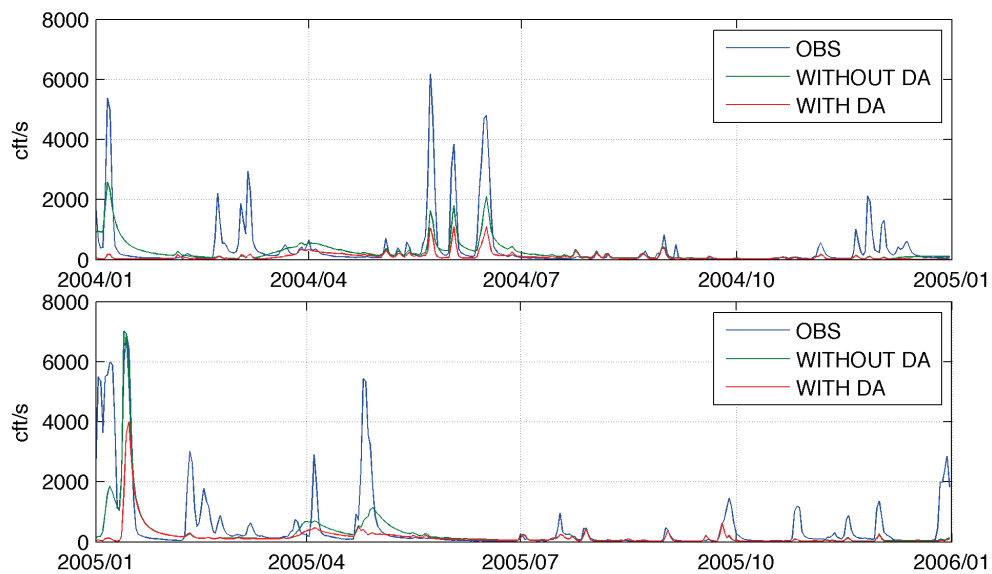


Figure 6.35 Observed streamflow series and simulated streamflow series with and without data assimilation by Noah LSM and NLDAS-2 forcing data in FDYO1 watershed for 2004 and 2005.

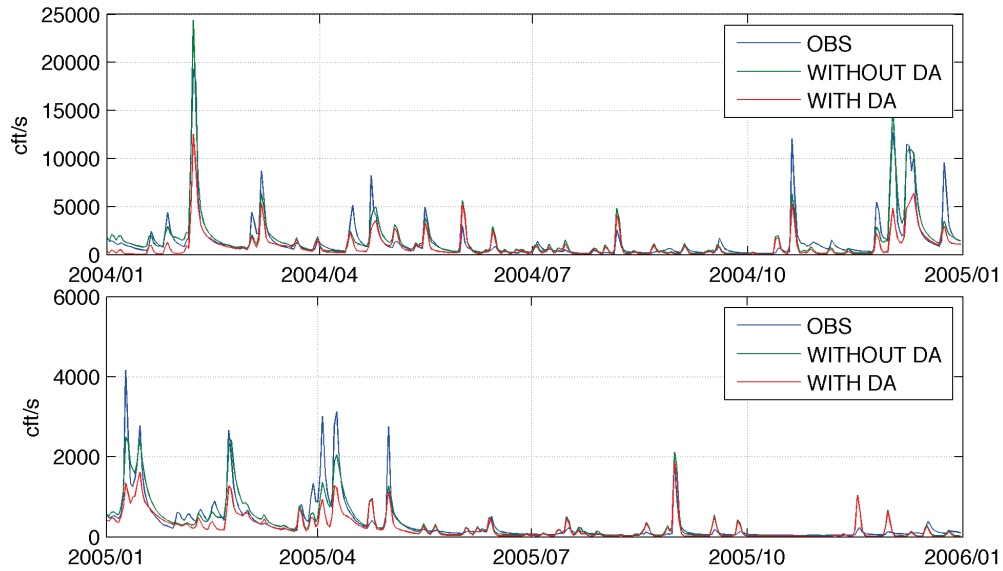


Figure 6.36 Observed streamflow series and simulated streamflow series with and without data assimilation by Noah LSM and NLDAS-2 forcing data in KINT1 watershed for 2004 and 2005.

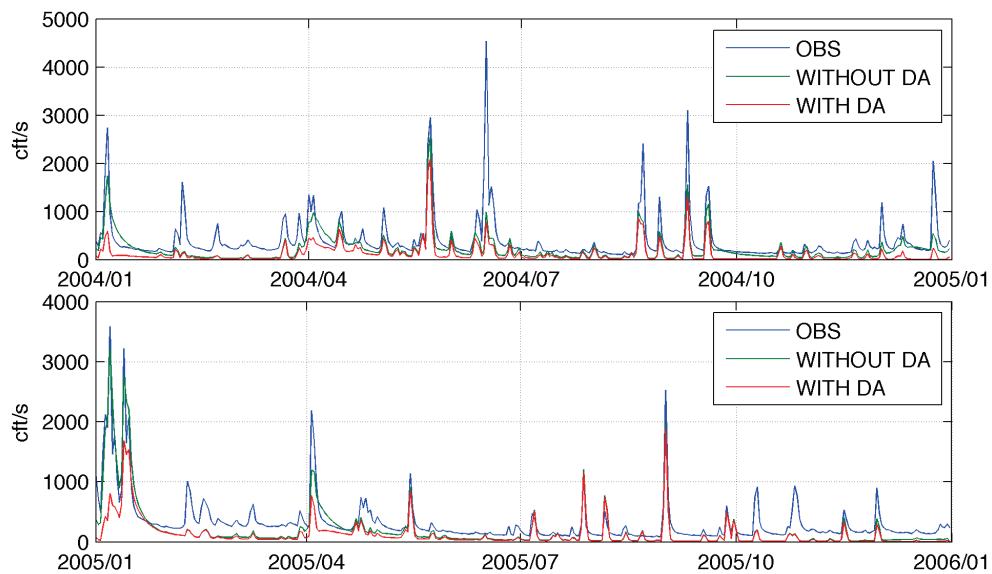


Figure 6.37 Observed streamflow series and simulated streamflow series with and without data assimilation by Noah LSM and NLDAS-2 forcing data in NHSO1 watershed for 2004 and 2005.

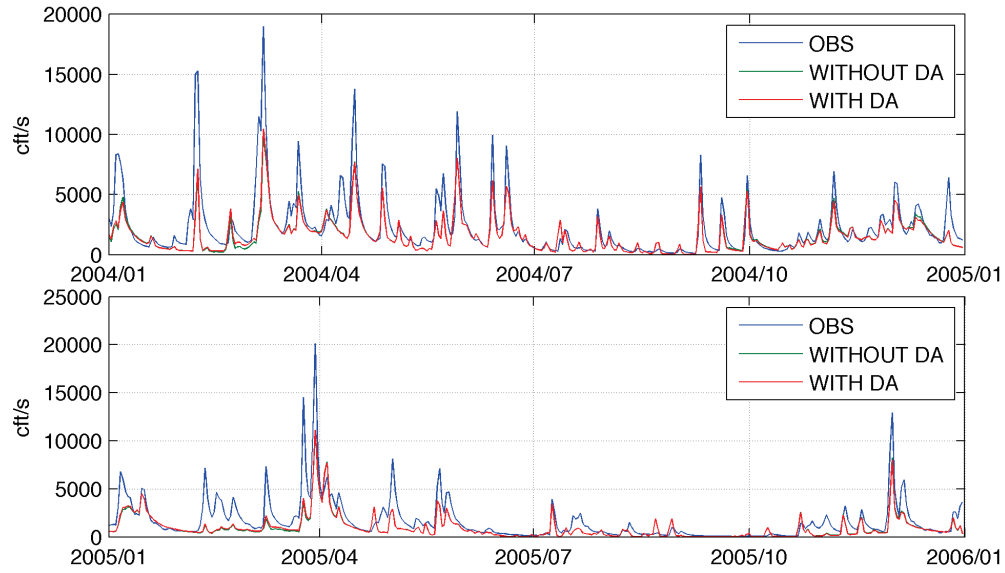


Figure 6.38 Observed streamflow series and simulated streamflow series with and without data assimilation by Noah LSM and NLDAS-2 forcing data in PSNW2 watershed for 2004 and 2005.

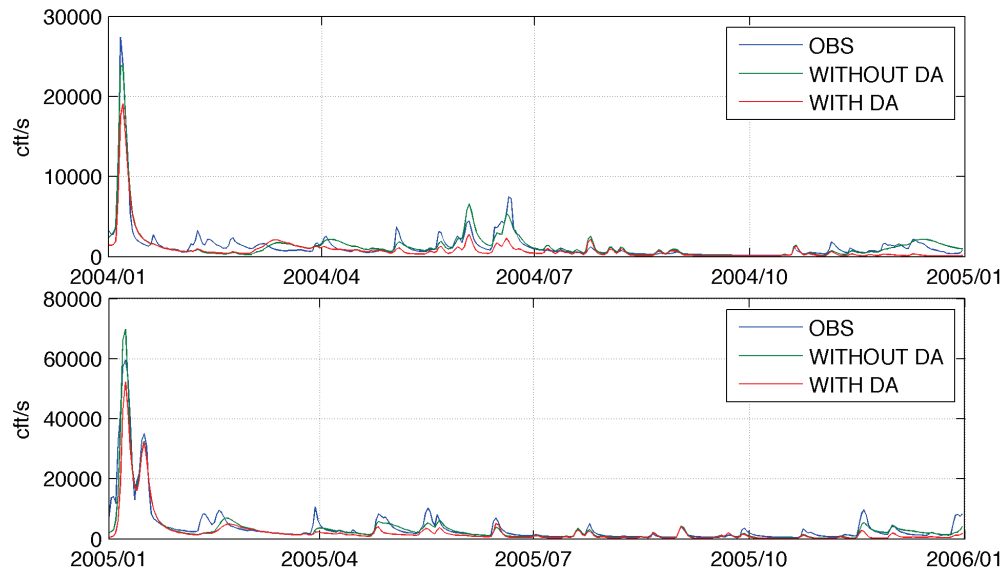


Figure 6.39 Observed streamflow series and simulated streamflow series with and without data assimilation by Noah LSM and NLDAS-2 forcing data in SERI3 watershed for 2004 and 2005.

6.4.3 Assessment in the simulation of evapotranspiration

In Noah LSM, total evapotranspiration (called ETA hereafter) mainly includes evaporation from bare soil and transpiration extracted from soil layers. Both of them are under the influences of soil moisture contents. Theoretically, if data assimilation increases soil moisture contents, then ETA will increased, whereas, if data assimilation decreases soil moisture contents, then ETA will decreased. In order to assess the influences of data assimilation on the simulation of evapotranspiration, the spatial average of daily ETA simulated by Noah and NLDAS-2 forcing data with and without data assimilation have been plotted in Figure 6.40 to Figure 6.53 for February, May, August and November in 2004. From these figures, firstly we can see that significant differences between ETAs simulated with and without data assimilation can be found in watersheds except ALDW2, ELRP1 and ALDW2. For all watersheds except KINT1, ETAs simulated with data assimilation are larger than ETAs simulated without data assimilation in some times of February. The reason for this result is that SMCs simulated with data assimilation are larger than SMCs simulated without data assimilation in these times. For plots of May, August and November, ETAs simulated with data assimilation are smaller than ETAs simulated without data assimilation for most of experimental watershed. This is because data assimilation decreases SMCs in these times.

These results indicate that data assimilation increases ETA in cold months and decreases ETA in the rest months of 2004. If hydrological simulation is evaluated using streamflow as reference, then data assimilation may deteriorate ETA simulation for most of watersheds over most of the time. However, this doesn't mean that data assimilation methods cannot help to improve ETA simulation. Instead, the deteriorations due to the quality of the AMSR-E data are

biased estimates. If unbiased satellite-measured data are available, or not as biased as the AMSR-E data used in this study, there are good chances that data assimilation would improve ETA simulation.

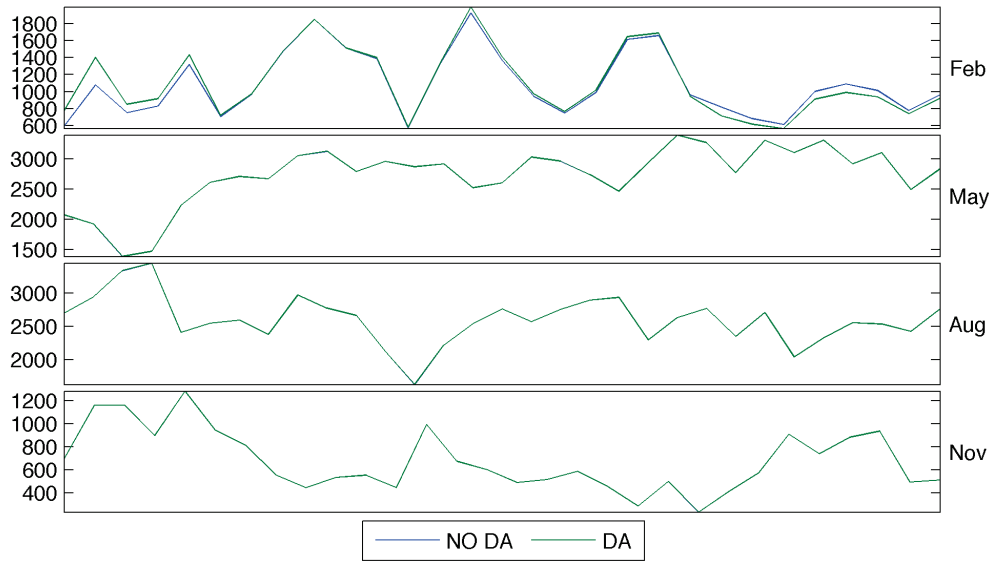


Figure 6.40 Spatial averages of simulated total evapotranspiration (W/m^2) with and without data assimilation by Noah LSM and NLDAS-2 forcing data in ALDW2 watershed in February, May, August and November of 2004.

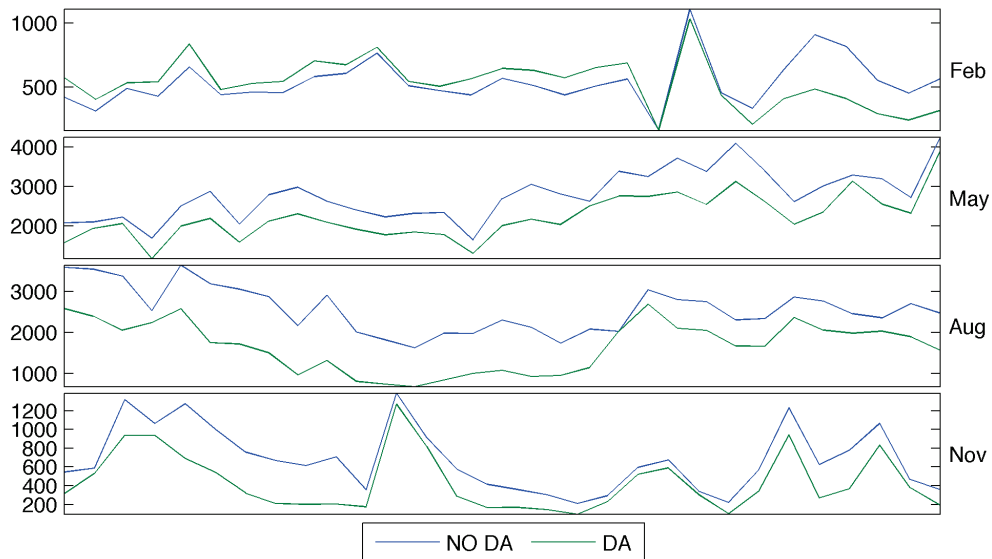


Figure 6.41 Spatial averages of simulated total evapotranspiration (W/m^2) with and without data assimilation by Noah LSM and NLDAS-2 forcing data in ALPI3 watershed in February, May, August and November of 2004.

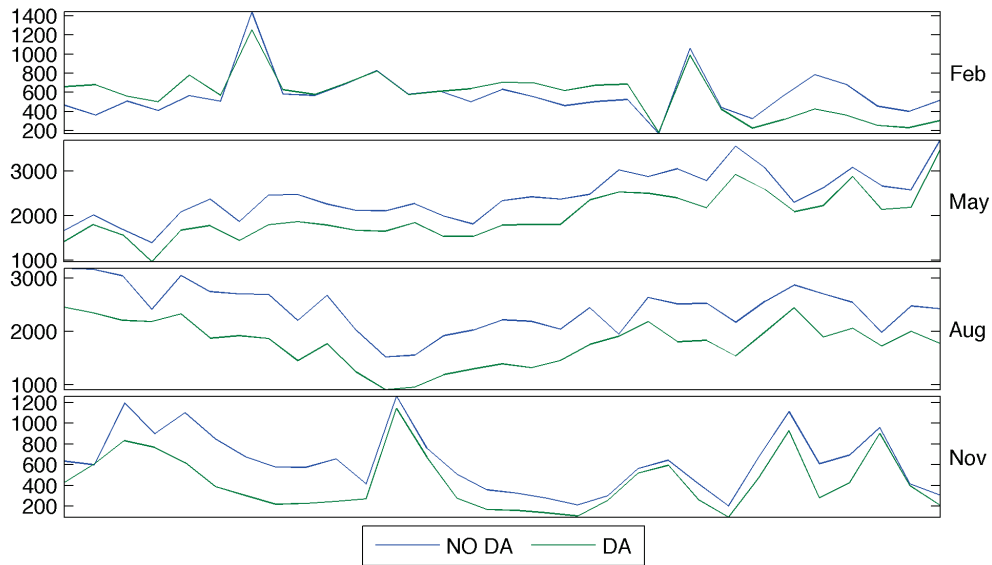


Figure 6.42 Spatial averages of simulated total evapotranspiration (W/m^2) with and without data assimilation by Noah LSM and NLDAS-2 forcing data in BAKI3 watershed in February, May, August and November of 2004.

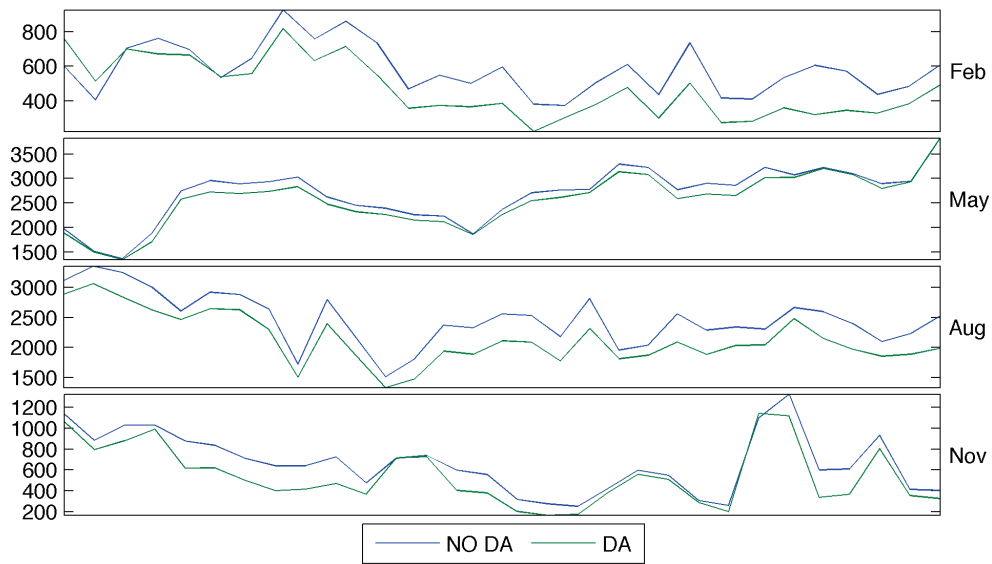


Figure 6.43 Spatial averages of simulated total evapotranspiration (W/m^2) with and without data assimilation by Noah LSM and NLDAS-2 forcing data in BSNK2 watershed in February, May, August and November of 2004.

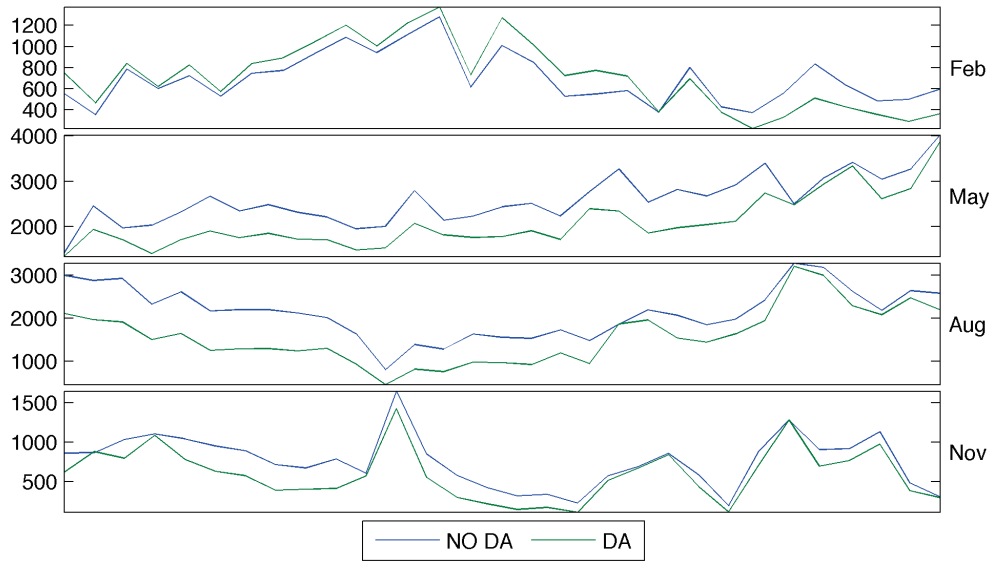


Figure 6.44 Spatial averages of simulated total evapotranspiration (W/m^2) with and without data assimilation by Noah LSM and NLDAS-2 forcing data in CLAI2 watershed in February, May, August and November of 2004.

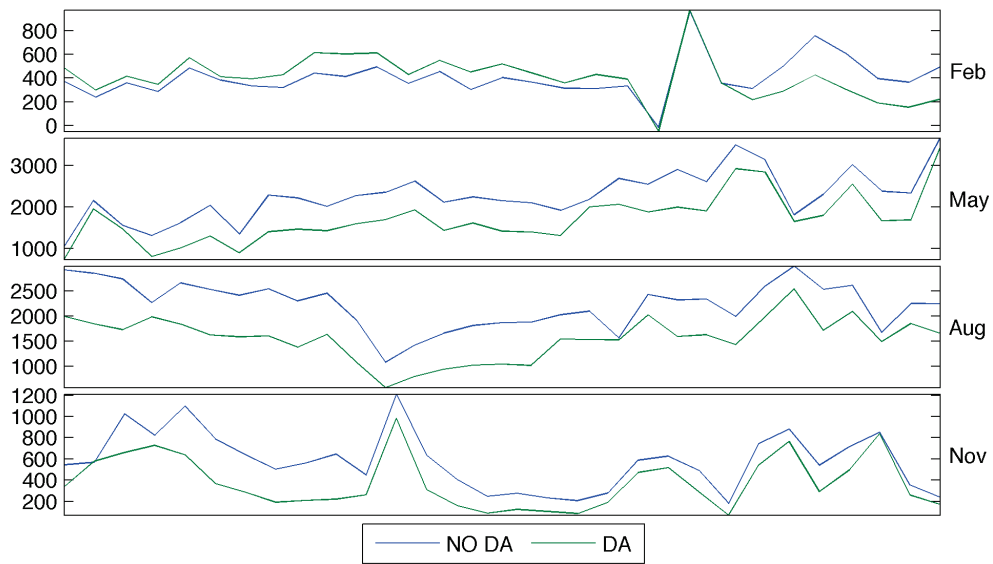


Figure 6.45 Spatial averages of simulated total evapotranspiration (W/m^2) with and without data assimilation by Noah LSM and NLDAS-2 forcing data in CRWI3 watershed in February, May, August and November of 2004.

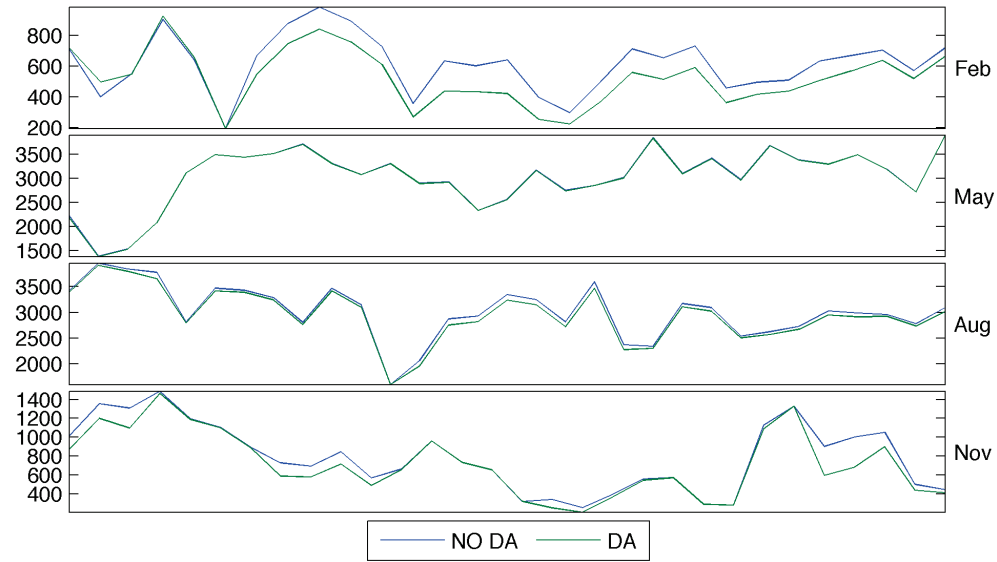


Figure 6.46 Spatial averages of simulated total evapotranspiration (W/m^2) with and without data assimilation by Noah LSM and NLDAS-2 forcing data in CYCK2 watershed in February, May, August and November of 2004.

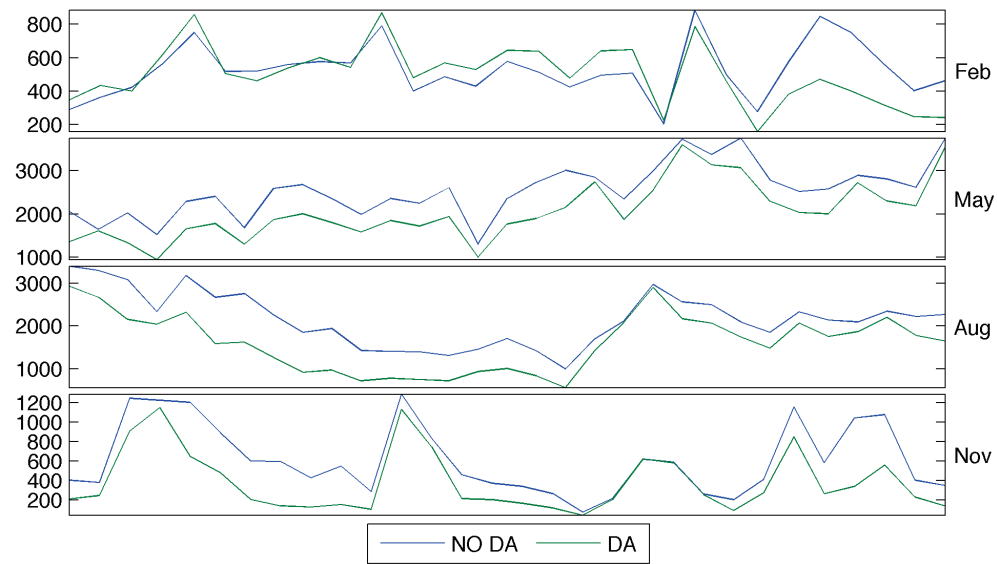


Figure 6.47 Spatial averages of simulated total evapotranspiration (W/m^2) with and without data assimilation by Noah LSM and NLDAS-2 forcing data in DBVO1 watershed in February, May, August and November of 2004.

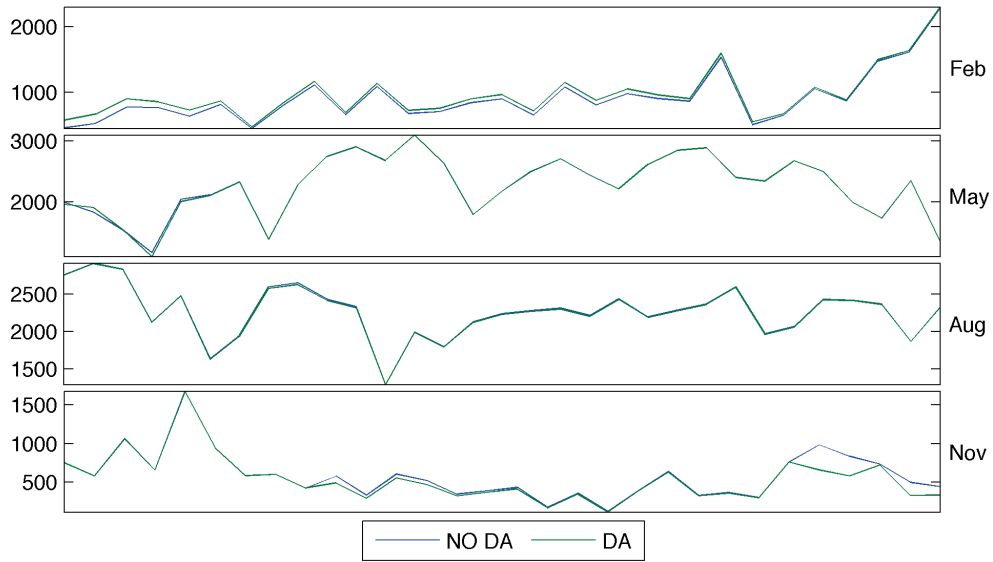


Figure 6.48 Spatial averages of simulated total evapotranspiration (W/m^2) with and without data assimilation by Noah LSM and NLDAS-2 forcing data in ELRP1 watershed in February, May, August and November of 2004.

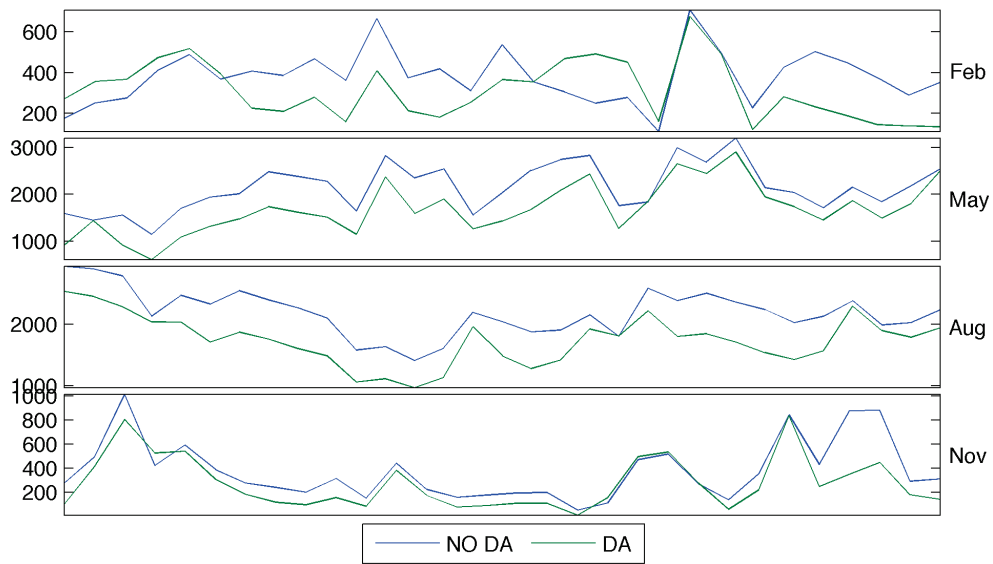


Figure 6.49 Spatial averages of simulated total evapotranspiration (W/m^2) with and without data assimilation by Noah LSM and NLDAS-2 forcing data in FDYO1 watershed in February, May, August and November of 2004.

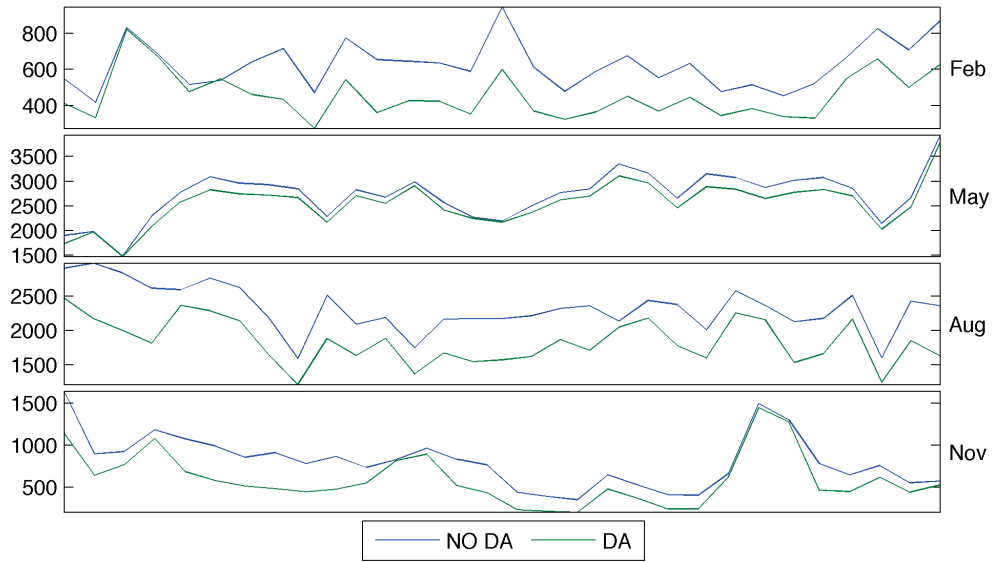


Figure 6.50 Spatial averages of simulated total evapotranspiration (W/m^2) with and without data assimilation by Noah LSM and NLDAS-2 forcing data in KINT1 watershed in February, May, August and November of 2004.

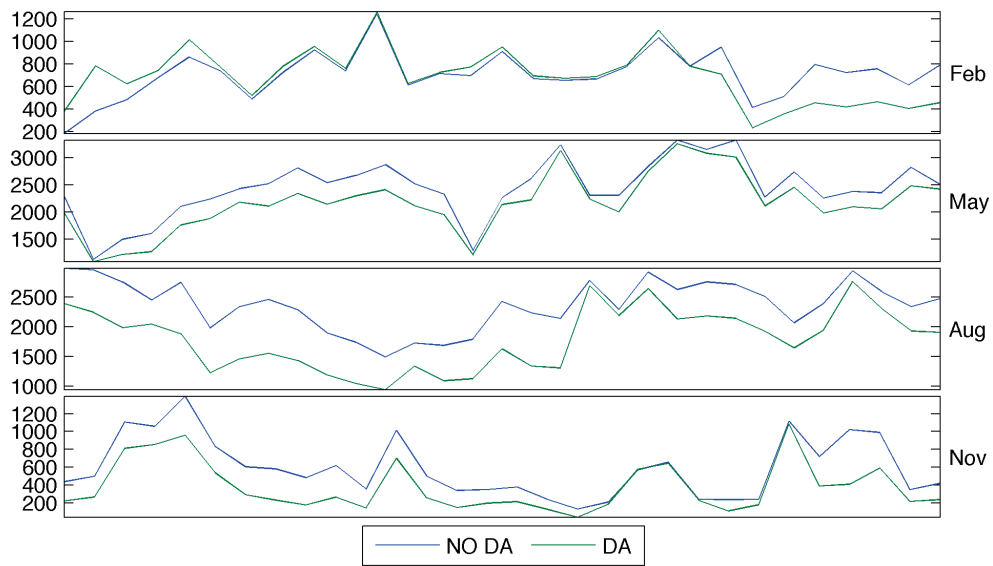


Figure 6.51 Spatial averages of simulated total evapotranspiration (W/m^2) with and without data assimilation by Noah LSM and NLDAS-2 forcing data in NHSO1 watershed in February, May, August and November of 2004.

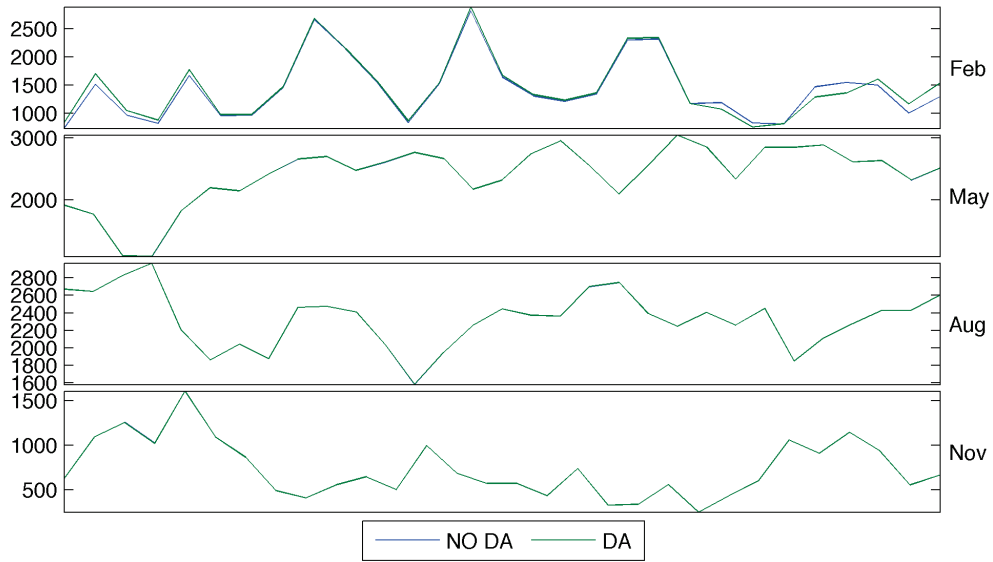


Figure 6.52 Spatial averages of simulated total evapotranspiration (W/m^2) with and without data assimilation by Noah LSM and NLDAS-2 forcing data in PSNW2 watershed in February, May, August and November of 2004.

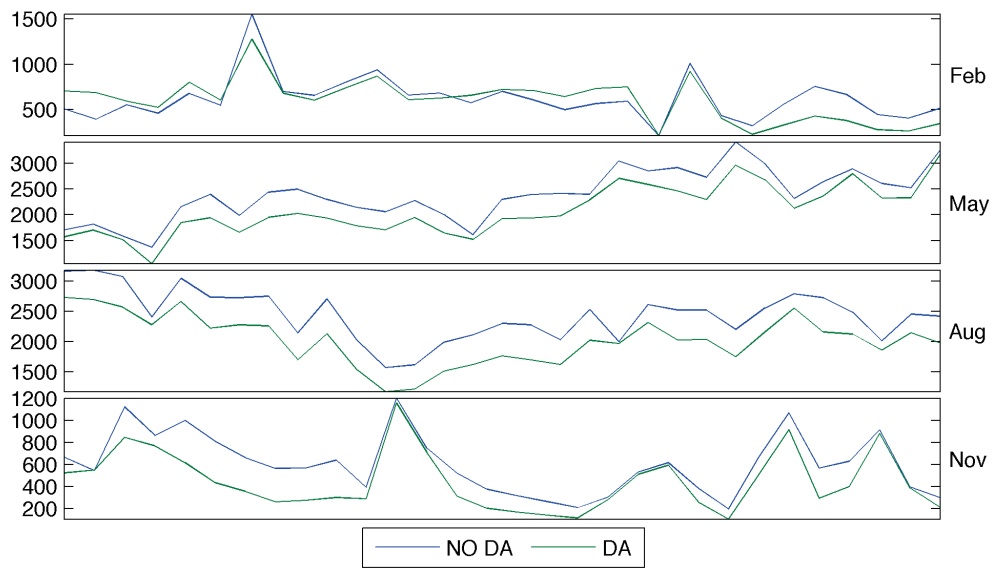


Figure 6.53 Spatial averages of simulated total evapotranspiration (W/m^2) with and without data assimilation by Noah LSM and NLDAS-2 forcing data in SERI3 watershed in February, May, August and November of 2004.

6.5 SUMMARY AND CONCLUSIONS

In this study, the impacts of soil moisture data assimilation on hydrological simulations have been investigated through simulations of soil moisture contents, streamflow and evapotranspiration. This study is featured for its multiple watersheds, multiple precipitation inputs and multiscale of data assimilation. Firstly, assessments are conducted in the 14 experimental watersheds, which represent watersheds with relatively cold and relatively warm climates in the Ohio River Basin. Secondly, for each watershed, we have five precipitation inputs, namely NLDAS-2, RADAR, FUSED-1, FUSED-2 and FUSED-3. The first two are widely-used precipitation data and the last three are derived precipitation data. Therefore, conclusions of this study are well applicable in the Ohio River Basin for scientific or operational purposes. Thirdly, this study assimilates the AMSR-E data into Noah LSM simulation, while the measurement and the simulation are at 1/4 degree and 1/8 degree respectively. A multiscale data fusion algorithm, namely MKS algorithm, is used in data assimilation.

Results of this study show that soil moisture data assimilation has significant impacts on simulated soil moistures, streamflow and evapotranspiration. In other words, data assimilation is an effective tool to improve hydrological simulation if satellite-measured soil moisture data have good quality. However, the performance of data assimilation on improving hydrological simulations heavily depends on the quality of measurements. In this study, the AMSR-E data are biased compared with model simulations using Noah LSM and the five precipitation inputs in all of experimental watersheds. In the cold months, the AMSR-E data overestimate liquid soil moisture contents, whereas in the rest months, AMSR-E data underestimate liquid soil moisture contents. This makes data assimilation deteriorate streamflow simulation for most of watersheds

in most of the time. If hydrological simulation is evaluated in terms of streamflow simulation, soil moisture contents and evapotranspiration are also deteriorated for most of watersheds in most of the time. Due to the feature of the AMSR-E data, data assimilation improves hydrological simulations only if precipitation is overestimated in the rest time other than cold months.

Even no significant improvements of hydrological simulations are obtained through soil moisture data assimilation; results of this study demonstrate that data assimilation of near surface soil moisture content can effectively change the state variables (e.g. SMCs) and outputs of hydrological model. In the future, soil moisture data assimilation needs to be further assessed with more reliable satellite-measured soil moisture data. In addition, there is one more topic need further investigation. The penetration depth of AMSR-E data is usually 3 – 5 cm but the thickness of the 1st layer of Noah model is 10 cm. This dimension mismatch may cause errors in soil moisture data assimilation.

7.0 SUMMARY AND CONCLUSIONS

For the purpose of improving hydrological forecast, this study has assessed the influences of precipitation data fusion and soil moisture data assimilation on the simulations of streamflow, soil moisture contents and evapotranspiration. A comprehensive hydrological information system has been developed as the basis of the assessments. This system includes modules of land surface simulation with Noah LSM, large-scale flow routing scheme for LSM, parameter calibration scheme for Noah LSM with multiple precipitation inputs, multiscale precipitation data fusion and multiscale soil moisture data assimilation. Scientific details of these modules are given in Chapter 2.0 , Chapter 3.0 , Chapter 5.0 and Chapter 6.0 . In addition, Chapter 4.0 systematically investigates the performance of the multiscale data fusion algorithm used in multiscale precipitation data fusion and multiscale soil moisture data assimilation. In order to increase the applicability of this study in operational hydrological forecast, the assessments of the precipitation data fusion and soil moisture data fusion are conducted in 14 experimental watersheds selected from the Ohio River Basin.

Major findings and conclusions of this study are summarized as follows:

- 1) The large-scale flow routing scheme proposed in Chapter 2.0 is a complete scheme for streamflow simulation with land surface models. It includes a derivation algorithm of large-scale flow network, a grid-ordering algorithm for sequential flow routing, and descriptions of

in-grid routing and between-grid routing. It has been proved that the proposed routing scheme is effective in routing runoffs simulated by Noah LSM into streamflow in the extensive applications in Chapter 5.0 and Chapter 6.0 .

- 2) The parameter calibration scheme proposed in Chapter 3.0 is innovative in terms of the consideration of consistencies between parameters, the reduction of dimension of optimization problem, multiobjective optimization for multiple precipitation inputs and parallel optimization algorithm. This calibration scheme provides a fair basis for comparing the reliabilities of multiple precipitation datasets through hydrological simulations. Applications in Chapter 5.0 and Chapter 6.0 have demonstrated that this calibration scheme can effectively identify optimal parameters for multiple precipitation inputs.
- 3) Before assessing the precipitation data fusion and soil moisture data assimilation, the performance of the multiscale data fusion algorithm, namely Multiscale Kalman Smoother (MKS) based framework, has been systematically investigated in Chapter 4.0 over a large watershed for one-year's precipitation events. The MKS based framework has been found significantly effective in removing white noises in multiscale measurements, especially for the noises in the measurements at coarser resolutions. In addition, the MKS based framework can also remove the biases of measurements, which, however, relies on the method of estimating the areal mean of state variables.
- 4) The assessment of precipitation data fusion has been conducted in terms of the simulations of streamflow, soil moisture contents and evapotranspiration over 14 experimental watersheds in Chapter 5.0. NLDAS-2 precipitation data (at 1/8 degree resolution) and NEXRAD MPE precipitation data (at approximately 1/32 degree resolution) are fused by the MKS based framework with three settings for estimating the areal mean of precipitation. In total, five

precipitation datasets including NLDAS-2, NEXRAD MPE and three derived precipitation datasets are compared. It has shown that precipitation data fusion is a statistically effective approach to improve hydrological simulations. Based on the assessments over the 14 experimental watersheds for a period of three years, essential improvements in streamflow simulations are found in 21 water/year over 42 watershed/year. In addition, significant differences of simulated soil moisture contents and simulated evapotranspiration can be made through precipitation data fusion. The improvements made through precipitation data fusion vary over watersheds. Both the mean magnitudes and the spatial patterns of NEXRAD MPE data can help to improve the NLDAS-2 precipitation data. However, the mean magnitudes usually play a much bigger role.

- 5) The assessment of soil moisture data assimilation has been conducted in terms of the simulations of streamflow, soil moisture contents and evapotranspiration over the 14 experimental watersheds in Chapter 6.0. AMSR-E near surface soil moisture data have been assimilated into the land surface simulation by Noah LSM with the five precipitation inputs used in the assessments of precipitation data fusion. It has revealed that, compared with the liquid soil moisture content simulated by Noah LSM with the five precipitation inputs, AMSR-E data overestimate the liquid soil moisture content during cold months (e.g. December, January and February) but underestimate the liquid soil moisture content during the rest months. Due to this reason, the assimilation of AMSR-E data deteriorated hydrological simulations over most of the experimental watersheds in most of time except the cases that precipitation data significantly overestimate real precipitation. In addition, significant changes in simulated soil moisture contents and evapotranspiration have been made by soil moisture data assimilation. The findings in Chapter 6.0 also demonstrate the

potential of soil moisture data assimilation to improve hydrological simulations. Once the satellite-measured soil moisture with better accuracies are available, it is expected that hydrological simulations can be improved through soil moisture data assimilation.

Even though experiments of this study are well designed for the purposes of assessing precipitation data fusion and soil moisture data assimilation, there are two limitations of this study. One is that the influences of precipitation data fusion and soil moisture data assimilation on the simulations of soil moisture contents and evapotranspiration are not directly assessed against measurements. Further assessments are necessary once reliable spatial measurements of soil moisture contents and evapotranspiration are available. The other is that Noah LSM may have poor performances in simulating snow accumulation and melting processes, which introduces uncertainties to the findings of this study in cold climate. In the future, further research can be conducted with other LSMs and better description of the snow accumulation and melting process.

BIBLIOGRAPHY

- Anagnostou, E. N., C. A. Morales, et al. (2001). "The use of TRMM precipitation radar observations in determining ground radar calibration biases." Journal of Atmospheric and Oceanic Technology **18**(4): 616-628.
- Aron, G. and E. L. White (1982). "Fitting a Gamma Distribution Over a Synthetic Unit Hydrograph." Journal of the American Water Resources Association **18**(1): 95-98.
- Arora, V., F. Seglenieks, et al. (2001). "Scaling aspects of river flow routing." Hydrological Processes **15**(3): 461-477.
- Arora, V. K. (2001). "Streamflow simulations for continental-scale river basins in a global atmospheric general circulation model." Advances in Water Resources **24**(7): 775-791.
- Arora, V. K. and G. J. Boer (1999). "A variable velocity flow routing algorithm for GCMs." Journal of Geophysical Research-Atmospheres **104**(D24): 30965-30979.
- Arora, V. K., F. H. S. Chiew, et al. (1999). "A river flow routing scheme for general circulation models." Journal of Geophysical Research-Atmospheres **104**(D12): 14347-14357.
- Arora, V. K. and S. Harrison (2007). "Upscaling river networks for use in climate models." Geophysical Research Letters **34**(21): -.
- Aubert, D., C. Loumagne, et al. (2003). "Sequential assimilation of soil moisture and streamflow data in a conceptual rainfall-runoff model." Journal of Hydrology **280**(1-4): 145-161.
- Basseville, M., A. Benveniste, et al. (1992). "Modeling and Estimation of Multiresolution Stochastic-Processes." Ieee Transactions on Information Theory **38**(2): 766-784.
- Bastidas, L. A., T. S. Hogue, et al. (2006). "Parameter sensitivity analysis for different complexity land surface models using multicriteria methods." Journal of Geophysical Research-Atmospheres **111**(D20): -.
- Beven, K. (1997). "Topmodel: A Critique." Hydrological Processes **11**(9): 1069-1085.
- Beven, K. and J. Freer (2001). "A dynamic TOPMODEL." Hydrological Processes **15**(10): 1993-2011.

- Bocchiola, D. (2007). "Use of scale recursive estimation for assimilation of precipitation data from TRMM (PR and TMI) and NEXRAD." Advances in Water Resources **30**(11): 2354-2372.
- Bocchiola, D. and R. Rosso (2006). "The use of scale recursive estimation for short term quantitative precipitation forecast." Physics and Chemistry of the Earth **31**(18): 1228-1239.
- Bonan, G. B., P. J. Lawrence, et al. (2011). "Improving canopy processes in the Community Land Model version 4 (CLM4) using global flux fields empirically inferred from FLUXNET data." J. Geophys. Res. **116**(G2): G02014.
- Brooks, R. H. and A. T. Corey (1966). "Properties of Porous Media Affecting Fluid Flow." Journal of irrigation and drainage engineering **6**(61).
- Cashion, J., V. Lakshmi, et al. (2005). "Microwave remote sensing of soil moisture: Evaluation of the TRMM microwave imager (TMI) satellite for the Little River Watershed Tifton, Georgia." Journal of Hydrology **307**(1-4): 242-253.
- Chen, F. and J. Dudhia (2001). "Coupling an advanced land surface-hydrology model with the Penn State-NCAR MM5 modeling system. Part I: Model implementation and sensitivity." Monthly Weather Review **129**(4): 569-585.
- Chen, F., Z. Janjic, et al. (1997). "Impact of atmospheric surface-layer parameterizations in the new land-surface scheme of the NCEP mesoscale Eta model." Boundary-Layer Meteorology **85**(3): 391-421.
- Chen, F., K. Mitchell, et al. (1996). "Modeling of land surface evaporation by four schemes and comparison with FIFE observations." Journal of Geophysical Research-Atmospheres **101**(D3): 7251-7268.
- Chou, K. C., S. Golden, et al. (1991). Modeling and estimation of multiscale stochastic processes. Acoustics, Speech, and Signal Processing, 1991. ICASSP-91., 1991 International Conference on.
- Chou, K. C., S. A. Golden, et al. (1993). "Multiresolution Stochastic-Models, Data Fusion, and Wavelet Transforms." Signal Processing **34**(3): 257-282.
- Chou, K. C. and A. S. Willsky (1991). Modeling and estimation of multiscale processes. Signals, Systems and Computers, 1991. 1991 Conference Record of the Twenty-Fifth Asilomar Conference on.
- Chou, K. C., A. S. Willsky, et al. (1994). "Multiscale recursive estimation, data fusion, and regularization." Automatic Control, IEEE Transactions on **39**(3): 464-478.

- Chou, K. C., A. S. Willsky, et al. (1994). "Multiscale Systems, Kalman Filters, and Riccati Equations." Ieee Transactions on Automatic Control **39**(3): 479-492.
- Coe, M. T. (1998). "A linked global model of terrestrial hydrologic processes: Simulation of modern rivers, lakes, and wetlands." Journal of Geophysical Research-Atmospheres **103**(D8): 8885-8899.
- Coe, M. T. (2000). "Modeling terrestrial hydrological systems at the continental scale: Testing the accuracy of an atmospheric GCM." Journal of Climate **13**(4): 686-704.
- Cosby, B. J., G. M. Hornberger, et al. (1984). "A Statistical Exploration of the Relationships of Soil Moisture Characteristics to the Physical Properties of Soils." Water Resour. Res. **20**(6): 682-690.
- Cosgrove, B. A., D. Lohmann, et al. (2003). "Real-time and retrospective forcing in the North American Land Data Assimilation System (NLDAS) project." J. Geophys. Res. **108**(D22).
- Costa, M. H. and J. A. Foley (1997). "Water balance of the Amazon Basin: Dependence on vegetation cover and canopy conductance." Journal of Geophysical Research-Atmospheres **102**(D20): 23973-23989.
- Croley, T. E. (1980). "Gamma synthetic hydrographs." Journal of Hydrology **47**(1-2): 41-52.
- Croley, T. E. (1980). "A micro-hydrology computation ordering algorithm." Journal of Hydrology **48**(3-4): 221-236.
- Croley, T. E. and C. S. He (2005). "Distributed-parameter large basin runoff model. I: Model development." Journal of Hydrologic Engineering **10**(3): 173-181.
- Crow, W. T., M. Drusch, et al. (2001). "An observation system simulation experiment for the impact of land surface heterogeneity on AMSR-E soil moisture retrieval." Ieee Transactions on Geoscience and Remote Sensing **39**(8): 1622-1631.
- Crow, W. T., E. F. Wood, et al. (2003). "Multiobjective calibration of land surface model evapotranspiration predictions using streamflow observations and spaceborne surface radiometric temperature retrievals." Journal of Geophysical Research-Atmospheres **108**(D23): -.
- Dai, Y. J., R. E. Dickinson, et al. (2004). "A two-big-leaf model for canopy temperature, photosynthesis, and stomatal conductance." Journal of Climate **17**(12): 2281-2299.
- Dai, Y. J., X. B. Zeng, et al. (2003). "The Common Land Model." Bulletin of the American Meteorological Society **84**(8): 1013-+.

- Davies, H. N. and V. A. Bell (2009). "Assessment of methods for extracting low-resolution river networks from high-resolution digital data." Hydrological Sciences Journal-Journal Des Sciences Hydrologiques **54**(1): 17-28.
- de Vyver, H. V. and E. Roulin (2009). "Scale-recursive estimation for merging precipitation data from radar and microwave cross-track scanners." Journal of Geophysical Research-Atmospheres **114**: -.
- DelGreco, S., D. Kim, et al. (2005). Operational Issues from NCDC Perspective. Q2 - Next Generation QPE and QPF Workshop. Norman OK.
- Demarty, J., C. Otle, et al. (2005). "Constraining a physically based Soil-Vegetation-Atmosphere Transfer model with surface water content and thermal infrared brightness temperature measurements using a multiobjective approach." Water Resources Research **41**(1): -.
- Drusch, M., E. F. Wood, et al. (1999). "The impact of the SSM/I antenna gain function on land surface parameter retrieval." Geophysical Research Letters **26**(23): 3481-3484.
- Du, J. K., S. P. Xie, et al. (2007). "Development and testing of a simple physically-based distributed rainfall-runoff model for storm runoff simulation in humid forested basins." Journal of Hydrology **336**(3-4): 334-346.
- Duan, Q. Y., S. Sorooshian, et al. (1992). "Effective and Efficient Global Optimization for Conceptual Rainfall-Runoff Models." Water Resources Research **28**(4): 1015-1031.
- Duan, Q. Y., S. Sorooshian, et al. (1994). "Optimal Use of the Sce-Ua Global Optimization Method for Calibrating Watershed Models." Journal of Hydrology **158**(3-4): 265-284.
- Ek, M. B., K. E. Mitchell, et al. (2003). "Implementation of Noah land surface model advances in the National Centers for Environmental Prediction operational mesoscale Eta model." Journal of Geophysical Research-Atmospheres **108**(D22): -.
- Farina, A., F. C. Morabito, et al. (2001). Fusion of radar images: state of art and perspective. Radar, 2001 CIE International Conference on, Proceedings.
- Fekete, B. M., C. J. Vorosmarty, et al. (2001). "Scaling gridded river networks for macroscale hydrology: Development, analysis, and control of error." Water Resources Research **37**(7): 1955-1967.
- Francois, C., A. Quesney, et al. (2003). "Sequential assimilation of ERS-1 SAR data into a coupled land surface-hydrological model using an extended Kalman filter." Journal of Hydrometeorology **4**(2): 473-487.
- Gill, M. K., Y. H. Kaheil, et al. (2006). "Multiobjective particle swarm optimization for parameter estimation in hydrology." Water Resources Research **42**(7).

- Gong, L., E. Widen-Nilsson, et al. (2009). "Large-scale runoff routing with an aggregated network-response function." Journal of Hydrology **368**(1-4): 237-250.
- Gorenburg, I. P., D. McLaughlin, et al. (2001). "Scale-recursive assimilation of precipitation data." Advances in Water Resources **24**(9-10): 941-953.
- Grimes, D. I. F., E. Pardo-Iguzquiza, et al. (1999). "Optimal areal rainfall estimation using raingauges and satellite data." Journal of Hydrology **222**(1-4): 93-108.
- Guo, J. H., X. Liang, et al. (2004). "A new multiscale flow network generation scheme for land surface models." Geophysical Research Letters **31**(23): -.
- Gupta, R., V. Venugopal, et al. (2006). "A methodology for merging multisensor precipitation estimates based on expectation-maximization and scale-recursive estimation." Journal of Geophysical Research-Atmospheres **111**(D2): -.
- Gupta, V. K. and E. C. Waymire (1993). "A Statistical-Analysis of Mesoscale Rainfall as a Random Cascade." Journal of Applied Meteorology **32**(2): 251-267.
- Gusev, E. M., O. N. Nasonova, et al. (2008). "The application of the land surface model for calculating river runoff in high latitudes." Water Resources **35**(2): 171-184.
- Habib, E., B. F. Larson, et al. (2009). "Validation of NEXRAD multisensor precipitation estimates using an experimental dense rain gauge network in south Louisiana." Journal of Hydrology **373**(3-4): 463-478.
- Hagemann, S. and L. Dumenil (1998). "A parametrization of the lateral waterflow for the global scale." Climate Dynamics **14**(1): 17-31.
- Harris, P. P., C. Huntingford, et al. (2004). "Calibration of a land-surface model using data from primary forest sites in Amazonia." Theoretical and Applied Climatology **78**(1-3): 27-45.
- Huang, C. L., X. Li, et al. (2008). "Retrieving soil temperature profile by assimilating MODIS LST products with ensemble Kalman filter." Remote Sensing of Environment **112**(4): 1320-1336.
- Jain, M. K., U. C. Kothyari, et al. (2004). "A GIS based distributed rainfall-runoff model." Journal of Hydrology **299**(1-2): 107-135.
- Jain, M. K. and V. P. Singh (2005). "DEM-based modelling of surface runoff using diffusion wave equation." Journal of Hydrology **302**(1-4): 107-126.
- Johnsen, K. P., H. T. Mengelkamp, et al. (2005). "Multi-objective calibration of the land surface scheme TERRA/LM using LITFASS-2003 data." Hydrology and Earth System Sciences **9**(6): 586-595.

- Kannan, A., M. Ostendorf, et al. (2000). "ML parameter estimation of a multiscale stochastic process using the EM algorithm." IEEE Transactions on Signal Processing **48**(6): 1836-1840.
- Kennedy, J. and R. Eberhart (1995). Particle swarm optimization. Neural Networks, 1995. Proceedings., IEEE International Conference on.
- Klingaman, N. P., J. Butke, et al. (2008). "Mesoscale Simulations of the land surface effects of historical logging in a moist continental climate regime." Journal of Applied Meteorology and Climatology **47**(8): 2166-2182.
- Koren, V., J. Schaake, et al. (1999). "A parameterization of snowpack and frozen ground intended for NCEP weather and climate models." Journal of Geophysical Research-Atmospheres **104**(D16): 19569-19585.
- Krajewski, W. F., G. Villarini, et al. (2010). "Radar-Rainfall Uncertainties Where Are We after Thirty Years of Effort?" Bulletin of the American Meteorological Society **91**(1): 87-+.
- Kumar, P. (1999). "A multiple scale state-space model for characterizing subgrid scale variability of near-surface soil moisture." Geoscience and Remote Sensing, IEEE Transactions on **Volume 37, Issue 1, Part 1**: 182-197.
- Lawrence, D., K. W. Oleson, et al. (2010). "Parameterization Improvements and Functional and Structural Advances in Version 4 of the Community Land Model." Journal of Advances in Modeling Earth Systems **Submitted**.
- LDAS. (2011, 07/02/2011). "LDAS Homepage." Retrieved 07/10, 2011, from <http://ldas.gsfc.nasa.gov/>.
- Li, K. Y., M. T. Coe, et al. (2005). "Investigation of hydrological variability in west Africa using land surface models." Journal of Climate **18**(16): 3173-3188.
- Liang, X., D. P. Lettenmaier, et al. (1994). "A Simple Hydrologically Based Model of Land-Surface Water and Energy Fluxes for General-Circulation Models." Journal of Geophysical Research-Atmospheres **99**(D7): 14415-14428.
- Liang, X. and Z. H. Xie (2001). "A new surface runoff parameterization with subgrid-scale soil heterogeneity for land surface models." Advances in Water Resources **24**(9-10): 1173-1193.
- Liang, X. and Z. H. Xie (2003). "Important factors in land-atmosphere interactions: surface runoff generations and interactions between surface and groundwater." Global and Planetary Change **38**(1-2): 101-114.

- Liston, G. E., Y. C. Sud, et al. (1994). "Evaluating Gcm Land-Surface Hydrology Parameterizations by Computing River Discharges Using a Runoff Routing Model - Application to the Mississippi Basin." Journal of Applied Meteorology **33**(3): 394-405.
- Liu, J. T., X. Chen, et al. (2009). "Coupling the Xinanjiang model to a kinematic flow model based on digital drainage networks for flood forecasting." Hydrological Processes **23**(9): 1337-1348.
- Lohmann, D., K. E. Mitchell, et al. (2004). "Streamflow and water balance intercomparisons of four land surface models in the North American Land Data Assimilation System project." Journal of Geophysical Research-Atmospheres **109**(D7): -.
- Lohmann, D., R. Nolte-Holube, et al. (1996). "A large-scale horizontal routing model to be coupled to land surface parametrization schemes." Tellus Series a-Dynamic Meteorology and Oceanography **48**(5): 708-721.
- Lohmann, D., E. Raschke, et al. (1998). "Regional scale hydrology: I. Formulation of the VIC-2L model coupled to a routing model." Hydrological Sciences Journal-Journal Des Sciences Hydrologiques **43**(1): 131-141.
- Marengo, J. A., J. R. Miller, et al. (1994). "Calculations of River-Runoff in the Giss Gcm - Impact of a New Land-Surface Parameterization and Runoff Routing Model on the Hydrology of the Amazon River." Climate Dynamics **10**(6-7): 349-361.
- Matsui, T., A. Beltran-Przekurat, et al. (2007). "Continental-scale multiobservation calibration and assessment of Colorado State University Unified Land Model by application of Moderate Resolution Imaging Spectroradiometer (MODIS) surface albedo." Journal of Geophysical Research-Biogeosciences **112**(G2): -.
- McCabe, M. F., S. W. Franks, et al. (2005). "Calibration of a land surface model using multiple data sets." Journal of Hydrology **302**(1-4): 209-222.
- Mengelkamp, H. T., K. Warrach, et al. (2001). "Simulation of runoff and streamflow on local and regional scales." Meteorology and Atmospheric Physics **76**(1-2): 107-117.
- Miller, J. R., G. L. Russell, et al. (1994). "Continental-Scale River Flow in Climate Models." Journal of Climate **7**(6): 914-928.
- Montaldo, N., J. D. Albertson, et al. (2007). "Dynamic calibration with an ensemble kalman filter based data assimilation approach for root-zone moisture predictions." Journal of Hydrometeorology **8**(4): 910-921.
- Naden, P., P. Broadhurst, et al. (1999). "River routing at the continental scale: use of globally-available data and an a priori method of parameter estimation." Hydrology and Earth System Sciences **3**(1): 109-124.

- Nasonova, O. N. and E. M. Gusev (2008). "Investigating the ability of a Land Surface Model to reproduce river runoff with the accuracy of hydrological models." Water Resources **35**(5): 493-501.
- Nasonova, O. N., E. M. Gusev, et al. (2011). "Application of a land surface model for simulating rainfall streamflow hydrograph: 1. Model calibration." Water Resources **38**(2): 155-168.
- Nelson, B. R., D. Seo, et al. (2006). Multisensor Precipitation Reanalysis. American Meteorological Society 2006 Annual Meeting. Atlanta, GA.
- Nijssen, B., R. Schnur, et al. (2001). "Global retrospective estimation of soil moisture using the variable infiltration capacity land surface model, 1980-93." Journal of Climate **14**(8): 1790-1808.
- Nounou, M. N. (2006). Enhanced State Estimation using Multiscale Kalman Filtering. Proc. 45th IEEE Conference on Decision and Control.
- Oki, T., T. Nishimura, et al. (1999). "Assessment of annual runoff from land surface models using Total Runoff Integrating Pathways (TRIP)." Journal of the Meteorological Society of Japan **77**(1B): 235-255.
- Oki, T. and Y. C. Sud (1998). "Design of Total Runoff Integrating Pathways (TRIP),—A Global River Channel Network." Earth Interactions **2**(1): 1.
- Olivera, F., J. Famiglietti, et al. (2000). "Global-scale flow routing using a source-to-sink algorithm." Water Resources Research **36**(8): 2197-2207.
- Olivera, F. and D. Maidment (1999). "Geographic information systems (GIS)-based spatially distributed model for runoff routing." Water Resources Research **35**(4): 1155-1164.
- Olivera, F. and R. Raina (2003). "DEVELOPMENT OF LARGE SCALE GRIDDED RIVER NETWORKS FROM VECTOR STREAM DATA." JAWRA Journal of the American Water Resources Association **39**(5): 1235-1248.
- Over, T. M. and V. K. Gupta (1994). "Statistical Analysis of Mesoscale Rainfall: Dependence of a Random Cascade Generator on Large-Scale Forcing." Journal of Applied Meteorology **Volume 33, Issue 12**.
- Ozdogan, M., M. Rodell, et al. (2010). "Simulating the Effects of Irrigation over the United States in a Land Surface Model Based on Satellite-Derived Agricultural Data." Journal of Hydrometeorology **11**(1): 171-184.
- Pan, M., H. B. Li, et al. (2010). "Assessing the skill of satellite-based precipitation estimates in hydrologic applications." Water Resources Research **46**: -.

- Pan, M. and E. F. Wood (2009). "A Multiscale Ensemble Filtering System for Hydrologic Data Assimilation. Part II: Application to Land Surface Modeling with Satellite Rainfall Forcing." Journal of Hydrometeorology **10**(6): 1493-1506.
- Pan, M., E. F. Wood, et al. (2009). "A Multiscale Ensemble Filtering System for Hydrologic Data Assimilation. Part I: Implementation and Synthetic Experiment." Journal of Hydrometeorology **10**(3): 794-806.
- Parada, L. M. and X. Liang (2004). "Optimal multiscale Kalman filter for assimilation of near-surface soil moisture into land surface models." Journal of Geophysical Research-Atmospheres **109**(D24): -.
- Parada, L. M. and X. Liang (2008). "Impacts of spatial resolutions and data quality on soil moisture data assimilation." J. Geophys. Res. **113**.
- Paz, A. R., W. Collischonn, et al. (2006). "Improvements in large-scale drainage networks derived from digital elevation models." Water Resources Research **42**(8): -.
- Reed, S. M. (2003). "Deriving flow directions for coarse-resolution (1-4 km) gridded hydrologic modeling." Water Resources Research **39**(9): -.
- Reichle, R. H. and R. D. Koster (2003). "Assessing the impact of horizontal error correlations in background fields on soil moisture estimation." Journal of Hydrometeorology **4**(6): 1229-1242.
- Reichle, R. H., J. P. Walker, et al. (2002). "Extended versus ensemble Kalman filtering for land data assimilation." Journal of Hydrometeorology **3**(6): 728-740.
- Renssen, H. and J. M. Knoop (2000). "A global river routing network for use in hydrological modeling." Journal of Hydrology **230**(3-4): 230-243.
- Seo, D. J. (1998). "Real-time estimation of rainfall fields using radar rainfall and rain gage data." Journal of Hydrology **208**(1-2): 37-52.
- Seo, D. J. (1998). "Real-time estimation of rainfall fields using rain gage data under fractional coverage conditions." Journal of Hydrology **208**(1-2): 25-36.
- Seo, D. J., J. P. Breidenbach, et al. (1999). "Real-time estimation of mean field bias in radar rainfall data." Journal of Hydrology **223**(3-4): 131-147.
- Sheffield, J., A. D. Ziegler, et al. (2004). "Correction of the high-latitude rain day anomaly in the NCEP-NCAR reanalysis for land surface hydrological modeling." Journal of Climate **17**(19): 3814-3828.
- Simone, G., F. C. Morabito, et al. (2000). Radar image fusion by multiscale Kalman filtering. Proc. Third International Conference on Information Fusion FUSION 2000.

- Singh, V. P. and P. K. Chowdhury (1985). "On Fitting Gamma Distribution to Synthetic Runoff Hydrographs " Nordic Hydrology **16**(3): 177-192.
- Slater, A. G., T. J. Bohn, et al. (2007). "A multimodel simulation of pan-Arctic hydrology." Journal of Geophysical Research-Biogeosciences **112**(G4): -.
- Slatton, K. C., M. Crawford, et al. (2001). Multiscale adaptive estimation for fusing interferometric radar and laser altimeter data. Proc. IEEE 2001 International Geoscience and Remote Sensing Symposium IGARSS '01.
- Slatton, K. C., M. Crawford, et al. (2002). Multiscale fusion of INSAR data for improved topographic mapping. Proc. IEEE International Geoscience and Remote Sensing Symposium IGARSS '02.
- Smith, J. A., D. J. Seo, et al. (1996). "An intercomparison study of NEXRAD precipitation estimates." Water Resources Research **32**(7): 2035-2045.
- Sorooshian, S., K. L. Hsu, et al. (2000). "Evaluation of PERSIANN system satellite-based estimates of tropical rainfall." Bulletin of the American Meteorological Society **81**(9): 2035-2046.
- Troy, T. J., E. F. Wood, et al. (2008). "An efficient calibration method for continental-scale land surface modeling." Water Resources Research **44**(9): -.
- Tustison, B., E. Foufoula-Georgiou, et al. (2002). "Scale-recursive estimation for multisensor Quantitative Precipitation Forecast verification: A preliminary assessment." Journal of Geophysical Research-Atmospheres **108**(D8): -.
- van Genuchten, M. T. (1980). "A closed-form equation for predicting the hydraulic conductivity of unsaturated soils." Soil Science Society of America Journal **44**(5): 892-898.
- Vorosmarty, C. J., B. M. Fekete, et al. (2000). "Geomorphometric attributes of the global system of rivers at 30-minute spatial resolution." Journal of Hydrology **237**(1-2): 17-39.
- Vrugt, J. A., H. V. Gupta, et al. (2003). "Effective and efficient algorithm for multiobjective optimization of hydrologic models." Water Resources Research **39**(8): -.
- Vrugt, J. A., H. V. Gupta, et al. (2006). "Application of stochastic parameter optimization to the Sacramento Soil Moisture Accounting Model." Journal of Hydrology **325**(1-4): 288-307.
- Walker, J. P. and P. R. Houser (2004). "Requirements of a global near-surface soil moisture satellite mission: accuracy, repeat time, and spatial resolution." Advances in Water Resources **27**(8): 785-801.

- Wang, S. G. (2010). Studies on Parameter Estimation Methods for Hydrological Model and Associated Uncertainties. Zhengzhou, China, Yellow River Conservancy Press.
- Wang, S. G., X. Liang, et al. (2011). "How much improvement can precipitation data fusion achieve with a Multiscale Kalman Smoother-based framework?" Water Resour. Res. **In press**.
- Wang, X. W., H. J. Xie, et al. (2008). "Validating NEXRAD MPE and stage III precipitation products for uniform rainfall on the Upper Guadalupe River Basin of the Texas Hill Country." Journal of Hydrology **348**(1-2): 73-86.
- Willisky, A. S. (2002). "Multiresolution Markov models for signal and image processing." Proceedings of the IEEE **90**(8): 1396-1458.
- Xia, Y. L., Z. L. Yang, et al. (2004). "Impacts of data length on optimal parameter and uncertainty estimation of a land surface model." Journal of Geophysical Research-Atmospheres **109**(D7): -.
- Xie, Z. H., F. Yuan, et al. (2007). "Regional parameter estimation of the VIC land surface model: methodology and application to river basins in China." Journal of Hydrometeorology **8**(3): 447-468.
- Zeng, X. B. and M. Decker (2009). "Improving the Numerical Solution of Soil Moisture-Based Richards Equation for Land Models with a Deep or Shallow Water Table." Journal of Hydrometeorology **10**(1): 308-319.
- Zhao, R. J. (1992). "The Xinanjiang Model Applied in China." Journal of Hydrology **135**(1-4): 371-381.
- Zhou, Y. H., D. McLaughlin, et al. (2006). "Assessing the performance of the ensemble Kalman filter for land surface data assimilation." Monthly Weather Review **134**(8): 2128-2142.
- Zhou, Y. H., D. McLaughlin, et al. (2008). "An ensemble multiscale filter for large Nonlinear data assimilation problems." Monthly Weather Review **136**(2): 678-698.